Investigations into the Role of 4,5-Diazafluorenone

in Aerobic Palladium Catalyzed Oxidations

by

Jonathan N. Jaworski

A dissertation submitted in partial fulfillment of the requirements for the degree of

Doctor of Philosophy

(Chemistry)

at the

UNIVERSITY OF WISCONSIN – MADISON

2017

Date of final oral examination: 8/15/2016

The dissertation was approved by the following members of the Final Oral Committee:
  Shannon S. Stahl, Professor, Chemistry (Organic)
  Clark R. Landis, Professor, Chemistry (Organic)
  Tehshik P. Yoon, Professor, Chemistry (Organic)
  Jennifer M. Schomaker, Professor, Chemistry (Organic)
  Thomas C. Brunold, Professor, Chemistry (Inorganic)

Investigations into 4,5-Diazafluorenone and its Role in Aerobic Palladium Catalyzed Oxidation Reactions

Jonathan N. Jaworski

Under the supervision of Professor Shannon S. Stahl

At the University of Wisconsin–Madison

Abstract:

Aerobic palladium catalyzed oxidation reactions proceed through an oxidase-style mechanism where O_2 is used as a terminal oxidant and Pd^{II} performs substrate oxidation. Ligands are often employed to help facilitate Pd^0 reoxidation but also decrease the electrophilicity of Pd^{II} which is important for substrate oxidation. Understanding the balance between Pd^{II} electrophilicity and Pd^0 stabilization is important for performing efficient aerobic Pd-catalysis. Aerobic catalysis often employs pyridine derived ligands that strongly coordinate to Pd^{II} and inhibit substrate catalysis. 4,5-Diazafluoren-9-one (DAF) has been identified as a unique ligand for aerobic catalysis that enables very efficient aerobic turn over as well as substrate oxidation. This thesis is an in-depth investigation of how this ligand promotes aerobic palladium oxidation catalysis.

Chapter 1 highlights the mechanistic aspects of palladium catalyzed alkene oxygenation as well as palladium catalyzed allylic C-H acyloxylation. Chapter 2 is a review of all of the recent reactions that have been developed that utilize DAF as a ligand. Chapter 3 is an extensive study of the coordination chemistry of DAF with $Pd(OAc)_2$ as well as permutations of DAF and Pd^{II} carboxylates that have been utilized in catalysis previously. Chapter 4 explores the implications of the coordination chemistry in the context of the intramolecular aza-Wacker reaction. Chapter 5 reports the characterization a novel DAF ligated Pd^I species that forms in both the intramolecular aza-Wacker reaction as well as the acetoxylation reaction and explores its implications in catalysis. Chapter 6 is a kinetic mechanistic investigation of the DAF-promoted allylic C-H acetoxylation reaction in which the resting state of the catalyst is investigated using X-ray absorption spectroscopy and NMR spectroscopy.

Acknowledgements:

First and foremost, I would like to thank Professor Shannon Stahl for his patient mentorship in helping me develop as a scientist and a chemist. His enthusiasm for science is infectious and inspiring. I am grateful for all the opportunities he has given me to pursue my scientific curiosities as well as cultivating a great atmosphere to work in.

Secondly, I would like to thank my palladium cohort for many good scientific discussions as well as their comradery. A special thanks to Andrei Iosub for his numerous engaging late night discussions. I am grateful to Paul White for helping me develop my NMR skillset and being patient with me early on in the DAF projects. Adam Weinstein for his tutorage in helping me push my projects in useful directions. Dian Wang also for being a great colleague and helping me pursue tangential mechanistic hypotheses with computations. Also, thank you to Caitlin Kozack and Chase Salazar for allowing me to participate in the beginning of their graduate career and helping me learn to become a better mentor.

Many other people here at Wisconsin have helped make this experience especially valuable and contributed to my development as a scientist. Scott McCann for his numerous mechanistic conversations and assistance with calculations. Prof. Ian Tonks for his insights on catalysis, organometallic chemistry and reactor design. To Jamie Chen for their help with doing x-ray absorption studies and enduring the tireless trips to Argonne. To Damian Hruszkewycz for answering all my pesky palladium(I) questions and being a great friend.

Numerous other people who were helpful in various scientific endeavours include who I am grateful to are Ravi Pohkrel, Brad Ryland, Alison Suess, Matt Rigsby, Doris Pun, Jinho Kim, Jessica Hoover, Alison Campbell, and Yusuke Izawa. Thank you to Sue Zultanski, Alastair Lennox, Stephen Tereniak, Colin Anson, Michael Ryan and Alison Wendlandt for their numerous conversations about chemistry. Thank you to Nick Beach, Kendall Schneider and Steve Myer for assisting me in the machine shop and designing my

reactor for Argonne. To Charlie Fry who has been incredibly helpful and an invaluable resource for myself and the Stahl group. Without him none of these projects would have been possible.

I would also like to acknowledge all the other scientists not at Wisconsin who have helped me over the years. Ankona Datta for taking me on as an undergraduate in the Raymond lab at U. C. Berkeley. Yan Lou at Roche for allowing me to get a glimpse into the pharmaceutical research setting at Roche. Ronald Zuckermann for allowing me to work at Lawrence Berkeley and build molecules together in the foundry. To Romas Kudirka and Kamil Godula for helping me to navigate my time at LBNL.

Last but not least, I would like to thank my family. My parents for always being incredibly supportive of my decisions. To my sister for allowing me to rant to her numerous times and being a great friend. And also to my brother for teaching me that my passion and intensity needs to be tempered with compassion and humility.

Acronyms:

AP - amidopalladation
BPM – 2,2'-bipyrimidine
BPY – 2,2'-bipyridine
BQ – 1,4-benzoquinone
DA - Diels-Alder adduct of benzoquinone and 1,3-cyclohexadiene
Co(TPP) - 5,10,15,20-Tetraphenyl-21H,23H-porphine cobalt(II)
DAF - 4,5-diazafluoren-9-one
DMA - Dimethylacetamide
Dioxane – 1,4-Dioxane
DIPEA - N,N-Diisopropylethylamine
DFT – Density Functional Theory
DMF – N,N-Dimethylformamide
DMPA – N,N-Dimethylpropionamide
DMSO – Dimethylsulfoxide
dr – diastereomeric ratio
EXAFS – Extended X-ray Absorption Fine Structure
EXSY – Exchange Spectroscopy
Fe(Pc) - Iron(II) phthalocyanine
GC – Gas Chromatography
HMBC – Heteronuclear Multiple-Bond Correlation
HSQC – Heteronuclear Single Quantum Coherence
IPr - 1,3-bis(2,4,6-tri-isopropyl)imidazol-2-ylidene
KIE – Kinetic Isotope Experiment
NOESY - NOESY – Nuclear Overhauser effect spectroscopy
2,6-Me2BQ – 2,6-Dimethyl-1,4-benzoquinone
Me_2DAF – 9,9'-Dimethyl-4,5-diazafluorene
Nc, Neocuproine – 2,9-Dimethyl-1,10-phenanthroline
NMP – N-methyl pyrrolidine
2-Phenyl-1,4-Benzoquinone - PhBQ
PhTMS – trimethyl(phenyl)silane
Phen – 1,10-Phenathroline
Py – pyridine
sp - -(-)-sparteine
TBAI - tetrabutylammonium iodide
TFA – trifluoroacetate
THF – tetrahydrofuran
TOCSY – Total Correlation Spectroscopy
TON – Turn over number
TOF – Turn over frequency
Ts, tosyl – p-toluenesulfonyl
XAS – X-ray absorption spectroscopy

Table of Contents

List of Figures:

Chapter 1: Highlight of Oxidative Pd-Catalyzed C-O Bond Formation Reactions

1.1 Abbreviated Historical Aerobic Alkene Oxidation with Pd.

The field of aerobic oxidative catalysis has been an area of extensive research for the past century. Many chemical oxidants are often used to oxidize a catalyst in performing oxidations such as peroxides, nitrates and chlorite related species, metal salts of copper, silver, iron, chromium, manganese, hypervalent iodine, quinones, etc.; however, these oxidants produce stoichiometric amounts of waste and sometimes toxic byproducts.[1] Molecular oxygen is a cheap and abundant chemical oxidant that produces only water when reduced and can serve as the oxidant in a wide range of metal-catalyzed oxidation reactions.[2] Pure O_2 is hazardous however, the dangers associated with O_2 can mitigated through dilution and engineering design.[3] O_2 has been successfully utilized on large scale for the synthesis of largely commodity scale products. Some examples include the cumene process to produce acetone and phenol, the synthesis of terephthalic acid from *p*-xylene or the Wacker (-Hoechst) process where acetaldehyde is obtained from ethylene and water.[4] The Wacker process is a prominent example of an oxidase style mechanism where O_2 is a stoichiometric oxidant used to turn over an oxidation catalyst.[5] An oxidase mechanisn is often juxtaposed to an oxygenase mechanism where the O_2 is incorporated into the product (Scheme 1.1) and toggling between the two can sometimes be challenging.
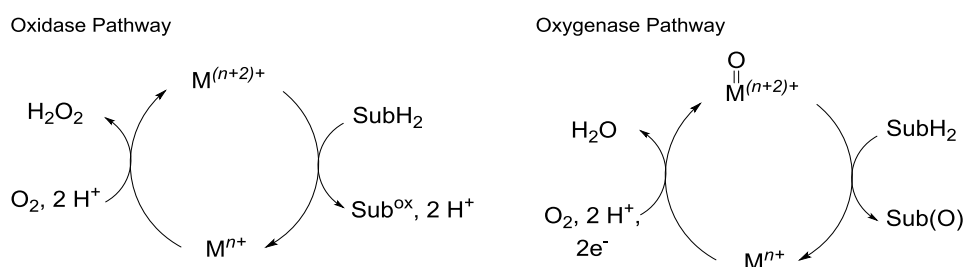
Scheme 1.1: Mechanistic Pathways in Aerobic Oxidation Catalysis

Palladium catalyzed aerobic oxidations have been extensively investigated since early 20th century.[6] The Wacker process ushered in the field of oxidative aerobic catalysis with its remarkably simple reaction conditions of $PdCl_2$ with co-catalytic amounts of $CuCl_2$ in water and air as the oxygen source. The Wacker process is still one of the largest homogeneous reactions carried out on large scale in industry to transform

ethylene to acetylaldehyde.[4] Concurrently with the Wacker process were investigations into the synthesis of related compounds such as vinyl acetate from ethylene and acetic acid.[7] Large scale homogeneous syntheses of related acetoxylated alkenes have not been implemented in favor of gas phase processes.[8] The mechanism of the Wacker reaction is shown below (Scheme 1.2). Pd^{II} coordination to the alkene is followed by nucleopalladation (oxypalladation) of water. This is followed by β-hydride elimination the produce enol product that tautomerizes to the desired aldehyde product. The generated Pd-H species then undergoes reductive elimination to form HX and Pd^0. Catalyst reoxidation is then thought to proceed through a redox pathway where two Cu^{II} oxidize Pd^0 to Pd^{II} and while O_2 reoxidizes Cu^I to Cu^{II}.
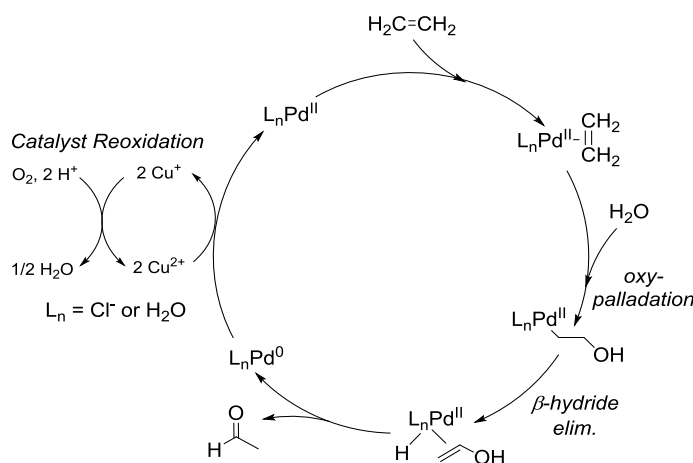
Scheme 1.2: Wacker Oxidation Reaction Mechanism

The Wacker reaction has also seen many synthetic applications in complex molecule synthesis and many analogous reaction methodologies have been developed.[9] Regioselective methods to control Markovnikov or anti- Markovnikov selectivity has been an active field of research where nitrate additives have been shown to help select for the terminal aldehyde product over the more traditional Markovnikov (internal) product.[10] Intermolecular couplings with tethered oxygen or nitrogen nucleophiles have also been investigated,[11] however, they are limited in scope and often produce only enimide products as opposed to the allylic amine.[12] Products in Wacker-type cyclizations are typically limited to 5 and 6 membered rings and still require fairly high catalyst loadings of 1-10 mol % loadings. The aza-Wacker variants can tolerate

a large variety of sulfonyl amide derivatives and can be performed with high diastereo- and enantioselectivity.[13]

1.2 Development of Methods for Acetoxylation of Dienes.

Mechanistically similar to the Wacker reaction and chronologically, the next class of reactions to be developed was the diacetoxylation of 1,3-dienes. The mechanism for the 1,4-diacetoxylation of dienes starts with oxypalladation to form a Pd-alkyl intermediate followed by coordination of the alkene and π-allyl formation. The formation of a π-allyl is distinct from Wacker oxidations which would proceed via β-hydride elimination to give an unsaturated product. Reductive elimination from the π-allyl provides the diacetoxylated product. These 1,4-diacetoxylation catalyst utilize benzoquinone to help differentiate reactivity away from Wacker-type oxidations (and β-hydride elimination) in that benzoquinone promotes reductive elimination (Scheme 1.3).[14]
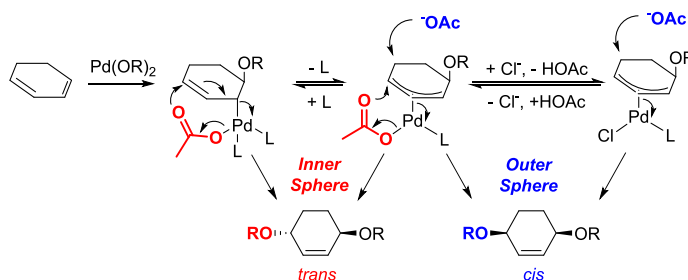
Scheme 1.3: Mechanistic Proposal for Observed Diastereoselectivity

The catalyst systems developed for the diacetoxylation of 1,3-dienes systems also allowed for exquisite control of diastereoselectivity.[15] An inner sphere reductive elimination pathway is favored in the absence of additives to give *trans* diacetoxylation products (Scheme 1.3). With additives such as phosphines or chlorides, an outer sphere reductive elimination pathway was favored to give *cis* diacetoxylation products. Superior reactivity of 6-membered 1,3-dienes was observed whereas 5- or 7-member 1,3-diene substrates reacted slower. Large ring sizes were generally less reactive and substitution on the ring results in a mixture of regioisomers and diastereomers. Larger ring sizes also preferred *cis* product formation. Linear 1,3-dienes

were also tolerated for the 1,4-diacetoxylation reaction with moderate success. Other nucleophiles such as

alcohols, chlorides and mixed TFA/OAc systems have been developed.[16]

Initially the diacetoxylation of dienes employed stoichiometric amounts of benzoquinone as an

oxidant.[17] Numerous permutations of these conditions were later developed that utilized catalytic quinone.

For example, stoichiometric oxidants such as MnO_2 (Scheme 1.4)[18] or tBuOOH[19] can be coupled with

catalytic quinone. The use of electron-transfer mediators (ETMs) such as Co(TPP), FePc or heteropolyacids

were successful in coupling O_2 with catalytic amounts of benzoquinone thereby enabling aerobic catalyst

turn over.[20] ETMs has since became common place in the field of aerobic catalysis for a variety of

transformations beyond 1,4-diacetoxylation (Scheme 1.5).[21]
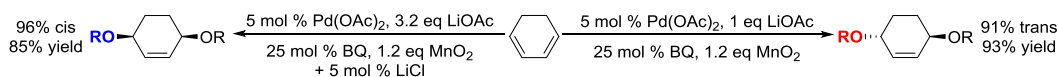
Scheme 1.4: Diasteroselectivity for 1,4-Diacetoxylation of 1,3-Butadienes
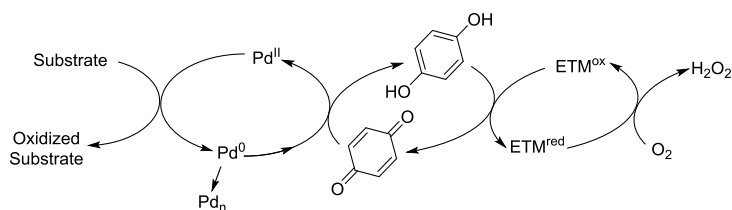
Scheme 1.5: Oxidation of Substrate Facilitated by ETMs in Catalysis

Alkene ligands have also been used in Pd-catalyzed 1,4-diacetoxylation of 1,3-dienes to promote

diastereoselectivity and rate of product formation. Bäckvall and co-workers designed a sulfoxide ligand

with an appended quinone that helped to improve diasteroselectivity and product formation. [22] This

improved the reaction in multiple ways. The sulfoxide-quinone ligand enabled aerobic turnover as it worked

synergistically with ETMs such as iron(II) phthalocyanine (FePc)to promote reoxidation of the quinone

moiety by O_2. Additionally, the rate of product formation was increased compared to quinone alone and the

selectivity for the *trans* product was improved (Scheme 1.6A). The sulfinyl group of the ligand is believed

to coordinate to a monomolecular π-allyl species before the π-allyl species can dimerize (Scheme 1.6B).

Arresting the Pd π-allyl dimerization allows for *cis* migration of the acetate to occur and the *trans*

diacetoxylation products is obtained. The mechanism was probed through titration experiments in acetic acid using catalytic amounts of DMSO and CH3CN ligands which concluded that these ligands can help disrupt the dimeric π-allyl structure. No reductive elimination was observed in these titrations and DMSO has been previously observed to break up π-allyls ([Pd(η³-allyl)(OAc)]₂, [Pd(η³-allyl)Cl]₂) to their monomeric species.[23] An enantioselective method using the sulfinyl quinone scaffold was able fairly successful where a 41% ee was obtained in performing the 1,4-dialkoxylation with added methanesulfonic acid.[24]
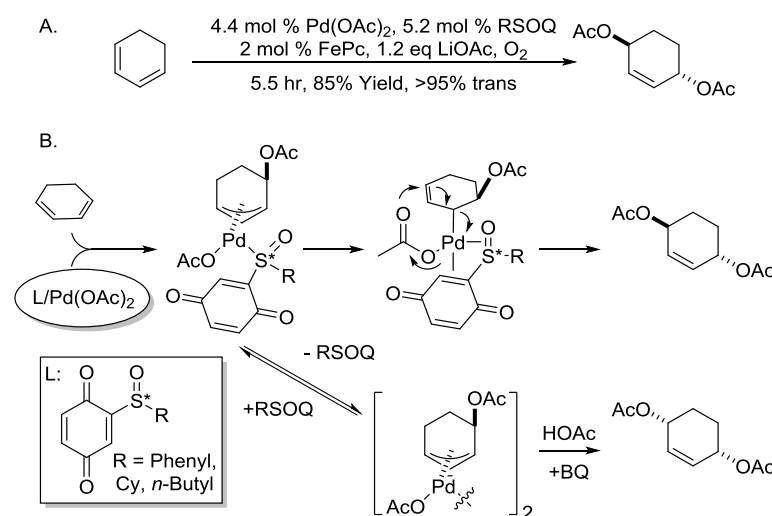
Scheme 1.6: Sulfoxide-Quinone (RSOQ) Ligand in 1,4-Diacetoxylation of 1,3-Dienes

Mechanistic investigations by Eastgate and coworkers into the 1,4-diacetoxylation of 1,3-cyclobutadiene with stoichiometric BQ revealed a change in the diasteromeric ratio over time. [19] Further investigations led them to discover an in situ generated ligand from the Diels-Alder reaction between benzoquinone and 1,3-cyclohexadiene. They found that utilizing the "DA" ligand provided faster reaction rates and improved the diastereomeric ratio. This led to the development of a the new pre-catalyst [Pd(DA)₂] (Figure 1.1) for 1,4-diacetoxylation of 1,3-butadienes that is used on process scale for the productin of the *cis*-diastereomer of the diacetoxylation of 1,4-cyclohexadiene.[19] In the reaction mechanism, the DA ligand is believed to force the reaction to proceed through a cationic intermediate which promotes the rate of product formation.
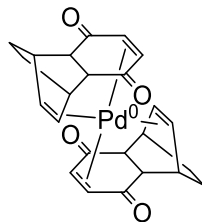
Figure 1.1: Pd(DA)$_2$ Precatalyst

1.3   Oxidative Allylic C-H Acetoxylations and Related C-O Bond Formations

Despite the early successes with the 1,4-diacetoxylation of 1,3-dienes, direct allylic C–H acetoxylation lagged behind. Early reports of allylic C–H acetoxylation date back to 1963 by Anderson and Winstein who observed stoichiometric reactivity with Pd(OAc)$_2$ and cyclohexene.[25] Acetoxylation of cyclohexene was explored as a model system in many stoichiometric studies,[26] however it was not until 1982 that the first catalytic reactions were reported by Uemura and co-workers.[27] The Uemura system utilized 5 mol % PdCl$_2$ with cocatalytic amounts of AgOAc and TeO$_2$ with tBuOOH as the oxidant to acetoxylate cyclopentene. A subsequent system developed by Heumann and Åkermark was more efficient; using 0.5 mol % Pd(OAc)$_2$, 5 mol % BQ, and 1 eq MnO$_2$ in acetic acid and 95% yield of mono-acetoxylated cyclohexene was obtained. Concurrent with the systems of Uemura and Heumann-Åkermark, a system was developed by McMurry and Kočovsky that ulitized Pd(TFA)$_2$, *o*-methoxyacetophenone and stoichiometric benzoquinone.[28] This last report was likely inspired by a seminal work by Trost regarding the synthesis and stability of various π-allyls that could be synthesized by Pd(TFA)$_2$ and their dehydrogenation/disproportionation to make aromatics.[29]

Allylic C-H acetoxylation of cyclohexenes and related substrates were achieved aerobically with catalytic benzoquinone and the incorporation of ETMs such as macrocycles with iron and cobalt[30] (Scheme 1.7A) or heteropolyacids such as phosphomolybdovanadic acids.[31] In addition to simple cyclic alkenes, terminal linear alkenes or internal symmetric alkenes were compatible with these conditions as well as dienes. Unfortunately, these reactions were plagued by poor mass balance and substitutions of the cyclic or internal alkene substrates resulted in a mixture of diastereomers and regioisomers (Scheme 1.7B).[32] The

change in reactivity is partially dictated by the substrate however catalysts that utilize PdCl$_2$ salts with added water are more commonly used in Wacker-type chemistry than acetoxylation. Acetoxylation methods with terminal blocking groups such a phenyl or cyano group to stop isomerization and improve selectivity were developed[33] but competing Wacker oxidation was difficult to suppress.
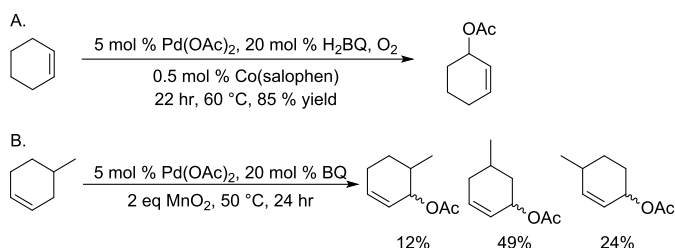
Scheme 1.7: Illustrative Acetoxylation Reactions of Cyclohexene Substrates [30]

Directing group effects can also be used to control the diastereoselectivity for the acetoxylation of alkenes. Initial investigations were performed on 4-vinyl-1-cyclohexene using PdCl$_2$ and phosphine ligands. The appended alkene directs the Pd center to form the more sterically encumbered η^3-allyl and the phosphine helps to force the isomerization to the σ-allyl in order to restrict an outer sphere reduction elimination (Scheme 1.8).[34] Additional directing group effects have been investigated with limonene derivatives to probe regioselectivity of acetoxylation and methoxylation.[35] In these studies, regioselectivity was improved with the incorporation of sulfonic acid derivatives (Scheme 1.9). It was proposed that a counterion exchange from acetate to tosylate helps promote the formation of a cationic π-allyl and similar mechanistic hypotheses have been proposed before.[19]
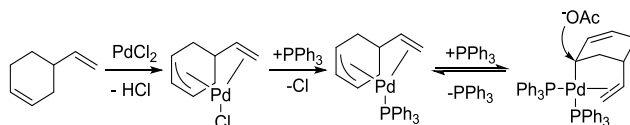
Scheme 1.8: Diastereoselective Directed Acetoxylation of 4-vinyl-1-cyclohexene
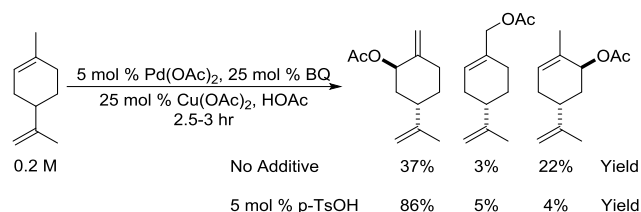
Scheme 1.9: *p*-Toluenesulfonic Acid Effect on Limonene Acetoxylation

Oxidative methods to functionalize allylic C-H bonds were often hard to distinguish mechanistically as two distinct mechanisms could be operative. Acetoxypalladation followed by β-hydride elimination could be operative (similar to Wacker oxidation) or a mechanism that involved allylic C-H activation followed by reductive elimination (direct allylic C-H acetoxylation). In fact, both mechanisms can be operative (Scheme 1.10)[36] and dehydrogenated products can form via β-hydride elimination from a π-allyls.[37] Elucidation of the operative mechanism and being able to toggle between them is important for designing selective catalyst systems. The development of new allylic C-H acetoxylation methods stagnated with fairly basic cyclic substrates as reactivity and selectivity seemed to be problematic. This field of oxidative allylic C-H functionalization was surpassed by the development of Tsuji-Trost chemistry where pre-oxidized allyl groups such as allyl chlorides were used to make functionalized allyl groups.[38]
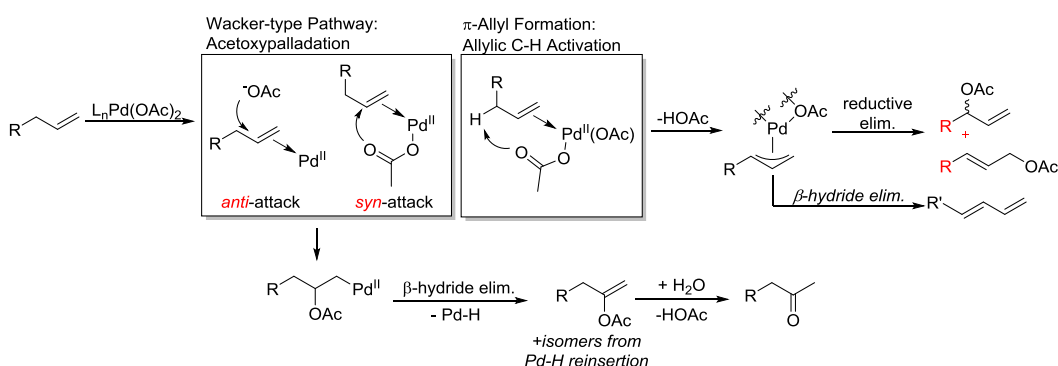
Scheme 1.10: Possible Mechanistic Pathways for C-H Acetoxylation

The field of allylic C-H acetoxylation was reinvigorated by M. C. White and her studies of the acetoxylation of linear terminal alkenes. It was discovered that sulfoxide ligands were able to modulate the selectivity of linear and branched acetoxylation products (Scheme 1.11).[39] A solvent mixture of AcOH and

DMSO resulted in formation of mostly linear acetoxylation products whereas AcOH resulted in Wacker products. Inclusion of [1,2-bis(benzylsulfinyl)ethane] as a ligand with Pd(OAc)$_2$ shifted product selectivity to branched acetoxylation (Scheme 1.11). Additional investigations showed the phenyl *bis*-sulfoxide ligand was just as effective and that the *bis*-sulfoxide ligands decompose to vinyl sulfoxides which also promoted branched selectivity.[40,41] These sulfoxide promoted acetoxylation reactions require long reaction times up to 72 hours, high catalyst loadings of 10 mol % and provide modest yields (2-7 TONs for Pd catalyst).

	Linear	Branched	Vinyl Acetate	Methyl Ketone	L : B
1. AcOH	3	5	17	14	1:2
2. DMSO/AcOH 1:1	40	2	3	6	20:1
3. DCM/AcOH 1:1 10 mol % [BnSOCH$_2$]$_2$	8	66	<1	<1	1:8
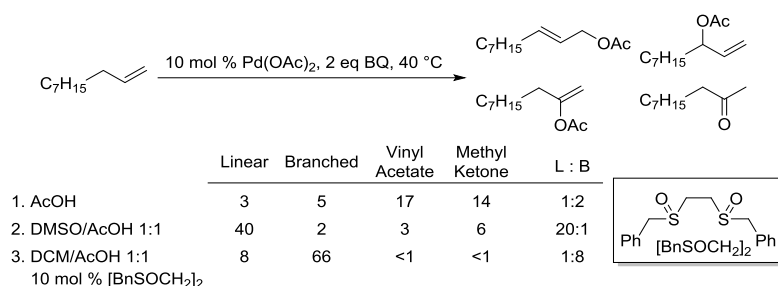
Scheme 1.11: Ligand Modulated Regioselective Acetoxylation of Terminal Alkenes

Initial stoichiometric studies showed that the ligands, BQ and *bis*-sulfoxide, act in tandem to promote separate steps in the reaction mechanism and this phenomena became known as serial ligand catalysis. It was proposed that the sulfoxide ligand promotes the C-H activation step and benzoquinone promotes reductive elimination (Scheme 1.12). Stoichiometric studies where π-allyl acetate dimer is subjected to BQ without the *bis*-sulfoxide ligand provided acetoxylated products that favor branched over linear by 9:1 with mass balance of 58%. This selectivity pattern in the reductive elimination is thought to be a result of a *trans* effect imbued from the electron-deficient benzoquinone. The quinone coordinates to the sterically less congested site on Pd[II] and promotes the buildup of positive charge on the internal carbon. Inner sphere reductive elimination from the electronically differentiated allyl ligand results in selectivity for branched product (Scheme 1.12). A monomeric Pd π-allyl is believed to be the relevant catalytic intermediate; however only dimerized π-allyl was observed in the reaction conditions. These observations are reminiscent of some of the observations that Bäckvall and Eastgate had regarding the 1,4-diacetoxylation diene systems.[19,22] Sulfoxide ligands have been shown to disrupt π-allyl dimer structure however M. C. White

and co-workers were unsuccessful in characterizing sulfoxide interactions by UV-vis or NMR. The mechanism for reductive elimination with the DMSO/AcOH system has not been investigated. The authors speculated that a change in the mechanism of reductive elimination is likely operative.[42]
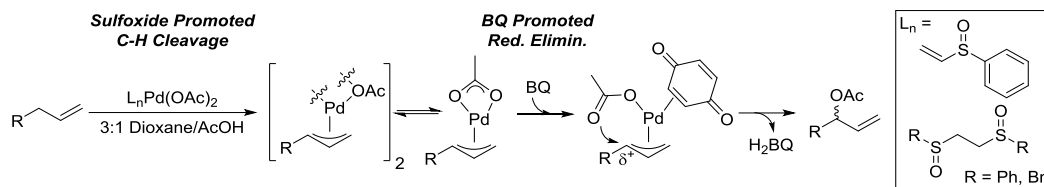
Scheme 1.12: Proposed Model for Branched Acetoxylation of Linear Alkenes

Bercaw and co-workers developed a system using 2,2'-bipyrimidine (BPM) with Pd(OAc)$_2$ for the acetoxylation of alkenes with stoichiometric BQ.[43] Mechanistic investigations showed that optimal catalysis was achieved with 1:2 ratio of BPM to Pd(OAc)$_2$ leading the authors propose that the active catalyst is a dimeric Pd species with stoichiometry of (BPM)Pd$_2$(OAc)$_4$. The binding of a second Pd(OAc)$_2$ to BPM is proposed to weaken the Pd-N bond and enhance ligand lability which is important for substrate coordination. The authors observe a zero-order dependence on BQ in reductive elimination and only linear allyl acetate products are observed in stoichiometric reactions between BQ and (κ^2-BPM)Pd(η^3-cinnamyl) – *distinctly different product selectivity compared to the M. C. White system*. Acetate exchange between cinnamyl acetate was observed in the presence of (κ^2-BPM)Pd(η^3-cinnamyl) and solvent d_3-AcOH. These results suggest that reductive elimination is promoted by BPM and that BQ is solely responsible for product displacement and reoxidation of Pd^0. This is a surprising finding in that BQ is often proposed to be intimately involved in reductive elimination. The authors proposed that either acetate attack on the Pd π-allyl or alkene coordination are rate-determining in this mechanism. A catalytic cycle is presented below, (Scheme 1.13) with either a dimeric or monomeric catalyst being involved in reductive elimination.
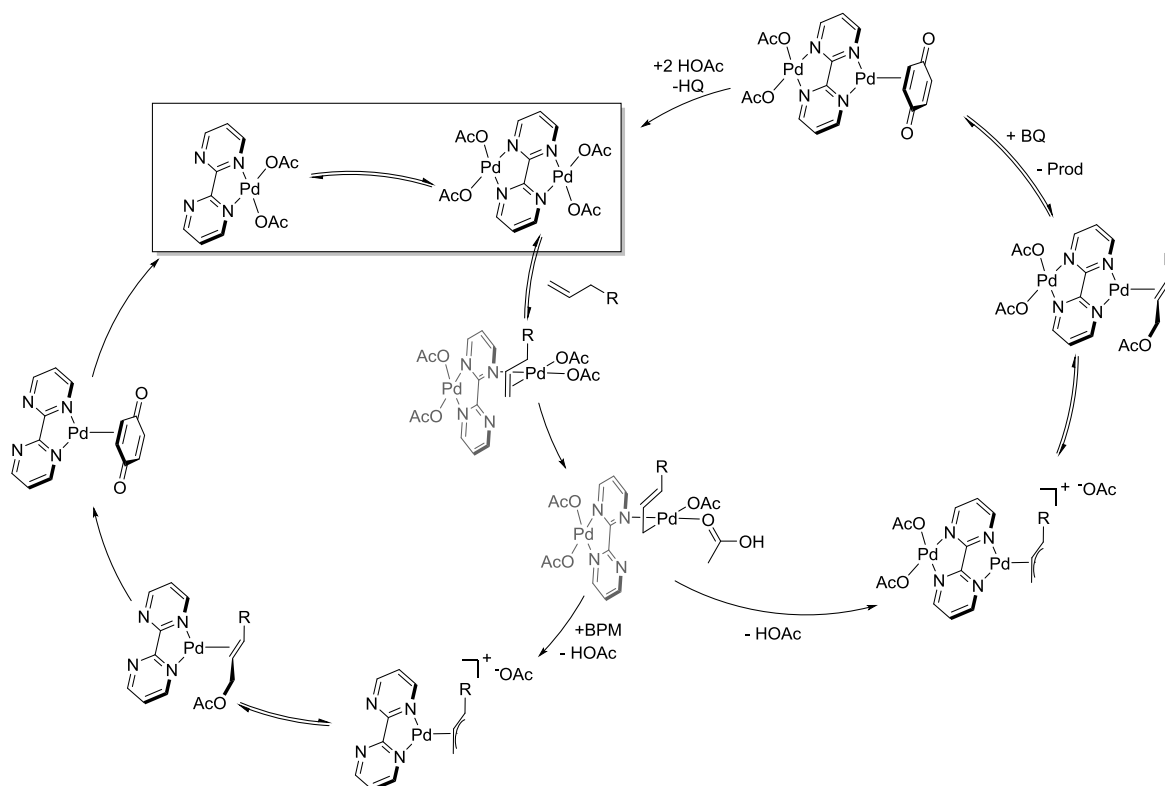
Scheme 1.13: Mechanism of Acetoxylation with bipyrimidine/Pd(OAc)$_2$ and BQ

Other conditions have been developed to accommodate carboxylic acid coupling partners other than acetic acid for allylic C-H oxidation of linear terminal alkenes (Scheme 1.14). Muzart developed a method using aliphatic carboxylic acids and stoichiometric BQ or catalytic BQ with MnO$_2$. The method was tolerant of allylic alcohol moieties and provided interesting 1,4-dioxygenated alkene products in moderate yields (50-60%).[44] M. C. White and co-workers also developed two similar systems that supported low stoichiometry of the carboxylic acid coupling partner. Initial conditions were reported using Pd(OAc)$_2$ and 5.3 eq of DMSO relative to alkene. A change from BQ to 2-phenyl-benzoquinone (PhBQ) improved the yield. The addition of the organic base, DIPEA, is rationalized as a way of activating the carboxylic acid as a nucleophile. An alternative hypothesis could be that DIPEA promotes the reduction of Pd^{II} to Pd^0 and generates a new Pd-carboxylate in situ through the protonolysis of a Pd-peroxo. In situ catalyst generation via reduction is a common strategy employed in the cross coupling literature to generate the active Pd^0 catalyst with the oxidation of trimethylamine.[45] A switch from Pd(OAc)$_2$ to Pd(CH$_3$CN)$_4$(BF4)$_2$ also helps

improve the coupling efficiency as up to 20 mol % of the undesired ester could be synthesized with Pd(OAc)$_2$ if the coupling partner is not AcOH.
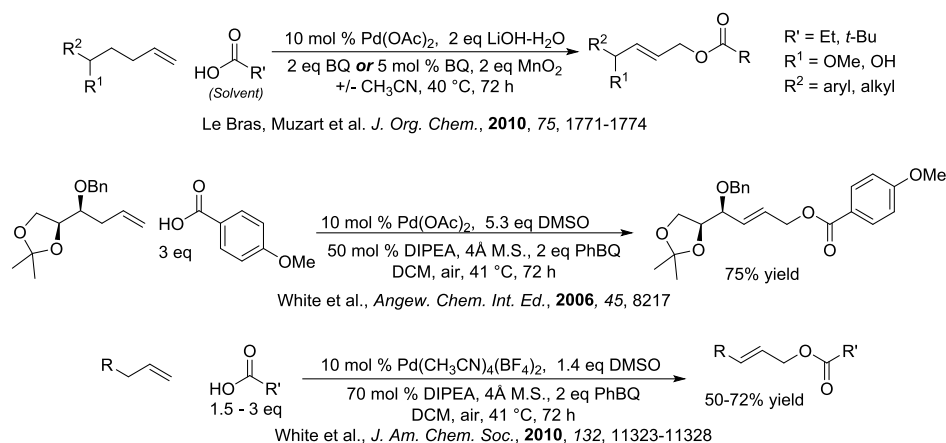
Scheme 1.14: Development of Low Stoichiometry Carboxylate Coupling Conditions

Szabó and coworkers have developed acyloxylation systems that utilize peroxide[46] or hypervalent iodine[47] reagents (Scheme 1.15). These acyloxylation methods invoke Pd(IV) and utilize low stoichiometry of coupling partner relative to alkene. These reactions are proposed to proceed via a Pd(IV)-mediated C-H activation which is rare in the Pd-catalyzed C-H functionalization literature (Scheme 1.16).[48] These methods exhibit exquisite diastereoselectivity for *trans* product formation.
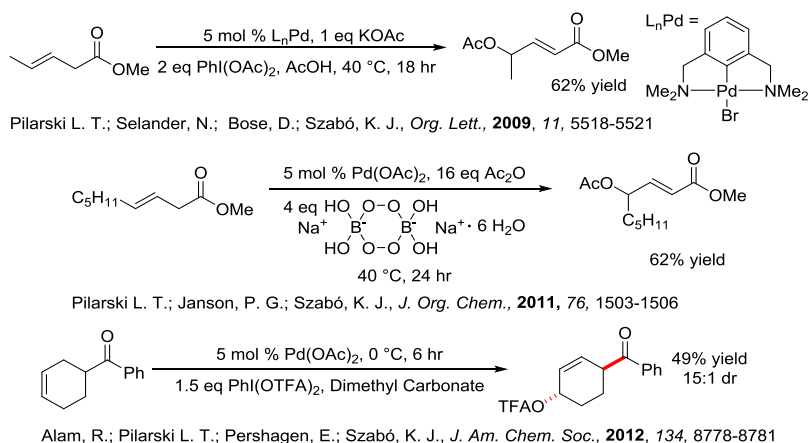
Scheme 1.15*:* Select Examples of Szabó's High-Valent Pd Methods
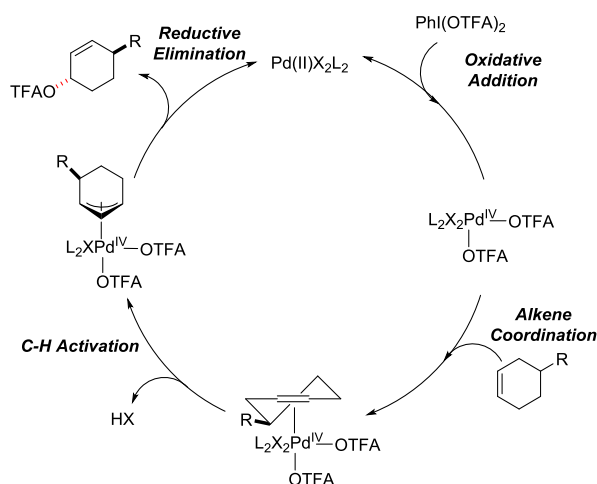
Scheme 1.16: Proposed Catalytic Cycle for High-Valent Pd Alkene Acetoxylation

Stoltz and co-workers developed a system that uses oxone in allylic oxidation of sterically congested substrates (Scheme 1.17).[49] Many of the substrates were derived from lactam substrates that had been previously functionalized by decarboxylative allylation chemistry.[50] Product selectivity for acetoxylation was dependent on keeping the reaction anhydrous through the addition of molecular sieves and acetic anhydride. Enal products were formed with the addition of water.
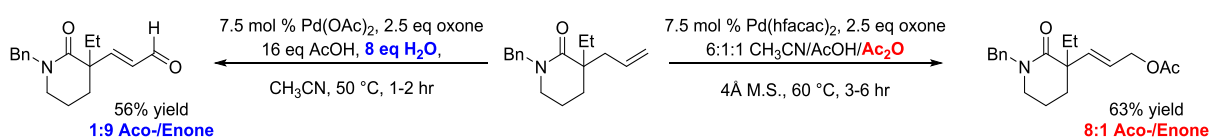
Scheme 1.17: Pd/Oxone System for Allylic C-H Oxidation

1.4 Methods for Diastereo- and Enantioselective Allylic C-H Acyloxylation.

Methods for diastereoselective and enantioselective acyloxylation of allylic C-H bonds have also been developed to modest success. Enantioselective acetoxylation of allylic C-H bonds is challenging. The rapid isomerization of Pd^{II}-allyls can prevent enantioselective C-H activation from being enantiodetermining and shifts the product selectivity to be determined by reductive elimination. Intermolecular couplings suffer from additional complexity in templating a highly fluxional allyl ligand on Pd and controlling the face of exogeneous acetate attack.

M. C. White and co-workers have been the most successful in exploring diastereoselective and enantioselective acyloxylation of allylic C-H bonds. The addition of chiral chromonium(III) salen derivatives to the *bis*-sulfoxide/Pd(OAc)$_2$ catalyst was successful in providing modest enantioselectivity. A 92% yield with 59% ee and 5.3:1 branched/linear with 1-undecene was obtained (Scheme 1.18).[51] This was the first successful Pd-method for allylic C-H acetoxylation of terminal, linear alkenes. Also noteworthy is that this system exhibited a high coupling fidelity with a stoichiometry of 1:1.1 alkene to acetic acid. Preliminary mechanistic experiments suggest that the quinone carbonyl moiety coordinates to the chiral Lewis acid; however, the authors do not rule out a beneficial interaction between the chiral salen complex and acetate as the stoichiometric control reaction with the acetate salt of the chiral Lewis acid and π-allyl provided a modest 22% ee. The addition of L$_n$*Cr(F) also resulted in a 10x fold rate increase for the stoichiometric reductive elimination.
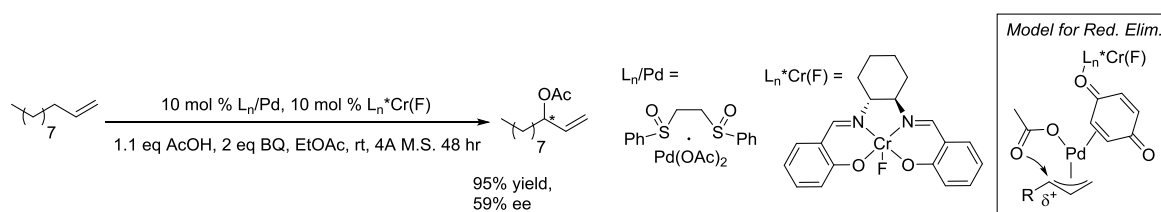
Scheme 1.18: Enantioselective Acetoxylation of Terminal Alkenes

Enantioselective reactions for intermolecular acetoxylation were attempted using a ligand-based approach. Liu and Itami discovered that the use of a sulfoxide with appended chiral oxazoline (sox) ligand provided branched selectivity in the catalytic reaction where benzoquinone is used as the terminal oxidant (Scheme 1.19).[52] They postulated that the stronger donor nature of the oxazoline would keep the ligand bound to the Pd center (as compared to a sulfoxide) and help to promote enantioselective reductive elimination through its appended chiral auxiliary group. Many variations of the sox ligand are successful in promoting the branched selectivity and the method was optimized to provide greater than 99:1 branched:linear selectivity. Unfortunately, product yields were still low (below 70%) and reactions times up to 72 hours are reported and enantioinduction beyond 5% ee was never observed when enantiopure chiral SOX ligands were used. The authors attribute the lack of enantioinduction to the rapid π-σ-π

isomerization of the Pd π-allyl intermediate and the inability of the ligand to control this isomerization. This ligand scaffold has since been successful in performing an intramolecular enantioselective allylic C-H oxidation of terminal olefins to form isochromans.[53] The lack of enantioinduction suggests that BQ is the operative reagent controlling reductive elimination, as previously characterized by M. C. White (Scheme 1.12) and that the SOX ligand does not participate in reductive elimination and only C-H activation.
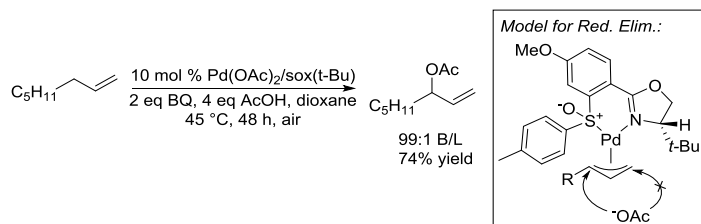
Scheme 1.19: Liu-Itami Acetoxylation with Pd/SOX

The intramolecular oxidative coupling of alkenes with carboxylates have seen more success for catalyst-controlled stereoselectivity. M. C. White developed systems for oxidative ring closing of alkenes with appended carboxylates to synthesize lactones. These methods provide the exo-cyclic alkene (branched selectivity) products with yields up to 60% using 10 mol % Pd/bis-sulfoxide catalyst.[54] This methodology was applied in the synthesis of different epimers of 6-deoxyerythronolide (Scheme 1.20).[55] Using the catalyst previously developed for branched selective intermolecular acetoxylation, a 40:1 dr was obtained, presumably via formation of a chelate with the substrate. This dr was eroded to 1:1.3 favoring the opposite diastereoisomer with the introduction of tetrabutyl ammonium fluoride (TBAF) as an additive (Scheme 1.20). The addition of fluoride is thought to interact with the coordination sphere around the Pd π-allyl, either helping to promote π-σ-π isomerization or displacing a bound carboxylate from the Pd-center and preventing inner sphere/chelate controlled reductive elimination. Similar effects have been previously reported by Bäckvall and Heumann with the addition of chloride or phosphine additives to allow for the outer sphere attack of the carboxylate.[15] Noteworthy is the observation that a method to synthesize lactone products with an internal alkene has not been developed.
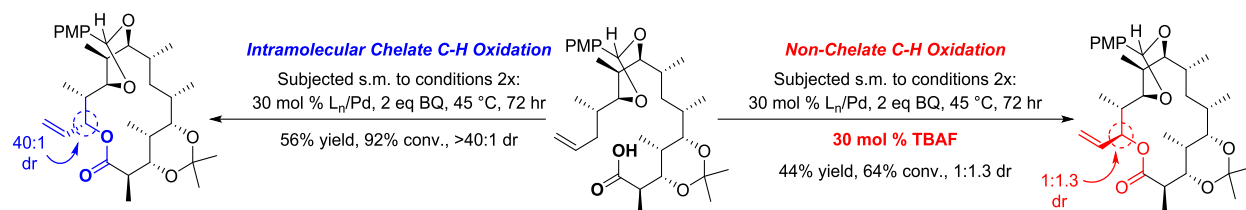
Scheme 1.20: Oxidative Ring Closing for Synthesis of 6-Deoxyerythronolide B and Epimer

Small lactone formation was developed that exhibited high diastereoselectivity via substrate control. An inner sphere/chelate controlled reductive elimination is thought to be operative in this case as well. Addition of Cr(salen)Cl was found to improve the overall yield however, it did not affect the dr and only exo-cyclic alkenes were observed (Scheme 1.21). This method found great utility in complex natural product syntheses as it is a great way to access polyoxidized motifs such as *syn*-1,2-diols and densely functionalized pyrans (Scheme 1.22).
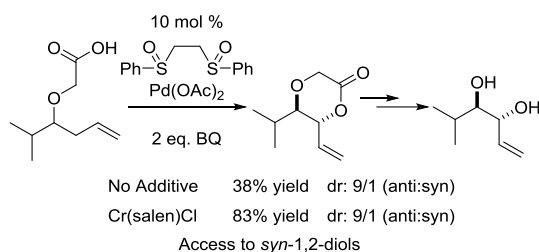
Scheme 1.21: Diasteroselective Lactone Formation for 6-Membered Rings

Saito, T. et al. Org. Lett. **2009,** *11,* 5274.
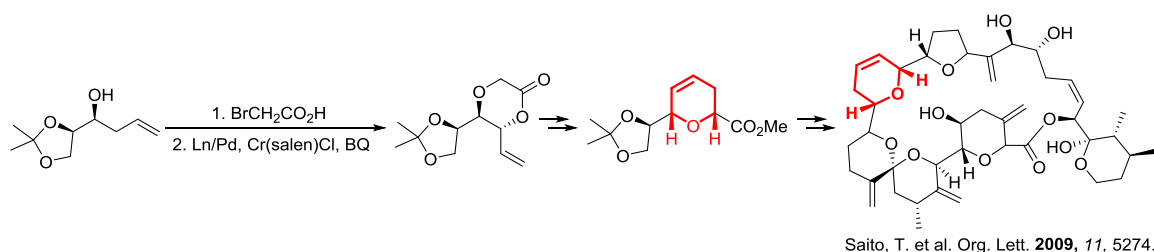
Scheme 1.22: Synthesis of a Densely Functionalized Pyran

An enantioselective intramolecular coupling was successful using SPRIX with Pd(OAc)$_2$. An impressive 98% yield with 82% ee was obtained using the ligand (M,S,S)-i-Pr-SPRIX for the formation of γ-lactams (Scheme 1.23).[56] Other ligands such as Sparteine, BINAP and BOXAX ligand scaffolds all afforded enantio-enriched products. The authors propose a mechanism that involves π-allyl formation; however the

PRIX ligand is strongly coordinating and could disfavor substrate coordination/C-H activation. Moreover, these type of ligands have been used previously in Wacker-type functionalizations. The investigators observe a primary intermolecular KIE when the terminal gem-dimethyl groups are deuterated and suggest that C-H activation (for allylic oxidative functionalization) is rate determining. Alternatively, β-hydride elimination (for Wacker-type pathway) could be just as likely to be operative and could possibly produce a similar KIE.
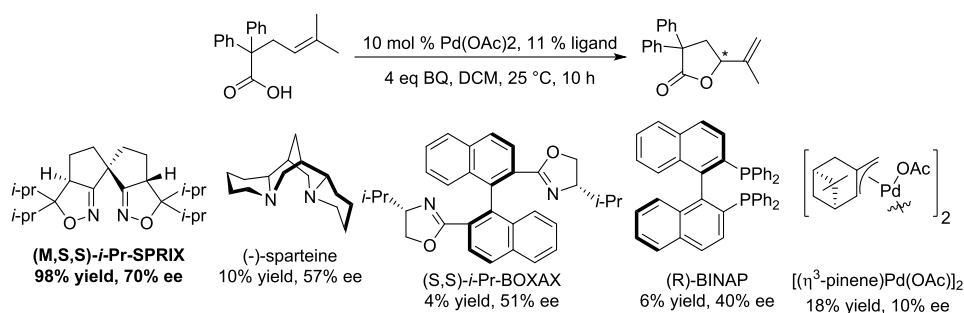
Scheme 1.23: Enantioselective Intramolecular Coupling with SPRIX Ligand

1. Bäckvall, J. E. Modern Oxidation Methods, Wiley-VCH, Weinheim, 2004.

2. (a) Stahl, S. S. Science **2005**, *309*, 1824-1826. (b) Stahl, S. S.; Alsters, P. L. *Liquid Phase Aerobic Oxidation Catalysis: Industrial Applications and Academic Perspectives*, John Wiley & Sons, 2016

3. Osterberg, P. M.; Niemeier, J. K.; Welch, C. J.; Hawkins, J. M.; Martinelli, J. R.; Johnson, T. E.; Root, T. W; Stahl, S. S. Org. Process Res. Dev. **2015**, *19*, 1537–1543.

4. Weber, M. Kleine-Boymann, in Ullmann's Encyclopedia of Industrial Chemistry, Wiley-VCH Verlag GmbH & Co. KGaA, 2000, See chapters on Acetaldehyde for Wacker Process, Phenol for Cumene Process and Terephthalic Acid, Dimethyl Terephthalate, and Isophthalic Acid

5. Cornell, C. N.; Sigman, M. S. *Inorg. Chem.* **2007**, *46*, 1903-1909.

6. (a) Stahl, S. S. *Angew. Chem. Int. Ed.* **2004**, *43*, 3400-3420 (b) Muzart, J. *Chem. Asian J.* **2006**, *1*, 508-515.

7. Moiseew, J. J.; Vargaftik, M. N.; Syrkin, J. K., *Dokl. Akad. Nauk SSSR* **1960,** *133*, 377-380.

8.   Weber, M. Kleine-Boymann, in Ullmann's Encyclopedia of Industrial Chemistry, Wiley-VCH Verlag GmbH & Co. KGaA, 2000, See chapter on Vinyl Esters.

9.   Takacs, J. M.; Jiang, X.-T., *Curr. Org. Chem.* **2003**, *7*, 369 – 396.

10. Wickens, Z. K.; Guzman, P. E.; Grubbs, R.H. *Angew. Chem. Int. Ed.* **2014**, *53*, 1-6.

11. (a) Larock, R. C.; Hightower, T. R., *J. Org. Chem.* **1993**, *58*, 5298-5300 (b) Larock, R. C.; Hightower, T. R.; Hasvold, L. A.; Peterson, K P., *J. Org. Chem.* **1996,** *61,* 3584-3585. (c) Kotov, V.; Scarborough , C. C.; Stahl, S. S. *Inorg. Chem.* **2007**, *46*, 1910-1923. (d) McDonald, R. I.; Liu, G.; Stahl, S. S. *Chem. Rev.* **2011**, *111*, 2981-3019.

12. Brice, J. L.; Harang, J. E.; Timokhin, V. I.; Anastasi, N. R.; Stahl, S. S. *J. Am. Chem. Soc.* **2005**, *127*, 2868-2869.

13. (a) Redford, J. E.; McDonald, R. I.; Rigsby, M. L.; Wiensch, J. D.; Stahl, S. S. *Org. Lett.* **2012**, *14*, 1242-1245. (b) McDonald, R. I.; White, P. B.; Weinstein, A. B.; Tam, C. P.; Stahl, S. S. *Org. Lett.* **2011**, *13*, 2830-2833.

14. Johnson, J. B.; Rovis, T., *Angew. Chem. Int. Ed.* **2008**, *47*, 840 - 871

15. (a) Bäckvall, J.-E.; Byetröm, S. E.; Nordberg, R. E., *J. Org. Chem.* **1984**, *49*, 4619-4631 (b) Bäckvall, J.-E.; Nordberg, R. E.; Wilhelm, D., *J. Am. Chem. Soc.*, **1985**, *107,* 6892-6898.

16. (a) Bäckvall, J.-E., Nystrom, J.-E., Nordberg, R. E, *J. Am. Chem. Soc.*, **1985,** *107*, 3676-3686 (b) Aranyos, A.; Szabo´, K. J.; Bäckvall, J., *J. Org. Chem.*, **1998**, *63*, 2523-2529.

17. Bäckvall, J. E. and Nordberg, R. E. *J. Am. Chem. Soc.* **1981**, *103*, 4959.

18. Bäckvall, J. E.; Byström, S. E.; Nordberg, R. E. *J. Am. Chem. Soc.* **1984**, *49*, 4619.

19. (a) Eastgate, M. D.; Buono, F. G. *Angew. Chem. Int. Ed.* **2009**, *48*, 5958 (b) Zheng, B.; Schmidt,M. A.; Eastgate, M. D. *J. Org. Chem.* **2016**, *81*, 3112

20. (a) Bcckvall, J. E.; Awasthi, A. K.; Renko, Z. D. *J. Am. Chem. Soc.* **1987**, *109*, 4750. (b) Bäckvall, J. E.; Hopkins, R. c.; Grennberg, H.; Mader, M. M.; Awasthi, A. K. *J. Am. Chem. Soc.* **1990**, *112*, 5695. (c) Grennberg, H.; Gogoll, A.; Bäckvall, J. E. *J. Org. Chem.* **1991**, *56*, 5808. (d) Bergstad, K.; Grennberg, H.; Bäckvall, J., *Organomet.*, **1998**, *17*, 45-50.

21. Piera, J.; Bäckvall, J., *Angew. Chem. Int. Ed.,* **2008**, *47*, 3506-3523.

22. Grennberg, H.; Gogoll, A.; Bäckvall, J. *J. Org. Chem.*, **1991**, *56*, 5808-5811

23. Ramey, K. C.; Statton, G. L. *J. Am Chem. Soc.*, **1966**, *88*, 4387 b. Powell, J. *J. Chem. Soc. A.*, **1971**, 2233.

24. Itami, K.; Palmgren, A.; Thorarensen, A.; Bäckvall, J., *J. Org. Chem.*, **1998**, *63*, 6466-6471.

25. Anderson, C. B.; Winstein, S. J. Org. Chem. **1963**, *28*, 605-606.

26. (a) Kitching, W.; Rappoport, Z.; Winstein, S., *J. Am. Chem. Soc.* **1966**, *88*, 2054-2055 (b) Wolfe, S.; Campbell, P. G. C., *J. Am. Chem. Soc.* **1971**, *93*, 1497-1499. (c) Wolfe, S.; Campbell, P. G. C., *J. Am. Chem. Soc.* **1971**, *93*, 1499-1501. (d) Kikukawa, K.; Sakari, K.; Asada, K.; Matsuda, T., *J. Organomet. Chem.*, **1974**, *77*, 131-145. (e) Brown, R. G.; Chaudhari, R. V.; Davidson, J. M., *J. Chem. Soc., Dalton Trans.*, **1977**, 176-183.

27. Uemura, S.; Fukuzawa, S.; Toshimitsu, A.; Okani, Masaya, *Tet. Lett.*, **1982**, *23*, 87-90

28. McMurry, J. E.; Kočovský, Pavel Tet. Lett. **1984**, *25*, 4187-4190.

29. Trost, B. M.; Metzner, P. J. *J. Am. Chem. Soc.* **1980**, *102*, 3572

30. Bäckvall, J. E.; Hopkins, R. B.; Grennberg, H.; Mader, M. M.; Awasthi, A. K., *J. Am. Chem. Soc.*, **1990**, *112,* 5160-5166.

31. Grennberg, H.; Bergstad, K.; Bäckvall, J., *J. Mol. Catal. A: Chem.,* **1996**, *113*, 355-358

32. Hansson, S.; Heumann, A.; Rein, T.; Åkermark., *J. Am. Chem. Soc.*, **1990**, *55*, 975-97984

33. Principato, B.; Maffei, M.; Siv, C.; Buono, G.; Peiffer, G. *Tetrahedron*, **1996**, *52*, 2087-2096

34. Heumann, A.; Reglier, M.; Waegell, B., *Angew. Chem. Int. Ed.*, **1982***, 21*, 366-367

35. (a)Ferret, N.; Mussate-Mathieu, L; Zahra, J.P.; Waegell, B., *J. Chem. Soc., Chem. Commun.* **1994**, 2589-2590. (b) Jia, C.; Mueller, P.; Mimoun, H. *J. Mol. Cat. A.* **1995**, 127-136 (c) Gusevskaya, E., Gonsalves, J. A., *J. Mol. Catal. A: Chem.* **1997**, *121*, 131-137. (d) Bueno, A. C.; de Souza, Á. O.; Gusevskaya, E. V., *ChemCatChem* **2012,** *4*, 1382-1388. € Czapiewski, M.; Meier, M. A. R. *Catal. Sci. Technol.*, **2014**, *4*, 2318-2325.

36. Hannsson, S.; Heumann, A.; Rein, T.; Åkermark, B., *J. Am. Chem. Soc.*, **1990**, *55*, 975-97984

37. (a) Trost, B. M.; Metzner, P. J. *J. Am. Chem. Soc.* **1980**, *102*, 3572 (b) Bercaw, J. E.; Hazari, N.; Labinger, J. A., *J. Org. Chem.*,**2008**,*73*, 8654–8657 (c) Stang, E. M.; White, M. C. *J. Am. Chem. Soc.*, **2011**, *133*, 14892–14895 (d) Kandukuri, S. R.; Oestreich, M., *J. Org. Chem.*, **2012**, *77*, 8750–8755 (e) Iosub, V. A.; Stahl, S. S. *J. Am. Chem. Soc.* **2015**, *137,* 3454−3457

38. Trost, B. M.; Van Vranken, D. L., *Chem. Rev.*, 96, **1996**, pp 395–422

39. Chen, M. S.; White, M. C., *J. Am. Chem. Soc.,* **2004**, *126*, 1346-1347

40. Chen, M. S.; Prabagaran, N.; Labenz, N. A.; White, M. C., J. *Am. Chem. Soc.* **2005**, *127*, 6970-6971.

41. Vinyl sulfoxide ligands have been previously used in allylic amination and alkylation chemistry. See Kurosawa, H.; Kajimaru, H.; Miyoshi, M.-A.; Ohnishi, H.; Ikeda, I., *J. Mol. Catal.,* **1992**, *74*, 481-488.

42. Åkermark, G.; Hegedus, L.; Zetterberg, K. J. Am. Chem. Soc. **1981**, *103*, 3037-3040.

43. Lin, B.-L.; Labinger, J. A.; Bercaw, J. E., *Can. J. Chem.* **2009**, *87*, 264–271.

44. Thiery, E.; Aouf, C.; Belloy, J.; Harakat, D.; Le Bras, J.; Muzart, J., *J. Org. Chem.*, **2009**, *75*, 1771-1774

45. (a) Amatore, C.; Jutand, A.; M'Barki, M. A. *Organometallics* **1992**, *11*, 3009. (b) Amatore, C.; Carre´, E.; Jutand, A.; M'Barki, M. A. *Organometallics* **1995**, *14*, 1818 (c) Amatore, C.; Jutang, A.; Thuilliez, A., *Organometallics*, **2001**, *20*, 3241–3249

46. Pilarski L. T.; Janson, P. G.; Szabó, K. J., *J. Org. Chem.,* **2011**, *76*, 1503-1506

47. (a) Pilarski L. T.; Selander, N.; Bose, D.; Szabó, K. J., *Org. Lett.*, **2009**, *11*, 5518-5521 (b) Alam, R.; Pilarski L. T.; Pershagen, E.; Szabó, K. J., *J. Am. Chem. Soc.*, **2012**, *134*, 8778-8781

48. Topczewski, J. J.; Sanford, M. S., *Chem. Sci.*, **2015**,*6*, 70-76

49. Xing, X.; O'Connor, N. R.; Stoltz, B. M., *Angew. Chem. Int. Ed.*, **2015**, *54*, 11186-11190

50. Weaver, J. D.; Recio III, A.; Grenning, A. J.; Tunge, J. A., *Chem. Rev.,* **2011**, *111*, 1846–1913

51. Covell, D. J.; White, M. C., *Angew. Chem. Int. Ed.*, **2008,** *47*, 6448-6451

52. Kondo, H.; Yu, F.; Yamaguchi, J.; Liu, G.; Itami, K., *Org. Lett.*, **2014**, *16*, 4212-4215

53. Ammann, S. E.; Liu, W.; White, M. C., *Angew. Chem. Int. Ed.,* **2016**, *55*, 9571-9575

54. Fraunhoffer, K. J.; Prabagaran, N.; Sirois, L. E.; White, M. C., *J. Am. Chem. Soc.*, **2006**, *128*, 9032-9033

55. Stang, E. M.; White, M. C., *Nat. Chem.,* **2009**, *1*, 547-551

56. (a) Takenaka, K.; Akita, M.; Tanigaki, Y.; Takizawa, S.; Sasai H., *Org. Lett.*, **2011**, 3506–3509 (b) Takenaka, K.; Dhage, Y. D.; Sasai, H., *Chem. Commun.*, **2013**, *49*, 11224-11226.

Chapter 2: Diazafluorene-Promoted Transition Metal Catalysis

2.1   Aerobic Allylic C-H Acetoxylation with Pd-Catalysis without ETMs.

Historically, the use of O_2 as the terminal oxidant for allylic acetoxylation reactions required the use of cocatalytic quinones and ETMs.[1] The substrate scope was mostly restricted to simple cyclic olefins (see above, Chapter 1.3) as well. Renewed interest in using O_2 for allylic C-H acetoxylation was initiated by Kaneda and co-workers. They found that $PdCl_2$ in DMA to could perform allylic C-H acetoxylation of terminal, linear alkenes without the use of ETMs.[2] The reaction conditions are fairly harsh in that they require 6 atm of O_2 but are able to utilize low catalyst loadings of 1 mol % or less (Scheme 2.1).[3]
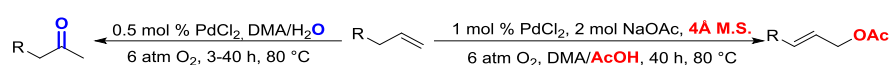
Scheme 2.1: Kaneda Conditions for Wacker and Allylic C-H Acetoxylation

More recently, Stahl and co-workers disclosed the use of a ligand based strategy for enabling aerobic conditions for the allylic C-H acetoxylation.[4] The bipyridyl ligand 4,5-diazafluoren-9-one (DAF) enabled the use of 1 atm of O_2 at 60-80 °C. This method is remarkable in that it tolerates water (a byproduct of O_2 reduction) and does not require extreme pO_2 nor co-catalytic additives such as ETMs or BQ. DAF was a unique ligand for this reaction. Of all the pyridyl ligands screened, it was the only ligand that promoted product formation past one turnover (Scheme 2.2). The DAF ligand has a longer N-N distance compared to that of the canonical 2,2'-bipyridine ligands, such as bpy or phen.[5] DAF was shown to promote reductive elimination in stoichiometric experiments with π-allyls and reductive elimination is reversible under standard conditions. The extent of reversible reductive elimination was found to be controlled by pO_2 and was rationalized by the ability of O_2 to trap Pd^0 alkene complexes formed after reductive elimination.
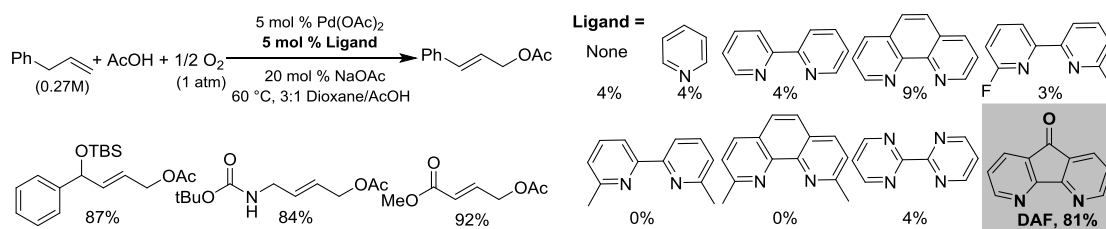
Scheme 2.2: DAF in Aerobic Pd-Catalyzed C-H Acetoxylation

The identification of useful ligands for aerobic oxidative catalysis has been challenging.[6] Much of the research into ligand design for Pd-catalysis have involved anaerobic conditions that are ultimately redox neutral such as traditional cross-coupling reactions.[7] These reactions often use air sensitive phosphine ligands that are incompatible with aerobic conditions. The formation of phosphine oxide is problematic and the harsh oxidizing conditions of aerobic catalysis requires ligands to be more robust. N-Heterocyclic carbene (NHC) ligands have been used for Pd catalyzed cross-coupling[8] and have been successfully utilized in aerobic Pd-catalysis however the strong donor nature of the NHC inhibits substrate oxidation. The use of pyridyl ligands have become common place in aerobic catalysis, especially in Pd-catalyzed reactions. Aerobic Pd-catalysis has employed pyridyl ligands to perform many reactions that terminate in β-hydride elimination; however DAF has been seen shown to be instrumental in new oxidative reactions that involve reductive elimination.[9]

Since the initial report of DAF promoted acetoxylation methodology, other investigators have started to employ DAF for oxidative functionalizations, in particular, new allylic functionalizations. Hartwig and co-workers used DAF/Pd(OAc)$_2$ with tert-butyl benzoyl peroxide to couple benzoate with linear terminal alkenes as part of a two-stage allylic enantioselective functionalization (Scheme 2.3).[10] Other DAF variants functionalized at the 9 position were tested, but the parent DAF ligand was found to be the best for yield and selectivity for linear allylic benzoate.

Scheme 2.3: Tandem Functionalization of Alkenes
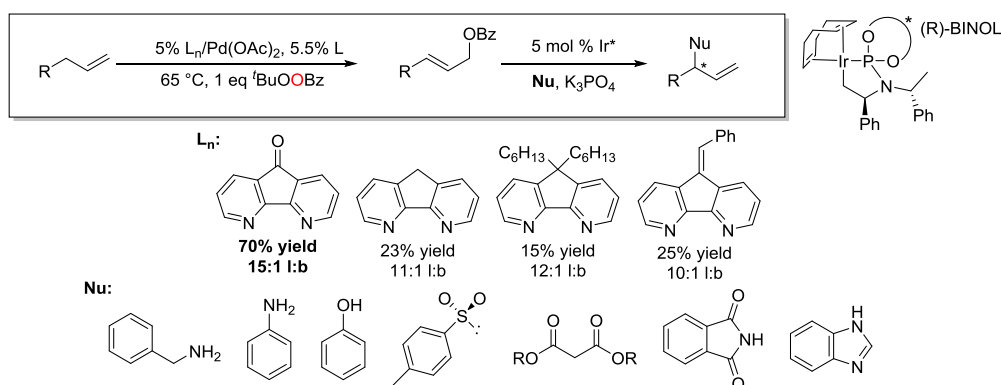
A collaboration by DuBois, Houk and Novartis investigated the scope of the *bis*-sulfoxide/Pd(OAc)$_2$ branched acetoxylation system and the DAF system for linear terminal alkene acetoxylations in the

presence of Lewis-basic heterocycles (Scheme 2.4).[11] They found that with slight perturbation of the reaction conditions, both systems could tolerate pyridine N-oxides and alkylated carbazole substrates. Interesting to note was the additional tolerance of bentriazoles, benzathiazoles, benzofurans and phenazine. The addition of exogenous Lewis acids such as Sc(III) salts or BF_3-Et_2O did not improve product yields. Additionally, they discovered an inverse correlation between binding affinity of the Lewis basic heterocycle and catalyst turn over, suggesting that the binding affinity of the various N-heterocycles are poisoning the catalysts.
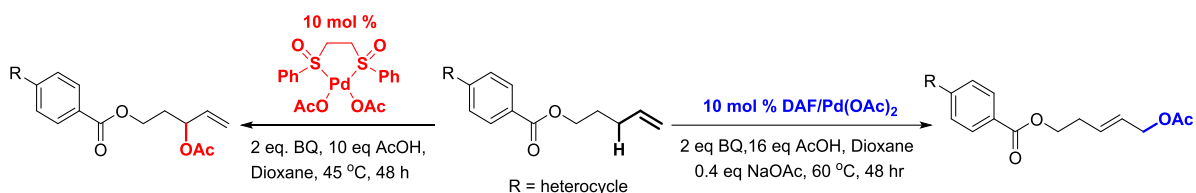
Scheme 2.4: Divergent Methodologies for Heterocycle Functionalization

2.2 DAF in Reductive Elimination Reactions with Pd.

After the initial report of aerobic C-H acetoxylation method in 2010, DAF was reported to be useful in the oxidative coupling of benzene and indoles under aerobic conditions.[12] DAF and the analogous Me_2DAF ligand were found to be the best in promoting the overall yield of the reaction and that modification of the reaction conditions toggle between C2 and C3 arylation (Scheme 2.5). The selectivity for C2 arylation of indole was favored with a DAF/Pd(OPiv)$_2$ combination whereas Me_2DAF/Pd(TFA)$_2$ favored C3 arylation. A primary kinetic isotope effect was observed when C_6D_6 was used, suggesting that benzene C-H activation could be rate determining. Extensive C3 deuterium incorporation was observed on the indole coupling partner with minimal C2 deuteration with both catalyst systems. These observations could support a switch in mechanism and the following statements are speculation. C3 product formation could come from a mechanism involving C-H activation, transmetallation and reductive elimination. C2 product formation could involve a mechanism that involves C-H activation of benzene followed by carbopalladation of the Pd-aryl to the indole followed by β-hydride elimination. These results are not conclusive and require additional experimental work in order to determine the mechanism.
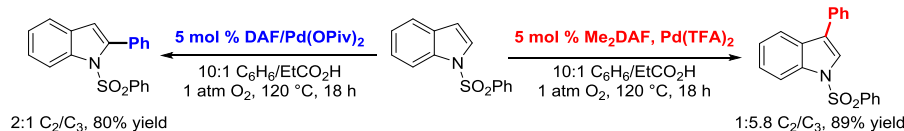
Scheme 2.5: Arylation of Indoles Promoted by DAF

DAF also found synergistic effects with a Pd/NHC catalyst system for the oxidative intramolecular C-O formation to form dibenzofuran derivatives from phenols with appended phenyls moieties (Scheme 2.6).[13] The reaction performed well with just Pd/IPr however the addition of DAF allowed the reaction to proceed to near quantitative yield using just air. The authors believed that the large bulky NHC ligand helps to promote reductive elimination[14] and DAF is responsible for helping to reoxidize the Pd-center. The absence of a C-H/C-D KIE suggests that reductive elimination is the rate-determining step. Control experiments show that DAF alone does not promote this reaction (0% yield with just DAF and no NHC). In the allylic C-H acetoxylation system, the ability of the ligand to promote reductive elimination is cited as key for promoting catalysis and the rate-determining step of the dibenzofuran system is thought to be reductive elimination. This oxidative intramolecular C-O formation system shows that while DAF could be playing an important role in promoting reductive elimination but there are also other roles DAF could play such as catalyst reoxidation. The ability of DAF to be hemi-labile may be beneficial in reoxdation of the catalyst with air.
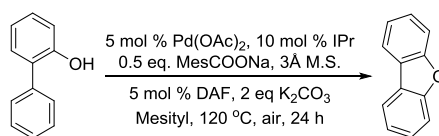
Scheme 2.6: Oxidative Dibenzofuran Synthesis

Another catalytic system where synergistic effects between NHC ligands and the bidentate amine ligand, (-)-sparteine, was observed is the alkene hydroarylation with boronic esters (Scheme 2.7).[15] Sparteine in this case was thought to help break up [NHC/PdCl$_2$]$_2$ dimers, stabilize Pd^0 during reoxidation with O$_2$ and facilitate proton shuttling.[16] The authors speculate that the active catalyst is a monomolecular (SPr)(κ^1-(-)-sparteine)PdCl$_2$ based on preliminary mechanistic investigations (Scheme 2.8). A similar structure could be active for the dibenzofuran synthesis where DAF coordinates κ^1 to a NHC/Pd species to

help promote catalysis in a similar fashion (Scheme 2.6). Additional parallels with DAF and sparteine have

been noted and are elaborated below (Chapter 2.3 pp.33).
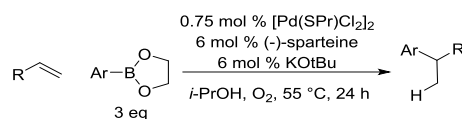
Scheme 2.7: Sigman's Hydroarylation with Boronic Esters

Proposed Active Catalyst
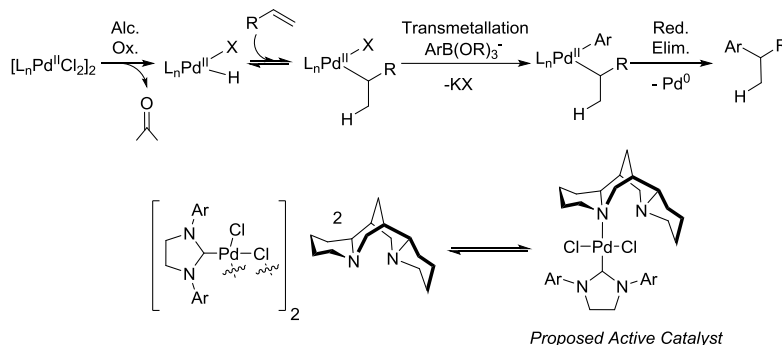
Scheme 2.8: Mechanism of Hydroarylation

DAF/Pd(OAc)$_2$ has been observed to decompose 1,4-dioxane in the presence of O$_2$ for in situ formation

of a peroxide oxidant. Access to high-valent Pd species are often observed to help promote reductive

elimination reactions. During investigations of the cyclization of N-protected aminobiphenyl under aerobic

conditions, it was found that the reaction could be performed under more mild conditions than previously

reported using 1,4-dioxane.[17] Control experiments showed that decomposed dioxane worked much better

than pure, peroxide free dioxane. A time course revealed a induction period followed by product formation

that was concurrent with the formation of peroxide decomposition product. The addition of glycolic acid

was found to be helpful, which is a decomposition product of dioxane. Glycolic acid is thought to help

facilitate the formation of hydroperoxide species that initiate auto-oxidation of the solvent to generate

peroxides. These observations are evidence that DAF/Pd(OAc)$_2$ is promoting the decomposition of 1,4-

dioxane in the presence of O$_2$ to generate a competent peroxide oxidant (Scheme 2.9A). A Pd(II)/Pd(IV)

catalytic cycle was proposed where Pd(II) performs C-H activation to form a substrate derived Pd(II)

palladacycle (Scheme 2.9B). The palladacycle is oxidized to Pd(IV) via the in situ generated peroxide

oxidant. The high valent substrate-bound Pd(IV) species undergoes facile reductive elimination to generate

Pd(OAc)$_2$ for C-H activation. The authors were able to exclude DAF as being important in substrate oxidation as comparable yields without DAF and peroxide oxidants were obtained.[18] This report illustrates a new way to utilize O$_2$ to generate a more activated oxidant to perform oxidative catalysis that involves reductive elimination.
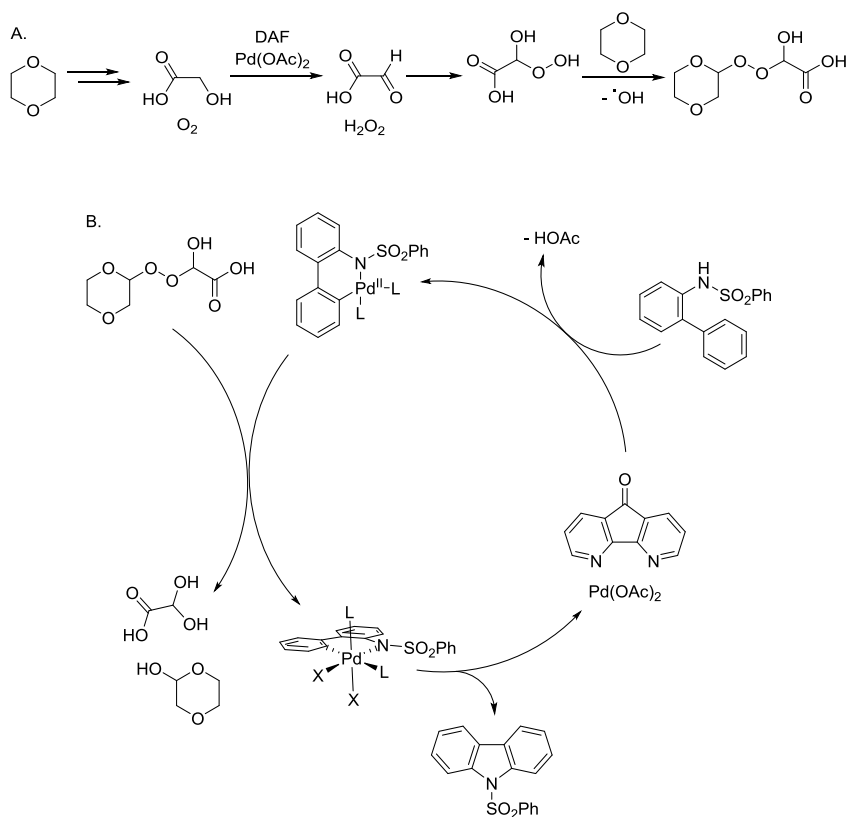
Scheme 2.9: Access to High-Valent Pd-Species Using in situ generated Oxidants

2.3 DAF in β-Hydride Elimination Reactions with Pd.

Aerobic Pd-catalyzed reactions that terminate in β-hydride elimination are particularly efficient.[6a,9,19] Reactions that involve C-C, C-O and C-N dehydrogenations are common place. Many methods involve nanoparticulate and/or heterogeneous catalysts on fairly sophisticated supports to perform these dehydrogenations.[20] Additionally, extensive work has been done to develop effective homogeneous catalysts, enabled by the use of sulfoxide or nitrogen-based ligands that prevent catalyst decomposition as well as promote catalyst activity in dehydrogenations.[6] Aerobic Pd-catalyzed dehydrogenation of acyclic

ketones and aldehydes with DAF was simultaneously developed by the laboratory of Huang and Zhao[21] and Stahl (Scheme 2.10A).[22] The substrate scope was mainly limited to β-aryl carbonyl compounds as high yields are obtained only mono-dehydrogenation is possible. Stahl and co-workers also applied the Pd/DAF method for the dehydrogenation of a cyclopentanone precursor to a mGluR antagonist for which other Pd-catalyzed aerobic methods were less successful (Scheme 2.10B). This methodology was also adapted by Minnard in the total synthesis of herbertenediol, enokipodin A and enokipodin B as a strategy of controlling regioselective methylation of a cyclic ketone.
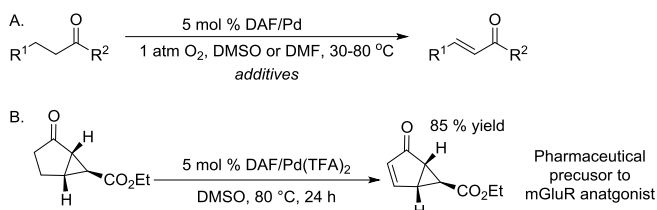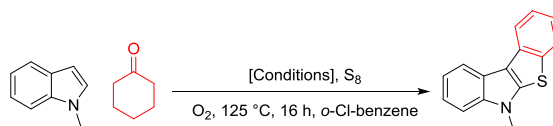
Scheme 2.10: DAF in Dehydrogenation of Ketones and Aldehydes
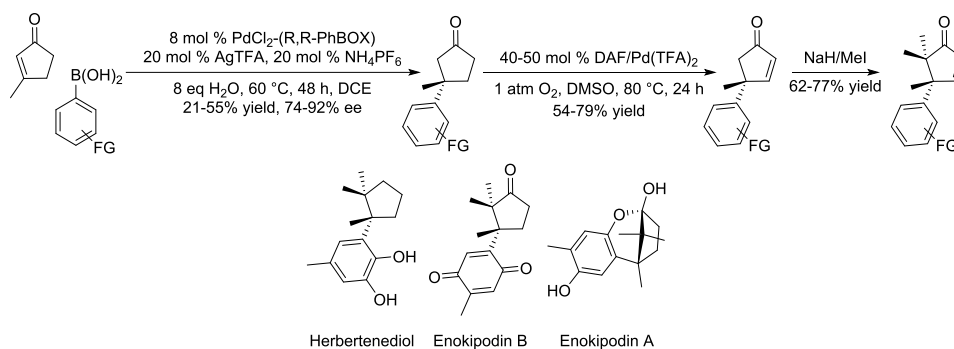
Scheme 2.11: DAF Promoted Dehydrogenations in Natural Product Synthesis

C.-J. Li and co-workers reported a system for the synthesis of benzothieno[2,3-b]indoles using elemental sulfur powder, indoles and cyclohexanone derivatives.[23] This methodology has the advantage of using cheap, odorless elemental sulfur and provides a very quick way of generating otherwise complex sulfur-containing heterocycles. This reaction was found to be promoted by catalytic iodine alone but was improved with the addition of PdI_2. Other sources of iodine such as NIS, KI, CuI were less effective. PdI_2 was superior to other Pd salts and the observation of product in the presence of only I_2 suggests that iodine plays a role in substrate oxidation. Interesting to note was that addition of phen and DMAP with PdI_2 shut down the reaction whereas DAF allowed the reaction to go to 80% yield. The reaction mechanism is unclear. The authors proposed that Pd-performs a double vinylic C-H activation followed by a Pd^{II}-mediated incorporation of sulfur, the details of which are vague. Dehydrogenation of the cyclohexyl group provides the aromatized benzene ring on the product. The authors do not discuss how such a mechanism is consistent with an I_2 only mediated process or discuss the role of I_2 in the reaction as cocatalytic ETM that could assist Pd-turn over in aerobic conditions. The synergy between Pd^{II}, O_2 and I_2 is complicated and not well understood.[24]

Table 2.1: Benzothienol[2.3-b]indole Control Reactions

Condition	Yield	Condition	Yield
1. No additive	trace	6. Phen/PdI$_2$	10%
2. I$_2$	35 %	7. DMAP/PdI$_2$	trace
3. Ki	trace	8. DAF/PdI$_2$	62%
4, CuI	13%	9. DAF/PdI$_2$, 2 eq. cyclohexanone	80%
5. PdI$_2$	42%	10. Above w/ Ar atm	0%

Dehydrogenative Heck (also known as oxidative Heck or Fujiwara-Moritani)[25] reactions that couple arene sp^2 C-H bonds with electron deficient olefins such as acrylates have also benefited from the use of DAF as an auxiliary ligand. Piotrowicz and co-workers have successfully coupled ferrocene derivatives with acrylates using O_2 as the sole oxidant in the reaction (Scheme 2.12).[26] The use of O_2 was crucial for

this reaction, as other oxidants traditionally employed in oxidative Heck reactions resulted in the oxidation of the ferrocene moiety. This method was also applied to the olefination of pyrenes where traditional Heck couplings were difficult to access (Scheme 2.13).[27] Vinyl pyrene derivatives are important building blocks in the synthesis of organic fluorophores found in various applications of molecular electronics, photovoltaic cells and fluorescence probes. Access to the 4-alkenylated pyrene derivatives is challenging. Bromination of pyrene overwhelmingly favors the 1-position whereas Friedel-Crafts type chemistry favors the 4-position.

74% yield, 100% E isomer
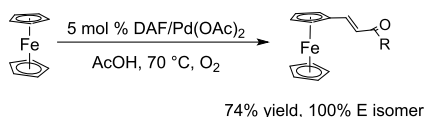
Scheme 2.12: Oxidative Olefination of Ferrocene

71% yield
84:16 C4/C1 product
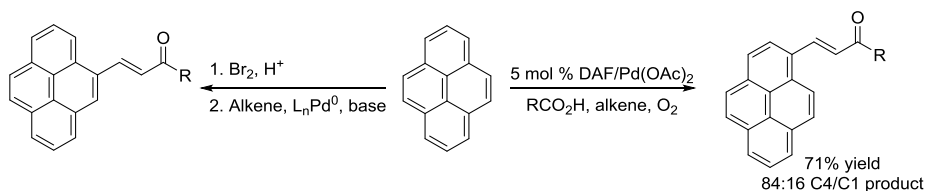
Scheme 2.13: Oxidative Olefination of Pyrene

Muzart and co-workers also used DAF in promoting olefination of heterocycles under aerobic conditions with DAF/Pd(OAc)$_2$ (Scheme 2.14).[28] Interesting to note is that 3,5-dichloropyridine was also an effective ligand. The substrate scope encompasses a diverse array of heterocycles that includes furans and thiophenes that can be functionalized in high yields. The investigators suggest an electrophilic C-H activation pathway is operative based on a 1.67 KIE and propose that DAF is beneficial to all the steps of the catalytic cycle (ie C–H bond activation, alkene insertion, stereodetermining step, and regeneration of the catalyst). The authors propose a pre-equilibrium between DAF and Pd(OAc)$_2$ and that monomolecular species are most active for catalysis. Based on in situ mass-spec data, an intriguing mechanism for catalyst reoxidation is proposed where DAF deprotonates a Pd-H in an intramolecular fashion, partially dissociates

to form a κ^1-pyridinium zwitterion, O_2 binds and is then protonated by the neighboring pyridinium (Scheme 2.15). This mechanism is similar to what Stahl and co-workers propose occurs with (-)-sparteine/PdCl$_2$ in aerobic catalysis.[29]
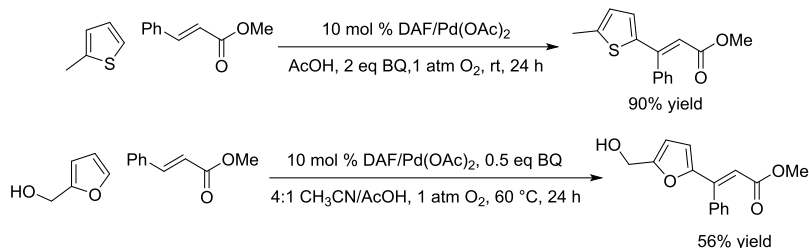
Scheme 2.14: Oxidative Heck Reactions of Hetereocycles with DAF/Pd(OAc)$_2$
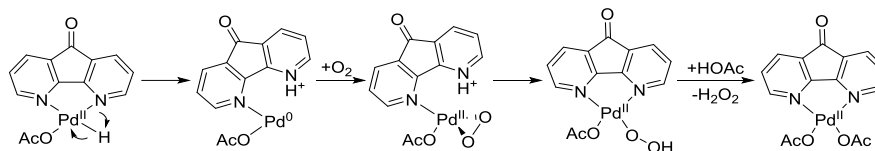
Scheme 2.15: Proposed DAF Promoted Aerobic Pd Reoxidation Pathway

2.4   DAF in Non-Pd Based Catalysis.

DAF has since been utilized in reactions outside of aerobic oxidation catalysis with Pd. Huang and co-workers have developed a method for the α-vinylidenation of aldehydes using Au-catalyzed electrophilic alkynylation with enamine catalysis (Scheme 2.16).[30] In this reaction, chelating nitrogen ligands were found to be very important in promoting the catalysis and in particular, DAF was critical in obtaining >90% yields. Au(I) or Au(III) precursors both worked equally well in these reaction conditions. Changing the atmosphere from argon to pure O_2 results in C-C bond cleavage to provide ynones from the iminium intermediate.[31] While DAF was critical for getting high yields, it is unclear what is the specific role of DAF as a ligand and there were no investigations into the reaction mechanism.
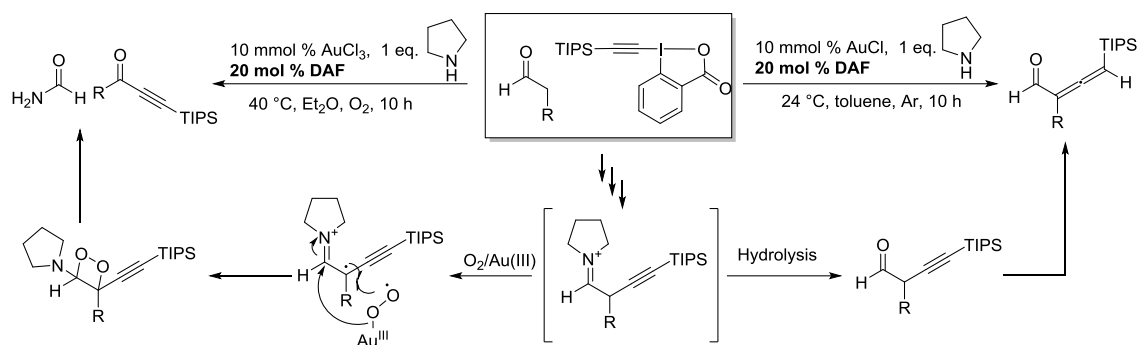
Scheme 2.16: DAF/Au System for Vinylidenation of Aldehydes

Cu-carbene chemistry has also benefited from the use of DAF. A method developed by Wang and co-workers for the synthesis of all-carbon quaternary centers using alkynes, α-diazo esters and alkyl halides employed 20% Cu(I)/DAF catalyst with tetrabutylammonium iodide (TBAI) as a crucial additive (Scheme 2.17). TBAI was believed to be a phase-transfer catalyst as well as helping to perform halogen exchange with the alkyl bromides and chlorides used in the reaction to form a more reactive electrophilic coupling partner. Phen provided the investigators with a 27% yield whereas DAF boosted the yield to 57% that was further optimized to 87% for the model substrates. The removal of NaH enabled the incorporation Michael Acceptors such as acrylate derivatives.
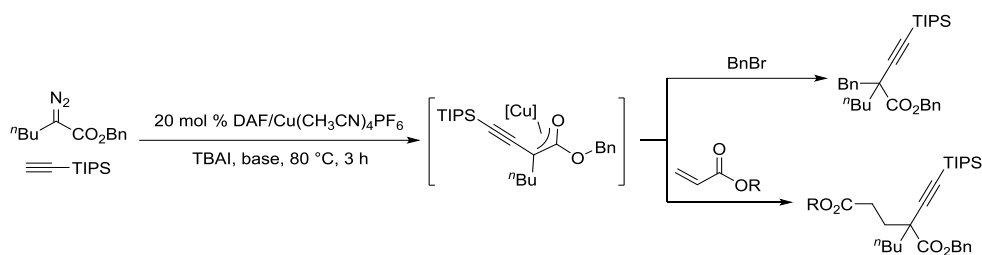
Scheme 2.17: Functionalization of in situ Generated Cu-Enolates with Electrophiles

1. Piera, J.; Bäckvall, J., *Angew. Chem. Int. Ed.,* **2008**, *47*, 3506-3523

2. Mitsudome, T.; Umetani, T.; Nosaka, N.; Mori, K.; Mizugaki, T.; Ebitani, K.; Kaneda, K., *Angew. Chem. Int. Ed.* **2006**, *45*, 481-485.

3. DMSO was entirely ineffective for the Wacker reaction.

4. Campbell, A. N.; White, P. B.; Guzei, I. A.; Stahl S. S. *J. Am. Chem. Soc.* **2010**, *132*, 15116–15119.

5. Having a carbonyl group on the 9-position has been found to be optimal in many cases however, more electron-rich derivatives such as 9,9'-Me₂DAF has been shown to be effective in catalysis as well.

6. (a) Stahl, S. S. *Angew. Chem. Int. Ed.* **2004**, *43*, 3400-3420. (b) Gligorich, K. M.; Sigman, M. S. *Chem. Commun.* **2009**, *26*, 3854-3867.

7. (a) Martin, R.; Buchwald, S. L., Acc. Chem. Res., **2008**, *41*, 1461-1473. (b) Surry, D. S.; Buchwald, S. L., *Angew. Chem. Int. Ed.*, **2008**, *47*: 6338–6361.

8. Kantchev, E. A. B.; O'Brien, C. J.; Organ, M., *Angew. Chem. Int. Ed.* **2007**, *46*, 2768 – 2813.

9. Campbell, A. N.; Stahl, S. S. *Acc. Chem. Res.* **2012**, *45*, 851-863.

10. Sharma, A.; Hartwig, J. F., *J. Am. Chem. Soc.*, **2013**, *135*, 17983-17989.

11. Malik, H. A.; Taylor, B. L. H.; Kerrigan, J. R.; Grob, J. E.; Houk, K. N.; Du Bois, J.; Hamann, L. G.; Patterson, A. W., *Chem. Sci.*, **2014**, *5*, 2352-2361.

12. Campbell, A. N.; Meyer, E. B.; Stahl, S. S., *Chem. Commun,* **2011**, *47*, 10257-10259.

13. Xiao, B.; Gong, T.-J.; Liu, Z.-J; Liu, J.-H.; Luo, D.-F.; Xu, J.; Liu, L., *J. Am. Chem. Soc.*, **2011**, *133*, 9250-9253.

14. (a) Littke, A. F.; Fu, G. C. *Angew. Chem., Int. Ed.* **2002**, *41*, 4176- 4211. (b) Mann, G.; Incarvito, C.; Rheingold, A. L.; Hartwig, J. F. *J. Am. Chem. Soc.* **1999**, *121*, 3224- 3225. (c) Aranyos, A.; Old, D. W.; Kiyomori, A.; Wolfe, J. P.; Sadighi, J. P.; Buchwald, S. L. *J. Am. Chem. Soc.* **1999**, *121*, 4369-4378.

15. Iwai, Y.; Gligorich, K. M.; Sigman, M. S., *Angew. Chem. Int. Ed.* **2008**, *47*, 3219-3222.

16. Decharin, N.; Popp, B. V.; Stahl, S. S*., Am. Chem. Soc.* **2011**,*133*, 13268–13271.

17. Weinstein, A. B.; Stahl, S. S. *Catal. Sci. Technol.* **2014**, *4*, 4301-4307. See also, Tsang, W. C. P.; Zheng, N.; Buchwald, S. L*., J. Am. Chem. Soc.* **2005**, *127*, 14560-14561.

18. Weinstein, A. B., Development, Application and Mechanistic Investigation of Palladium Catalyzed Aerobic Oxidative Amination Methods, PhD Thesis, 2015, pp. 146.

19. McDonald, R.I.; Liu, G.; Stahl, S. S., *Chem. Rev.*, **2011**, *111*, 2981-3019.

20. (a) Dobereiner; G. E.; Crabtree, R. H., *Chem. Rev.* **2010,** *110,* 681-703. (b) Iosub, A.V.; Stahl, S.S. ACS. Catal. **2016**, *6*, 8201-8213.

21. Gao, W.; He, Z.; Qian, Y.; Zhao, J.; Huang, Y., *Chem. Sci.* **2012**, *3*, 883-886.

22. Diao, T.; Wadzinski, T. J.; Stahl, S. S. *Chem. Sci.* **2012**, *3*, 887-891.

23. Liao, Y.; Peng, Y.; Qi, H.; Deng, G.-J.; Gong, H.; Li, C.-J., *Chem. Commun.*, **2015**, *51*, 1031-1034.

24. See references for additional discussion regarding I$_2$ in aerobic catalysis: Wendlandt, A. E.; Stahl, S. S., *J. Am. Chem. Soc.*, **2014**, *136*, 506-512.

25. Le Bras, J.; Muzart, J. *Chem. Rev.* **2011**, *111*, 1170–1214.

26. Piotrowicz, M.; Zakrzewski, J. *Organometallics,* **2013**, *32*, 5709-5712.

27. Piotrowicz, M.; Zakrewski, Métivier, R.; Brosseau, A.; Makal, A.; Woźniak, K. *J. Org. Chem.,* **2015**, *80*, 2573-2581.

28. Vasseur, A.; Laugel, C.; Harakat, D.; Muzart, J.; Le Bras, J., *Eur. J. Org. Chem.,* **2015**, *5,* 944–948.

29. Decharin, N.; Popp, B. V.; Stahl, S. S., *J. Am. Chem. Soc.* **2011**,*133*, 13268–13271.

30. Wang, Z.; Li, X.; Huang, Y., *Angew. Chem. Int. Ed.*, **2013**, *52*, 14219-14223.

31. Wang, Z.; Li, L.; Huang, Y., *J. Am. Chem. Soc.*, **2014**, *136*, 12233-12236.

Chapter 3: Structurally Diverse Diazafluorene-Ligated Palladium(II) Complexes and their Implications for Aerobic Oxidation Reactions

This work was done in collaboration with Paul B. White, Charles G. Fry, Brian S. Dolinar, Ilia A. Guzei, Shannon S. Stahl*

Footnotes included in the body of the text to designate the independent work of PBW and JNJ.

Data for sections 0, 3.2.1-3.2.6 was the independent work of PBW.

Drafts for sections 3.1, 3.2.7-3.2.10, 3.3 and 3.4 were co-written by PBW and JNJ

Supporting information section A1 was co-written by PBW and JNJ.

Supporting information sections A2, A3.1-A3.8 was the independent work of PBW.

Supporting information sections A3.9-A3.11 was the independent work of JNJ.

Crystal structures for A, B, E were obtained independently by PBW and the corresponding data can be found in his thesis or in the above publication's supporting information.

Crystal structures for G, H, I, J, K, L, Me$_2$DAF ligand, and cyclometallated species, (κ^2-DAF)Pd(OPiv) were obtained independently by JNJ. Corresponding data can be found in supporting information section A4.

3.1   Introduction.[a]

The renaissance of Pd-catalyzed aerobic oxidation reactions over the past 10-15 years can be attributed, at least in part, to the identification of ancillary ligands that have enabled new synthetic transformations and support improved catalyst activity, selectivity, and stability.[1] The ligands tune catalyst sterics and electronics, and thereby influence elementary steps, such as ligand substitution, β-hydride elimination, and reductive elimination, and provide the basis for catalyst-controlled regio- and stereoselective transformations. Continued identification and/or development of new ligands remains a crucial goal to reduce catalyst loadings, enhance catalyst lifetimes and promote the discovery of novel transformations.

Pd-catalyzed aerobic oxidation reactions require the use of oxidatively stable ligands. Monodentate pyridine derivatives are especially common;[2] however, catalysts containing these ligands are often susceptible to decomposition, especially at elevated temperatures.[3] Catalyst stability can be enhanced through the use of bidentate ligands, such as 2,2'-bipyridine (bpy) and 1,10-phenanthroline (phen) derivatives. These ligands have been used effectively in Pd-catalyzed aerobic oxidation reactions, although the results are typically observed in polar solvents (e.g., H_2O, DMSO, DMF)[4] or at high temperatures (120-200 °C),[5] which are often needed to enable anionic ligand dissociation from (N~N)PdX$_2$ species to access open coordination at the Pd^{II} center. Under mild conditions and/or in non-polar solvents, bidentate ligands such as bpy and phen often strongly inhibit Pd-catalyzed aerobic oxidation reactions.[6,7]

4,5-Diazafluoren-9-one (DAF) is a rare exception to the observations just noted. In 2010, we reported that DAF is a uniquely active bipyridine-type ligand in Pd-catalyzed allylic acetoxylation of terminal olefins.[7] Other bidentate ligands, such as bpy and phen, were found to strongly inhibit the reaction. Subsequent to this discovery, DAF has been used in numerous other Pd-catalyzed reactions, including oxidative C–C and C–O coupling reactions of arenes,[8] dehydrogenation of cyclic ketones[9] and oxidative

---

[a] Introduction written by PBW independently, revised by JNJ to include additional discussion of permutations of DAF, Pd-carboxylate discussion.

Heck reactions.[10,11] The unique behavior of DAF, relative to bpy and phen, in several of these reactions is illustrated in Scheme 3.1.[7,8,9a]
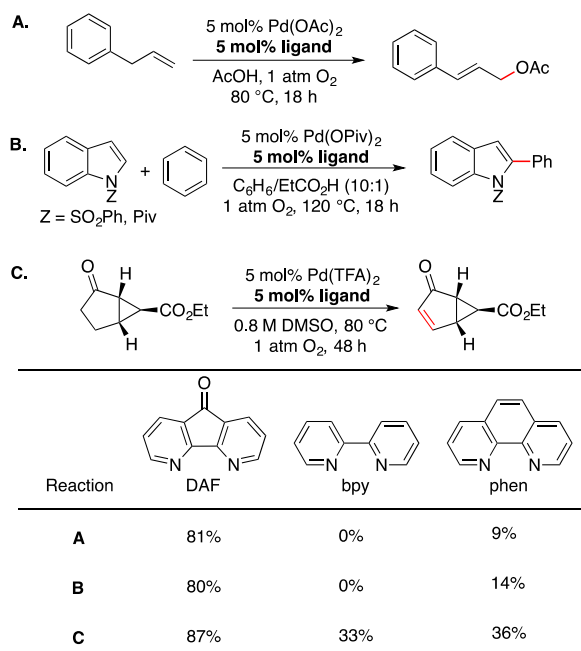
Scheme 3.1: Representative Pd-Catalyzed Aerobic Oxidation Reactions Promoted by DAF.[7,8,9a]

The beneficial effect of DAF in these reactions could arise from its unique coordination properties relative to more-traditional bidentate nitrogen ligands. Evidence of unusual DAF coordination chemistry are evident from previously reported complexes with first-row transition metals,[12] palladium(0),[13] and other examples[14] in which pentahapto (η^5), bridging (μ) and monodentate (κ^1), in addition to traditional bidentate, coordination modes have been identified. On the other hand, previously reported DAF/Pd^{II} complexes are limited to two examples (Scheme 3.2),[15] both of which exhibit the canonical bidentate coordination mode.
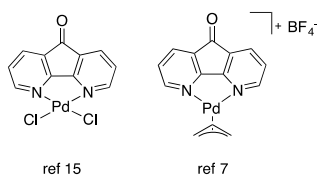
Scheme 3.2: Previously Characterized DAF/Pd^{II}-Coordinated Complexes

In the present study, we show that the DAF/Pd^{II} coordination chemistry is much richer and more complex than the structures in Scheme 3.2 might suggest. Through the use of multinuclear NMR

spectroscopy, single crystal X-ray diffraction analysis and density functional theory (DFT) calculations, we have identified and characterized six independent coordination complexes that arise from the combination of DAF and Pd(OAc)$_2$. These complexes include both monomeric and dimeric structures, in which DAF exhibits κ^1, κ^2, and μ coordination modes. Complementary studies with the structurally similar 9,9-dimethyl-4,5-diazaflourene (Me$_2$DAF) ligand provide insight into the effect of electronic perturbation of the diazafluorene ligand framework. Finally, the synergy between the coordination properties of DAF and the anionic carboxylate ligand is probed by replacing acetate with sterically and electronically different carboxylates, trifluoroacetate (TFA) and pivalate (OPiv). The unique coordination properties of DAF identified herein are compared to other bidenate ligands, and they are proposed to contribute directly with the beneficial, ligand-acceleration effect of DAF in Pd^{II}-catalyzed oxidation reactions. This hypothesis is validated in a companion study, in which we compare the mechanistic influence of several different bidentate ligands in Pd-catalyzed aerobic aza-Wacker reactivity and show that the fluxionality and weak coordination of DAF relative to other traditional bidentate ligands underlies its activation of Pd^{II} catalysts.[16]

3.2   Results.

3.2.1   DAF:Pd(OAc)$_2$ Titration Experiments.[b]

^{1}H NMR spectroscopic analysis of a 1:1 mixture of DAF and Pd(OAc)$_2$ in CDCl$_3$ reveals the presence of a complex mixture of species (Figure 3.1). This spectrum contrasts the spectra obtained from 1:1 mixtures of Pd(OAc)$_2$ and more typical bidentate nitrogen ligands, such as 4,4'-*t*Bu$_2$bpy and 2,9-Me$_2$phen (Figure 3.1). The latter solutions feature single Pd(κ^2-N~N)(OAc)$_2$ species, which have been described previously in the literature.[17]

---

[b] DAF/Pd(OAc)$_2$ experiments were performed independently by PBW
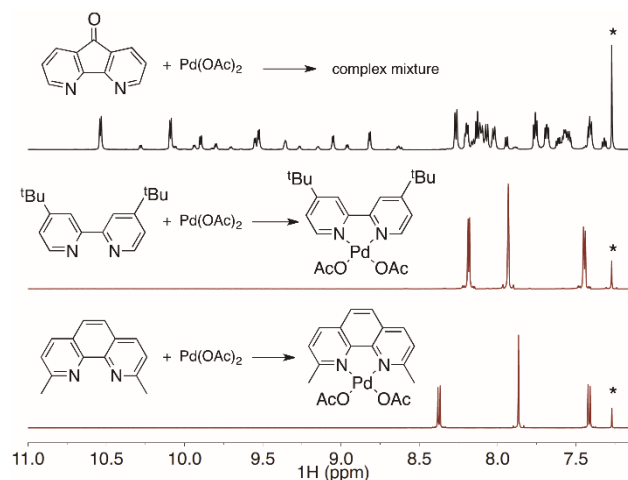
Figure 3.1: ^{1}H NMR spectra of 1:1 solutions of Pd(OAc)$_2$ with bidentate nitrogen ligandshighlighting the complexity of the DAF/Pd(OAc)$_2$ mixture. [Pd(OAc)$_2$] = 40 mM, [Ligand] = 40 mM, T = -45 °C (top) and 24 °C (middle and bottom), solvent = CDCl$_3$ (0.5 mL); * designates the CHCl$_3$ solvent peak.

In an effort to begin identifying the species present in the 1:1 DAF:Pd(OAc)$_2$ ^{1}H NMR spectrum, we performed a titration experiment in which different quantities of DAF were added to a solution of Pd(OAc)$_2$ (Figure 3.2). The most diagnostic region of the ^{1}H NMR spectrum is from 8.6–10.9 ppm, where the *ortho* protons of the DAF ligand appear. With 0.5 equiv of DAF, a single peak assigned to species **A** predominates in this region of the spectrum. At 1 equiv of DAF, several pairs of resonances are evident, with the major pair designated as species **B**. The pairs of resonances are attributed to Pd^{II} complexes with unsymmetrically coordinated DAF ligands. Free DAF is also present in this spectrum. When ≥ 2 equiv of DAF are added, only small quantities of **A** and **B** are present, and the spectra reveal four new species, three with unsymmetrical DAF ligands, **C–E**, and one with a symmetrical DAF ligand, **F**. The growth and/or decay of each of these species were tracked as a function of DAF equivalents (Figure 3.2C). This plot provided the conditions under which the concentration of individual species could be maximized to facilitate more-thorough structural characterization.

A) NMR Titration of DAF with Pd(OAc)$_2$

B) Nomenclature for Spectral Assignment

C) [Species] vs Equivalents DAF
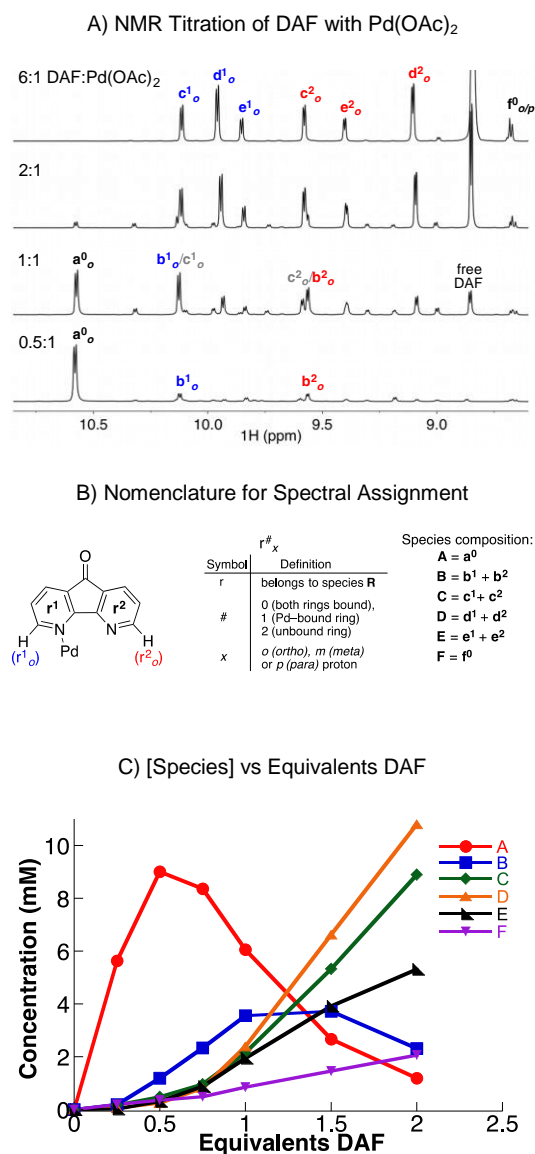
Figure 3.2: ^{1}H NMR Spectra Obtained from the Titration of DAF with Pd(OAc)$_2$ at -45 °C. (A). Description of the nomenclature used to assign resonances in the NMR spectra (B). Speciation plot associated with the six DAF/Pd(OAc)$_2$ complexes identified in the titration experiments (C).

The nomenclature employed for the spectral assignments is presented in Figure 3.2B. Within a given complex, protons belonging to each DAF ligand are labeled with the lower-case letter of the complex name, **a**–**f**. A superscript "0" is used to designate resonances associated with a symmetrical DAF ligand in which both pyridyl rings are coordinated to Pd. For complexes with monodentate (κ^1) DAF ligands, a superscript

"1" is used to designate the coordinated ring, and a superscript "2" for the uncoordinated ring. Finally, subscripts o, m, and p are used to designate the *ortho*, *meta*, and *para* protons.

3.2.2   Overview of Methods Used to Characterize DAF/Pd(OAc)$_2$ Complexes.[b]

The integration of the ^{1}H NMR peaks together with selective 1D TOCSY,[18] 1D and 2D ROESY[19] and 2D ^{1}H-^{15}N HMBC[20] experiments provided key insights into the identity of complexes **A**–**F** (Scheme 3.3). The 1D TOCSY experiments enabled assignment of the *ortho*, *meta*, and *para* protons within individual rings of the DAF ligand, even when significant overlap was present among resonances from different complexes. The ROESY experiments revealed through-space interactions between ligands within the Pd coordination sphere, including DAF↔DAF and DAF↔OAc interactions. ROESY experiments were used in place of NOESY experiments at lower temperature because the NOE sign and intensity depend on temperature and molecular size, and use of NOESY led to false-negative results. These data, together with integration of the DAF and OAc resonances, were used to determine the DAF:OAc:Pd stoichiometry for each of the complexes **A**–**F**.
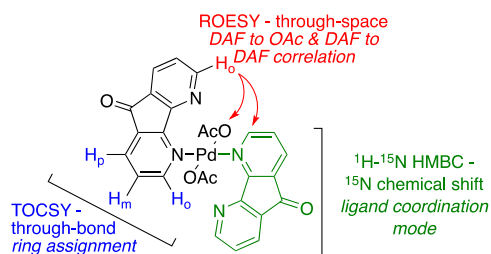
Scheme 3.3: Application of NMR Techniques for Structure Assignment

The ^{1}H-^{15}N HMBC experiment provided a means to determine the ^{15}N chemical shift of the DAF nitrogen atoms without isotopic enrichment, and this experiment clearly distinguished between coordinated and uncoordinated nitrogen atoms. Uncoordinated pyridine ligands exhibit ^{15}N chemical shifts at ~300 ppm, whereas Pd[II]-coordinated pyridine ligands appear at ~200 ppm (Scheme 3.4).[21] These differences allowed distinction between monodentate and bidentate DAF coordination modes.

15N Chemical Shift of Free and Coordinated Bpy

$\delta(^{15}N)$ = 307 ppm $\delta(^{15}N)$ = 217 ppm

Application of ^{15}N Chemical Shift to DAF Coordination

$\delta(^{15}N)$ near 200 ppm $\delta(^{15}N)$ near 200 and 300 ppm
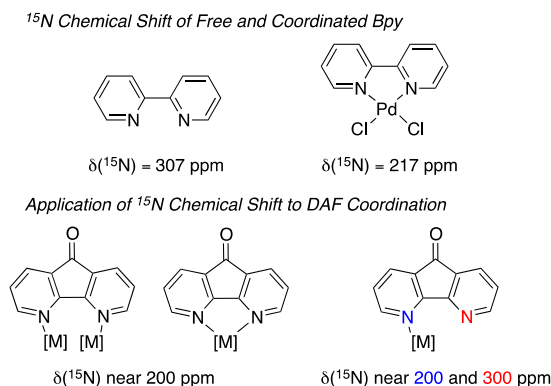
Scheme 3.4: Effect of Coordination on ^{15}N Chemical Shift

The NMR spectroscopic data were complemented by X-ray crystallography, which provided solid-state structural information that could be compared to the solution-phase NMR data. Finally, DFT calculations facilitated structural assignment of the closely related structures **C–E**. Application of these techniques to determine the identity of complexes **A–F** is elaborated below.

3.2.3   Structural Assignment (μ-DAF)Pd$_2$(OAc)$_4$, Species A.[b]

The first species evident in the ligand titration is complex **A**. As mentioned previously, **A** grows to its maximum concentration at 0.5 equiv DAF relative to Pd(OAc)$_2$. The TOCSY experiment correlates a single set of *ortho*, *meta*, and *para* resonances, indicating that the two DAF pyridyl rings are equivalent in **A** (Figure 3.3A, Figure A 1). The ^{1}H-^{15}N HMBC spectrum reveals a single ^{15}N resonance at 204 ppm, indicating that $\mathbf{a^0_o}$ and $\mathbf{a^0_m}$ are associated with a coordinated pyridyl ligand (Figure 3.3B). The presence of both $^2J_{NH}$ and $^3J_{NH}$ cross-peaks in the HMBC spectrum complements the results from the TOCSY experiment and confirms that the resonances belong to the same complex.
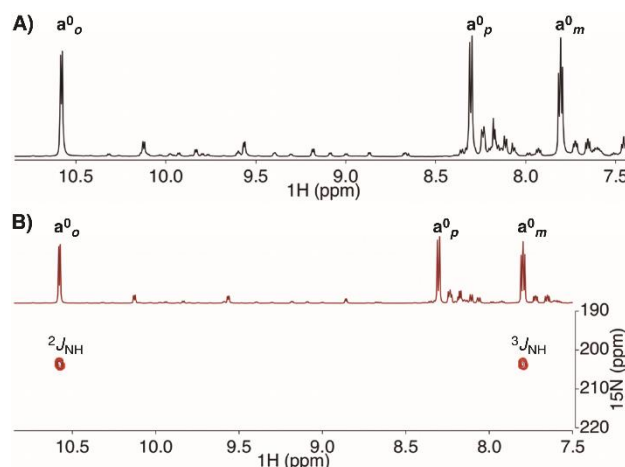
Figure 3.3: 1D ^{1}H and ^{1}H-^{15}N HMBC Spectra of a solution of Pd(OAc)$_2$ and 0.5 eq. DAF in CDCl$_3$ focusing on aromatic region. Cross-peaks for both 2- and 3-bond N–H coupling are observed. [Pd(OAc)$_2$] = 40 mM, [DAF] = 20 mM, T = -45 °C, solvent = CDCl$_3$ (0.5 mL). ^{1}H-^{15}N HMBC: dof = 250 ppm, sw1 = 250 ppm, nt = 16, d1 = 4, ni = 256. The integrated 1D ^{1}H NMR spectrum of **A** reveals a DAF:OAc stoichiometry of 1:4, and a 1D ROESY experiment shows through-space interactions between the DAF ligand and two chemically distinct acetate ligands (Scheme 3.5, Figure A 4). Integration of the two acetate resonances reflects three and six protons, corresponding to a DAF:OAc^1:OAc^2 ratio of 1:1:2. A third acetate peak is evident in the 1D ^{1}H NMR spectrum, which has an integration of three protons. This third acetate resonance does not appear in the ROESY spectra (Figure A 4), however, suggesting that it is too distant from DAF to observe an ROE.[22]
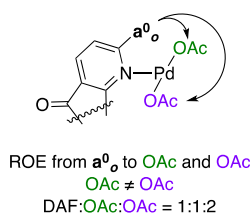
Scheme 3.5: Observed DAF-to-OAc ROE Correlations for A

Crystals suitable for single crystal X-ray analysis were obtained from a 0.5:1 DAF:Pd(OAc)$_2$ mixture in CDCl$_3$, and the structure reveals a C_s-symmetric Pd^{II} dimer with a one DAF and two acetate ligands bridging the two Pd atoms (Figure 3.4). Each of the Pd centers has an additional monodentate (κ^1) acetate ligand, which are eclipsed with respect to the Pd–Pd axis. This structure is consistent with the NMR data, and

redissolution of the crystals in CDCl$_3$ reproduces the spectrum of **A** present in the 0.5:1 DAF:Pd(OAc)$_2$ solution.
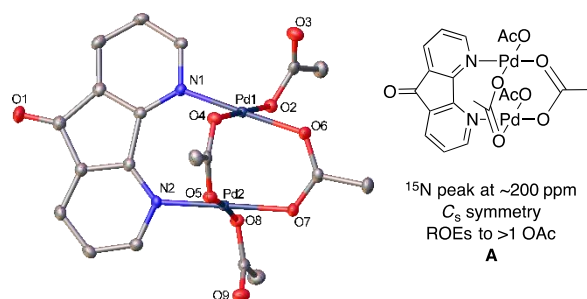
Figure 3.4: X-ray structure and summary of NMR spectroscopic data for Species A.The crystal structure is drawn with 50% probability ellipsoids and all H atoms are ombitted for clarity. See supporting information for details.

This structure exhibits a mirror plane perpendicular to the Pd–Pd axis that rationalizes the chemical equivalence of two pyridyl rings of the DAF ligand evident in the 1D ^{1}H NMR spectrum. It also accounts for the ^{1}H-^{15}N HMBC data showing that both DAF pyridyl rings are coordinated to Pd. The μ-OAc and two κ^1-OAc ligands adjacent to the DAF ligand are the origin of the observed ROEs. The μ-OAc *trans* to the DAF ligand is too far from the DAF protons to be detected by the ROESY experiment.[23]

3.2.4 Structural Assignment (κ^1-DAF)$_2$Pd$_2$(OAc)$_4$, Species B.[b]

Addition of more DAF to the solution of **A** results in conversion to **B**. Analysis of the NMR data revealed that **B** has a DAF ligand with two chemically distinct pyridyl rings, **b^1** and **b^2** (Figure 3.5A). A Pd-bound pyridyl ring (**b^1**) is clearly evident from the ^{15}N resonance at 189 ppm, and an unbound ring (**b^2**) is associated with the resonance at 305 ppm (Figure 3.5B).
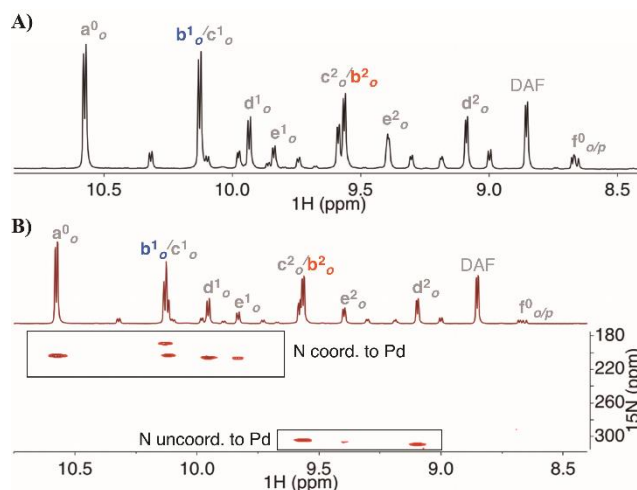
Figure 3.5: 1D ^{1}H (A) and ^{1}H-^{15}N HMBC spectra (B) of a solution of Pd(OAc)$_2$ and 1 equiv of DAF in CDCl$_3$ focusing on the aromatic spectral region. The resonances appearing at <220 ppm correspond to coordinated nitrogen atoms of DAF ligands, while those appearing at >300 ppm correspond to unbound nitrogen atoms. [Pd(OAc)$_2$] = 40 mM, [DAF] = 40 mM, T = -45 °C, solvent = CDCl$_3$ (0.5 mL). ^{1}H-^{15}N HMBC: dof = 250 ppm, sw1 = 250 ppm, nt = 40, d1 = 6 s, ni = 256. The 2D ROESY spectrum reveals two acetate cross-peaks, indicating that **B** contains chemically inequivalent acetate ligands (Figure A 5, Figure A 6). Furthermore, ROEs are observed from **b^1** and **b^2** to both of these acetates, demonstrating that **b^1** and **b^2** are present in the same complex (i.e., **B** = **b^1** + **b^2**) (Scheme 3.6). These conclusions are supported by 1D ROESY experiments in which ROEs were observed between each of the acetate resonances and the **b^1_o** and **b^2_o** ring resonances (Figure A 7). Integration of the DAF and OAc resonances in the 1D ^{1}H NMR spectrum reveals a DAF:OAc stoichiometry of 1:2.

ROEs from **b^1_o** and **b^2_o** to OAc and OAc
OAc ≠ OAc
DAF:OAc:OAc = 1:1:1
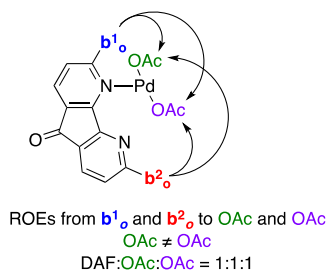
Scheme 3.6: Observed DAF to OAc ROE Correlations for B

Crystals suitable for single crystal X-ray analysis were obtained from a 1.5:1 DAF:Pd(OAc)$_2$ mixture in CDCl$_3$, and the structure reveals a C_2-symmetric Pd^{II} dimer with two acetate ligands bridging the */ atoms (Figure 3.6). Each Pd center is also coordinated by a κ^1-DAF and a κ^1-OAc ligand.
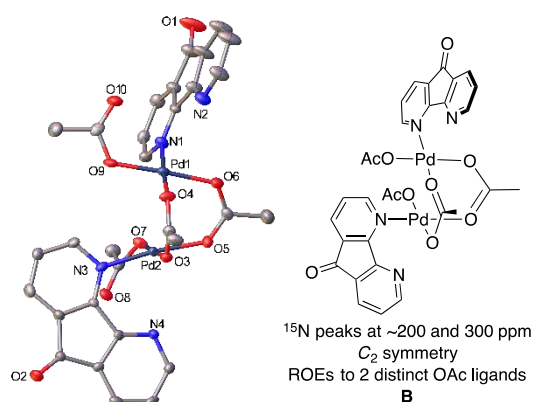
Figure 3.6: X-ray crystal structure and summary of NMR spectroscopic data for species B. The crystal structure is drawn with 50% probability ellipsoids and all H atoms are omitted for clarity. See Supporting Information for details. This structure has a C_2 axis perpendicular to the Pd–Pd axis that bisects the two bridging acetate ligands, rationalizing the chemical equivalence of the two κ^1-DAF ligands and the pairs of μ- and κ^1-OAc ligands evident in the 1D ^{1}H NMR spectrum. This structure also explains the ^{1}H-^{15}N HMBC data showing both bound and unbound DAF pyridyl rings. The ROESY data showing through-space interactions between DAF and two chemically distinct acetate ligands are also readily rationalized by this structure.

3.2.5 Structural Assignment of Isomers of $(\kappa^1$-DAF$)_2$Pd(OAc)$_2$, Species C, D, and E.[b]

Addition of more DAF results in the conversion of species **A** and **B** into a mixture of four new species **C–F**. At a DAF:Pd(OAc)$_2$ ratio of 6:1, seven resonances associated with the *ortho* protons of the DAF ligand are present in the ^{1}H NMR spectrum, together with four distinct OAc peaks (Figure 3.7A, Figure A 8 and Figure A 10). Six of the seven DAF resonances correspond to three pairs of peaks with 1:1 integration, and they are assigned to species **C**, **D**, and **E**. The remaining resonance is assigned to **F** and will be discussed separately below. The concentrations of **C**, **D**, and **E** exhibit a squared dependence on the DAF concentration, suggesting that these structures exhibit a 2:1 DAF:Pd stoichiometry (cf. Figure 3.2C). The ^{1}H-^{15}N HMBC spectrum reveals six cross-peaks for **C**, **D**, and **E** (Figure 3.7B), with $\mathbf{c^1}$, $\mathbf{d^1}$, and $\mathbf{e^1}$ corresponding to Pd-bound DAF pyridyl rings (δ 203-207 ppm) and $\mathbf{c^2}$, $\mathbf{d^2}$, and $\mathbf{e^2}$ corresponding to unbound

rings (δ 304-310 ppm). These data indicate that each of the complexes **C**, **D**, and **E** contains DAF ligands bound in a κ^1 coordination mode.
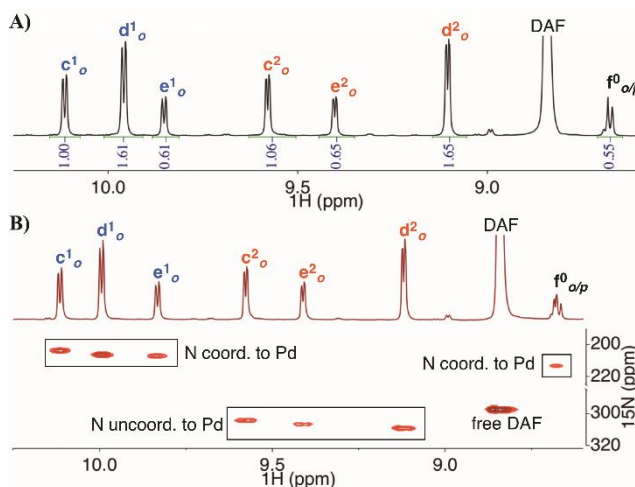
Figure 3.7: 1D ^{1}H and ^{1}H-^{15}N HMBC spectra of a solution of Pd(OAc)$_2$ and 6 equiv of DAF in CDCl$_3$ focusing on the aromatic spectral region. The resonances appearing at <220 ppm correspond to coordinated nitrogen atoms of DAF ligands, while those appearing at >300 ppm correspond to unbound nitrogen atoms. [Pd(OAc)2] = 40 mM, [DAF] = 240 mM, T = -45 °C, solvent = CDCl3 (0.5 mL). 1H-15N HMBC: dof = 250 ppm, sw1 = 250 ppm, nt = 32, d1 = 4 s, ni = 256.

1D ROESY spectra for each complex reveal through-space interactions between each of the two (inequivalent) DAF *ortho* protons and a single acetate resonance (Figure 3.7A and Figure A 9, Figure A 10). Furthermore, integrations of the DAF and OAc resonances reveal a DAF:OAc ratio of 1:1 for each complex. The 1D ROESY experiments also reveal through-space interactions between the chemically inequivalent DAF *ortho* protons in **C** and **E** (i.e., from $c^1_o \leftrightarrow c^2_o$ and $e^1_o \leftrightarrow e^2_o$), but analogous ROE correlations are not present in **D**. The distance between the *ortho* protons within an individual DAF ligand ($d \sim 7.0$ Å) is too large to show an ROE; however, these signals can arise from interactions between two separate DAF ligands within the same complex. Computational modeling confirms that two DAF ligands with an *anti* relationship have *ortho* protons with sufficient proximity to exhibit an ROE correlation (Figure 3.7B and Figure A 9, Figure A 10). No ROE correlation is expected for two DAF ligands with a *syn* relationship.

A. DAF↔OAc ROESY
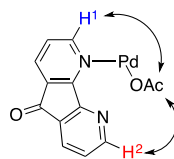
ROEs from **H¹** and **H²** to OAc

B. DAF↔DAF ROESY
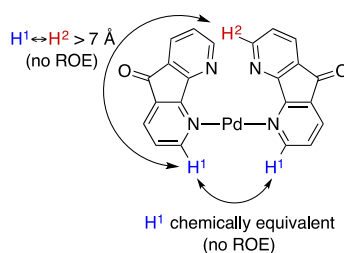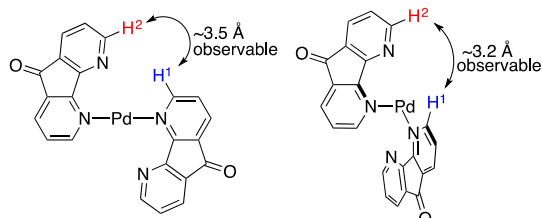
Scheme 3.7: Observed DAF↔DAF and DAF↔OAc ROE Correlations for C–E.

Four possible isomeric structures, **1–4**, satisfy the constraints of the NMR spectroscopic data of species **C**, **D**, and **E** (Table 3.1) and correspond to Pd(κ^1-DAF)$_2$(OAc)$_2$ complexes that are distinguished by *cis* vs. *trans* and *syn* vs. *anti* relationships between two κ^1 DAF ligands in the Pd coordination sphere. The viability of these structures is supported by X-ray crystallographic characterization of one of these complexes (Figure 3.8). The X-ray quality crystals were obtained from a 6:1 DAF:Pd(OAc)$_2$ mixture in CDCl$_3$.

Table 3.1: Assignments of C-E from NMR Spectroscopic and DFT Results

	1	**2**	**3**	**4**
DAF-DAF relation:	*trans/syn*	*trans/anti*	*cis/anti*	*cis/syn*
Static Point Group:	C_2	C_i	C_2	C_s
ΔG_{rel} (kcal/mol):	0.00	0.15	1.54	6.02
Assignment:	**D**	**E**	**C**	not observed
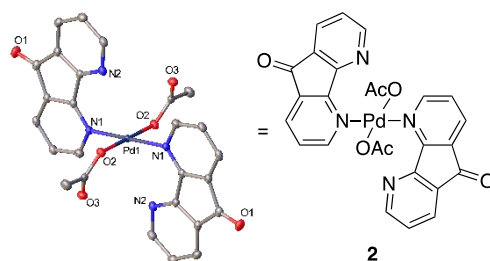
Figure 3.8: X-ray crystal structure of trans/anti-Pd(κ^1-DAF)$_2$(OAc)$_2$, species E. The crystal structure is drawn with 50% probability ellipsoids and all H atoms are omitted for clarity. See Supporting Information for details.

The relative energies of structures **1–4** were assessed by performing DFT computations.[24] Structures **1–3** are within 1.6 kcal/mol of each other, with **1** having the lowest energy. Structure **4**, however, is significantly higher in energy (ΔG = +6.0 kcal/mol relative to **1**) and would have a population that would not be detected by NMR spectroscopy (Table 3.1). The higher energy of this complex may be rationalized by the steric clash between the *cis/syn* relationship between the two DAF ligands. These data suggest the three species detected in solution consist of a mixture of structures **1**, **2** and **3**.

ROESY experiments reveal chemical exchange between **D** and **E** (Scheme 3.8A and Figure A 8). The exchange process converts one of the DAF *ortho* protons in **D** ($\mathbf{d^1_o}$) into an equal mixture of the two *ortho* protons in **E** ($\mathbf{e^1_o}$ and $\mathbf{e^2_o}$). The temperature dependence of this exchange process was used to estimate an activation energy of $\Delta G^\ddagger$ = 13 ± 0.5 kcal/mol (Figure A 11, Figure A 12).[25] These observations may be rationalized by an intramolecular exchange process that interconverts the *trans/syn* and *trans/anti* bis-DAF complexes **1** and **2** (cf. Table 3.1). A mechanism for this process was identified by DFT methods, and the calculated barrier is 11 kcal/mol, which is in good agreement with the experimental value.
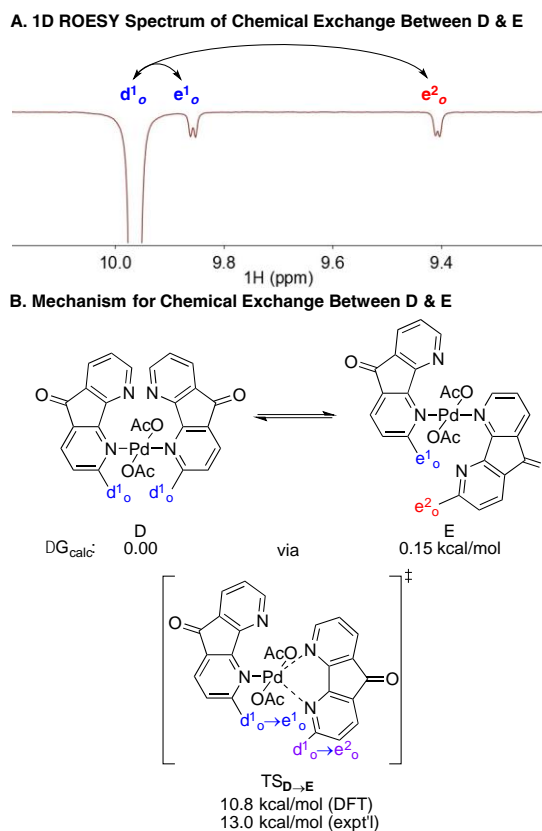
Scheme 3.8: Chemical Exchange Process between D and E.

Together, the ROESY and DFT computational data enable structural assignment of complexes **C**, **D**, and **E**. The DAF↔DAF ROEs observed for **C** and **E** (cf. Scheme 3.7) require an *anti* relationship between the DAF ligands and thereby limit these species to structures **2** and **3** (cf. Table 3.1). The chemical exchange between **D** and **E** permits assignment of complex **E** to the *trans/anti* structure **2** and complex **D** to the *trans/syn* structure **1**. Structure **4** is not believed to be among the observed structures on the basis of the DFT energy and, therefore, complex **C** is assigned to the *cis/anti* structure **3**. These assignments are supported by comparison of the ^{1}H NMR chemical shifts of the acetate -CH_3 groups for these three complexes with the general trends observed in chemical shifts of *cis-* and *trans-*acetate ligands.[26]

3.2.6   Structural Assignment (κ^2-DAF)Pd(OAc)$_2$, Species F.

Complex **F** appears together with **C**, **D**, and **E** as the DAF concentration increases. Unlike **C–E**, however, its concentration increases with a linear, rather than squared, dependence on DAF concentration,

suggesting that it has a 1:1 DAF:Pd(OAc)$_2$ stoichiometry (cf. Figure 3.2C). The 1D ^{1}H NMR spectrum for **F** reveals a symmetrical DAF ligand, and ^{1}H-^{13}C HSQC, variable temperature and 1D TOCSY data show that the resonances at 8.66 ppm corresponds to both *ortho* and *para* protons (**f**$_{o/p}$ in Figure 3.7A; see also Figure A 16 - Figure A 18). 1D ROESY data reveal a through-space interaction between the *ortho* proton of DAF and an acetate ligand, and integration of the acetate peak reveals a DAF:OAc stoichiometry of 1:2 (Figure A 10). Finally, the ^{1}H-^{15}N HMBC spectrum (cf. Figure 3.7B) exhibits only a single cross-peak for **F** at 213.3 ppm, showing that the symmetrical pyridyl rings of the DAF ligand are coordinated to Pd. The monomeric structure in Scheme *3.9* is consistent with all of these data.

^{15}N resonance at ~200 ppm
C_2 symmetry reflects daf rings
ROEs to 1 OAc resonance
F
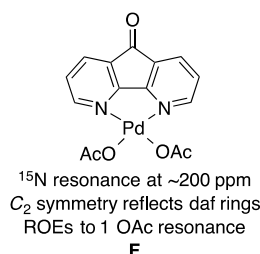
Scheme 3.9: Structure of F Derived from NMR Spectroscopic Methods

3.2.7 Characterization of Me$_2$DAF/Pd(OAc)$_2$ & DAF/Pd(O$_2$CR) (R = CF$_3$, tBu) Complexes.

Several variants of the DAF/Pd(OAc)$_2$ catalyst system have been used in catalytic aerobic oxidation reactions. For example, as shown in Scheme 3.1, DAF has been replaced with 9,9-dimethyl-4,5-diazafluorene (Me$_2$DAF) and acetate has been replaced with trifluoroacetate (TFA) or pivalate (OPiv) (cf. Scheme 3.1).[8,9] In an effort to assess the potential influence of these catalyst modifications, we investigated Me$_2$DAF/Pd(OAc)$_2$, DAF/Pd(TFA)$_2$, and DAF/Pd(OPiv)$_2$ in a manner analogous to DAF/Pd(OAc)$_2$.

3.2.8 Structural Assignment of Me$_2$DAF/Pd(OAc)$_2$ Species G and H.[c]

Titration of Me$_2$DAF into a solution of Pd(OAc)$_2$ reveals the formation of only two species **G** and **H**, and only **H** is observed when >1 equiv of Me$_2$DAF is present, relative to Pd(OAc)$_2$ (Figure 3.9). The

---

[c] Characterization of Me$_2$DAF/Pd(OAc)$_2$ species was performed by JNL.

simplicity of this mixture contrasts with the complex speciation observed with DAF/Pd(OAc)$_2$ (cf. Figure 3.1). Full NMR spectroscopic analysis of these species was performed (see Supporting Information, Figure A 19 – Figure A 24). TOCSY data reveal that the Me$_2$DAF ligand in both **G** and **H** have equivalent pyridyl rings, and ^{1}H-^{15}N HMBC data reveal a single ^{15}N resonance for each complex, with chemical shifts in a region associated with bound *N* atoms: 199.4 ppm (**G**) and 209.7 ppm (**H**). For **G**, an ROE correlation was observed between the DAF ligand and two chemically distinct acetates, designated OAc^1 and OAc^2, and another between OAc^2 and a third acetate ligand, OAc^3. Integration of the 1D ^{1}H NMR spectrum of **G** reveals a DAF:OAc stoichiometry of 1:4, with a DAF:OAc^1:OAc^2:OAc^3 ratio of 1:1:2:1. In contrast, the acetate ligands in **H** are equivalent and the DAF:OAc stoichiometry is 1:2.

Crystals of **G** and **H** suitable for single crystal X-ray analysis were obtained from chloroform solutions of 0.5:1 and 1:1 Me$_2$DAF:Pd(OAc)$_2$, respectively, and the resulting structures are consistent with the solution NMR data (Figure 3.9). **G** is a dimeric species with a bridging Me$_2$DAF ligand and two bridging and two κ^1 acetate ligands, matching the DAF/Pd(OAc)$_2$ structure **A** (cf. Figure 3.4). **H** is a monomeric species with the Me$_2$DAF ligand in a traditional κ^2 bidentate coordination mode, analogous to the DAF/Pd(OAc)$_2$ structure **F**.

A) NMR Titration of Me$_2$DAF with Pd(OAc)$_2$

B) [Speciation] vs Equivalents of Me$_2$DAF
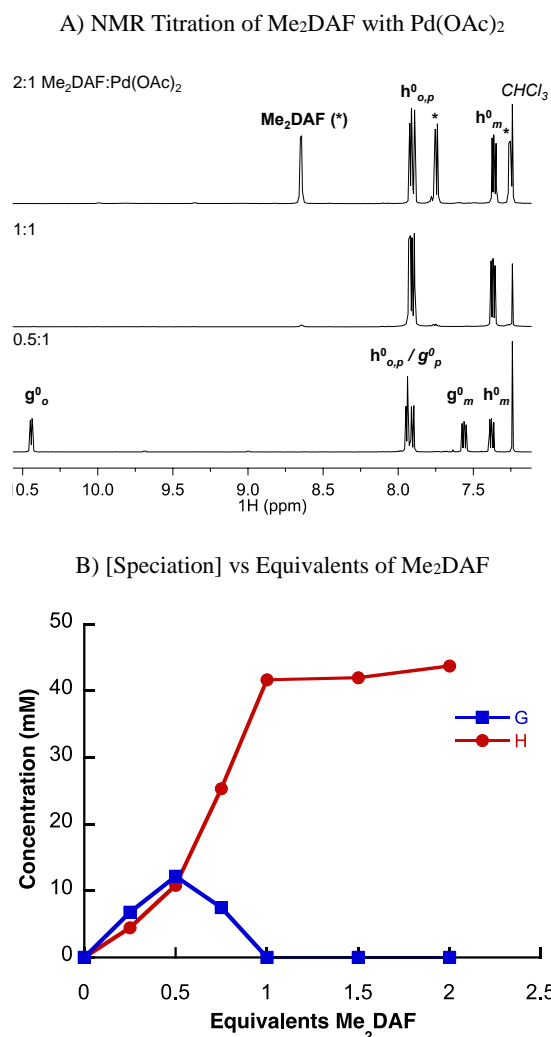
Figure 3.9: ^{1}H NMR spectra obtained from the titration of Me$_2$DAF with 40 mM Pd(OAc)$_2$ at 24 °C. (A). Speciation plot associated with the two Me$_2$DAF/Pd(OAc)$_2$ complexes identified in the titration experiments (B).
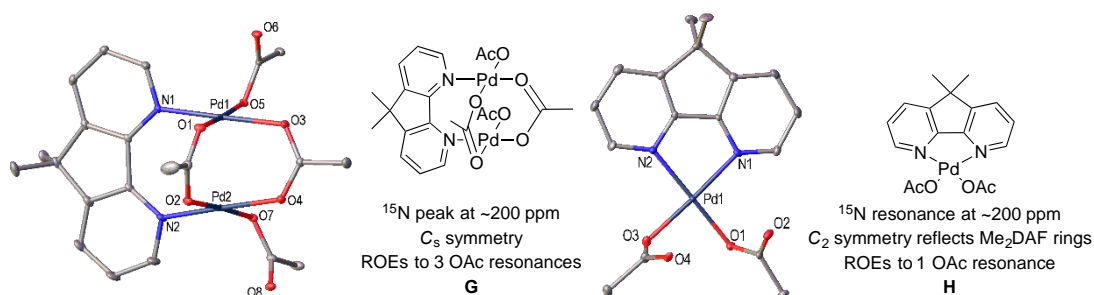
Figure 3.10: Summary of Data for Me$_2$DAF/Pd(OAc)$_2$ species. Pd(μ-Me$_2$DAF)(μ-OAc)(κ^1-OAc)$_2$ dimer G and Pd(μ^2-Me$_2$DAF)(κ^1-OAc)$_2$ monomer H. The crystal structures are drawn with 50% probability ellipsoids and all H atoms are omitted for clarity. See Supporting Information for details.

3.2.9 Structural Assignment of DAF/Pd(TFA)$_2$ Species, I, J and K.[d]

Pd(TFA)$_2$ is insoluble CDCl$_3$, but it dissolves in a 1:1 ratio of CDCl$_3$ and trifluoroacetic acid (TFAH). Titration of DAF into a solution of Pd(TFA)$_2$ in this solvent mixture reveals the sequential appearance of three species, **I**, **J**, and **K** (Figure 3.11), each of which was extensively characterized by NMR spectroscopic methods (see Appendix A, Figure A 27 - Figure A 31). Complex **I** maximizes at 0.5:1 DAF:Pd(TFA)$_2$ stoichiometry, but coexists with **J**. Complex **J** is essentially the only species present at a 1:1 DAF:Pd(TFA)$_2$ stoichiometry, while it begins to disappear in favor of **K** at higher DAF concentrations. It was possible to obtain X-ray crystal structures of **I** and **J** (**Figure 3.12**), and the solid-state structures are consistent with the solution NMR data. Complex **I** is the dimeric species Pd$_2$(μ-DAF)(μ-TFA)$_2$(κ^1-TFA)$_2$, which resembles structures **A** and **G** above (cf. Figure 3.4 and Figure 3.10), while **J** is the monomeric structure Pd(κ^2-DAF)(κ^1-TFA)$_2$, which resembles structures **F** and **H** above (Scheme 3.9 and Figure 3.10). Complex **K** only forms at high DAF concentrations, and it was not possible to obtain crystals of this complex. NMR data for this complex reveals dynamic behavior arising from rapid exchange between uncoordinated DAF and coordinated to **J** and **K**. The parabolic growth of **K** with increasing [DAF] and NMR integrations are consistent with a 2:1 DAF:Pd(TFA)$_2$ stoichiometry, and all of the data point toward this species being a mononuclear complex with two κ^1-DAF ligands, Pd(κ^1-DAF)$_2$(TFA)$_2$, similar to species **C**, **D** and **E** (cf. Table 3.1).

---

[d] Characterization of DAF/Pd(TFA)$_2$ species was performed by JNJ

A) NMR Titration of DAF with Pd(TFA)$_2$

B) [Speciation] vs Equivalents of DAF
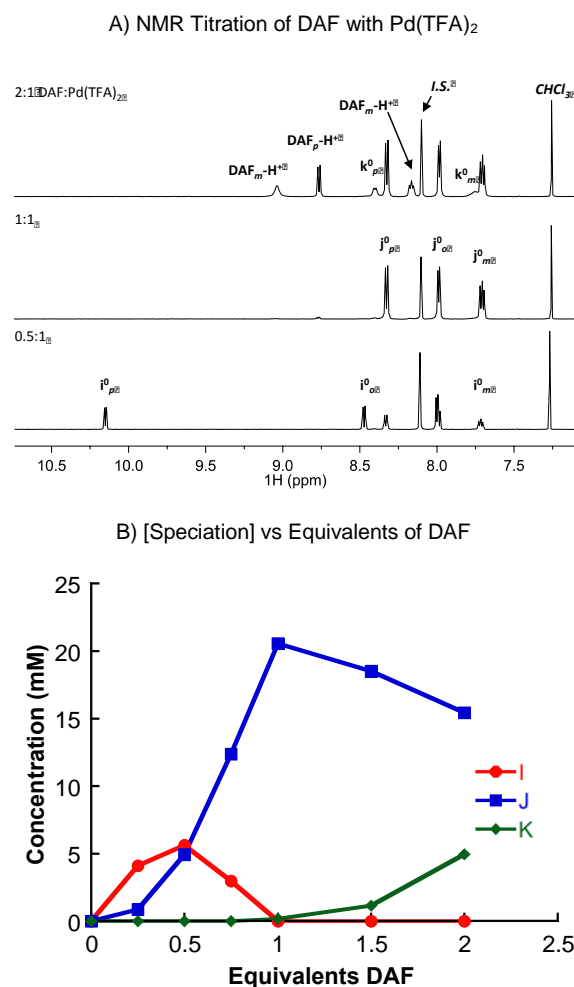
Figure 3.11: ^{1}H NMR spectra obtained from the titration of DAF with 20 mM Pd(TFA)$_2$ in 1:1 TFAH:CDCl$_3$ at 24 °C. (A). Speciation plot associated with the DAF/Pd(TFA)$_2$ complexes identified in the titration experiments (B).
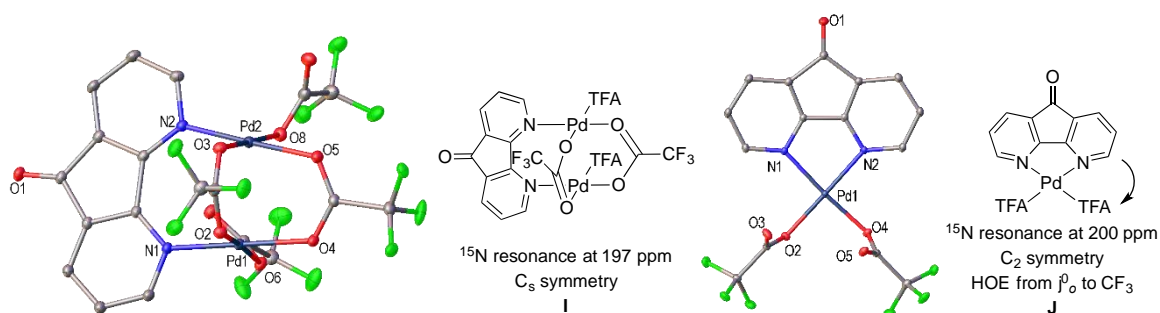
Figure 3.12: Summary of Data for DAF/Pd(TFA)$_2$ Speciation. Pd(μ-DAF)(μ-TFA)$_2$(κ^1-TFA)$_2$ dimer I and (κ^1-DAF)$_2$Pd(κ^1-TFA)$_2$ monomer J. The crystal structures are drawn with 50% probability ellipsoids and all H atoms are omitted for clarity. See Supporting Information for details.

3.2.10 Structural Assignment of (μ-DAF)$_2$Pd$_2$(κ^1-OPiv)$_4$.[e]

Titration of DAF into a solution of Pd(OPiv)$_2$ reveals a single major DAF-ligated Pd species **L** at all DAF:Pd(OPiv)$_2$ stoichiometries (Figure 3.13). In order to see any ligation occur, the reaction had to be incubated room temperature for over a week and only minor (<10%) contributions from other DAF-ligated species are evident. The NMR spectroscopic data show that the DAF and OPiv ligands are present in 1:2 stoichiometry and that the two pyridyl groups of DAF are equivalent and coordinated to Pd (see Supporting Information, Figure A 32 and Figure A 33). An X-ray crystal structure of **L** reveals that this complex is a C_2-symmetric dimer in which two *trans* DAF ligands bridge two Pd^{II} centers, each of which also has two κ^1-OPiv ligands (Figure 3.14).[27] An approximately 45° twist is evident between the N–Pd–N vectors of the two Pd^{II} centers, when the dimer is viewed down the Pd$\cdots$Pd axis. This structural feature differs from the DAF/Pd(OAc)$_2$ dimers **A** and **B**, for which the two Pd^{II} square planes have an eclipsed relationship (i.e., θ = 0°). Upon redissolving the crystals of **L** into CDCl$_3$, identical spectral data are observed. It seems likely that the symmetrical monomeric structure, Pd(κ^2-DAF)(OAc)$_2$, is disfavored by the steric bulk of the pivalate groups. Extended incubation of the DAF/Pd(OPiv)$_2$ mixture resulted in C-H activation of the pivalate CH$_3$ group and a well defined palladacycle was obtained that had a k^2-DAF ligated – see supporting information.

---

[e] Characterization of DAF/Pd(OPiv)$_2$ species was performed by JNJ

A) NMR Titration of DAF with Pd(OPiv)$_2$

B) [Speciation] vs Equivalents of DAF
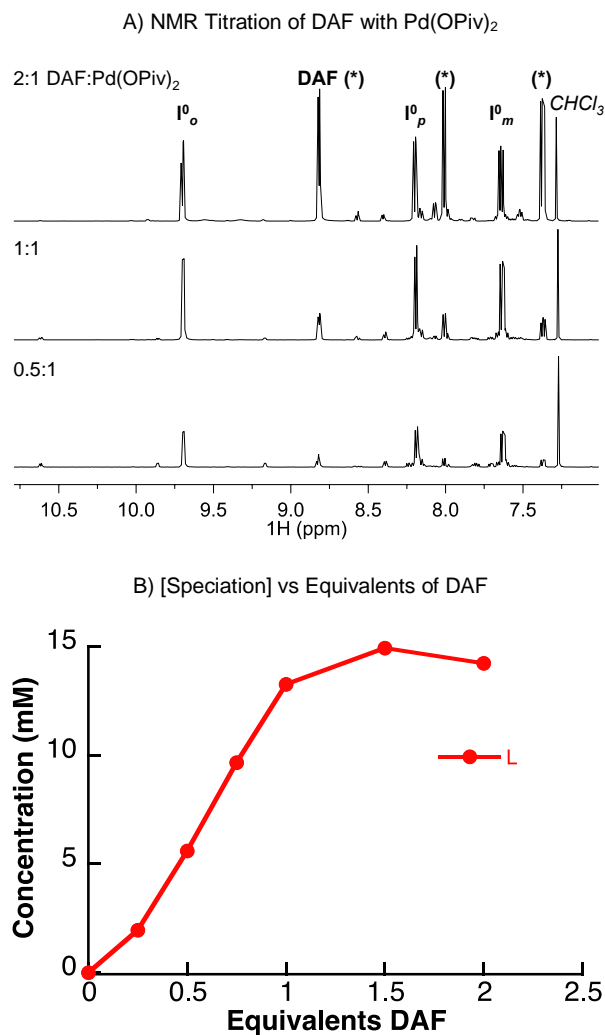
Figure 3.13: ^{1}H NMR spectra obtained from the titration of DAF with 40 mM Pd(OPiv)$_2$ at 24 °C (A). Speciation plot associated with the two DAF/Pd(OPiv)$_2$ complexes identified in the titration experiments (B).

^{15}N resonance at 214 ppm
NOE from i^0_o to Equivalent OPiv
C$_2$ symmetry
OPiv = OPiv, DAF:OPiv = 1:2
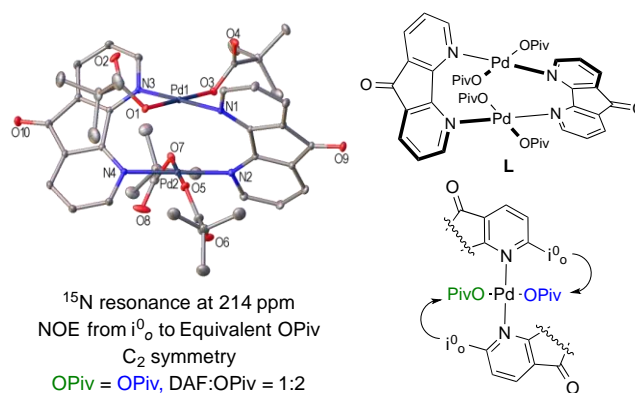
Figure 3.14: Summary of data for Pd$_2$(μ-DAF)$_2$(κ^1-OPiv)$_4$ dimer L. The crystal structures are drawn with 50% probability ellipsoids and all H atoms are omitted for clarity. See Supporting Information for details.

3.3   Discussion.[f]

3.3.1   Origin of Diverse Coordination Geometries with DAF.

The results presented here highlight the structural diversity of DAF coordination to Pd-carboxylate salts. The results show that DAF exhibits bridging (μ), κ^1- and κ^2-binding modes when coordinated to Pd^{II} centers bearing carboxylate anionic ligands, and most of the structures deviate from the classical κ^2-bidentate coordination mode typically associated with bipyridyl-type ligands. This rich diversity is evident in mixtures of DAF and Pd(OAc)$_2$. Under conditions with 1:1 DAF:Pd(OAc)$_2$ stoichiometry (a typical stoichiometry for catalytic reactions), six different structures are present in significant quantity (**A**–**F**, cf. Figure 3.2). The complexes are highly fluxional, but static structures suitable for NMR spectroscopic characterization were accessible at –45 °C. Upon replacing DAF with the more electron-rich ligand Me$_2$DAF or the acetate ligands with more electron-deficient trifluoroacetate ligands, equilibrium mixtures are still observed, but a smaller number of species are present (cf. Figure 3.9 and Figure 3.11). The corresponding complexes are also less fluxional than the DAF/Pd(OAc)$_2$ species, allowing NMR spectroscopic studies to be performed at room temperature. As expected, increasing the DAF concentration promotes the formation of monomeric structures, including complexes bearing a single κ^2-DAF and/or two κ^1-DAF ligands. Only the sterically encumbered Pd(OPiv)$_2$ species favors a single DAF complex at all DAF concentrations and, in this case, favors a unique dimeric Pd complex with two bridging DAF ligands.

This unique DAF/Pd-carboxylate coordination chemistry may be rationalized by the structural distortion of the DAF ligand relative to traditional bpy-type ligands. Two structural parameters that facilitate comparison of these ligands are the angle α, defined by the C2–N and C2'–N bond vectors of the two pyridyl rings, and the N$\cdots$N distance between the two pyridyl nitrogen atoms (Scheme 3.10). Introduction of a one-atom linker between the 3- and 3'-positions of 2,2'-bipyridine expands α from 53° in

---

[f] Discussion written by PBW, modified to include discussion of Me$_2$DAF/Pd(OAc)$_2$, DAF/Pd(TFA)$_2$ and DAF/Pd(OPiv)$_2$ results.

bpy to 73° in the unligated bpy and DAF ligands, and similarly increases the N···N distance from 2.66 Å to 3.06 Å, respectively.[28] The parameters for Me_2DAF (73°, 3.07 Å) are nearly identical to those for DAF.[29] The α angle for unligated bpy is similar to that observed in bpy-ligated complexes of Pd^{II}. For example, α = 49° and 54° in Pd(bpy)(OAc)$_2$ and Pd(2,9-Me$_2$phen)(OAc)$_2$, respectively.[17a,c] In contrast, the κ^2-DAF complexes of Pd^{II} require significant contraction of their α angle relative to unligated DAF: α = 61° and 60° in complexes **H** and **J**, respectively. The α angle expands considerably when DAF serves as a bridging ligand: α = 82-84° in complexes **A**, **G**, **I**, and **L**, while virtually no distortion is evident in the structures bearing κ^1-DAF ligands: α = 76°, complexes **B**, **C**, **D**, **E** (Scheme 3.10). Commensurate changes are evident in the N···N bond distances (Scheme 3.10). In short, unligated DAF exhibits structural features intermediate between the κ^2 (bidentate) and μ (bridging) coordinated DAF ligands, thereby enabling it to access both of these coordination modes. In addition, DAF can access the κ^1 coordination mode, which relieves the modest strain present in the other two modes. The small α value for unligated bpy makes it well suited for coordination to Pd^{II} as a bidentate (κ^2) ligand, but poorly suited to serve as a bridging (μ) ligand. Rare examples of Pd$_2$(μ-bpy) complexes exist,[30] but they accommodate this coordination via a significant dihedral angle between the two pyridyl rings of the bpy ligands (53° and 59° respectively).
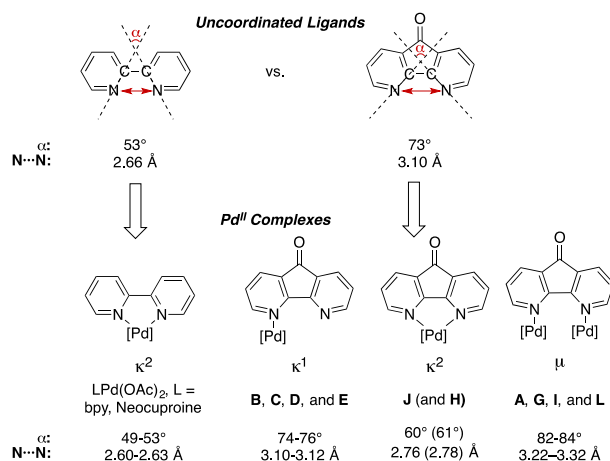
Scheme 3.10: Structural Comparison of 2,2'-Bipyridine, DAF and Corresponding Pd^{II} Complexes.

3.3.2 Relevance to Aerobic Oxidation Catalysis.

The unique coordination chemistry of DAF has important implications for Pd-catalyzed aerobic oxidation reactions. The simplified mechanism of these catalytic reactions consists of two half-reactions: substrate oxidation by Pd^{II} and catalyst reoxidation by O_2 (Scheme 3.11). The turnover-limiting step in most (if not all) of these reactions is associated with the Pd^{II}-mediated substrate oxidation half-reaction and corresponds to one of various fundamental steps, such as ligand substitution (i.e., substrate binding), alkene insertion (e.g., into a Pd–C or Pd–N bond), β-hydride elimination or C–H activation. Ligand steric and electronic properties influence the rate of the Pd^{II}-mediated reaction steps, and one or more ligands typically must dissociate from Pd^{II} to provide coordination sites for substrate reactivity. Steps associated with the catalyst reoxidation half-reaction are typically fast, by comparison, but ancillary ligands still play an important role.[31] Ligands not only promote the reaction of O_2 with Pd^0, but they also can minimize catalyst aggregation into inactive metallic Pd ("Pd-black").[32]
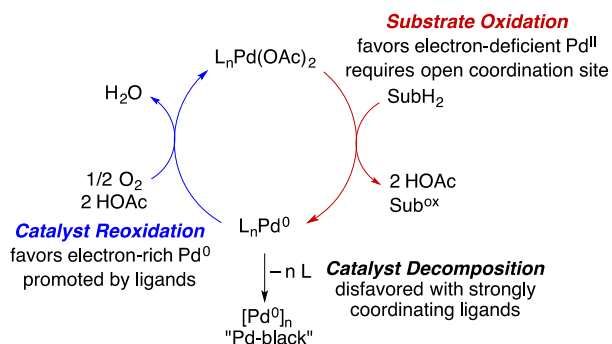
Scheme 3.11: Representative Catalytic Cycle for Pd-Catalyzed Aerobic Oxidations

Neutral monodentate ligands, such as pyridine, triethylamine (NEt_3) and DMSO, have been widely used in Pd-catalyzed aerobic oxidation reactions,[1] and typical catalyst systems employ a 2:1 $L:Pd^{II}$ stoichiometry. Mechanistic studies have revealed that faster initial rates may be obtained with a 1:1 $L:Pd^{II}$ stoichiometry, which enhances substrate accessibility to the Pd^{II} coordination sphere.[33] The use of $\geq$ 2:1 $L:Pd^{II}$ stoichiometry in reported catalyst systems represents the optimal balance between catalyst activity and stability. At $L:Pd^{II}$ ratios < 2:1, the catalyst often decomposes before the reaction reaches full conversion.

Bidentate ligands are appealing because they enhance catalyst stability, but they often inhibit catalytic turnover. The chelate effect disfavors neutral ligand dissociation and, therefore, anionic ligand dissociation is required to enable substrate access to the Pd^{II} coordination sphere. Formation of a charged complex has a strong solvent dependence, as illustrated by a recent study of amidopalladation of alkenes with a (bpy)Pd^{II}(amidate)Cl complex (Scheme 3.12).[34] Alkene insertion does not proceed in toluene, while it proceeds readily in DMSO at room temperature. The reaction was shown to proceed via pre-equilibrium dissociation of chloride, which is strongly inhibited in a non-polar solvent.

Solvent Effect

Toluene: No reaction
DMSO: Rapid reaction at rt;
Chloride inhibition
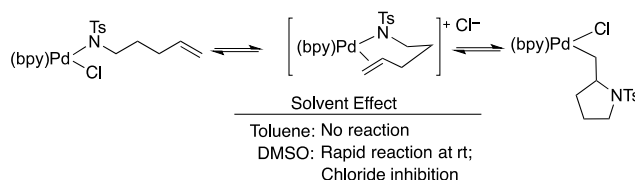
Scheme 3.12: Solvent Effect on X-Tpye Ligand Dissociation

The structures of DAF/Pd(OAc)$_2$ complexes presented herein show that DAF exhibits properties of both mono- and bidentate ligands. And, the empirical success of DAF in Pd-catalyzed aerobic oxidation reactions suggests that DAF can take advantage of the beneficial features of both ligand types. The κ^1 coordination mode, evident in structures **B–E**, provides access to open coordination sites at Pd^{II} without requiring dissociation of an anionic ligand. This feature should stabilize intermediates and/or transition states associated with key substrate oxidation steps, such as C–H activation, alkene insertion or β-hydride elimination (Scheme 3.13).[8-10] On the other hand, the bidentate character of DAF evident in **F**, **H**, **J**, Pd(DAF)(η^3-allyl)$^{+}$ [6b] and Pd(DAF)Cl$_2$ [15] provides a means to enhance catalyst stability upon formation of Pd^0 in the catalytic cycle.
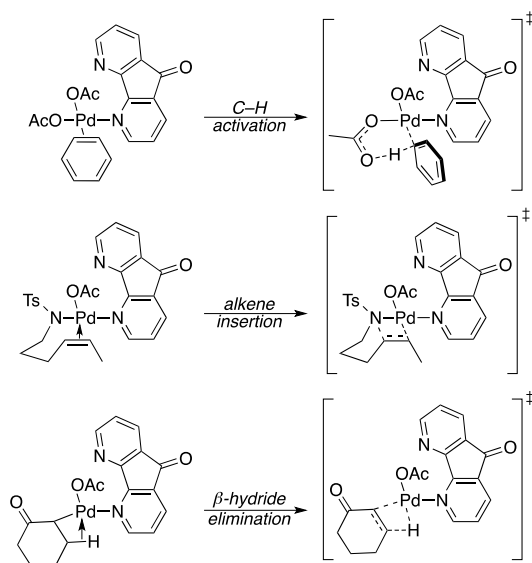
Scheme 3.13: Proposed Intermediates and Transition States in DAF-Promoted Catalysis.

The principles discussed here have implications for other Pd-catalyzed oxidation reactions. Of particular note are the allylic and aromatic C–H oxidation reactions that employ 2,2'-bipyrimidine (bpm)-Pd[II] catalysts, reported recently by Bercaw/Labinger[35a] and Yin,[35b] respectively (Scheme 3.14). These reactions are promoted by coordination of the bpm ligand to a second metal, Pd[II] or Al[III]. This coordination could lead to a structural distortion similar to that has been characterized for DAF in the present study.[36,37] Further investigation of this concept in catalytic reactions is the focus of ongoing investigation.
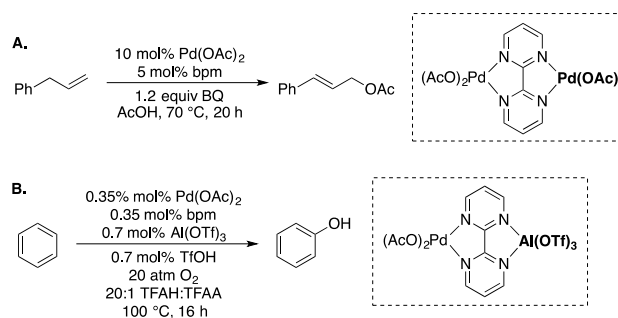
Scheme 3.14: Pd(bpm)(OAc)$_2$-Catalyzed C–H Oxidation Reactions Promoted by Ligand Coordination to a Second Metal.

3.4   Conclusion.

The rich coordination chemistry of 4,5-diazafluoren-9-one (DAF)-Pd(OAc)$_2$ has been characterized by diverse NMR spectroscopic methods, X-ray crystallography and DFT calculations. In particular, ^{1}H-^{15}N HMBC and ROESY experiments played a critical role in determining the coordination mode of the DAF ligand in solution. The data show that DAF is able to adopt bridging (μ), chelating (κ^2) and monodentate (κ^1) coordination modes in monomeric and dimeric Pd^{II} complexes. Six different DAF/Pd(OAc)$_2$ species have been characterized and compared to analogous Me$_2$DAF/Pd(OAc)$_2$, DAF/Pd(TFA)$_2$, DAF/Pd(OPiv)$_2$ and DAF/Pd(O$_2$CC$_6$F$_5$)$_2$ species. The equilibrium population changes systematically as a function of [DAF], with monomeric structures favored at higher [DAF]. The hemilabile character of DAF provides a compelling rationale for the beneficial reactivity of DAF, relative to other bidentate ligands, in Pd-catalyzed aerobic oxidation reactions, and it provides a valuable foundation for future studies in this field.

3.5   Acknowledgements.

1. For reviews, see: (a) Stahl, S. S. *Angew. Chem. Int. Ed.* **2004**, *43*, 3400-3420. (b) Gligorich, K. M.; Sigman, M. S. *Chem. Commun.* **2009**, *26*, 3854-3867.

2. For representative examples, see the following: (a) Nishimura, T.; Onoue, T.; Ohe, K.; Uemura, S. *J. Org. Chem.* **1999**, *64*, 6750-6755. (b) Fix, S. R.; Brice, J. L.; Stahl, S. S. *Angew. Chem. Int. Ed.* **2002**, *41*, 164-166. (c) Ferreira, E. M.; Stoltz, B. M. *J. Am. Chem. Soc.* **2003**, *125*, 9578-9579. (e) Iwasawa, T.; Tokunaga, M.; Obora, Y.; Tsuji, Y. *J. Am. Chem. Soc.* **2004**, *126*, 6554-6555. (f) Zhang, Y.-H.; Shi, B.-F.; Yu, J.-Q. *J. Am. Chem. Soc.* **2009**, *131*, 5072-5074. (g) Izawa, Y.; Stahl, S. S. *Adv. Synth. Catal.* **2010**, *352*, 3223-3229. (h) Izawa, Y.; Pun, D.; Stahl, S. S. *Science* **2011**, *333*, 209-213. (i) John, L. C.;

Gunay, A.; Wood, A. J.; Emmert, M. H. *Tetrahedron* **2013**, *69*, 5758-5764.

3. (a) Steinhoff, B. A.; Guzei, I. A.; Stahl, S. S. *J. Am. Chem. Soc.* **2004**, *126*, 11268-11278. (b) Komano, T.; Iwasawa, T.; Tokunaga, M.; Obora, Y.; Tsuji, Y. *Org. Lett.* **2005**, *7*, 4677-4679. (c) Kubota, A.; Emmert, M. H.; Sanford, M. S. *Org. Lett.* **2012**, *14*, 1760-1763.

4. (a) ten Brink, G.-J.; Arends, I. W. C. E.; Papadogianakis, G.; Sheldon, R. A. *Appl. Catal., A* **2000**, 435-442. (b) Hu, J.; Gu, Y.; Guan, Z.; Li, J.; Mo, W.; Li, T.; Li, G. *Chem. Sus. Chem.* **2011**, *4*, 1767-1772. (c) Ye, M.; Gao, G.-L.; Yu, J.-Q. *J. Am. Chem. Soc.* **2011**, *133*, 6964-6967. (d) Ben-Yahia, A.; Naas, M.; Kazzouli, S. E.; Essassi, E. M.; Guillaumet, G. *Eur. J. Org. Chem.* **2012**, *36*, 7075-7081.

5. Ref 4b and 4c. See also: (a) Shiotani, A.; Itatani, H.; Inagaki, T. *J. Mol. Catal.* **1986**, *34*, 57-66. (b) Gasperini, M.; Ragaini, F.; Cenini, S.; Gallo, E.; Fantauzzi, S. *Applied Organomet. Chem.* **2007**, *21*, 782-787.

6. Ref 2g and the following: (a) Andappan, M. M. S.; Nilsson, P.; Larhed, M. *Chem. Commun.* **2004**, *2*, 218-219. (b) Zheng, C. W.; Wang, D.; Stahl, S. S. *J. Am. Chem. Soc.* **2012**, *134*, 16496-16499.

7. Campbell, A. N.; White, P. B.; Guzei, I. A.; Stahl, S. S. *J. Am. Chem. Soc.* **2010**, *132*, 15116-15119.

8. (a) Campbell, A. N.; Meyer, E. B.; Stahl, S. S. *Chem. Commun.* **2011**, *47*, 10257-10259. (b) Xiao, B.; Gong, T.-J.; Liu, Z.-J.; Liu, J.-H.; Luo, D.-F.; Xu, J.; Liu, L. *J. Am. Chem. Soc.* **2011**, *133*, 9250-9253.

9. (a) Gao, W.; He, Z.; Qian, Y.; Zhao, J.; Huang, Y. *Chem. Sci.* **2012**, *3*, 883-886. (b) Diao, T.; Wadzinski, T. J.; Stahl, S. S. *Chem. Sci.* **2012**, *3*, 887-891. (c) Buter, J.; Moezelaar, R.; Minnaard, A. J. *Org. Biomol. Chem.* **2014**, *12*, 5883-5890.

10. (a) Piotrowicz, M.; Zakrzewski, J. *Organometallics* **2013**, *32*, 5709-5712. (b) Piotrowicz, M.; Zakrzewski J.; Métivier, R.; Brosseau,A.; Makal, A.; Woźniak K. *J. Org. Chem.* **2015**, *80*, 2573-2581. (c) Vasseur, A.; Laugel, C.; Harakat, D.; Muzart, J.; Le Bras, J., *Eur. J. Org. Chem. 5*, **2015**, 944-948.

11. For other applications of DAF in Pd-catalyzed oxidation reactions, see: (a) Sharma, A.; Hartwig, J. F. *J. Am. Chem. Soc.* **2013**, *135*, 17983-17989. (b) Malik, H. A.; Taylor, B. L. H.; Kerrigan, J. R.; Grob, J. E.; Houk, K. N.; Du Bois, J.; Hamann, L. G.; Patterson, A. W. *Chem. Sci.* **2014**, *5,* 2353-2361.

12. (a) Li, B.; Li, B.; Zhu, X.; Zhang, Y. *Inorg. Chem. Commun.* **2003**, *6*, 1304-1306. (b) Siemeling, U.;

Scheppelmann, I.; Neumann, B.; Stammler, H.-G.; Schoeller, W. W. *Organometallics* **2004**, *23*, 626-628. (c) Yang, H.-J.; Kou, H.-Z.; Gao, F.; Cui, A.-L.; Wang, R.-J. *Acta Crystallogr., Sec. E* **2004**, *60*, m611-613. (d) Zhang, R.-L.; Zhao, J.-S.; Yang, S.-Y.; Ng, S. W. *Acta Crystallogr., Sec. E* **2004**, *60*, m262-263. (e) Tian, A.; Han, Z.; Peng, J.; Ying, J.; Sha, J.; Dong, B.; Zhai, J.; Liu, H. *Inorg. Chim. Acta* **2008**, *361*, 1332-1338. (f) Feng, X.-L.; Zhang, Y.-P. *Acta Crystallogr., Sec. E: Struct. Rep. Online* **2011,** *67*, m1171.

13. Klein, R. A.; Witte, P.; van Belzen, R.; Fraanje, J.; Goubitz, K.; Numan, M.; Schenk, H.; Ernsting, J. M.; Elsevier, C. J. *Eur. J. Inorg. Chem.* **1998**, *3*, 319-330.

14. For numerous other examples, see the following "perspective" article and references cited therein: Annibale, V. T.; Song, D. *Dalton Trans.*, **2016**, *45*, 32-49.

15. See ref. 7 and the following: Xu, Z.-G.; Liu, H.-Y.; Zhan, Q.-G.; Chen, J.; Xu, M.-J. *Acta Crystallogr., Sec. E* **2009**, *65*, m1166.

16. White, P. B.; Jaworski, J. N.; Zhu, G. H.; Stahl, S. S. unpublished results.

17. (a) Milani, B.; Alessio, E.; Mestroni, G.; Sommazzi, A.; Garbassi, F.; Zangrando, E.; Bresciani-Pahor, N.; Randaccio, L. *J. Chem. Soc,. Dalton Trans.* **1994**, *13*, 1903-1911. (b) Ragaini, F.; Gasperini, M.; Cenini, S.; Arnera, L.; Caselli, A.; Macchi, P.; Casati, N. *Chem. Eur. J.* **2009,** *15*, 8064-8077. (c) Bercaw, J. E.; Day, M. W.; Golisz, S. R.; Hazari, N.; Henling, L. M.; Labinger, J. A.; Schofer, S. J.; Virgil, S. *Organometallics* **2009**, *28*, 5017-5024. (d) Ye, Y.; Ball, N. D.; Kampf, J. W.; Sanford, M. S. *J. Am. Chem. Soc.* **2010**, *132*, 14682-14687.

18. TOCSY = Total Correlation Spectroscopy. This technique uses scalar coupling to transfer magnetization from one nuclei to another. The extent of transfer depends on the mixing time, with longer mixing times unveiling more of the coupling network, and will proceed until a quaternary center or non-protonated heteroatom is encountered.

19. ROESY = Rotating-frame Nuclear Overhauser Effect Spectroscopy. This technique is similar to NOESY in that it detects through-space interactions between protons. The ROESY experiment locks the selected magnetization along a specific direction in the transverse plane (rotating frame) by a high-

power spinlock rather than along the z-axis (NOESY). The sign of an ROE is always positive, whereas the sign of an NOE is dependent on the tumbling frequency of the molecule relative to the static magnetic field. At the temperatures used in the experiments in this study, NOE data cannot unambiguously distinguish between through-space interactions and chemical exchange. See the Supporting Information for more details.

20. HMBC = Heteronuclear Multiple-Bond Correlation spectroscopy is a long-range scalar coupling experiment that involves polarization transfer from 1H to X-nuclei that are typically 2 or 3 bonds away. It is often used to resolve the chemical shift of insensitive nuclei in structure determination studies.

21. This upfield shift in the ^{15}N resonance when Pd^{II} is coordinated is due to the occupation of the lone-pair in bonding. The ^{15}N chemical shift is also sensitive to the oxidation state of the metal, the coordination geometry (axial vs equatorial) and the ligand *trans* to the nitrogen. See: (a) Mason, J. *Chem. Rev.* **1981**, *81*, 205-227. (b) Pazderski, L.; Szłyk, E.; Sitkowski, J.; Kamieński, B.; Kozerski, L.; Toušek, J.; Marek, R. *Magn. Reson. Chem.* **2006**, *44*, 163-170.

22. ROESY experiments aimed at observing an ROE from OAc1 or OAc2 to OAc3 are complicated by chemical exchange that occurs among the acetate resonances (see Figure A 4).

23. The chemical shifts of the acetate -CH_3 groups seem to follow some general trends that are helpful to guide structural assignment (cf.Table A.1). For example, we find that the cis acetates in Pd(κ^2-N-N)(OAc)$_2$ complexes typically have -CH_3 1H resonances >2.1 ppm, while the trans acetates in PdL$_2$ (OAc)$_2$ complexes typically have 1H resonances <1.9 ppm. The bridging acetates that are present in the Pd dimers observed in this study have chemical shifts fall into a chemical shift region between the cis- and trans-κ^1-acetates (1.9–2.1 ppm).

24. See Supporting Information for full computational details. Optimization and frequencies calculations were performed with rB3LYP/6-31+G* for all non-Pd atoms and the Stuttgart 1997 basis set/ECP was used for Pd. PCM solvation calculations were performed with CHCl3 solvent parameters and at a higher basis set (6-311+G**) for all non-Pd atoms.

25. The experimental barrier was calculated from observing the lineshape of the acetate peaks for **D** and **E** variable-temperature NMR experiments (Figure A 11, Figure A 12).

26. The chemical shift of the acetate -C*H*3 groups of **C** at 1.85 ppm is significantly more downfield than the acetate resonances associated with **D** (1.66 ppm) and **E** (1.52 ppm). These relative chemical shifts align with the general trends that we observe for chemical shifts of *cis-* versus *trans*-acetates ligands in other complexes (cf. ref. 23).

27. A similar structure was obtained with pentafluorobenzoate ligands. See Supporting Information for X-ray crystallographic data for this species (Structure M, Figure A 45).

28. (a) 1,10-Phenanthroline: Nelyubina, Y. V.; Korlyukov, A. A.; Lyssenko, K. A. *Mendeleev Commun.* **2014**, *24*, 286-289. (b) 4,4'-Di-tert-butyl-2,2'-bipyridine: Amarante, T. R.; Figueiredo, S.; Lopes, A. D.; Gonçalves, I. S.; Paz F. A. A. *Acta Cryst.* **2009**, E65, o2047. (c) 2,2'-bipyridine: Kavitha, S. J.; Panchanatheswaran, K.; Low, J. K.; Glidewell, C. *Acta Crystallogr., Sect. C* **2005**, *61*, o473. (d) DAF: Fun, H.-K., Sivakumar, K., Zhu, D.-R., You, X.-Z. *Acta Cryst.* **1995**, *C51*, 2076-2078.

29. See Supporting Information for crystal structure data.

30. (a) Klein, A.; Lepski, R. *Z. Anorg. Allg. Chem.* **2009**, *635,* 878-848. (b) Fornies, J.; Navarro, R.; Sicilia, V.; Tomas, M. *Inorg. Chem.* **1993**, *32*, 3675-3681.

31. (a) Wilke, G.; Schott, H.; Heimbach, P. *Angew. Chem. Int. Ed.* **1967**, *6*, 92. (b) Konnick, M. M.; Guzei, I. A.; Stahl, S. S. *J. Am. Chem. Soc.* **2004**, *126*, 10212-10213. (c) Konnick, M. M.; Stahl, S. S. *J. Am. Chem. Soc.* **2008**, *130*, 5753-5762. (d) Konnick, M. M.; Decharin, N.; Popp, B. V.; Stahl, S. S. *Chem. Sci.* **2011**, *2*, 326-330.

32. Steinhoff, B. A.; Stahl, S. S. *J. Am. Chem. Soc.* **2006**, *128*, 4348-4355.

33. See refs. 2f, 3c and the following for examples: (a) Steinhoff, B. A.; Stahl, S. S. *Org. Lett.* **2002**, *4*, 4179-4181. (b) Schultz, M. J.; Park, C. C.; Sigman, M. S. *Chem. Commun.* **2002**, 3034-3035. (c) Ye, X. A.; Liu, G. S.; Popp, B. V.; Stahl, S. S. *J. Org. Chem.* **2011**, *76*, 1031-1044.

34. White, P. B.; Stahl, S. S. *J. Am. Chem. Soc.* **2011**, *133*, 18594-18597.

35. (a) Lin, B.-L.; Labinger, J. A.; Bercaw, J. E. *Can. J. Chem.* **2009**, *87*, 264-271. (b) Guo, H. J.; Chen,

Z.; Mei, F.; Zhu, D.; Xiong, H.; Yin, G. *Chem.–Asian J.* **2013**, *8*, 888-891.

36. We thank Dr. Jay A. Labinger (Caltech) for drawing our attention to this relationship between DAF/Pd(OAc)$_2$ and the bpm-[Pd(OAc)$_2$]$_2$ catalyst system.

37. For related observations made recently in the study of stoichiometric reactions of Pd(bpym)Ar2, see: Liberman-Martin, A. L.; Levine D. S.; Liu, W.; Bergman R. G.; Tilley, T. D. *Organometallics* **2016**, *35*, 1064-1069.

Chapter 4: Diazafluorenone-Promoted Oxidation Catalysis: Insights into the Role of Bidentate Ligands in Pd-Catalyzed Aerobic Aza-Wacker Reactions

This work was done in collaboration with Paul B. White, Geyunjian Harry Zhu, Shannon S. Stahl*

This work has been published on April 11th 2016 in ACS Catalysis: White, P. B.; Jaworski, J. N.; Geyunjian, H. Z.; Stahl, S. S. ACS Catal. **2016**, *6*, 3340-3348. DOI:10.1021/acscatal.6b00953

Footnotes included to designate the independent work of PBW, GHZ and JNJ in this body of work.

Screening Table 4-1 was the combined effort of PBW and GHZ and reproduced by JNJ

Data in Figures 4-1, 4-3 and 4-4 as well as data in section B5, B6 (kinetic and titration data) are the combined effort of PBW and JNJ

Discovery and data concerning $Pd(\kappa^1\text{-DAF})(pyridine)(OAc)_2$ (Figure 4-5) and $Pd(\kappa^1\text{-}Me_2bpy)(pyridine)(OAc)_2$ (Scheme 4-3) were independently obtained by PBW. Calculated values in scheme 4-4 and other all calculations were performed by PBW. Elucidation of amidopalladation mechanistic pathway was determined by PBW (Scheme 4.3). Supplemental Data in sections B4, B7 and B8 were all independently collected by PBW. Additional details for these sections can be found in the publication (reference above) or P. B. White thesis appendix.

Data in Figure 4-2, Table 4-2 and the crystal structure for $Pd(\kappa^1\text{-}Me_2DAF)(pyridine)(OAc)_2$ (Section B9), was collected independently by JNJ.

4.1 Introduction.[a]

The discovery of ligand-modulated palladium(II) catalysts has played a major role in the growth of homogeneous palladium-catalyzed aerobic oxidation reactions over the past 15+ years.[1,2] Ancillary ligands often provide the basis for dioxygen-coupled catalytic turnover without requiring cocatalysts or other stoichiometric oxidants, such as benzoquinone or Cu^{II} salts. Synthetic and mechanistic studies of these reactions highlight multiple roles of the ligands in this chemistry (Scheme 4.1). The ligands play a crucial role in stabilizing the catalyst[3] and promoting reoxidation of Pd^0 by O_2 (Scheme 4.1: a and c).[4,5] Ligands also enable control over reaction selectivity, prominent examples of which include kinetic resolution of secondary alcohols,[6] and regio-[7] and enantioselective[8] oxidative Heck reactions. But, the role of ligands is not always beneficial. Ligands often inhibit catalytic turnover or slow the rate by attenuating the electrophilicity of the Pd^{II} center and/or occupying open coordination sites needed for substrate oxidation. The characteristics of ligands that contribute to favorable, rather than deleterious, effects are not well understood, and insights into such factors could have a major impact on the field.[9]
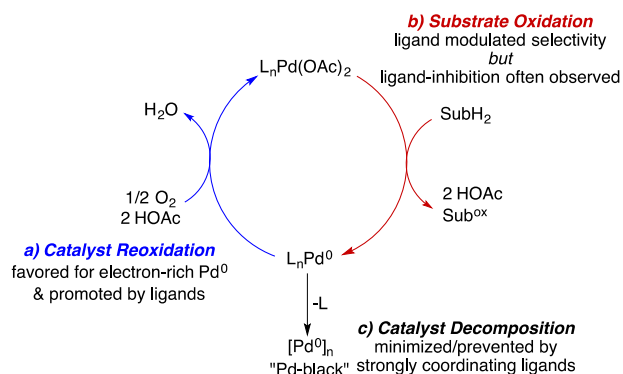
Scheme 4.1: Simplified Mechanism and Overview of Ligand Effects in Pd-Catalyzed Aerobic Oxidations Reactions.

Pyridine (py)-based ligands are widely used in Pd-catalyzed aerobic oxidation reactions.[1,2] In one of the earliest examples, Uemura and coworkers reported that $Pd(OAc)_2$/py (1:4 ratio) is a highly effective catalyst for aerobic alcohol oxidation (eq 1).[10] Upon finding that a similar catalyst system, $Pd(OAc)_2$/py (1:2 ratio), mediates efficient intramolecular oxidative amination of alkenes (eq 2; aza-Wacker reactions),[11]

---

[a] Introduction written by PBW, revised by JNJ to include additional ligand discussion.

we undertook mechanistic studies of these reactions to gain insight into the ligand effects.[5e,12] In the alcohol oxidation reaction, $Pd(OAc)_2$ shows no catalytic turnover in the absence of pyridine. The initial catalytic rate maximizes at 1:1 $Pd(OAc)_2$/py; however, catalyst decomposition into Pd black limits the total turnover numbers. The catalyst is less active but more stable at higher [py], and the optimized 1:4 $Pd(OAc)_2$/py catalyst system represents the compromise between catalyst activity and stability that achieves the highest synthetic yields.[10b] Related pyridine effects were observed for the aza-Wacker reaction, with the optimal balance observed with a 1:2 $Pd(OAc)_2$/py catalyst system.[12c,13]
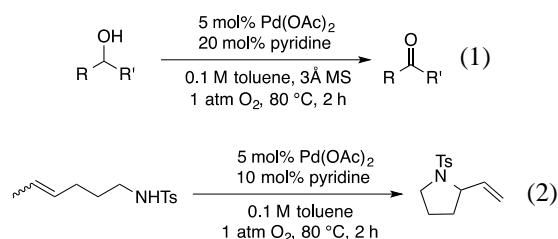
Bidentate ligands, such as 2,2'-bipyridine (bpy) and phenanthroline (phen), are appealing ligands to consider for Pd-catalyzed aerobic oxidation reactions because their chelating ability should enhance the stability of Pd^0 and promote its oxidation by O_2 (cf. Scheme 4.1). But, bpy and phen strongly inhibit the reactions shown in eqs 1 and 2,[10,14] and similar inhibitory effects have been observed in numerous other reactions.[15,16] In an investigation of aerobic acetoxylation of allylic C–H bonds,[17] we observed negligible catalytic activity with $Pd(OAc)_2$, both in the absence of an ancillary ligand and in the presence of pyridine or numerous bpy and phen ligand derivatives (eq 3). The sole exception was 4,5-diazafluoren-9-one (DAF). DAF/$Pd(OAc)_2$ proved to be an effective catalyst for aerobic allylic C–H acetoxylation of allyl benzene and numerous other terminal alkene substrates. Subsequent studies have shown that DAF is uniquely effective in a number of other Pd-catalyzed aerobic oxidation reactions, including oxidative C–C and C–O coupling reactions with arenes,[18] α,β-dehydrogenation of cyclic ketones,[19] oxidative Heck reactions,[20] and also various non-aerobic oxidation reactions.[21]

$$Ph \diagdown + \xrightarrow[\substack{AcOH, 1 \text{ atm } O_2 \\ 80\,°C, 18\text{ h}}]{\substack{5 \text{ mol\% Pd(OAc)}_2 \\ \mathbf{5 \text{ mol\% ligand}}}} Ph \diagdown OAc \qquad (3)$$
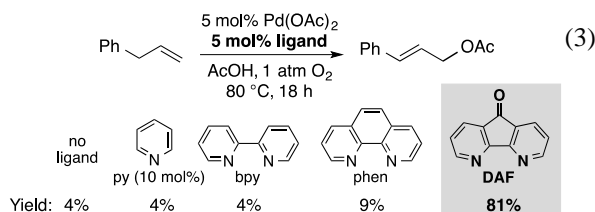
The basis for the unique effect of DAF in eq 3 and the other reactions is not well understood. In a recently completed study,[22] we characterized *six* different complexes, including both monomeric and dimeric species, that are simultaneously present in a 1:1 mixture of DAF and Pd(OAc)$_2$ (Chart 4.1). The complex coordination chemistry of DAF[23] sharply contrasts the behavior of other bidentate ligands, such as bpy and phen, which form 1:1 adducts as the sole structure in solution. The unique ligand behavior of DAF correlates with the unique catalytic behavior noted above, but the mechanistic basis for the catalytic effects has not been established.

Chart 4.1: Structures Present in a 1:1 Solution of DAF and Pd(OAc)$_2$.[22]
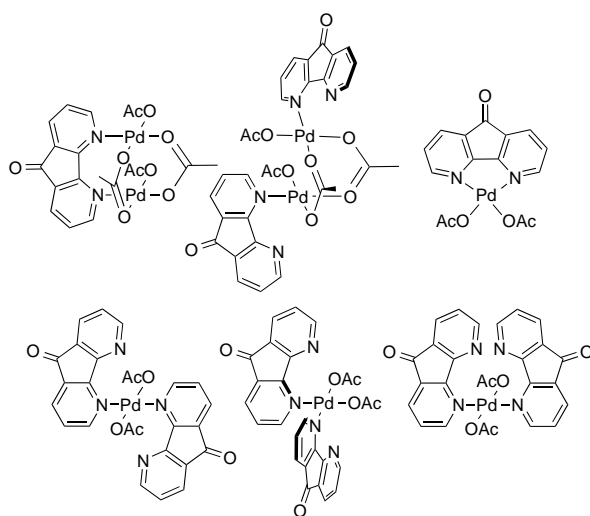
In an effort to gain further insights into the role of DAF, we decided to revisit the reactivity of bidentate ligands in Pd-catalyzed aza-Wacker reactions. This reaction class is one of the most extensively studied among Pd-catalyzed aerobic oxidations, with efforts leading to the identification of numerous catalyst systems, synthetic applications, and mechanistic insights.[24,25] These precedents provide an excellent framework for the investigation of ligand contributions to reactivity. Here, we show that whereas most

bidentate ligands strongly inhibit catalytic turnover, both DAF and 6,6'-dimethyl-2,2'-bipyridine (6,6'-Me$_2$bpy) support reactivity. Only DAF, however, exceeds the utility of pyridine and exhibits "ligand accelerated catalysis". Kinetic, spectroscopic, X-ray crystallographic, and DFT computational studies show that DAF and 6,6'-Me$_2$bpy exhibit hemilabile behavior in solution. The collective data provide valuable insights into ligand properties that promote efficient catalytic turnover and have broad implications for the field of Pd-catalyzed aerobic oxidation, as well as other catalytic applications.

4.2   Results and Discussion.

4.2.1   Comparison of Ligand Effects on Pd-Catalyzed Aerobic Aza-Wacker Reactivity.

4-Alkenyltosylamides (cf. eq 2) have been widely used for the development of new Pd catalyst systems[26] and characterization of catalytic mechanisms.[27] Therefore, *cis*-4-hexenyltosylamide (**1**) was chosen to assess the influence of bidentate ligands on aerobic aza-Wacker reactivity. A broad series of bpy and phen derivatives were evaluated in this reaction at 50 °C under conditions similar to those described previously with the Pd(OAc)$_2$/py-catalyst system (Table 4.1). Ligand-free Pd(OAc)$_2$ and the Pd(OAc)$_2$/py were included for comparison.[28] The ligand-free conditions (entry 1) give a moderate product yield, but poor mass balance. By-products were not fully characterized, but sulfonyl imine and its aldehyde hydrolysis product are detected. In contrast, Pd(OAc)$_2$/py catalyzes clean conversion to the pyrrolidine product in 86% yield (entry 2).[11] Use of four different phen derivatives, 4,4'-^{t}Bu$_2$bpy, and bipyrimidine (entries 3–8) resulted in nearly complete inhibition of the reaction (yield ≤ 10%). Use of 2,2'-dipyridyl ketone and 6-Mebpy resulted led to a moderate yield (26% and 38%, respectively; entries 9 and 10), however, and the yield improved considerably upon use of 6,6'-Me$_2$bpy (81%, entry 11). The best results were observed with 9,9-dimethyl-4,5-diazafluorene (Me$_2$DAF) and DAF, which led to near-quantitative yield (92% and 97%, respectively; entries 12 and 13). The relative effects of 6,6'-Me$_2$bpy and the DAF derivatives were further analyzed at room temperature. Under these conditions, Me$_2$DAF and DAF proved to be quite effective, again affording excellent yield (92% and 97%, respectively), whereas a considerably lower yield was

observed with 6,6'-Me$_2$bpy (40%). That all reactions except the ligand-free reaction exhibited excellent mass balance highlights the beneficial effect of ligands on reaction chemoselectivity. A number of traditional bidentate ligands strongly inhibit catalytic reactivity, but this preliminary screen also shows that certain bidentate ligands, specifically, 6,6'-Me$_2$bpy, Me$_2$DAF and DAF, match or exceed the performance of pyridine.

Table 4.1: Assessment of Bidentate Ligands on Oxidative Amidation. a. Conditions: substrate (75 μmol, 0.1 M), Pd(OAc)$_2$ (3.75 μmol), O$_2$ (1 atm), toluene (0.75 mL), 50 °C, 24 h. b. Yield determined by 1H NMR spectroscopy, int. std. = PhSiMe$_3$.[b]

Reaction time-course studies performed with selected ligands at 50 °C provided further insight into the ligand effects. Reactions with DAF, 6,6'-Me$_2$bpy and the structurally related 2,9-Me$_2$phen ligand were compared to the ligand-free and Pd(OAc)$_2$/py-catalyzed reactions (Figure 4.1).[29] The latter benchmark reactions exhibit similar rates of substrate consumption, and the reaction with 6,6'-Me$_2$bpy is only moderately slower. The impact of the moderately slower rates observed with pyridine and 6,6'-Me$_2$bpy relative to the ligand-free conditions is offset by the improved mass balance/reaction selectivity observed

---

[b] Screening initially performed by GHZ and PBW. Reproduced by JNJ and included additional data for 9,9'-Me$_2$DAF

in the presence of these ligands, as manifested in the product yields obtained from the reactions (cf. Table 4.1). 2,9-Me$_2$phen almost completely inhibits of the reaction, while the reaction with DAF is significantly faster than all of the other reactions. DAF enables complete conversion to the pyrrolidine product in approximately 1 h, with excellent mass balance.
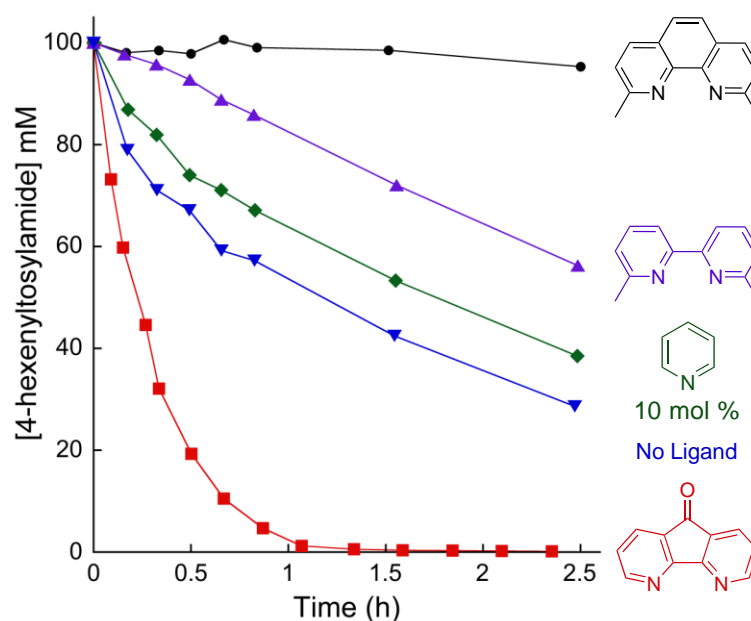
Figure 4.1: Kinetic time courses of the oxidative cyclization of (Z)-4-hexenyltosylamide. Conditions: 5 mol % Pd(OAc)$_2$ (3.4 mg, 15 μmoles), ligand (2,9-Me$_2$phen, 6,6'-Me$_2$bpy, DAF = 5 mol % 15 μmoles; pyridine: 10 mol % 30 μmoles), 1 (76 mg, 300 μmoles, 0.1 M), 50 °C, 1 atm O$_2$, toluene (3 mL), int. std. = 1,3,5-trimethoxybenzene. The reaction was followed for 2.5 hours for with data collected every 5 min for DAF, and the other ligands were followed with data collected every 10 min for the first 50 min and every hour for two more hours.[c]

Next, the influence of Pd(OAc)$_2$:ligand stoichiometry on the catalytic reaction was evaluated (Figure 4.2). The pyridine data (Figure 4.2A) resemble those obtained previously under slightly different conditions.[11c] A modest increase in rate is observed from 0–1 equiv of pyridine with respect to Pd(OAc)$_2$. Beyond this stoichiometry, additional pyridine exhibits an inhibitory effect until it reaches a non-zero plateau at high [py]. The bidentate ligands 6,6'-Me$_2$bpy and 2,9-Me$_2$phen inhibit Pd(OAc)$_2$ in direct proportion to their stoichiometry with respect to Pd(OAc)$_2$ (Figure 4.2B,C); however, 2,9-Me$_2$phen

---

[c] Kinetic data in Figure 4.1 collected by PBW. Figure 4.1 reproduced by JNJ and JNJ added data for neocuproine.

completely inhibits the reaction at ≥1 equiv of ligand relative to Pd(OAc)$_2$, while 6,6'-Me$_2$bpy/Pd(OAc)$_2$ retains moderate catalytic activity beyond 1:1 stoichiometry. The behavior of DAF is unique. No inhibitory effect is observed, even with a large excess of DAF (Figure 4.2D). This type of ligand-acceleration effect with a neutral-donor ligand is, to our knowledge, unprecedented in Pd-catalyzed aerobic oxidations.
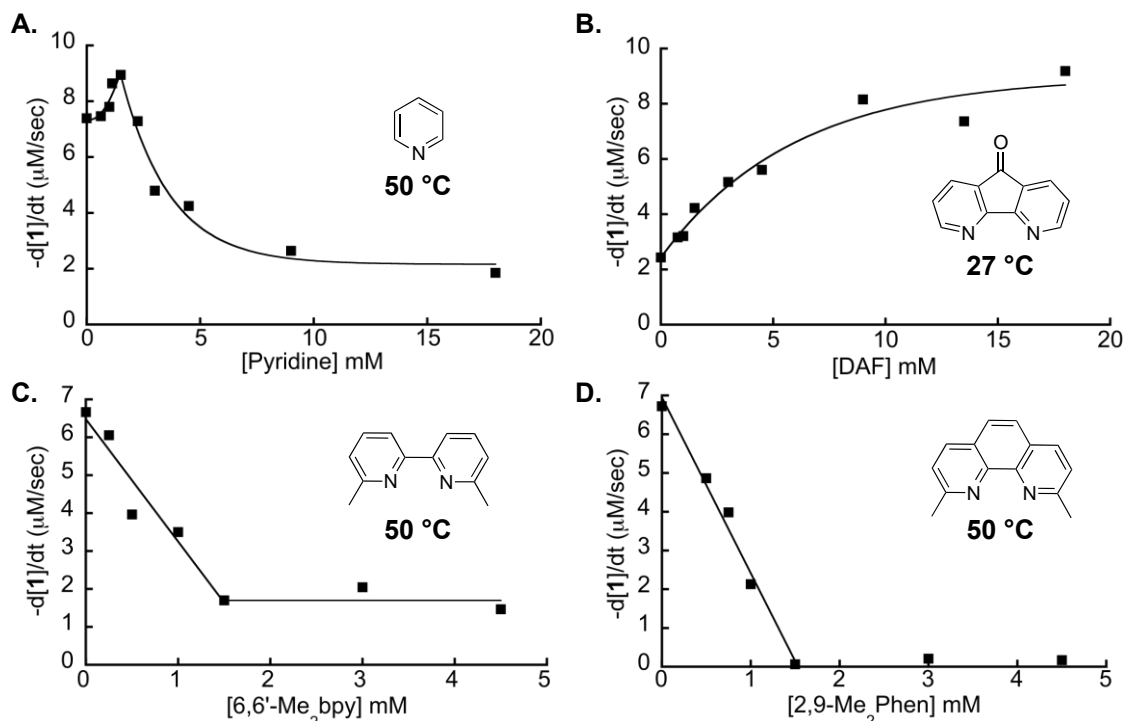
Figure 4.2: Kinetic dependence of initial rate of the oxidation of (Z)-4-hexenyltosylamide on [ligand]. Conditions were as followed: [Substrate] = 0.1 M, [Pd(OAc)$_2$] = 1.5 mM, 3 mL, pO$_2$ = 730 torr, toluene (3 mL). (A) [Py] = 0-18 mM, 27 °C. (B) [DAF] = 0-18 mM 50 °C. (C) [6,6'-Me$_2$bpy] = 0-4.5 mM, 50 °C. (D) [2,9-Me$_2$phen] = 0-4.5 mM, 50 °C.[d]

4.2.2   Ligand Coordination Properties and Relative Binding Strength.

As noted in the Introduction, DAF forms six nearly isoenergetic coordination compounds upon reaction with Pd(OAc)$_2$ (cf Chart 4.1).[22] This unusual coordination chemistry was the focus of a recent study and was attributed to structural distortions of DAF relative to traditional bpy and phen ligands (Figure 4.3). Meanwhile, 6,6'-Me$_2$bpy and 2,9-Me$_2$phen also show unusual coordination behavior resulting from the steric clash between the methyl groups and other ligands in the square plane. An X-ray crystal obtained for

---

[d] Kinetic dependencies in Figure 4.2 collected independently by JNJ

Pd(6,6'-Me$_2$bpy)(OAc)$_2$ (Figure 4.4A) highlights the distorted coordination geometry of this complex. The plane of the 6,6'-Me$_2$bpy ligand lies at a 33° angle with respect to the Pd^{II} square plane, which reduces the steric interaction between the two ligand methyl groups and the acetate ligands. Similar structural behavior has been reported previously for Pd(2,9-Me$_2$phen)(OAc)$_2$, in which the phen ligand bends out of the square plane by 34°.[30] One difference is evident between the 6,6'-Me$_2$bpy and 2,9-Me$_2$phen ligands: the 6,6'-Me$_2$bpy ligand exhibits an unfavorable steric interaction between the hydrogen atoms in the 3 and 3' positions (Figure 4.4B), whereas the phenanthroline ligand has a covalent C=C bond in this position. This feature is believed to destabilize the binding of 6,6'-Me$_2$bpy relative to 2,9-Me$_2$phen, as elaborated below.
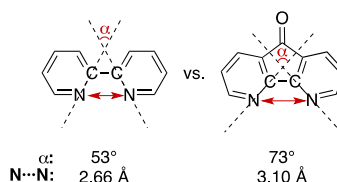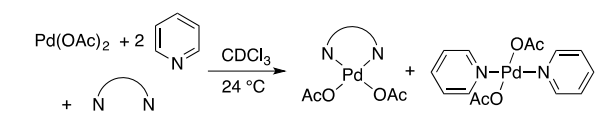
Figure 4.3: Comparison of uncoordinated bpy and DAF ligands, highlighting the structural distortion of DAF.

A. Crystal Structure of Pd(6,6'-Me$_2$bpy)(OAc)$_2$.

B. Steric Interactions Formed Upon Chelation to Pd(OAc)$_2$
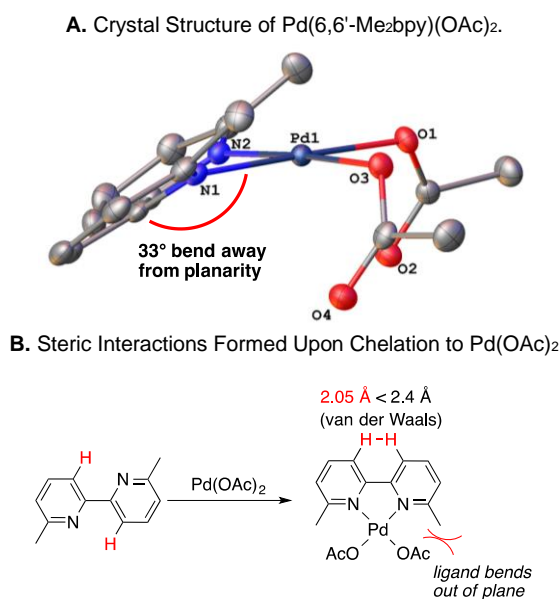
Figure 4.4: X-ray crystal structure of Pd(6,6'-Me$_2$bpy)(OAc)$_2$ depicting the steric effects of the methyl groups that causes bending of the 6,6'-Me$_2$bpy ligand out of the Pd^{II} square plane by 27°. (A; the molecular representation of the crystal structure is drawn with 50% thermal ellipsoids and the hydrogen atoms are omitted for clarity). Illustration of the steric clash between the 3 and 3' hydrogen atoms of the 6,6'-Me$_2$bpy ligand (B).

An effort was made to assess the relative binding strength among 4,4'-^{t}Bu$_2$bpy, 2,9-Me$_2$phen, 6,6'-Me$_2$bpy, and DAF as ligands. Each of these ligands was combined with Pd(OAc)$_2$ in a 1:1 ratio in CDCl$_3$, and variable quantities of pyridine (0.5–5 equiv) were then added to these solutions (see Supporting Information, Figure B 4-Figure B 8).[31] The different mixtures were analyzed by ^{1}H NMR spectroscopy and, in all cases except with DAF, the sole species observed in solution were the Pd(N~N)(OAc)$_2$ adduct and *trans*-Pd(py)$_2$(OAc)$_2$. Mixtures of Pd(OAc)$_2$, the N~N ligand, and pyridine in 1:1:2 ratios provide a diagnostic assessment of the relative binding strengths of the different ligands (Table 4.2). With 4,4'-^{t}Bu$_2$bpy, negligible quantities of the pyridine complex were observed (< 3%). With 2,9-Me$_2$phen, the bidentate ligand complex was favored 5:1 over the pyridine adduct, while an approximately inverted ratio (1:4.3) was observed with 6,6'-Me$_2$bpy.

Table 4.2: Relative Ligand Binding Strength of Bidentate Ligands Relative to Pyridine.[e]

N~N Ligand	(N~N)Pd(OAc)$_2$: Pd(py)$_2$(OAc)$_2$
4,4'-^{t}Bu$_2$bpy	40 : 1
2,9-Me$_2$phen	5 : 1
6,6'-Me$_2$bpy	1 : 4.3
DAF	1 : 5.4[a]

[a] The DAF ligated species is Pd(κ^1-DAF)(py)(OAc)$_2$, not Pd(κ^2-DAF)(OAc)$_2$. See Figure 5 and text for details

The DAF mixture was complicated at room temperature, but negligible contribution from the simple κ^2-DAF complex was evident. Broadened peaks implicated dynamic exchange processes, and the solution was cooled to -35 °C to facilitate characterization of the species in solution. Two major species were present: Pd(py)$_2$(OAc)$_2$ and a new species, which was characterized by 1D and 2D NMR spectroscopic methods (including 1D TOCSY, 1D ROESY, ^{1}H-^{13}C HSQC, ^{1}H-^{13}C HMBC, and ^{1}H-^{15}N HMBC methods; see Supporting Information for details, Figure B 9-Figure B 15). This species was identified as Pd(κ^1-

---

[e] Data in table 4.2 collected by PBW. Revised by JNJ.

DAF)(py)(OAc)$_2$ and was present in a 1:5.4 ratio relative to Pd(py)$_2$(OAc)$_2$. The identity of this complex was further established by X-ray crystallography (Figure 4.5).[32]

A. Species observed from mixtures of Pd(OAc)$_2$, DAF and pyridine.
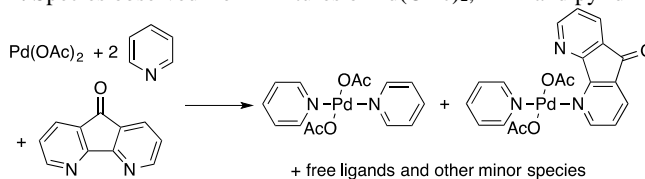
B. X-ray crystal structure of Pd(κ^1-DAF)(py)(OAc)$_2$.
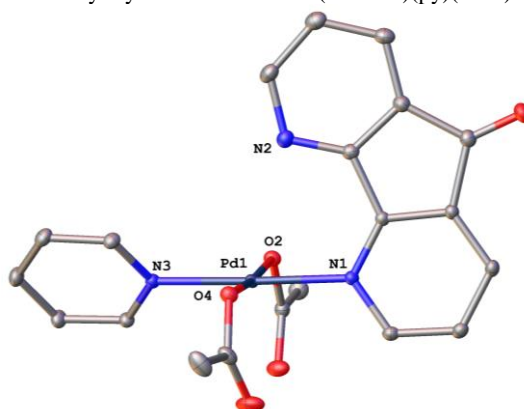
Figure 4.5: Observation of a mixed DAF/pyridine intermediate, 8, characterized by NMR spectroscopy (A) and X-ray crystallography (B). Molecular diagram of the crystal is drawn with 50% probability ellipsoids and all H atoms are omitted for clarity.[f]

The room-temperature mixtures of Pd(OAc)$_2$, 6,6'-Me$_2$bpy and pyridine also showed some evidence for dynamic behavior, reflected by changes in the chemical shift of peaks associated with the 6,6'-Me$_2$bpy as a function of the amount of pyridine in solution. As noted in Table 4.2, pyridine coordination is favored over coordination of 6,6'-Me$_2$bpy, and when pyridine was added to a solution of Pd(6,6'-Me$_2$bpy)(OAc)$_2$ at -70 °C, an intermediate species was detected. Upon warming a solution of this species, it converted into a simple mixture of Pd(6,6'-Me$_2$bpy)(OAc)$_2$ and Pd(py)$_2$(OAc)$_2$. NMR analysis of the intermediate showed evidence of dynamic exchange processes, even at -90 °C, which prevented heteronuclear 2D NMR characterization similar to that used with Pd(κ^1-DAF)(py)(OAc)$_2$. Nevertheless, ^{1}H 1D TOCSY, EXSY and ROESY experiments (Figure B 16, Figure B 17), in combination with integration of the 1D ^{1}H NMR spectrum,

---

[f] Crystals for DAF/pyridine intermediate collected by PBW.

revealed a 6,6'-Me$_2$bpy ligand with two inequivalent rings (Figure 4.6). Through-space interactions between the 6,6'-Me$_2$bpy, pyridine and two acetate ligands, and the integrations the respective peaks support a structure consisting of *trans*-Pd(κ^1-6,6'-Me$_2$bpy)(py)(κ^1-OAc)$_2$ (Figure 4.6). To our knowledge, this direct observation of reversible κ^1 coordination for 6,6'-Me$_2$bpy is unprecedented. No evidence for dynamic exchange processes were evident in the pyridine titration studies of 2,9-Me$_2$phen/Pd(OAc)$_2$ mixtures.
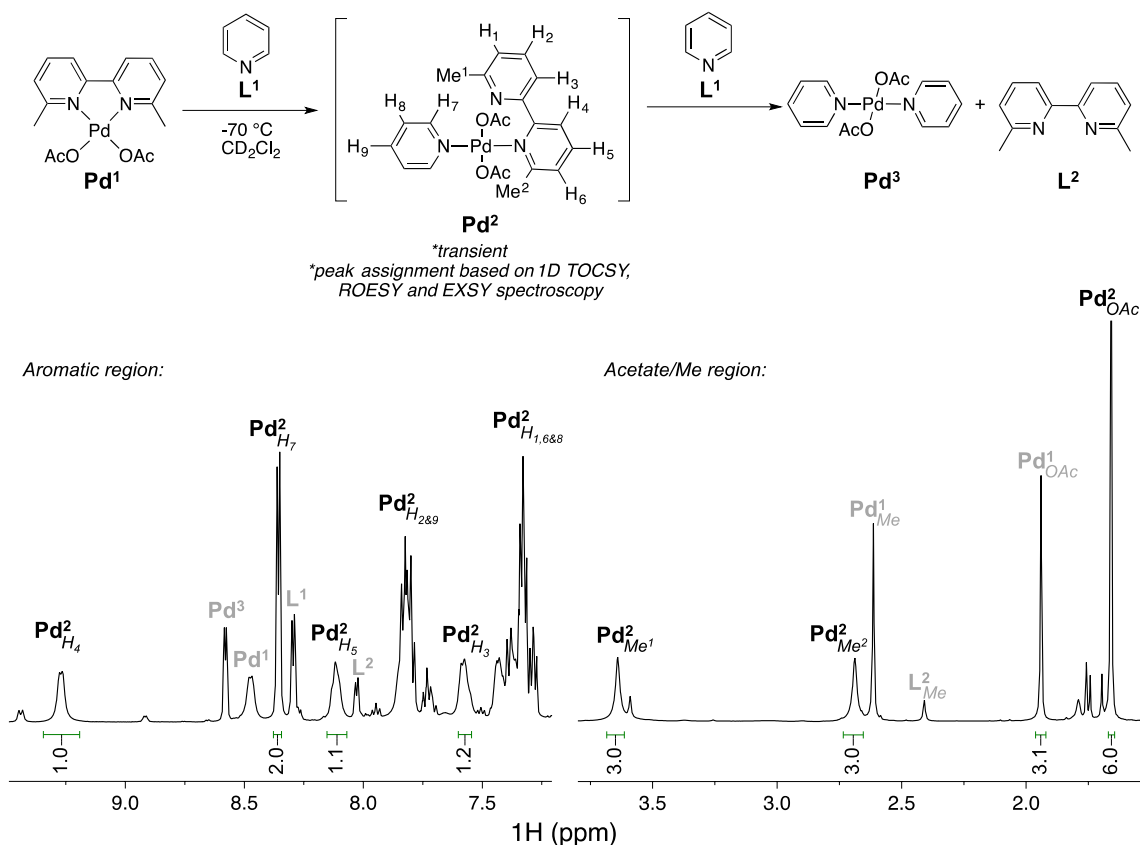
Figure 4.6: Observation of a mixed 6,6'-Me$_2$bpy/pyridine intermediate, β, characterized by NMR spectroscopy at -70 °C (ns = 8, ds = 2, d1 = 20 s). The integrations of the aromatic and aliphatic protons are consistent with trans-Pd(κ^1-6,6'-Me$_2$bpy)(py)(OAc)$_2$. Correlations within and between ligands were made with 1D TOCSY and ROESY experiments at -70 °C (See Supporting Information, Figure B 16, Figure B 17).[g]

To summarize, the pyridine titration studies suggest the ligand binding strength of the different bidentate ligands follows the trend 4,4'-^{t}Bu$_2$bpy > 2,9-Me$_2$phen > 6,6'-Me$_2$bpy ~ DAF. This trend inversely

---

[g] NMR Characterization of 6,6'-Me$_2$bpy/pyridine intermediate characterized by PBW independently.

correlates with the relative yields and rates observed with these ligands in the aza-Wacker reaction (Figure 4.1 and Figure 4.2). 4,4'-^{t}Bu$_2$bpy and 2,9-Me$_2$phen form static, strongly-bound 1:1 adducts with Pd(OAc)$_2$, and both strongly inhibit the catalytic reaction. In contrast, 6,6'-Me$_2$bpy exhibits dynamic behavior in the presence of a monodentate donor ligand (pyridine), with transient formation of a κ^1-ligated bpy adduct, while DAF exhibits dynamic interconversion between κ^2- and κ^1-coordination modes, even in the absence of a donor ligand (cf. Chart 4.1). The correlation between this bidentate ligand behavior and the respective catalytic activity supported by these ligands will be explored further below.

4.2.3   Assessment of Ligand Effects on the Aza-Wacker Reaction Mechanism.

Pd(OAc)$_2$/pyridine-catalyzed oxidative cyclization of 4-hexenyltosylamide has been the focus of previous mechanistic study and a simplified mechanism is depicted in Scheme 4.2. The reaction involves displacement of pyridine and an acetate ligand (as AcOH) to afford an alkene/amidate–Pd^{II} chelate, followed by insertion of the alkene into the Pd^{II}–N bond in a "*cis*-amidopalladation" reaction. Subsequent β-hydride elimination from the resulting alkyl–Pd^{II} species affords the vinyl-pyrrolidine product, and the Pd^{II}-hydride is then reoxidized by O$_2$ in a multistep process via a Pd^0 intermediate (Scheme 4.2).
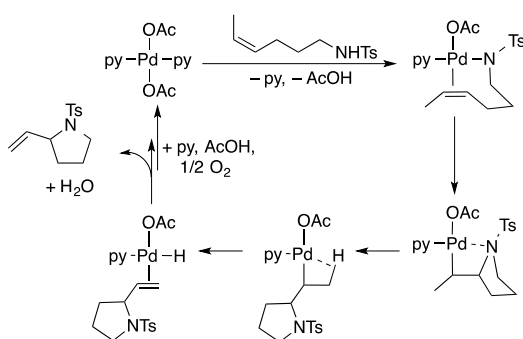
Scheme 4.2: Mechanism of Pd(OAc)$_2$/Pyridine-Catalyzed Aza-Wacker Cyclization.

Amidopalladation of alkenes can proceed via a *cis* or *trans* pathway, depending on the identity of the catalyst or reaction conditions.[24] Insight into the stereochemical course of the aza-Wacker reactions catalyzed by Pd(OAc)$_2$/6,6'-Me$_2$bpy and Pd(OAc)$_2$/DAF reaction was obtained by using the

stereospecifically labeled cyclopentene-d_1 derivative **I** (Scheme 4.3).[33] The bicylic product **II**, which arises from *cis*-amidopalladation of the alkene, was observed as the sole product of both reactions (72% and 98%, respectively). This outcome is consistent with a mechanism similar to the Pd(OAc)$_2$/pyridine-catalyzed pathway in Scheme 4.3.
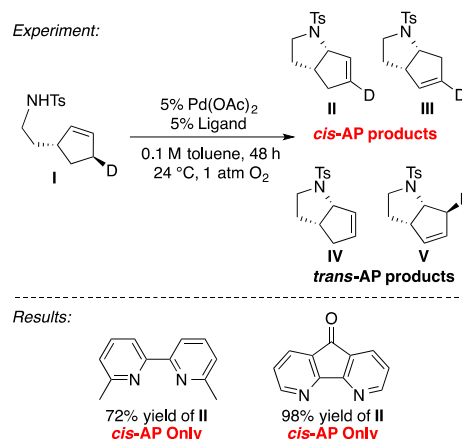
Scheme 4.3: cis- vs. trans-Amidopalladation (AP) Pathways with Bipyridyl Ligands and Pd(OAc)$_2$ where 6,6'-Me2bpy or DAF are used in catalysis.[h]

Density functional theory (DFT) methods were used to explore the aza-Wacker reaction pathway with three different ligands, 2,9-Me$_2$phen, 6,6'-Me$_2$bpy, and DAF. The calculations show that these ligands vary considerably in their binding strength to Pd(OAc)$_2$, consistent with the experimental results describe above (cf. Table 4.2). The bidentate ligand complexes range from strongly favored for 2,9-Me$_2$phen (-7.1 kcal/mol) to nearly isoergic for 6,6'-Me$_2$bpy (-1.4 kcal/mol) and DAF (-1.8 kcal/mol) (Scheme 4.4). For comparison, *trans*-Pd(py)$_2$(OAc)$_2$ has a calculated energy of (-8.1 kcal/mol), and coordination of the traditional bpy ligand 4,4'-^{t}Bu$_2$bpy, which lack steric features or structural distortions that would disfavor binding, is strongly favored ($\Delta G° = $ -15.8 kcal/mol).

---

[h] Elucidation of cis-amidopalladation pathway performed by PBW independently.
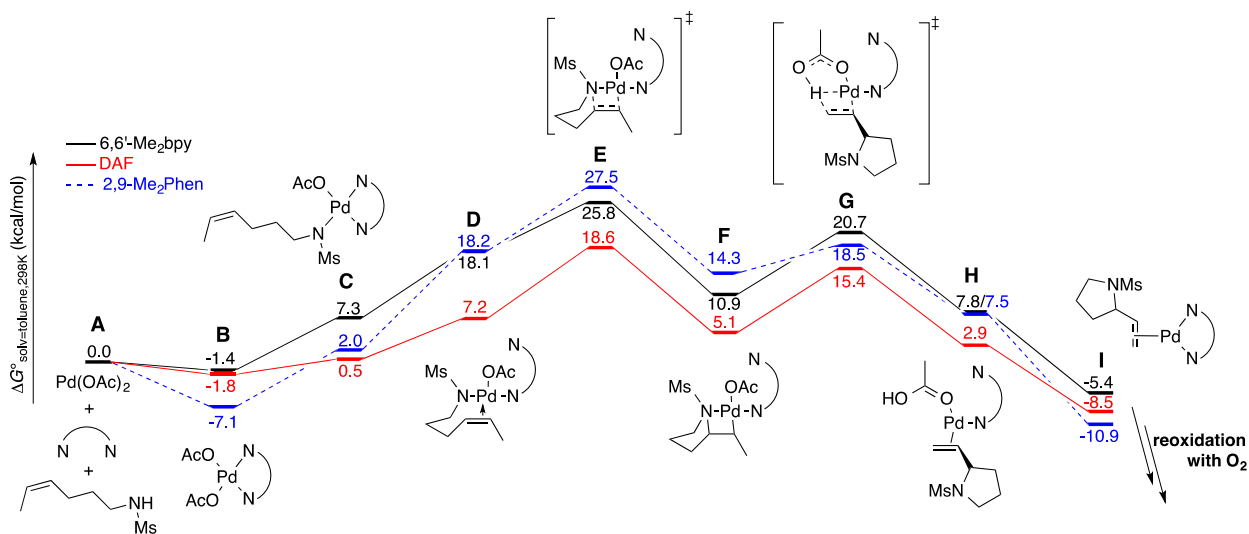
Scheme 4.4: Aza-Wacker Reaction Pathway and Energetics for DAF, 6,6'-Me₂bpy and 2,9-Me₂Phen[i]

(*Z*)-4-Hexenylmethanesulfonamide was the used as the substrate to assess aza-Wacker reaction pathways (Scheme 4.4). Formation of a Pd^{II}-amidate via proton-coupled displacement of an acetate ligand (i.e., with loss of AcOH) is uphill by approx. 9 kcal/mol for the 2,9-Me₂phen and 6,6'-Me₂bpy complexes, but only by 2.3 kcal/mol for the DAF complex. This difference reflects steric effects of the methyl groups in 2,9-Me₂phen and 6,6'-Me₂bpy, which disfavor binding of the larger mesylamide group relative to acetate. Coordination of the alkene to afford a chelated alkene/amidate structure requires dissociation of another ligand from Pd^{II}. Loss of acetate to afford a cationic complex is energetically costly in a non-polar solvent, such as toluene. For example, formation of the DAF complex [Pd(DAF)(alkene/amidate)]$^{+}$OAc^{-} (**D'**) is calculated to have an energy of 29.0 kcal/mol (Figure 4.7). The experimental evidence for κ^2/κ^1 interconversion of DAF and 6,6'-Me₂bpy (cf. Figure 4.5, Figure 4.6) prompted us to consider an alternative pathway involving dissociation of one of the pyridyl rings of the chelating ligand (i.e., **C → D**). This step is especially accessible with DAF. The alkene/amidate–Pd^{II} chelate lies at 7.2 kcal/mol, which is only 9 kcal/mol higher in energy than the initial Pd(OAc)₂/DAF complex. And, the subsequent transition state for alkene insertion into the Pd–N bond (**E**) (i.e., *cis*-amidopalladation of the alkene) is at 18.6 kcal/mol ($\Delta G^{\ddagger}$

---

[i] All calculations performed by PBW.

= 20.4 kcal/mol relative to Pd(DAF)(OAc)$_2$). The analogous transition state with 6,6'-Me$_2$bpy is higher in energy (25.8 kcal/mol), but still quite accessible. The absolute energies of the 2,9-Me$_2$phen and 6,6'-Me$_2$bpy transition states differ by less than 2 kcal/mol; however, Pd(2,9-Me$_2$phen)OAc$_2$ has significant ground-state stability that results in a very high net activation energy ($\Delta G^{\ddagger}$ = 34.6 kcal/mol) and accounts for the inhibitory effect of this ligand. For comparison, the previously reported computational study of the Pd(py)$_2$(OAc)$_2$-catalyzed reaction revealed a net activation energy for the reaction of 24.6 kcal/mol,[12c] which is higher than that of the DAF-based reaction, but lower than that of the reactions with 6,6'-Me$_2$bpy and 2,9-Me$_2$phen. The relative calculated activation-energies for the different ligands align with the relative experimental ligand-reactivity trends shown in Figure *4.1* and highlight the importance of both ground-state and transition-state ligand effects on the reaction.

D'
ΔG°$_{calc}$ = 29.0 kcal/mol
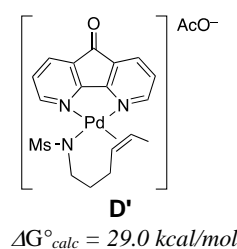
Figure 4.7: DAF complex [Pd(DAF)(alkene/amidate)]$^+$OAc$^-$ (D').

Subsequent β-hydride elimination from the Pd-alkyl intermediate **F** is lower in energy than the amidopalladation step. The preferred pathway identified for this process features a concerted "reductive β-hydride elimination" step in which the β-hydrogen of alkyl ligand is transferred directly to the free oxygen of the carboxylate ligand, resulting in formation of a Pd^0 product with a bound AcOH ligand (**H**), rather than a Pd^{II}–hydride species. A similar pathway was identified previously for a Pd-catalyzed alcohol oxidation reaction.[34] Loss of the AcOH ligand from this complex is energetically favorable, and subsequent oxidation of the resultsing Pd(N~N)(alkene) complex is expected to be very facile, on the basis of prior studies of this reaction.[5a,e,35]

4.3   Conclusions and Implications for Aerobic Oxidation Catalysis.[j]

The results presented above add another Pd-catalyzed aerobic oxidation method to the growing number of reactions that benefit from the use of DAF as an ancillary ligand. In the present case, DAF is the only bidentate bpy/phen-type ligand among numerous examples that supports efficient catalytic turnover at room temperature. Perhaps more importantly, the results described here provide some of the first clear insights into the unique ability of DAF to promote these reactions.

The unusual coordination properties of DAF, evident in Chart *4.1*[22] and elsewhere,[23] reflect the structural differences of DAF relative traditional bpy- and phen-type ligands that make it a non-ideal chelating ligand (cf. Figure 4.3). Coordination of DAF to Pd[II] as a bidentate ligand requires a distortion of the DAF ligand, and the resulting strain raises the ground-state energy of the catalyst. This strain contributes to the low-energy interconversion between κ^2/κ^1 ligand-coordination modes, which then facilitates binding of the alkene substrate to Pd[II] and lowers the transition-state energy of the rate-limiting *cis*-amidopalladation step. The reaction pathway in Scheme 4 highlights the synergistic participation of the basic X-type ligand (acetate), which undergoes proton-coupled exchange with the N–H group of the amide substrate (i.e., N–H activation), and a neutral L-type ligand (one of the pyridyl rings of DAF) that is readily displaced to enable activation of the neutral alkene.

There are aspects of the "ligand acceleration" effect that remain unclear, but the salient point is that DAF does not bind as strongly to Pd(OAc)$_2$ as does pyridine or traditional bidentate ligands. This point is highlighted in Table 4.2 and appears again in the computational studies (Scheme 4.4). More-stable catalyst ground states contribute to higher net activation barriers in the catalytic reaction.

Similar ligand effects are expected to play important roles in other Pd-catalyzed aerobic oxidations, which typically require coordination of both X- and L-type substrate fragments at the Pd[II] center. For example, α,β-dehydrogenation of ketones,[19] oxidative Heck (i.e., aryl-C–H/alkene) coupling[20] and allylic C–H oxidation reactions[17,21] have been promoted by DAF as an ancillary ligand. Each of these reactions

---

[j] Conclusions section written by PBW, modified by JNJ to include additional ligand discussion.

resemble the aza-Wacker reaction in that they feature steps that require simultaneous access to L- and X-type ligand sites by the substrate(s) and/or involve carboxylate-mediated activation of a substrate that is coordinated to Pd^{II} as a neutral donor ligand (Figure 4.8). Each of these reactions is expected to benefit from the strain-induced hemilability of the DAF ligand, which provide low-energy access to an open L-type coordinate site at Pd^{II}.
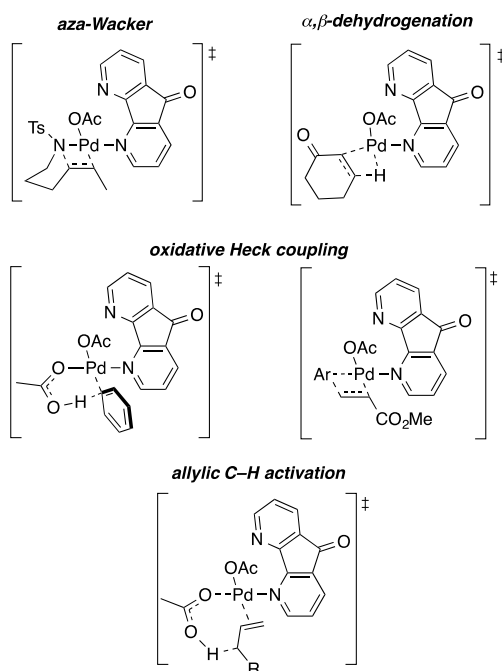
Figure 4.8: Representative transition-state structures in Pd-catalyzed aerobic oxidation reactions that feature substrate coordination to Pd^{II} in L- and X-type ligand sites and/or involvement of carboxylate-mediated activation of a substrate that is coordinated to Pd^{II} as a neutral donor ligand.

Collectively, the insight gained from this study illuminate features of DAF that make it especially effective in many Pd-catalyzed aerobic oxidation reactions. Current efforts are being directed toward the intentional design and testing of new ligands with similar features that could prove to be even more effective than DAF.

4.4 Acknowledgements.

1. For general reviews of this field, see: (a) Stahl, S. S. *Angew. Chem. Int. Ed.* **2004**, *43*, 3400-3420. (b) Gligorich, K. M.; Sigman, M. S. *Chem. Commun.* **2009**, *26,* 3854-3867.

2. For more-focused reviews/perspectives, see: (a) Sheldon, R. A.; Arends, I. W. C. E.; ten Brink, G.-J.; Dijksman, A. *Acc. Chem. Res.* **2002**, *35*, 774-781. (b) Toyota, M.; Ihara, M. *Synlett* **2002**, *8*, 1211-1222. (c) Nishimura, T.; Uemura, S. *Synlett* **2004**, 201-216. (d) Stoltz, B. M. *Chem. Lett.* **2004**, *33*, 362-367. (e) Sigman, M. S.; Jensen, D. R. *Acc. Chem. Res.* **2006**, *39*, 221-229. (f) Kotov, V.; Scarborough, C. C.; Stahl, S. S. *Inorg. Chem.* **2007**, *46*, 1910-1923. (g) Campbell, A. N.; Stahl, S. S. *Acc. Chem. Res.* **2012**, *45*, 851-863.

3. For studies probing ligand effects on catalyst stability, see: a) ten Brink, G.-J.; Arends, I. W. C. E.; Hoogenraad, M.; Verspui, G.; Sheldon, R. A. *Adv. Synth. Catal.* **2003**, *345,* 497-505. (b) ten Brink, G.-J.; Arends, I. W. C. E.; Hoogenraad, M.; Verspui, G.; Sheldon, R. A. *Adv. Synth. Catal.* **2003**, *345*, 497-505. (c) Steinhoff, B. A.; Fix, S. R.; Stahl, S. S. *J. Am. Chem. Soc.* **2002**, *124*, 766-767. (d) Steinhoff, B. A.; Stahl, S. S. *J. Am. Chem. Soc.* **2006**, *128*, 4348-4355.

4. For reviews of Pd/O_2 reactivity, see: (a) Muzart, J. *Chem. Asian J.* **2006**, *1*, 508-515 (b) Popp, B.; Stahl, S. S. *Top. Organomet. Chem.* **2007**, *22*, 149-189. (c) Scheuermann, M. L.; Goldberg, K. I. *Chem. Eur. J.* **2014**, *20,* 14556-14568.

5. For investigation of Pd^0 oxidation by O_2 in relation to aerobic oxidation catalysis, see: (a) Stahl, S. S.; Thorman, J. L.; Nelson, R. C.; Kozee, M. A. *J. Am. Chem. Soc.* **2001**, *123*, 7188–7189. (b) Landis, C. R.; Morales, C. M.; Stahl, S. S. *J. Am. Chem. Soc.* **2004**, 126, 16302-16303. (c) Konnick, M. M.; Guzei, I. A.; Stahl, S. S. *J. Am. Chem. Soc.* **2004**, *126*, 10212–10213. (d) Konnick, M. M.; Stahl, S. S. *J. Am. Chem. Soc.* **2008**, *130*, 5753–5762. (e) Popp, B. V.; Stahl, S. S. *Chem. Eur. J.* **2009**, *15*, 2915–2922. (f) Ingram, A. J.; Solis-Ibarra, D.; Zare, R. N.; Waymouth, R. M. *Angew. Chem. Int. Ed.* **2014**, *53*, 5648-

5652. (g) Ingram, A. J.; Walker, K. L.; Zare, R. N.; Waymouth, R. M. *J. Am. Chem. Soc.* **2015**, *137,* 13632-13646.

6. For leading references, see reference 2e and following leading references: (a) Ferreira, E. M.; Stoltz, B. M. *J. Am. Chem. Soc.* **2001**, *123*, 7725-7726. (c) Jensen, D. R.; Pugsley, J. S.; Sigman, M. S. *J. Am. Chem. Soc.* **2001**, *123*, 7475-7476. (d) Ebner, D. C.; Bagdanoff, J. T.; Ferreira, E. M.; McFadden, R. M.; Caspi, D. D.; Trend, R. M.; Stoltz, B. M. *Chem. Eur. J.* **2009**, *15*, 12978-12992.

7. (a) Andappan, M. M. S.; Nilsson, P.; von Schenck, H.; Larhed, M. *J. Org. Chem.* **2004**, *69*, 5212-5218. (b) Zheng, C.; Wang, D.; Stahl, S. S. *J. Am. Chem. Soc.* **2012**, *134*, 16496-16499. (c) Zheng, C.; Stahl, S. S. *Chem. Commun.* **2015**, *51*, 12771-12774.

8. (a) Yoo, K. S.; Park, C. P.; Yoon, C. H.; Sakaguchi, S.; O'Neil, J.; Jung, K. W. *Org. Lett.* **2007**, *9*, 3933-3935. (b) Sakaguchi, S.; Yoo, K. S.; O'Neill, J.; Lee, J. H.; Stewart, T.; Jung, K. W. *Angew. Chem. Int. Ed.* **2008**, *47*, 9326-9329. (c) Yoo, K. S.; O'Neill, J.; Sakaguchi, S.; Giles, R.; Lee, J. H.; Jung, K. W. *J. Org. Chem.* **2010**, *75*, 95-101. (d) Mei, T.-S.*;* Werner, E. W.; Burckle, A. J.; Sigman, M. S. *J. Am. Chem. Soc.* **2013**, *135*, 6830-6833. (e) Mei, T.-S.; Patel, H. H.; Sigman, M. S. *Nature* **2014**, *508*, 340-344. (f) Zhang, C.; Santiago, C. B.; Crawford, J. M.; Sigman, M. S. *J. Am. Chem. Soc.* **2015**, *137*, 15668-15671.

9. An important ligand class complementary to the ligands described here are amino acids, highlighted by the work of J. Q. Yu and coworkers. For leading references, see: (a) Shi, B.-F.; Maugel, N.; Zhang, Y.-H.; Yu, J.-Q. *Angew. Chem. Int. Ed.* **2008**, *47*, 4882-4886. (b) Wang, D. H.; Engle, K. M.; Shi, B. F.; Yu, J. Q. *Science* **2010**, *327*, 315-319. (c) Shi, B.-F.; Zhang, Y.-H.; Lam, J. K.; Wang, D.-H.; Yu, J.-Q. *J. Am. Chem. Soc.* **2010**, *132*, 460-461. (d) Engle, K. M.; Wang, D.-H.; Yu, J.-Q. *J. Am. Chem. Soc.* **2010**, *132*, 14137-14151. (e) Engle, K. M.; Thuy-Boun, P. S.; Dang, M.; Yu, J.-Q. *J. Am. Chem. Soc.* **2011**, *133*, 18183-18193. (f) Baxter, R. D.; Sale, D.; Engle, K. M.; Yu, J.-Q.; Blackmond, D. G. *J. Am. Chem. Soc.* **2012**, *134*, 4600-4606.

10. (a) Nishimura, T.; Onoue, T.; Ohe, K.; Uemura, S., *Tetrahedron Lett.* **1998**, *39*, 6011-6014. (b) Nishimura, T.; Onoue, T.; Ohe, K.; Uemura, S., *J. Org. Chem.* **1999**, *64*, 6750-6755.

11. Fix, S. R.; Brice, J. L.; Stahl, S. S., *Angew. Chem. Int. Ed.* **2002**, *41*, 164-166.

12. (a) Steinhoff, B. A.; Stahl, S. S. *Org. Lett.* **2002**, *4*, 4179-4181. (b) Steinhoff, B. A.; Guzei, I. A.; Stahl, S. S. *J. Am. Chem. Soc.* **2004**, *126*, 11268-11278. (c) Ye, X. A.; Liu, G. S.; Popp, B. V.; Stahl, S. S. *J. Org. Chem.* **2011**, *76*, 1031-1044.

13. For insights into pyridine ligand effects on Pd-catalyzed C–H oxidation reactions, see the following: (a) Zhang, Y. H.; Shi, B. F.; Yu, J. Q., *J. Am. Chem. Soc.* **2009**, *131*, 5072-5074. (b) Emmert, M. H.; Cook, A. K.; Xie, Y. J.; Sanford, M. *Angew. Chem. Int. Ed.* **2011**, *50*, 9409-9412. (e) Gary, J. B.; Cook, A. K.; Sanford, M. S. *ACS Catal.* **2013**, *3*, 700-703. (g) Kubota, A.; Emmert, M. H.; Sanford, M. S., *Org. Lett.* **2012**, *14*, 1760-1763. (g) Cook, A. K.; Sanford, M. S. *J. Am. Chem. Soc.* **2015**, *137*, 3109-3118.

14. Fix, S. R.; Stahl, S. S. unpublished results.

15. For representative examples, see the following references. In some cases, bpy and phen inhibit catalytic turnover, while other bidentate ligands show some utility. (a) ref. 7a. (b) Andappan, M. M. S.; Nilsson, P.; Larhed, M. *Chem. Commun.* **2004**, *2*, 218-219. (c) Izawa, Y.; Stahl, S. S. *Adv. Synth. Catal.* **2010**, *352*, 3223-3229. (d) Ying, C.-H.; Yan, S.-B.; Duan, W.-L. *Org. Lett.* **2014,** *16*, 500-503.

16. Bidentate ligands have been used successfully in Pd-catalyzed aerobic oxidation reactions, as documented in the following references. These examples invariably feature a polar/coordinating solvent (e.g., water, DMSO, dimethyl acetamide, DMF, CH3CN) or weakly coordinating anionic ligands (e.g., CF3CO2–, OTf–). The effectiveness of bidentate ligands in these reactions probably reflects the enhanced kinetic lability of anionic ligands under these conditions. See references 3a,b, 8, (a) ten Brink, G.-J.; W. C. E. Arends, I.; Papadogianakis, G.; A. Sheldon, R. *Chem. Commun.* **1998**, *21*, 2359-2360. (b) Bianchi, D.; Bortolo, R.; D'Aloisio, R.; Ricci, M. *Angew. Chem. Int. Ed.* **1999**, *38*, 706-708. (c) ten Brink, G.-J.; Arends, I. W. C. E.; Sheldon, R. A. *Science* **2000**, *287*, 1636-1639. (d) Conley, N. R.; Labios, L. A.; Pearson, D. M.; McCrory, C. C. L.; Waymouth, R. M. *Organometallics* **2007**, *26*, 5447-5453. (e) He, W.; Yip, K.-T.; Zhu, N.-Y.; Yang, D. *Org. Lett.* **2009**, *11*, 5626-5628. (f) Jensen, K. H.; Pathak, T. P.; Zhang, Y.; Sigman, M. S. *J. Am. Chem. Soc.* **2009**, *131*, 17074-17075. (g) McDonald, R.

I.; White, P. B.; Weinstein, A. B.; Tam, C. P. Stahl, S. S. *Org. Lett.* **2011**, *13*, 2830-2833. (h) Chung, K.; Banik, S. M.; De Crisci, A. G.; Pearson, D. M.; Blake, T. R.; Olsson, J. V.; Ingram, A. J.; Zare, R. N.; Waymouth, R. M. *J. Am. Chem. Soc.* **2013**, *135*, 7593-7602. (i) De Crisci, A. G.; Chung, K.; Oliver, A. G.; Solis-Ibarra, D.; Waymouth, R. M. *Organometallics* **2013**, *32*, 2257-2266.

17. Campbell, A. N.; White, P. B.; Guzei, I. A.; Stahl, S. S. *J. Am. Chem. Soc.* **2010**, *132*, 15116-15119.

18. (a) Campbell, A. N.; Meyer, E. B.; Stahl, S. S. *Chem. Commun.* **2011**, *47*, 10257-10259. (b) Xiao, B.; Gong, T.-J.; Liu, Z.-J.; Liu, J.-H.; Luo, D.-F.; Xu, J.; Liu, L. *J. Am. Chem. Soc.* **2011,** *133*, 9250-9253.

19. (a) Gao, W. M.; He, Z. Q.; Qian, Y.; Zhao, J.; Huang, Y. *Chem. Sci.* **2012**, *3*, 883-886. (b) Diao, T.; Wadzinski, T. J.; Stahl, S. S. *Chem. Sci.* **2012**, *3*, 887-891. (c) Buter, J.; Moezelaar, R.; Minnaard, A. J. *Org. Biomol. Chem.* **2014**, *12*, 5883-5890.

20. (a) Piotrowicz, M.; Zakrzewski, J. *Organometallics* **2013**, *32*, 5709-5712. (b) Piotrowicz, M.; Zakrzewski, J.; Métivier, R.; Brosseau, A.; Makal, A.; Woźniak, K. *J. Org. Chem.* **2015**, *80*, 2573-2581. (c) Vasseur, A.; Laugel, C.; Harakat, D.; Muzart, J.; Le Bras, J. *Eur. J. Org. Chem.* **2015**, *2015*, 944-948.

21. (a) Sharma, A.; Hartwig, J. F. *J. Am. Chem. Soc.* **2013**, *135*, 17983-17989. (b) Malik, H. A.; Taylor, B. L. H.; Kerrigan, J. R.; Grob, J. E.; Houk, K. N.; Du Bois, J.; Hamann, L. G.; Patterson, A. W. *Chem. Sci.* **2014**, *5*, 2352-2361.

22. White, P. B.; Jaworski, J. N.; Fry, C. G.; Dolinar, B. S.; Guzei, I. A.; Stahl, S. S. *J. Am. Chem. Soc.* **2016**, *138*, 4869-4880.

23. For a review of DAF coordination chemistry, see: Annibale, See V. T.; Song, D. *Dalton Trans.* **2016**, *45*, 32-49.

24. McDonald, R. I.; Liu, G. S.; Stahl, S. S. *Chem. Rev.* **2011**, *111*, 2981-3019.

25. For additional reviews, see: (a) Zeni, G.; Larock, R. C. *Chem. Rev.* **2004**, *104*, 2285–2309. (b) Beccalli, E.M.; Broggini, G.; Martinelli,M.; Sottocornola, S. *Chem. Rev.* **2007**, *107*, 5318–5365. (c) Minatti, A.; Muñiz, K. *Chem. Soc. Rev.* **2007**, *36*, 1142–1152.

26. See reference 16g and also the following: (a) Tamaru, Y.; Tanigawa, H.; Itoh, S.; Kimura, M.; Tanaka, S.; Fugami, K.; Sekiyama, T.; Yoshida, Z.-i. *Tetrahedron Lett.* **1992**, *33*, 631-634. (b) Vanbenthem, R.; Hiemstra, H.; Longarela, G. R.; Speckamp, W. N. *Tetrahedron Lett.* **1994**, *35*, 9281-9284. (c) Larock, R. C.; Hightower, T. R.; Hasvold, L. A.; Peterson, K. P. *J. Org. Chem.* **1996**, *61*, 3584-3585 (d) Fix, S. R.; Brice, J. L.; Stahl, S. S. *Angew. Chem. Int. Ed.* **2002**, *41*, 164-166. (e) Rogers, M. M.; Wendlandt, J. E.; Guzei, I. A.; Stahl, S. S. *Org. Lett.* **2006**, *8*, 2257-2260. (f) Scarborough, C. C.; Stahl, S. S. *Org. Lett.* **2006**, *8*, 3251-3254. (g) Lu, Z.; Stahl, S. S. *Org. Lett.* **2012**, *14*, 1234-1237.

27. See reference 12c and the following: (a) Liu, G.; Stahl, S. S. *J. Am. Chem. Soc.* **2007**, *129*, 6328-6335. (b) Ye, X.; White, P. B.; Stahl, S. S. *J. Org. Chem.* **2013**, *78*, 2083-2090.

28. In our previous study, focused on the coordination chemistry of DAF with Pd-carboxylate complexes, we investigated complexes bearing CF3CO2– (TFA) and *t*BuCO2– (OPiv) as anionic ligands. Unfortunately, Pd(TFA)2 and its DAF complexes are insoluble under the present catalytic conditions, unless TFAH is added or a very polar solvents are used (the latter approach, however, leads to dissociation of DAF). DAF/Pd(OPiv)2 in the catalytic reaction was attempted; however, the reaction is very slow. Consequently, systematic studies of the TFA- and OPiv-based catalyst systems were not performed.

29. See Figure A 3 in the Supporting Information for a comparison of DAF and Me₂DAF in catalytic reactions performed at room temperature. The reaction proceeds much better with DAF, and therefore DAF was used in the subsequent systematic studies.

30. (a) Milani, B.; Alessio, E.; Mestroni, G.; Sommazzi, A.; Garbassi, F.; Zangrando, E.; Bresciani-Pahor, N.; Randaccio, L. *J. Chem. Soc,. Dalton Trans.* **1994**, *13*, 1903-1911. (b) Moulin, S.; Pellerin, O.; Toupet, L.; Paul, F. *C. R. Chim.* **2014**, *17*, 521-525.

31. Note: We had hoped to perform all of the studies (catalytic and mechanistic) in a uniform solvent (toluene); however, use of toluene as a solvent in our fundamental studies resulted in precipitation of the ligated DAF/Pd(OAc)₂ complexes. It was necessary to use a more polar solvent in these stoichiometric reactions. Control reactions were performed to confirm that CDCl₃ is a competent

solvent for the catalytic reaction. The reactions are successful in CDCl3; however, this solvent results in more Pd decomposition (Pd black).

32. A similar structure of Pd(κ^1-Me$_2$DAF)(pyridine)(OAc)$_2$ was also characterized. See supporting information for details. For Pd^0 complexes bearing κ^1-DAF ligands, see: Klein, R. A.; Witte, P.; van Belzen, R.; Fraanje, J.; Goubitz, K.; Numan, M.; Schenk, H.; Ernsting, J. M.; Elsevier, C. J. *Eur. J. Inorg. Chem.* **1998**, *3*, 319-330.

33. For previous applications of this substrate probe, see references 12c, 27a,b, and the following: Weinstein, A. B.; Stahl, S. S. *Angew. Chem. Int. Ed.* **2012**, *51*, 11505–11509.

34. Nielsen, R. J.; Goddard, W. A. *J. Am. Chem. Soc.* **2006**, *128*, 9651-9660.

35. Popp, B. V.; Thorman, J. L.; Stahl, S. S. *J. Mol. Catal., A: Chem.* **2006**, 251, 2-7.

Chapter 5: Observation of Palladium(I) In Aerobic Oxidation Catalysis

This work was done in collaboration with Scott McCann, Ilia Guzei and Shannon S. Stahl*

This work has been submitted for publication.

5.1 Introduction.

The development of new Pd-catalyzed oxidation reactions has been the focus of extensive research in recent years.[1] Reactions that proceed via a Pd^{II}/Pd^0 cycle are appealing because they are often compatible with the use of O_2 as the terminal oxidant.[2] Prominent examples include the Wacker process,[3] alcohol oxidation,[4] Wacker-type cyclization[5] and the Fujiwara-Moritani (dehydrogenative/oxidative Heck) reaction.[6] The majority of Pd-catalyzed aerobic oxidations proceed through a catalytic cycle wherein Pd^{II} mediates substrate oxidation and Pd^0 is reoxidized by O_2 (Scheme 5.1).[7] The Pd^0 intermediate in this cycle is metastable and susceptible to decomposition via aggregation into Pd nanoparticles and/or bulk metallic Pd. Use of ancillary ligands can help to prevent catalyst decomposition and/or promote reoxidation of Pd^0 by O_2, thereby avoiding a requirement for undesirable oxidants, such as stoichiometric Cu^{II}, Ag^{I}, or benzoquinone (BQ). Nevertheless, the ligand-modulated aerobic oxidation reactions often feature high catalyst loading and low turnover numbers. The basis for this limitation is poorly understood, and efforts to overcome this issue are complicated by limited understanding of catalyst speciation under aerobic oxidation conditions. Here, we report the first observation of a Pd^{I} intermediate in ligand-modulated Pd-catalyzed oxidation reactions and assess its role in the catalytic mechanism.
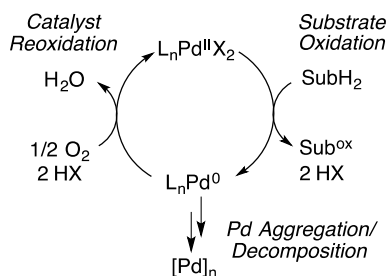
Scheme 5.1: Simplified Catalytic Cycle for Homogeneous Pd-Catalyzed Aerobic Oxidation Reactions.

Allylic C–H acetoxylation of alkenes and aza-Wacker reactions are two prototypical Pd-catalyzed aerobic oxidation reactions.[8] In previous studies of these reactions, we found that 4,5-diazafluoren-9-one

(DAF) is especially effective in promoting aerobic catalytic turnover [Eqs. (1) and (2)] [9,10] and that DAF adopts diverse coordination modes, including κ^1, κ^2, and bimetallic bridging (μ) ligation, under the catalytic conditions.[11,12]

5.2 Results and Discussion.
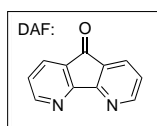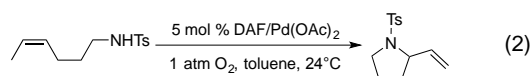
Our initial mechanistic studies of DAF/Pd(OAc)$_2$-catalyzed allylic acetoxylation revealed unusual kinetic behavior. The reaction time course exhibits two kinetic phases: an initial burst of product formation, followed by slower steady-state behavior (Figure 5.1). The initial color of the reaction mixture changes rapidly from a yellow solution to a deep red color upon addition of allyl benzene to a solution of the catalyst. When the beginning of the acetoxylation reaction was monitored by ^{1}H NMR spectroscopy (3:1 dioxane-d_8/AcOD-d_4), new DAF ligand peaks appeared during the burst phase, consistent with the formation of a symmetrical DAF-ligated Pd species. This new DAF species had well-dispersed ^{1}H chemical shifts (o-/m-/p-CH ^{1}H δ = 8.83, 7.54 and 8.21 ppm) and a ^{15}N chemical shift of 217 ppm (See Appendix C, Figure C 1).
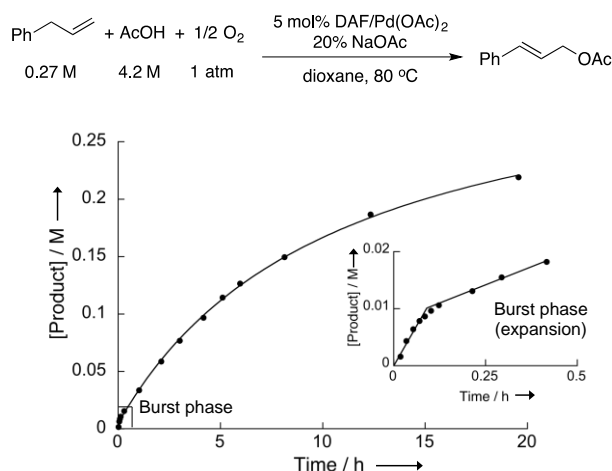
Figure 5.1: A 20 h time-course of DAF/Pd-catalyzed allylic acetoxylation of allyl benzene and expansion of the burst phase observed during the first 30 min of the reaction at 80 °C.

Complementary observations were made with the Pd-catalyzed aza-Wacker cyclization of (*Z*)-4-hexenyltosylamide. At 5 mol% catalyst loading, the reaction time course again exhibits two-phase kinetic behavior in which a burst of product formation is followed by a slower steady-state rate (Figure 5.2). Moreover, analysis of the aza-Wacker reaction by NMR spectroscopy in CDCl$_3$[13] revealed formation of a new symmetrical DAF species at early stages of the reaction. The ^{1}H and ^{15}N chemical shifts are similar to those observed in the acetoxylation reaction, with differences likely arising from the different reaction solvents (*o*-/*m*-/*p*-C*H* [1]H δ 8.71, 7.49 and 8.15 ppm and [15]N δ 219 ppm; see Figure C 2).
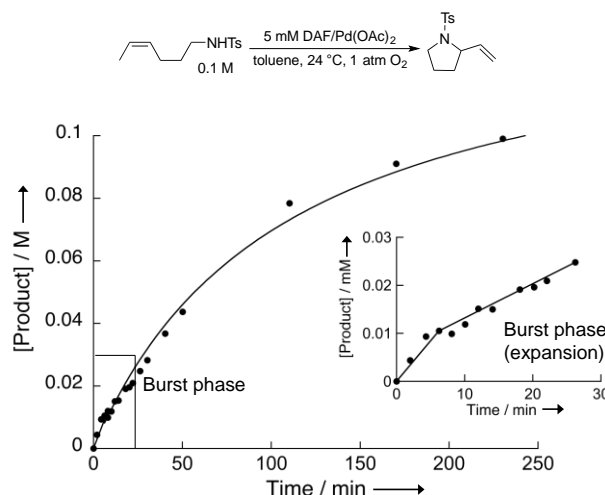
Figure 5.2: 5 h time course of DAF/Pd-catalyzed aza-Wacker and expansion of the burst phase observed during the first 30 min of the reaction at 24 °C.

Further studies of the aza-Wacker reaction yielded valuable insights. The initial rate of the reaction exhibited a nearly linear dependence on [Pd] at low catalyst loading, but shifted abruptly to a zero-order dependence at [Pd] = 2.5 mM (Figure 5.3A). This behavior implicated the onset of gas-liquid mass transport limitations at [DAF/Pd(OAc)$_2$] ≥ 2.5 mM, and O$_2$ pressure-dependence data support this hypothesis. The rate exhibits no dependence on pO$_2$ at low [DAF/Pd(OAc)$_2$] (0.5 mM) but a linear dependence at high [DAF/Pd(OAc)$_2$] (5 mM) (Figure 5.3B). Changes in the mixing technique (stirring versus orbital agitation) and use of different reaction vessels under otherwise identical conditions resulted in different rates. The rate plateau correlates with a color change from yellow to deep red and rapid precipitation of the Pd catalyst as a red solid.[14]
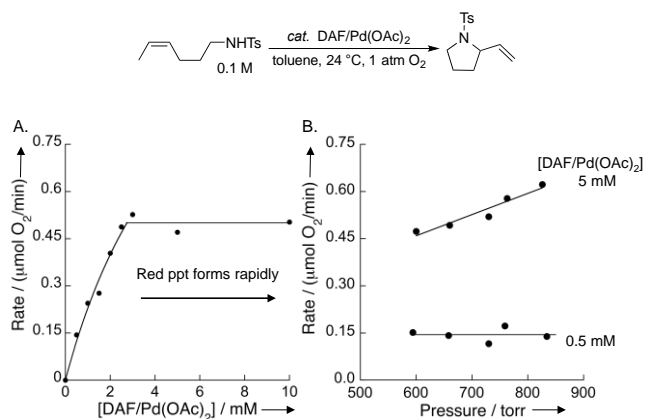
Figure 5.3: Catalyst and O_2 dependence on the aza-Wacker cyclization reaction. A. Catalyst dependence [DAF/Pd(OAc)$_2$] = 2 mM – 10 mM B. O_2 dependence with [DAF/Pd(OAc)$_2$] at 5 mM and 0.5 mM. All reaction performed with [(Z)-4-hexenyltosylamide] = 0.1 M and 730 torr O_2 and reactions monitored by O_2 gas consumption.

The new DAF/Pd(OAc)$_2$ species, observed by NMR spectroscopy in both reactions, does not match that of any previously characterized DAF/Pd(OAc)$_2$ species.[10,11] For example, the *ortho* and *para* protons of mononuclear κ^2-DAF- ligated Pd^{II} complexes overlap,[10] while the corresponding peaks of the new species are well resolved ($\Delta\delta > 0.5$ ppm). Dimeric Pd^{II} species with bridging DAF ligands have similarly well resolved chemical shifts for the *ortho* and *para* protons; however, the *o*-C*H* chemical shifts appear much further downfield (δ 9.9–10.6 ppm) than those in the new species (δ 8.6–8.7 ppm). The downfield ^{15}N chemical shift of DAF in the new species, detected by ^{1}H-^{15}N HMBC (δ 217-219 ppm), more closely resembles that of the dimeric Pd^{II} complex [(DAF)Pd(OPiv)$_2$]$_2$ (^{15}N δ 218 ppm) that those of mononuclear (κ^2-DAF)Pd^{II} complexes (^{15}N δ 199-213 ppm).

When the acetoxylation reaction was performed at room temperature, crystals suitable for single crystal X-ray diffraction (XRD) analysis were obtained from the red reaction mixture (see Experimental Details and Appendix C). XRD analysis of the red crystals revealed a Pd^I dimer with two bridging DAF ligands and a κ^1-acetate ligand capping each of the Pd centers (Figure 5.4). The Pd–Pd distance of 2.4764(7) Å is consistent with the presence of a bond between the two metals.[15] The 78.04(4)° dihedral angle between the planes of the two coordinated DAF ligands presumably allows Pd–N bonding to be maximized while

allowing the Pd centers to optimize Pd–Pd bonding. The acetate ligands exhibit a *syn* relationship, in which the carbonyl groups are oriented in the same direction. The [(DAF)Pd^I(OAc)]$_2$ complex co-crystallizes with one equivalent of dioxane and two equivalents of acetic acid (not shown in Figure 5.5), with the latter hydrogen bonding to the coordinated acetate ligands. This structure is an unusual example of a Pd^I dimer that does not have a bridging anionic (e.g., halide, allyl) or carbonyl ligand.[16,17]
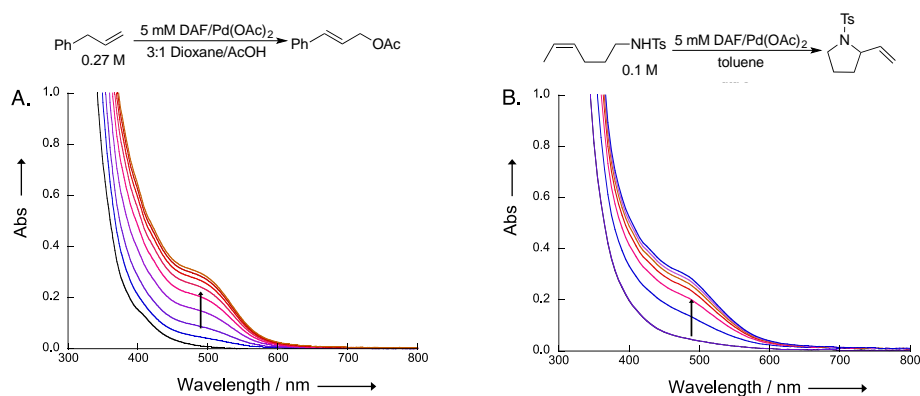
Figure 5.4: UV-visible spectra of an aza-Wacker and acetoxylation at room temperature under air. A. First 120 min of UV-visible time course 5 mM DAF/Pd(OAc)$_2$ in 3:1 Dioxane/AcOH with 0.27 M allylbenzene. B. First 60 s of UV-visible time course of a reaction of 5 mM DAF/Pd(OAc)$_2$ in toluene with 0.1 M (Z)-4-hexenyltosylamide.

The dimeric structure of the [Pd^I(μ-DAF)(OAc)]$_2$ complex was anticipated to be responsible for the UV-visible absorption band at 475 nm. But, to probe the origin of this feature, time-dependent density functional theory (TD-DFT) calculations were carried out. The calculations revealed an excitation at 497 nm, which is in good agreement with the experimental value. Electronic structural analysis of this transition show that is arises from excitation of an electron in the Pd–Pd σ bond as the HOMO into π* orbitals associated with the DAF ligand (Figure 5.6). The calculations predict an extinction coefficient of $\varepsilon = 0.99$ mM^{-1}·cm^{-1}, which is consistent with the experimental value from UV-visible titrations: $\varepsilon_{475\ nm} = 1.44$ mM^{-1} cm^{-1}.
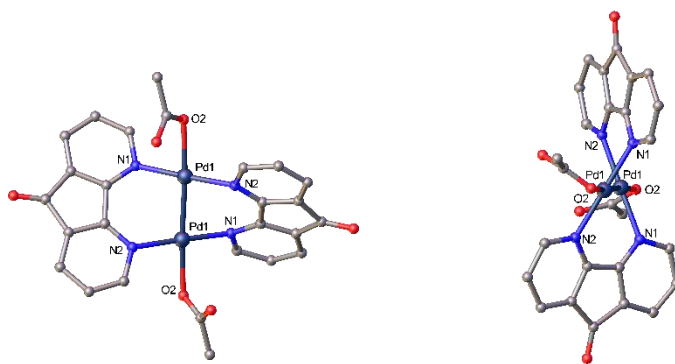
Figure 5.5: Two views of the structure of [Pd^I(μ-DAF)(OAc)]$_2$. H-atoms, two AcOH molecules and dioxane are omitted for clarity. Selected bond lengths [Å] and angles [°]: Pd1–Pd1 2.4764(7), Pd1–O2 2.2136(2), Pd1–N1 2.022(2), Pd1–N2 2.044(2). N1–Pd1–Pd1i–N2i 52.549(7). Symmetry code (i): 1-x, y, 1.5-z.

Formation of the Pd^I dimer may be rationalized by a reaction sequence involving oxidation of the substrate by Pd^{II}, followed by rapid reaction of the resulting Pd^0 intermediate with another equivalent of the Pd^{II} catalyst. To probe this mechanism of Pd^I formation, we performed the allylic acetoxylation and aza-Wacker reactions under anaerobic conditions [Eqs. (3) and (4)]. In both cases, approximately 50% yield of product was observed with respect to the original [Pd]. This result indicates that the Pd^{II} species reacts much faster with Pd^0 than with the substrate, resulting in formation of the Pd^I dimer. As an additional control experiment, Pd(OAc)$_2$ and 0.5 equivalents of Pd$_2$dba$_3$ were combined with 2 equivalents of DAF (DAF:Pd$_{total}$ = 1) in acetonitrile [Eq. (5)]. The dimeric Pd^I complex [Pd^I(μ-DAF)(OAc)]$_2$ formed rapidly and was isolated in 94% yield from this reaction. The NMR and UV-visible spectroscopic properties of this compound are identical to observed from the catalytic reactions.

HOMO: Pd^I-Pd^I ς-bond

hn

DAF-based p*
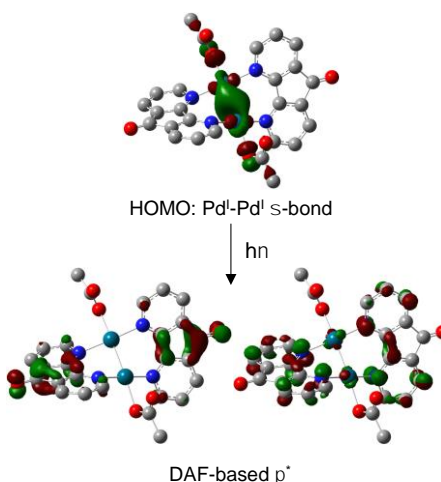
Figure 5.6: Calculated TD-DFT excitation corresponding to observed 475 nm absorbance of [Pd^I(μ-DAF)(OAc)]$_2$. Excitation from the Pd HOMO to different degenerate ligand antibonding orbitals (MLCT).
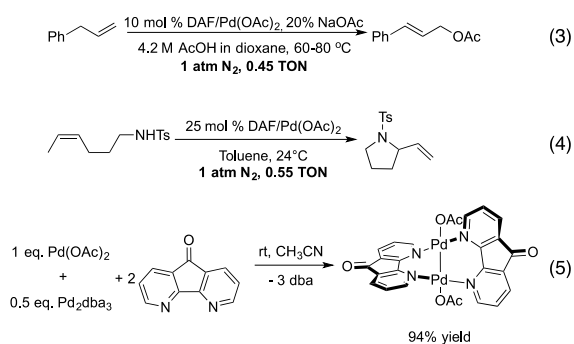
Additional control experiments demonstrate that the Pd^I dimer is a kinetically competent precatalyst for the the acetoxylation reaction. No kinetic burst is observed, and the reaction time course matches the steady-state profile of the reaction initiated with DAF/Pd(OAc)$_2$ as the pre-catalyst (see Figure C 13 in Appendix C). Furthermore, the Pd^I dimer reacts with O$_2$ in AcOH/dioxane to afford a product mixture that is spectroscopically indistinguishable from a 1:1 solution of DAF and Pd(OAc)$_2$ (see [Eq. (6)] and Figure C 14 in the Appendix C). The insolubility of the Pd^I dimer in toluene precluded kinetic competency tests for the aza-Wacker reaction.
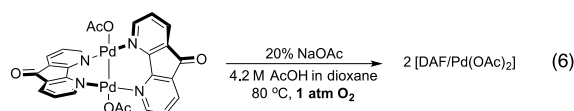
The collective observations above provide clear evidence for a palladium(I) intermediate in these Pd-catalyzed aerobic oxidation reactions, and they show that the Pd^I species arises from comproportionation of Pd^0 and Pd^{II} (left equilibrium, Scheme 5.2) These results may be compared to the involvement of Pd^I species in carbonylation[18] and cross-coupling reactions.[19,20] For example, dimeric Pd^I complexes have been used as pre-catalysts or observed as intermediates in diverse cross-coupling reactions.[19,21] We speculate that O_2 reacts with the reversibly generated Pd^0 species; however, direct reaction of O_2 with the Pd^I dimer cannot be excluded and will be the focus of future studies.[22]
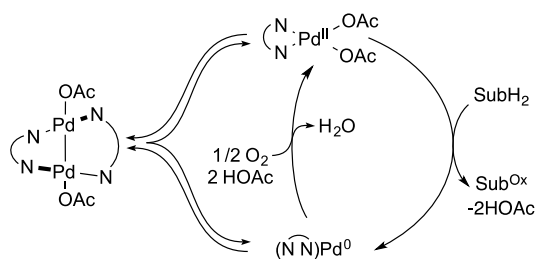
Scheme 5.2: Pd^0 Pathways in DAF-Promoted Reactions

These results have several implications for catalysis. On one hand, the Pd^I dimer appears to be an off-cycle species that slows catalytic turnover. This behavior is evident in the aza-Wacker reaction. The Pd^I dimer is not only off-cycle in this reaction, but it precipitates from the reaction mixture, thereby removing some of the Pd catalyst from solution. At sufficiently low catalyst concentration, oxidation of Pd^0 by O_2 can outcompete the bimolecular Pd^I dimer formation and accounts for the observed steady-state turnover (cf. Figure 5.3). In the allylic acetoxylation reaction, involvement of the Pd^I dimer is somewhat different. The Pd^I dimer is soluble under these reaction conditions, and it is a kinetically competent source of the active catalyst. The kinetic burst in this reaction (cf. Figure 5.1) indicates that the DAF/Pd(OAc)$_2$ pre-catalyst is more active than the Pd^I dimer; however, we speculated that formation of Pd^I has a net beneficial effect that partly accounts for the unique effectiveness of DAF as a ligand that promotes aerobic allylic acetoxylation. Specifically, the ability of DAF to promote comproportionation of Pd^0 and Pd^{II} into Pd^I by serving as a stabilizing bridging ligand could help to prevent aggregation of Pd^0 into inactive metallic Pd.[23]

5.3   Experimental Details.

Acetoxylation time course data was acquired using 0.27 M allylbenzene, 54 mM NaOAc, 13.5 mM DAF/Pd(OAc)$_2$ in 3:1 Dioxane/AcOH with 1 atm O$_2$ and 80 °C in a 48-well custom built orbital mixer at 50 rpm. Yields were assayed by sampling the reaction mixture via syringe, quenching with 0.1 M pyridine in EtOAc and analyzed using gas chromatography. Initial NMR acetoxylation speciation experiments were performed by using 67 mM allylbenzene (5 eq. relative to Pd) in a solvent mixture of 3:1 AcOD- d_4 / 1,4-dioxane-d_8 with 3.2 atm O$_2$ at 40 °C. O$_2$ was condensed into an J-Young as previously described.[24] Amidation time course data was acquired with 0.1 M (Z)-4-hexenyltosylamide, 5 mM DAF/Pd(OAc)$_2$ in toluene with 1 atm O$_2$ and at 24 °C. 1,3,5-Trimethoxybenzene was used as an internal standard. Reactions were processed by filtering the mixture through silica, washing with EtOAc and removing the solvent by vacuum centrifugation. The resulting concentrate was dissolved in CDCl$_3$ and analyzed by ^{1}H NMR spectroscopy. Gas uptake kinetics were performed in the same manner as previously reported.[25] [(Z)-4-hexenyltosylamide] = 0.1 M, [DAF/Pd(OAc)$_2$] varied accordingly, 3 mL toluene, p(O$_2$) = 730 Torr. UV-visible experiments were performed in a 1 mm cuvette using a Cary 60 spectrometer. DAF/Pd(OAc)$_2$ concentrations were kept the same for a direct comparison. The acetoxylation reaction mixture from the UV-visible experiment was subjected to vapour diffusion with pentane at 4 °C for two days to obtain red crystals suitable for XRD analysis. For the DFT studies, geometries were optimized via unrestricted DFT using the CAM-B3LYP functional, LANL2TZ(f) basis set and effective core potential for palladium and 6-31g(d) basis set for all other atoms using Gaussian09. TD-DFT calculations were performed using the CAM-B3LYP functional at the optimized geometries, employing the same basis set for palladium and the 6-311G(2df,p) basis set for other atoms. The SMD continuum solvation model was used to model the effects of dioxane. The computed extinction coefficient for the Pd^I dimer was estimated by viewing the predicted UV-visible spectrum in Gaussview using a 1 cm^{-1} gaussian fit.

5.4 Acknowledgements.

1. (a) P. M. Henry, *Palladium Catalyzed Oxidation of Hydrocarbons*, Springer, Boston, **1980**. (b) E.-i. Negishi, *Handbook of Organopalladium Chemistry for Organic Synthesis*; Wiley, New York, **2002**. (c) S. S. Stahl, *Angew. Chem. Int. Ed.* **2004**, *43*, 3400-3420. (d) X. Chen, K. M. Engle, D.-H. Wang, J.-Q. Yu, *Angew. Chem.* **2009**, *121*, 5196-5217; *Angew. Chem. Int. Ed.* **2009**, *48*, 5094–5115. (e) K. M. Gligorich, M. S. Sigman, *Chem. Commun.* **2009**, 3854-3867. (f) T. W. Lyons, M. S. Sanford, *Chem. Rev.* **2010**, *110*, 1147-1169.

2. S. S. Stahl, *Science* **2005**, *309*, 1824-1826.

3. M. Eckert, G. Fleischmann, R. Jira, H. M. Bolt, K. Golka, Acetaldehyde. *Ullmann's Encyclopedia of Industrial Chemistry* **2006**, p. 191-207.

4. For leading references, see: (a) K. P. Peterson, R. C. Larock, *J. Org. Chem.* **1998**, *63*, 3185-3189. (b) T. Nishimura, T. Onoue, K. Ohe, S. Uemura, *Tetrahedron Lett.* **1998**, *39*, 6011-6014. (c) T. Nishimura, T. Onoue, S. Uemura, *J. Org. Chem.* **1999**, *64*, 6750-6755. (d) G.-J. ten Brink, I. W. C. E. Arends, G. Pagadogianakis, R. A. Sheldon, *Science* **2000**, *287*, 1636-1639. (e) E. M. Ferreira, B. M. Stoltz, *J. Am. Chem. Soc.* **2001**, *123*, 7725-7726. (f) M. J. Schultz, C. C. Park, M. S. Sigman, *Chem. Commun.* **2002**, 3034-3035. (g) K. Chung, S. M, Banik, A. G. De Crisci, D. M. Pearson, T. R. Blake, J. V. Olsson, A. J. Ingram, R. N. Zare, R. M. Waymouth, *J. Am. Chem. Soc.* **2013**, *135*, 7593-7602.

5. For leading references, see: (a) T. Hosokawa, S. Yamashita, S.-I. Murahashi, A. Sonoda, *Bull. Chem. Soc. Jpn.* **1976**, *49*, 3662-3665. (b) L. A. Hasvold, K. P. Peterson, *J. Org. Chem.* **1996**, *61*, 3584-3585.

(c) S. R. Fix, J. L. Brice, S. S. Stahl, *Angew. Chem.,* **2002**, *114*, 172-174; *Angew. Chem. Int. Ed.* **2002**, *41*, 164-166. (d) R. M. Trend, Y. K. Ramtohul, E. M. Ferreira, B. M. Stoltz, *Angew. Chem. Int. Ed.* **2003**, *42*, 2892-2895. (e) R. I. McDonald, G. Liu, S. S. Stahl, *Chem. Rev.* **2011**, *111*, 2981-3019.

6. For leading references, see: (a) Y. Fujiwara, I. Moritani, S. Danno, R. Asano, S. Teranishi, *J. Am. Chem Soc.* **1969**, *91*, 7166-7169. (b) M. M. S. Andappan, P. Nilsson, M. Larhed, *Chem. Commu.* **2004**, 218-219. (c) M. Dams, D. E. De Vos, S. Celen, P. A. Jacobs, *Angew. Chem. Int. Ed.* **2003**, *42*, 3515-3515. (d) D.-H. Wang, K. M. Engle, B.-F. Shi, J.-Q. Yu, *Science* **2010,** *327*, 315-319. (e) K. M. Engle, D.-H. Wang, J.-Q. Yu, *J. Am. Chem. Soc.* **2010**, *132*, 14137-14151. (f) Le Bras, J.; Muzart, J. *Chem. Rev.* **2011**, *111*, 1170–1214. (g) C. Zheng, S. S. Stahl, *J. Am. Chem. Soc.* **2012**, *134*, 16496−16499. (h) A. Vasseur, C. Laugel, D. Harakat, J. Muzart, J. Le Bras, *Eur. J. Org. Chem.* **2015**, *2015*, 944-948.

7. (a) S. S. Stahl, J. L. Thorman, R. C. Nelson, M. A. Kozee, *J. Am. Chem. Soc.* **2001**, *123*, 7188-7189. (b) J. Muzart, *Chem. Asian J.* **2006**, *1*, 508-515. (c) A. N. Campbell, S. S. Stahl, *Acc. Chem. Res.* **2012**, *45*, 851-863. (d) A. J. Ingram, D. Solis-Ibarra, R. N. Zare, R. M. Waymouth, *Angew. Chem. Int. Ed.* **2014**, *53*, 5648-5652. (e) M. L. Scheuermann, K. I. Goldberg, *Chem. Eur. J.* **2014**, *20*, 14556-14568.

8. For reviews, see ref. 5e (Wacker-type cyclizations) and the following (allylic C–H oxidation): F. Liron, J. Oble, Mélanie M. Lorion, G. Poli, *Eur. J. Org. Chem.* **2014**, 5863-5883.

9. Campbell, A. N.; White, P. B.; Guzei, I. A.; Stahl, S. S. *J. Am. Chem. Soc.* **2010**, *132*, 15116-15119.

10. P. B. White, J. N. Jaworski, G. H. Zhu, S. S. Stahl, *ACS Catal.* **2016**, *6*, 3340-3348.

11. P. B. White, J. N. Jaworski, C. G. Fry, B. S. Dolinar, I. A. Guzei, S. S. Stahl, *J. Am. Chem. Soc.* **2016**, *138*, 4869-4880.

12. For articles describing the coordination of DAF to various transition metals, see: (a) R. A. Klein, P. Witte, R. van Belzen, J. Fraanje, K. Goubitz, M. Numan, H. Schenk, J. M. Ernsting, C. J. Elsevier, *Eur. J. Inorg. Chem.* **1998**, 319-330. (b) V. T. Annibale, D. Song, *Dalton Trans.* **2016**, *45*, 32-49.

13. The catalytic reaction is typically performed in toluene, but $CDCl_3$ was used for NMR studies to enable sufficient DAF/Pd concentrations to enable the reactions to be monitored.

14. Previously reported mechanistic studies of this reaction (see ref. [10]) were conducted in a well-behaved kinetic regime where mass-transfer effects and catalyst precipitation were not observed.

15. (a) E. Liu, S. T. Liddle, *Molecular Metal-Metal Bonds,* **2015***,* pp. 347-370, Wiley-VCH, Weinheim.

16. (a) T. A. Stromnova; I. I. Moiseev, *Russ. Chem. Rev.* **1998**, *67*, 485–514. (b) T. Murahashi, H. Kurosawa, *Coord. Chem. Rev.* **2002**, *231,* 207-228 (c) N. Hazari, D. P. Hruszkewycz, *Chem. Soc. Rev.* **2016**, *45*, 2871-2899.

17. For other related dimeric Pd[I] complexes, see: (a) R. K. Das, B. Saha, S. M. W. Rahaman, J. K. Bera, *Chem. Eur. J.* **2010**, *16*, 14459–14468. (b) S. Deeken, G. Motz, V. Bezugly, H. Borrmann, F. R. Wagner, R. Kempe, *Inorg. Chem.* **2006**, *45*, 9160−9162. (c) A. Bonet, H. Gulyás, I. O. Koshevoy, F. Estevan, M. Sanaú, M. A. Ubeda, E. Fernández, *Chem. Eur. J.* **2010**, *16*, 6382 – 6390. (d) A. Dervisi, P. G. Edwards, P. D. Newman, R. P. Tooze, S. J. Coles, M. B. Hursthouse, *J. Chem. Soc., Dalton Trans.* **1998**, 3771-3776.

18. (a) L. C. Bruk, I. V. Oshanina, A. P. Kozlova, E. V. Vorontsov, O. N. Temkin, *J. Mol. Cat. A.* **1995**, *104*, 9-16 (b) L. G. Bruk, A. P. Kozlova, O. V. Marshakha, I. V. Oshanina, O. N. Temkin, O. L. Kaliya, *Russ. Chem. Bull.* **1999**, *48*, 1875-1881. (c) Xu, Q.; Souma, Y.; Umezawa, J.; Tanaka, M.; Nakatani, H., *J. Org. Chem.* **1999,** *64*, 6306-6311 (d) O. N. Temkin, L. G. Bruk, *Kinet. Catal.* **2003**, *44*, 661-677 (e) T. A. Stromnova, *Platinum Metals Rev.* **2003**, *47*, 20-27. F. Ragaini, H. Larici, M. Rimoldi, A. Caselli, F. Ferretti, P. Maachi, N. Casati, *Organometallics* **2011**, *30,* 2385-2393.

19. For reviews, see ref. 16c and the following: (a) T. J. Colacot, *Platinum Metals Rev.* **2009**, *53*, 183-188. (b) K. J. Bonney, F. Schoenebeck, *Chem. Soc. Rev.* **2014**, *43*, 6609-6638.

20. For observation of Pd[I] in Pd-catalyzed oxidation with NBS, see: R. B. Bedford, M. F. Haddow, C. J. Mitchell, R. L. Webster, *Angew. Chem. Int. Ed.* **2011**, *50*, 5524-5527.

21. For leading primary references, see: (a) J. P. Stambuli, R. Kuwano, J. F. Hartwig, *Angew. Chem.* **2002**, *114*, 4940-4942; *Angew. Chem. Int. Ed.* **2002**, *41*, 4746-4748 (b) S. E. Denmark, J. D. Baird, *Org. Lett.* **2006**, *8*, 793-795. (c) X. Han, Z. Weng, T. S. A. Hor, *J. Organomet. Chem.* **2007***, 692*, 5690-5696. (d) L. L. Hill, J. L. Crowell, S. L. Tutwiler, N. L. Massie, C. C. Hines, S. T. Griffin, R. D. Rogers, K. H.

Shaughnessy, G. A. Grasa, C. C. C. Johansson Seechurn, H. Li, T. J. Colacot, J. Chou, C. J. Woltermann, *J. Org. Chem.* **2010**, *75*, 6477-6488. (e) D. P. Hruszkewycz, J. Wu, N. Hazari, C. D. Incarvito, *J. Am. Chem. Soc.* **2011**, *133*, 3280-3283. (f) K. J. Bonney, F. Proutiere, F. Schoenebeck, *Chem. Sci.* **2013**, *4*, 4434-4439. (g) D. P. Hruszkewycz, D. Balcells, L. M. Guard, N. Hazari, M. Tilset, *J. Am. Chem. Soc.* **2014**, *136*, 7300-7316. (h) F. Proutiere, E. Lyngvi, M. Aufiero, I. T. Sanhueza, F. Schoenebeck, *Organometallics* **2014**, *33*, 6879-6884. (i) S. Oldenhof, M. Lutz, B. de Bruin, J. I. van der Vlugt, J. N. H. Reek, *Organometalllics* **2014**, *33*, 7293-7298. (j) M. Aufiero, T. Sperger, A. S.-K. Tsang, F. Schoenebeck, *Angew. Chem. Int. Ed.* **2015**, *54*, 10322-10326. (k) M. Aufiero, T. Scattolin, F. Proutiere, F. Schoenebeck, *Organometallics* **2015**, *34,* 5191-5195. (l) D. P. Hruszkewycz, L. M. Guard, D. Balcells, N. Feldman, N. Hazari, M. Tilset, *Organometallics*, **2015**, *34*, 381-394. (m) P. R. Melvin, A. Nova, D. Balcells, W. D. N. Hazari, D. P. Hruszkewycz, H. P. Shah, M. T. Tudge, *ACS Catal.* **2015**, *5*, 3680-3688. (n) I. Kalvet, G. Magnin, F. Schoenebeck, *Angew. Chem. Int. Ed.* **2017**, *56*, Early View, DOI: 10.1002/anie.201609635.

22. For examples of stoichometric reactions of O_2 with Pd^I species, albeit not directly related to the present study, see: (a) V. Durà-Vilà, D. M. P. Mingos, R. Vilar, A. J. P. White, D. J. Williams, *Chem. Commun.* **2000**, 1525-1526. (b) R. Huacuja, D. J. Graham, C. M. Fafard, C.-H. Chen, B. M. Foxman, D. E. Herbert, G. Alliger, C. M. Thomas, O. V. Ozerov, *J. Am. Chem. Soc.* **2011**, *133*, 3820-3823.

23. For studies of Pd aggregation in (non-oxidative) allylic substitution reactions, see: (a) M. Tromp, J. R. A. Sietsma, J. A. van Bokhoven, G. P. F. van Strijdonck, R. J. van Haaren, A. M. J. van der Eerden, P. W. N. M. van Leeuwen, D. C. Koningsberger, *Chem. Commun.* **2003**, 128-129. (b) Markert, C.; Neuburger, M.; Kulicke, K.; Meuwly, M.; Pfaltz, A., *Angew. Chem. Int. Ed.* **2007**, *46*, 5892-5895.

24. B. A. Steinhoff, I. A. Guzei, S. S. Stahl, *J. Am. Chem. Soc.* **2004**, *126*, 11268–11278.

25. X. Ye, G. Liu, B. V. Popp, S. S. Stahl, *J. Org. Chem.* **2011**, *76*, 1031-1044.

Chapter 6: Mechanistic Characterization of Allylic C-H Acetoxylation with 4,5-Diazafluorenone Palladium Catalyst - Implications of Pd(I) In Catalysis and Identification of Catalyst Resting State

This work was done in collaboration with Stephen J. Tereniak, Caitlin Kozack, Spring Melody M. Knapp, Jeffrey T. Miller, Clark R. Landis, Shannon S. Stahl*

6.1   Introduction.

Methods for selective and mild oxidations are an important field of growing research in organic chemistry.[1] Since the discovery of the Wacker process for the oxidation of ethylene to acetaldehyde, aerobic Pd-catalyzed oxidations have been extensively investigated.[2] Utilization of O_2 as the terminal oxidant in Pd-catalyzed oxidations is ideal as it is an abundant and cheap oxidant and produces only water as the stoichiometric byproduct. Other chemical oxidants are often easier to handle however they generate stoichiometric waste, not readily available nor are they as inexpensive. Classic Wacker oxidation conditions typically employ $PdCl_2$ with cocatalytic $CuCl_2$ to reoxidize Pd^0 to Pd^{II} during catalysis and the reduced Cu^I is subsequently reoxidized by O_2. Significant effort has since been directed towards the discovery of simplified catalyst systems that allow Pd^0 to be reoxidized directly by O_2.[3,4] Simplified reaction conditions present a more economical system but also alleviate complexity involved in having multiple metals present in the same reaction. Ligands are often employed in catalysis to control substrate oxidation and the having multiple metals present in the same reaction mixture complicates ligand speciation. Simplified aerobic conditions are often paired best with reactions that proceed through β-hydride elimination mechanism. Examples of successful ligand modulated catalysis include applied in aerobic Pd-catalysis include Wacker oxidations with various nucleophiles,[5,6] dehydrogenative Heck reactions[7] and alcohol oxidations.[8,9] Despite these successes, utilizing O_2 for catalyst reoxidation is still challenging with Pd-catalyzed oxidation reactions that involve a reductive elimination step.[10]

Our group has a long-standing interest in developing synthetic methodologies that utilize O_2 as the terminal oxidant in Pd-catalyzed oxidation catalysis. Previously, we disclosed the use of the ligand 4,5-diazafluoren-9-one (DAF) with $Pd(OAc)_2$ in the aerobic Pd-catalyzed allylic C-H acetoxylation of linear terminal alkenes.[11] DAF was unique in that it enabled the reaction to proceed in high yield without the addition of co-catalysts or stoichiometric BQ which have been historically required for allylic C-H acetoxylation. Other pyridyl-based ligands that were screened such as canonical (bi)pyridyl ligands prevented catalyst turnover (Scheme 6.1). Historically, oxidants such as hypervalent iodine,[12] peroxides,[13]

benzoquinone[14] or any combination thereof were required to induce reductive elimination from an organometallic Pd[II] intermediate.[15] In some select cases, aerobic conditions can be utilized with the assistance of electron-transfer mediators (ETMs).[16] This system is superior in that it only requires O_2, DAF and Pd(OAc)$_2$ to perform efficient catalysis. Preliminary mechanistic investigations showed that DAF promoted reductive elimination of from π-allyls in the reaction solvent and O_2 could accelerate the rate of product formation.[11] Reductive elimination in catalysis was shown to be reversible and that the extent of reversible reductive elimination in catalysis was modulated by O_2 pressure. The proposed mechanism for the DAF-promoted Pd-catalyzed allylic C-H acetoxylation reaction proceeds via C-H activation and reductive elimination. Pd[0] then reacts directly with O_2 to form a Pd-peroxo and acetic acid protonolyzes the peroxo and to regenerate the DAF/Pd(OAc)$_2$ catalyst (Scheme 6.1).
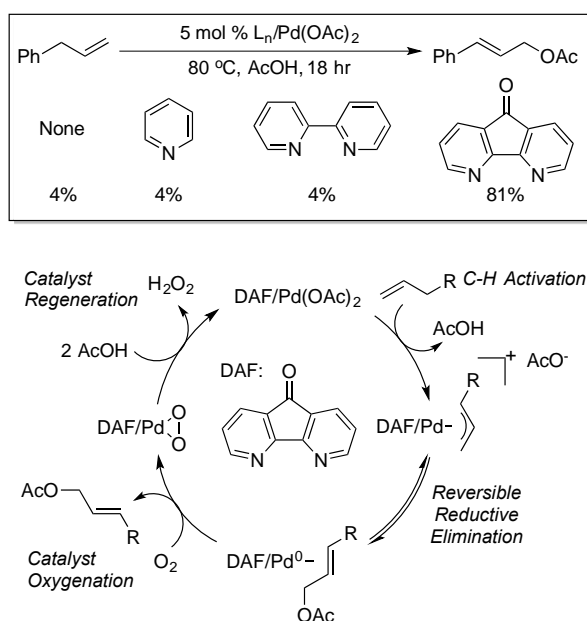
Scheme 6.1: Proposed Mechanism for DAF Promoted Pd-Catalyzed Aerobic Acetoxylation

We have since disclosed the elaborate coordination chemistry DAF/Pd(OAc)$_2$ and derivatives thereof.[17] It was subsequently discovered that the hemilability of DAF with Pd(OAc)$_2$ enables very mild catalysis for the aerobic intramolecular aza-Wacker reaction.[18] This was rationalized with two mechanistic proposals. First, the DAF/Pd(OAc)$_2$ ground state was destablized compared to 6,6'-MeBpy/Pd(OAc)$_2$ or neocuproine/Pd(OAc)$_2$, and second, DAF can easily adopt κ^1 coordination modes with Pd(OAc)$_2$ which allows substrate to easily bind. Both of these phenomena facilitate very efficient substrate oxidation. The catalysis was accelerated to such an extent that substantial Pd^I species form during catalysis when under high catalyst loading.[20] In this study we disclose a systematic mechanistic investigation of the DAF/Pd(OAc)$_2$ system for allylic C-H acetoxylation. Kinetic investigations reveal a two phase-reaction reaction paradigm due to the change of the catalyst resting state and rate-determining step. The evolution of the Pd-catalyst was characterized with X-ray absorption spectroscopy (XAS) as it evolves from a DAF/Pd(OAc)$_2$ species to two distinct π-allyl species with formation of a transient Pd^I species. These results provide new insights into the role of DAF in Pd catalysis as well as how to design more effective catalyst systems that can utilize O$_2$ as a terminal oxidant.

6.2 Results.

6.2.1 Initial Mechanistic Observations.

Initial mechanistic investigations of the DAF-promoted Pd-catalyzed aerobic acetoxylation reaction revealed a two-phase kinetic behavior. The beginning of the reaction is characterized by a burst in product formation followed by a slower rate of product formation (Figure 6.1A). The burst lasted for approximately 15 minutes and was accompanied by a rapid color change from yellow to red upon injection of allylbenzene. As the reaction progressed past the end of the burst, the coloration of the reaction changed to yellow which persisted for the duration of the reaction time course.[19] Subsequently, a red Pd^I species was able to be characterized by XRD crystallography and has a characteristic absorption at 475 nm in the UV-Vis spectrum (Figure 6.1B, C).[20]
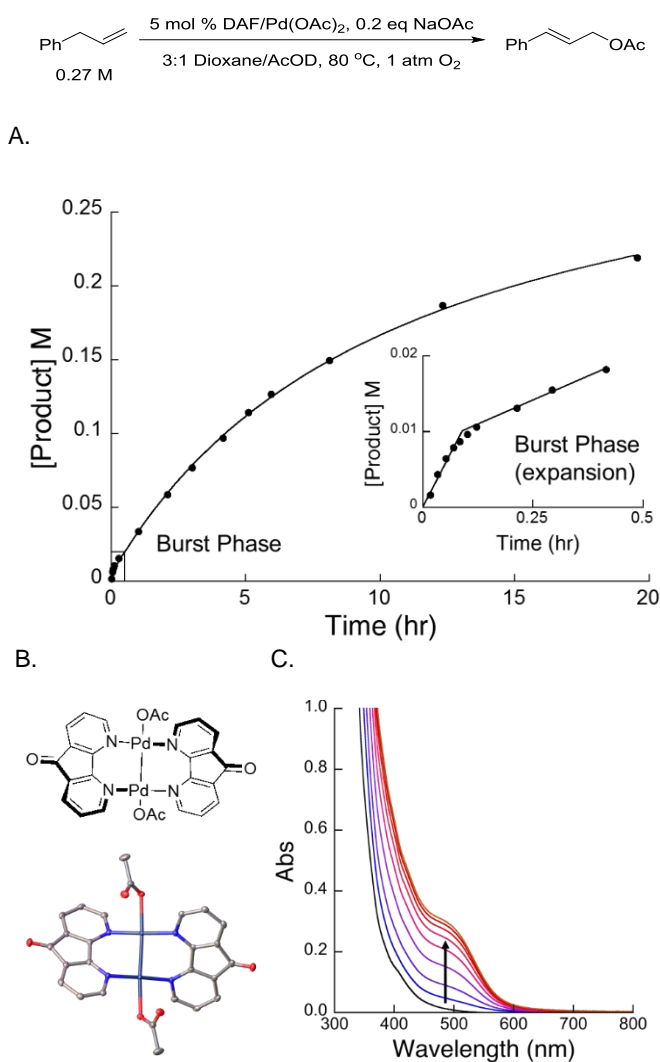
Figure 6.1: Initial Mechanistic Characterization A. Time course of the acetoxylation reaction at 80 °C. B. A Pd[I] intermediate [Pd[I](DAF)(OAc)]₂ C. Characteristic UV-Vis absorption of the [Pd[I](DAF)(OAc)]₂.

The DAF speciation during the reaction time course was interrogated by NMR spectroscopy. Without substrate, the predominant DAF-ligated palladium species is an "ate" complex, $Na[(\kappa^1\text{-}DAF)Pd(OAc)_3]$, arising from coordination of 3 equiv of acetate to the Pd[II] center (see appendix D for details, Figure D 1 - D 5). An NMR time course with 3.2 atm of O_2 shows rapid product formation concurrent with the consumption of $Na[(\kappa^1\text{-}DAF)Pd(OAc)_3]$ to form a DAF ligated Pd[I] dimer (Figure 6.2). The concentration of Pd[I] maximizes at the end of the burst phase and the rate of product formation then decreases. The amount

of unligated DAF starts to increase in concentration in the post-burst regime (Figure 6.2 – expansion). Titrations of DAF with [Pd^{II}(cinnamyl)(OAc)]$_2$ reveal a low binding affinity to the π-allyl dimer (Figure D 6) and attribute the formation of unligated DAF to the formation of π-allyl dimer.
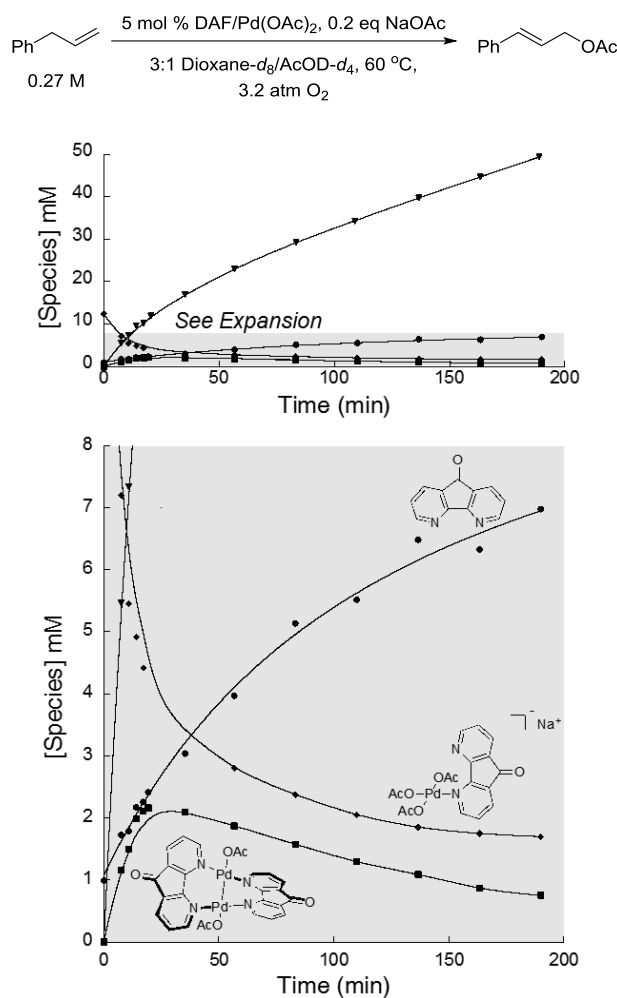

Figure 6.2: Initial investigations into the resting state of the catalyst as followed by NMR. A. Time course of product formation and DAF speciation with 3.2 atm O$_2$ at 60 °C. B. Expansion of DAF speciation in the NMR time course.

6.2.2   Kinetic Dependencies: DAF/Pd(OAc)$_2$, DAF, Substrate, O$_2$

The kinetic dependencies of the reaction components was determined with 1 atm O$_2$ for both the burst and post-burst regimes at 80 °C. (Figure 6.3, Figure 6.4). Both the burst and post-burst reaction component dependencies are similar qualitatively however the rates are significantly different with the burst being 3-4 times faster than the post-burst. The catalyst (1:1 DAF/Pd(OAc)$_2$) exhibits a saturation dependence in both

burst and post-burst. In both the burst and post-burst, the [DAF] dependence shows a near linear increase in the rate with increasing [DAF] up to 1:1 DAF/Pd(OAc)$_2$. Further increase in [DAF] beyond this 1:1 ratio resulted no rate change. A saturation dependence on [allylbenzene] is observed in the burst and a near linear dependence on [allylbenzene] was observed in the post-burst however there is a substantial non-zero intercept present.

A.   B.   C.
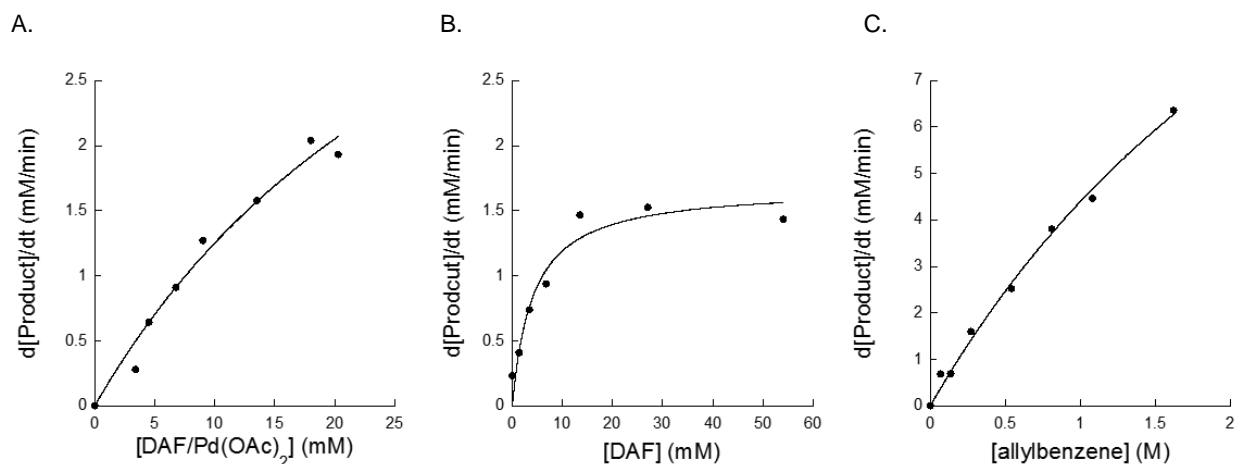
Figure 6.3: Kinetic Dependencies of Reaction Components for Burst Phase. All experiments were performed at 80 °C in an orbital mixer with 1 atm of O$_2$ and 54 mM NaOAc. A. [DAF/Pd(OAc)$_2$] = 0-18 mM, [allylbenzene] = 0.27 M. B. [DAF] = 0-54 mM, [Pd(OAc)2] = 13.5 mM, [allylbenzene] = 0.27 M. C. [DAF/Pd(OAc)$_2$] = 13.5 mM, [allylbenzene] = 0.14-1.8 M.

A.   B.   C.
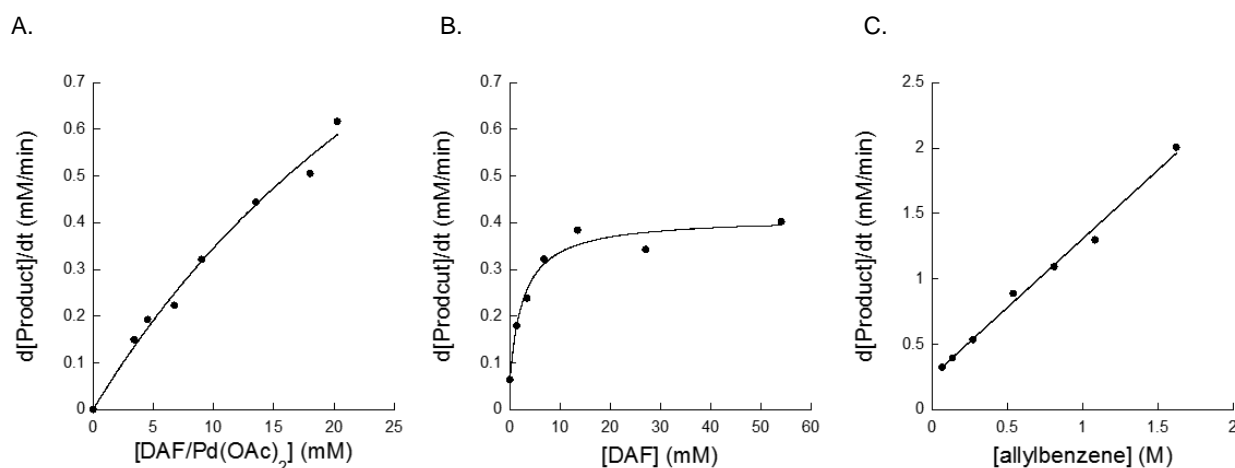
Figure 6.4: Kinetic Dependencies of Reaction Components in Post-Burst. All experiments were performed at 80 °C in an orbital mixer with 1 atm of O$_2$ and 54 mM NaOAc. A. [DAF/Pd(OAc)$_2$] = 0-27 mM, [allylbenzene] = 0.27 M. B. [DAF] = 0-54 mM, [Pd(OAc)2] = 13.5 mM, [allylbenzene] = 0.27 M. C. [DAF/Pd(OAc)$_2$] = 13.5 mM, [allylbenzene] = 0.14-1.8 M.

The O_2 dependencies were obtained using the Wisconsin High Pressure NMR Spectrometer apparatus (WiHP-NMRR).[21] The apparatus allows for constant gas circulation to replenish depleted O_2 in the solvent and rigorously probe longer reaction times than a static NMR tube. A gas mixture of 9% O_2 in N_2 was used in order to mitigate flammability concerns.[22] Analysis of the O_2 dependence on the burst reveals a zero-order dependence and a saturation dependence on the post-burst phase of the reaction.
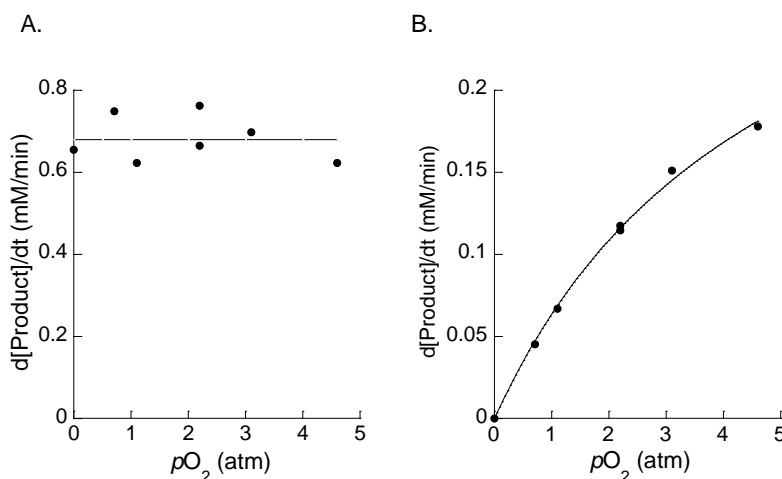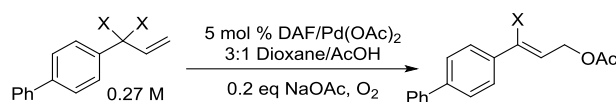

Figure 6.5: Kinetic Dependence of O_2 for Burst and Steady State Phase of Reaction. (A) Burst phase and (B). Experiments were performed at 60°C at 0-4.6 atm O_2 using 9% O_2 in N_2. NaOAc removed from reaction to prevent clogging. [DAF/Pd(OAc)$_2$] = 13.5 mM, [allylbenzene] = 0.27 M. ds = 0, ns = 2, d1 = 4s, circulation delay between scans = 0.5 s, aq = 0.3s, 30 mL/min

6.2.3   Interrogation of C-H activation.

Two isotopically labeled probes for the both intramolecular and intermolecular kinetic isotope studies were synthesized. A *p*-phenyl allylbenzene derivative was chosen as the probe because it is not volatile and easy to purify compared to the parent allylbenzene.[23] A decreased reaction temperature of 40 °C was used to probe the burst phase as the lower temperature resulted in an exaggerated distinction between the burst and post-burst phases; however high catalytic yields are not possible at 40 °C. Intermolecular KIEs were determined measuring the rate of product formation independently for both the h_2 and d_2 probes. Intramolecular KIEs were determined by the product formation derived from C-H or C-D activation. Kinetic isotope effects were observed at 40 °C for both intramolecular and intermolecular experiments.

Only an intramolecular KIE was observed at 80 °C and no intermolecular KIE were observed in the post-burst phase.

Table 6.1: Kinetic Isotope Effects in the Acetoxylation Reaction. Obtained via Independent Rate Measurement with h_2/d_2-Labeled Substrate and via Intramolecular Competition between the h_1d_1-Labeled Substrate.


Temp	Phase	Experiment	KIE
40 °C	Burst	Intermolecular h_2 vs d_2	1.6
		Intramolecular h_1d_1	2.0
80 °C	Post-Burst	Intermolecular h_2 vs d_2	1.1
		Intramolecular h_1d_1	1.7

6.2.4 Interrogation of the Catalyst Resting State– X-Ray Absorption Spectroscopy.

Our initial attempts to characterize the ligand speciation with NMR proved to be challenging. Unligated DAF appeared to be a prominent ligand species during the steady state portion of the reaction with the balance of the ligand not observed (see Initial Mechanistic Observations). We attribute the challenges observing catalyst speciation by NMR to π-allyl fluxionality under the reaction conditions. In order to gain additional information regarding the Pd-catalyst, we initiated a study using X-ray absorption spectroscopy (XAS) to complement the NMR observations. XAS is a technique that is sensitive to the average bulk oxidation state, symmetry and ligand environment of the Pd catalyst.[24,25] A reactor was constructed suitable for operando reaction analysis on the high photon-flux beamline at Argonne National Laboratories (See Figure D 14) with simultaneous UV-visible monitoring capabilities.[26]

Investigations into the resting state mainly focused on the x-ray absorption near edge spectrum (XANES) timecourse. Lower edge positions (edge shift left) correspond to lower oxidation states and higher edge positions (edge shift right) correspond to more oxidized Pd. Upon initiation of the reaction with an injection of allylbenzene, the edge shifted rapidly from its initial starting position (**1**) and a lower position, consistent with reduction of the catalyst. The new position almost overlaps [Pd^I(DAF)(OAc)]$_2$ (**2**) reference (Figure 6.6A). Three scatterings were observed during the initial phase of the reaction in the EXAFS

consistent the Pd^I reference (**2**) (See Appendix D, Figure D 13A) suggesting that substantial amounts of (**2**) were formed.[27] As the reaction proceeded, the edge slowly moved to higher energy and settled at an intermediate position between the Pd^I reference (**2**) and the DAF/Pd^{II}(OAc)$_2$ position (**1**). The steady state resembled the two π-allyl references, [Pd^{II}(cinnamyl)(OAc)]$_2$ (**4**) and cationic π-allyl Pd monomer, [Pd^{II}(DAF)(cinnamyl)]BF$_4$ (**5**). The edge was fit with a linear combination of references (**4**) and (**5**) a reasonable fit was provided with 42% [Pd^{II}(cinnamyl)(OAc)]$_2$ (**4**) and 58%, [Pd^{II}(DAF)(cinnamyl)]BF$_4$ (**5**). Significant contribution from (**1**) could be excluded through the absence of a strong feature above the absorption edge in the steady state (see Figure D 11). Analysis of the EXAFS during the steady state portion of the reaction was not informative as there is a lack of scatterings beyond ~1.5 Å (See Figure D 13B).
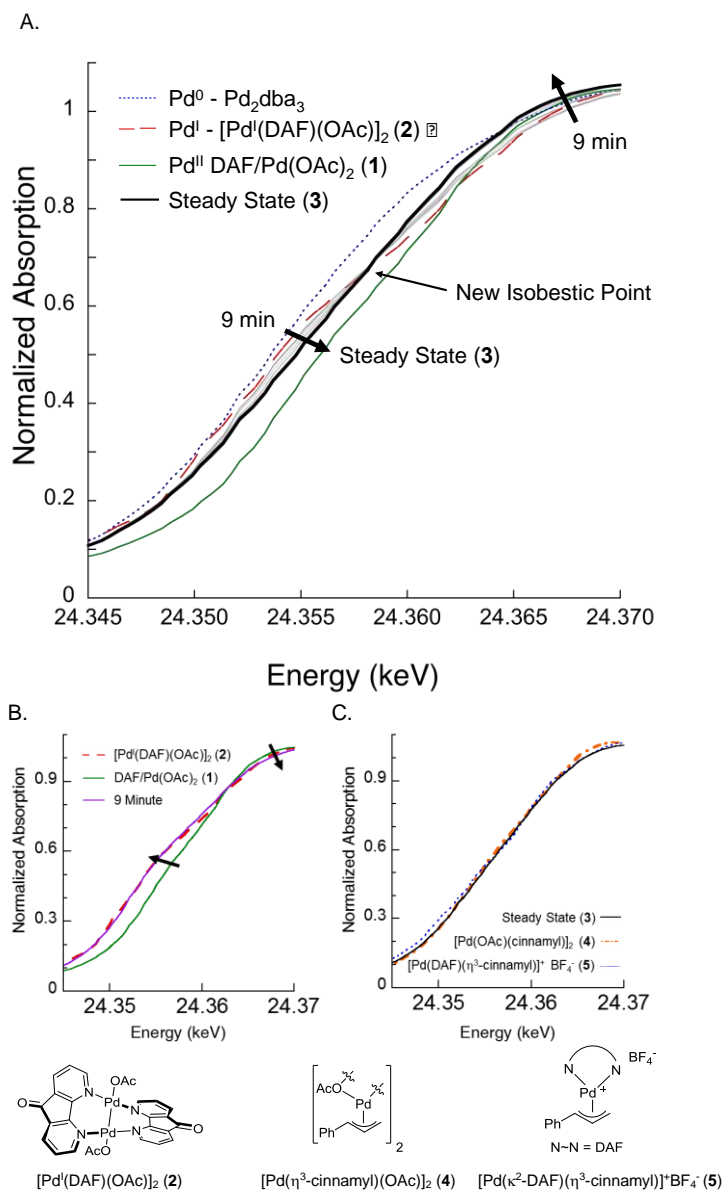
Figure 6.6: XAS Edge Analysis of Bulk Pd Catalyst. A. Pd K-Edge timecourse overlay from 9 minutes to 160 with overlaid references for comparison B. Pd K-Edge timecourse overlay from 0-9 minutes with comparison of [Pd^I(DAF)(OAc)]$_2$ (**2**) reference. C. Comparison of the steady state with neutral π-allyl Pd acetate dimer, [Pd^{II}(cinnamyl)(OAc)]$_2$ (**4**) and cationic π-allyl Pd monomer, [Pd^{II}(DAF)(cinnamyl)]BF$_4$ (**5**).

To quantify the change in oxidation state over the time course, the edge energy value E° was determined for the different time points (Figure 6.7). E° is a descriptor that corresponds to the first inflection point of the edge. The E° time course was consistent with a rapid reduction of the catalyst oxidation state from a starting value of 24.3550 keV for (**1**) to 24.3524 keV in the first 9 minutes. This now reduced E° is similar

to $[Pd^I(DAF)(OAc)]_2$ (**2**) (24.3521 keV). The edge shifted to a higher energy position, corresponding to oxidation of the Pd and plateaued at an E° value of 24.3538 keV which is between the E° of the references $[Pd^{II}(cinnamyl)(OAc)]_2$ (**4**) (24.3533 keV) and $[Pd^{II}(DAF)(cinnamyl)]^+BF_4^-$ (**5**) (24.3541 keV). The steady state oxidation level of the catalyst had become more reduced from where it started prior to the addition of allylbenzene, consistent with the qualitative observations above.
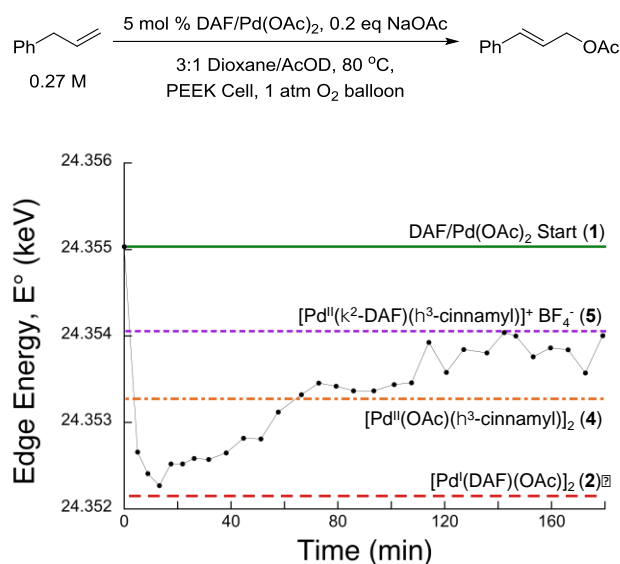
**Figure 6.7:** Edge Energy (E°) as a function of time.

Simultaneously acquired operando UV-visible spectra were acquired through the use of a dip probe. The 475 nm absorbance was previously characterized as being diagnostic for the MLCT of the $[Pd^I(DAF)(OAc)]_2$ (**2**) complex with an extinction coefficient of 1.44 mM^{-1} cm^{-1}.[20] When the reaction was initiated with injection of allylbenzene, the absorbance at 475 nm spiked which was consistent with the rapid formation of Pd^I in the reaction time course (Figure 6.8A). The concentration $[Pd^I(DAF)(OAc)]_2$ (**2**) maximizes to 4.5 mM at 9 minutes. 9 mM Pd is accounted for by UV-visible at 9 minutes with another 4.5 mM of Pd unaccounted as $[Pd]_T$ = 13.5 mM. As the reaction proceeds, the broad feature at 475 nm disappears however a non-zero baseline persists suggesting that a small amount of precipitate has formed in the reaction mixture (Figure 6.8B). The UV-visible data clearly showed the absence of Pd^I in the steady state portion of the reaction consistent with the steady state XAS data (Figure 6.8B).
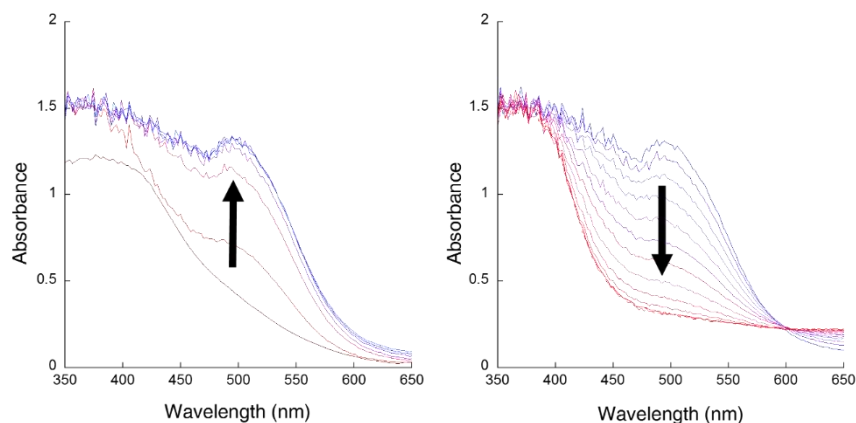
**Figure 6.8:** Operando UV-Visible Spectra of the Reaction Mixtureat A. 0-9 minutes and B. 10-160 minutes

A control reaction where the reaction was initiated from [Pd^{II}(cinnamyl)(OAc)]$_2$ (**4**) was performed. A time course of the reaction when initiated by (**4**) π-allyl provided a time course in which the burst phase of the reaction was absent. Additionally, the initial rate of the reaction when initiated by (**4**) resembled that of the post-burst regime of a reaction initiated with Pd(OAc)$_2$ (Figure 6.9). Initiating the reaction with the cationic π-allyl BF$_4$ complex (**5**) was not possible due to instability and insolubility. Curves in Figure 6.9 are for illustrative purposes only and not rigorous fits.
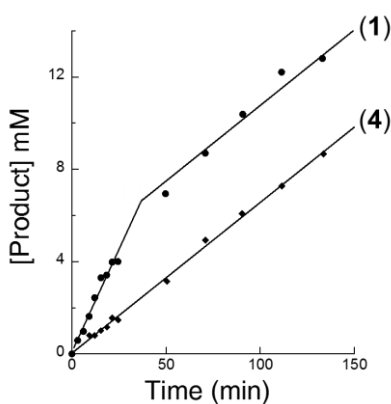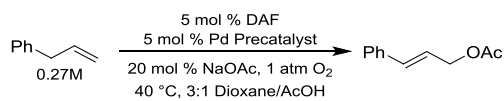
Figure 6.9: Kinetic Interrogation of the Resting State

6.2.5 Stoichiometric Reductive Elimination Reactions from π-allyl Complexes.

The complex [Pd^{II}(cinnamyl)(OAc)]$_2$ (**4**) was subjected to various conditions in order to probe its reactivity (Figure 6.10). Reactions were assembled in the glovebox and performed in toluene-d_8 under N$_2$ at 60 °C and aerobic reactions pressurized with additional O$_2$ using a custom NMR tube pressurization manifold (See Appendix D, Figure D 6).[28] In the absence of DAF, negligible cinnamyl acetate product was detected via thermolysis of the well-defined (**4**). The addition of DAF to (**4**) promoted product formation which was subsequently enhanced with the addition of AcOH and further enhanced with the ternary mixture of DAF, AcOH and allylbenzene. Additional rate enhancement can be seen with O$_2$ but only in the presence of O$_2$. See Appendix D, Figure D 8, Figure D 9 for various control reaction permutations.
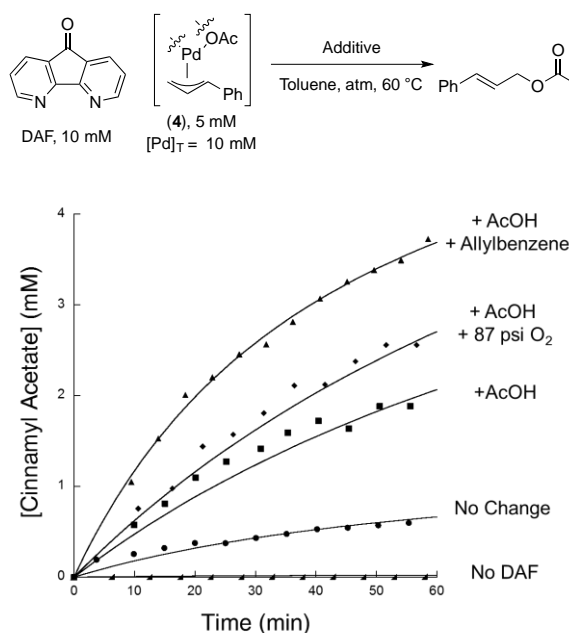
Figure 6.10: Stoichiometric Reductive Elimination Reactions with DAF and [Pd^{II}(cinnamyl)(OAc)]$_2$ (**4**). Time course analysis of the addition of DAF, allylbenzene and AcOH Conditions: [Pd^{II}(cinnamyl)(OAc)]$_2$ = 5 mM, [DAF] = 10 mM, [Allylbenzene] = 0.42 M, [AcOH] = 0.22 M, 60 °C, Toluene, N$_2$.

6.3 Discussion.

6.3.1 Catalytic Mechanism: Overview of Observations.

The data presented above provides key mechanistic insights into the two phase kinetic behavior of DAF/Pd(OAc)$_2$ allylic C-H acetoxylation reaction and characterization of the resting state of the catalyst.

Burst phase:

1. Faster product formation concurrent with growth of Pd^I.

2. Primary allylic C-H kinetic isotope effect.

3. No O$_2$ dependence.
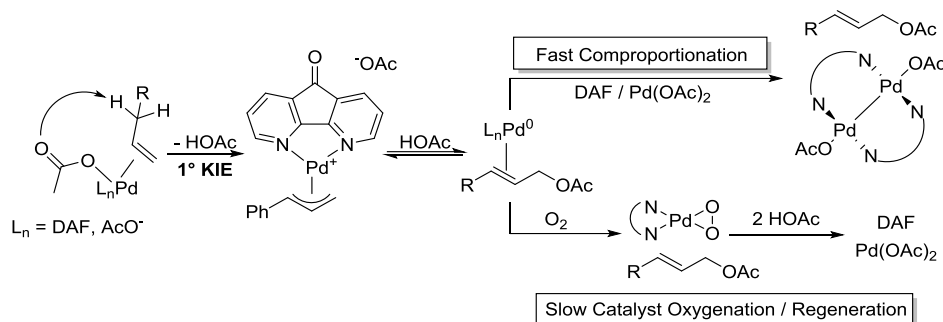
Steady State:

1. Slower rate of product formation.

2. The appearance of free DAF and unligated π-allyl dimer.

3. Resting state of the Pd catalyst to be mixture of cationic DAF ligated π-allyl and neutral dimeric π-allyl species.

4. No allylic C-H kinetic isotope effect detected.

5. O$_2$ dependence detected.

6.3.2 Analysis of the Burst Phase.

The beginning of the reaction was characterized by the rapid formation of Pd^I and fast product formation. The Pd^I concentration maximized at the termination of the burst with ~75% of Pd converting to Pd^I in the beginning of the reaction, as determined by XAS and UV-visible.[29] Similar behavior was observed by NMR at 3.2 atm of O$_2$. The rapid formation of Pd^I and product in the beginning of the reaction suggests a mechanistic correlation between product and Pd^I. Comproportionation of Pd^{II} and Pd^0 is the most commonly invoked method for Pd^I formation.[30] We believe that comproportionation of Pd(OAc)$_2$ kinetically traps the in situ generated Pd^0 from reductive elimination and pulls the reaction forward. This pull-type phenomena has been discussed previously in the context of aerobic acetoxylation where O$_2$ serves to trap out Pd^0 species.[15] In this case, the rapid comproportionation that the catalyst undergoes illustrates

the ability of $Pd(OAc)_2$ is able to act as a "better oxidant" for Pd^0 than O_2. The increased rates of Pd^0 trapping results in an observed intermolecular KIE of 1.6 where C-H activation becomes as dictating the reaction rate in the burst.[31] A summary of the key points are presented in Scheme 6.2 below.

**Scheme 6.2:** Simplified Burst Phase Mechanism

6.3.3 Analysis of the Steady State Phase.

The resting state of the reaction has been determined to be a mixture of Pd π-allyl species through the use of operando XAS and UV-visible techniques (Figure 6.6, Figure 6.7), complemented with NMR observations. This assignment is qualitatively consistent with the kinetic comparison between initiating the reaction with $Pd(OAc)_2$ versus Pd π-allyl (Figure 6.9). Initiating the reaction with a Pd π-allyl resulted in the absence of the burst phase and an approximate rate of product formation consistent with the steady state. The appearance of free DAF by NMR in the post-burst phase is symptomatic of a small equilibrium between (**4**) and DAF (See appendix, Figure D 6). The cationic DAF-bound π-allyl we believe is effectively invisible by NMR due to its highly fluxional nature and accounts for the rest of the mass balance in the NMR time course. Additionally, $[Pd^I(DAF)(OAc)]_2$ is not a persistent species in the steady state of the reaction. We have previously shown that $[Pd^I(DAF)(OAc)]_2$ can slowly become oxidized to $DAF/Pd^{II}(OAc)_2$ with just O_2 and AcOH at 80°C alone.[20] The transient nature of the Pd^I can also be partially attributed to the ability of alkenes to disproportionate the Pd^I dimers and help Pd^0 to become oxidized by O_2.[32] Additionally, sterically bulky allyl ligands such as a cinnamyl help to disfavor Pd^{II}/Pd^0 comproportionation.[33]

The rate of product formation in the steady state is much slower than the burst as illustrated by the reaction time course (Figure 6.2) and burst and post-bust reaction component dependencies (Figure 6.3 -

Figure 6.4). The steady state phase of the reaction did not have an observable KIE but does have an O_2 dependence, opposite that which was observed in the burst phase. This is interesting as most aerobic oxidation reactions that have been mechanistically studied do not have an O_2 dependent term in their rate law with the exception of reactions that exhibit mass transport limitations (i.e. oxygen starved conditions).[34] The observed linear allylbenzene dependence is inconsistent with mass transport limitations as the rate would level out at high allylbenzene concentration with the reaction becoming O_2 starved. Stoichiometric studies with the π-allyl dimer $[Pd^{II}(cinnamyl)(OAc)]_2$ revealed a similar kinetic beneficial effect with the addition of exogenous O_2 and exogenous allylbenzene in the presence of DAF and AcOH. A possible explanation is that alkenes and O_2 are binding to stabilize Pd^0 species generated from reductive elimination with the addition of DAF and AcOH. The rate of product formation can be accelerated by promoting the product displacement by allylbenzene which helps to trap out Pd^0 species that can then react with O_2. The non-zero intercept present in the allylbenzene dependency can be attributed to the fundamental rate of reductive elimination of the cationic DAF π-allyl.

The above discussion emphasizes the importance of alkene ligand exchange in the DAF-promoted allylic C-H acetoxylation reaction. The mechanism for alkene exchange on a DAF/Pd^0 complex has not been investigated however Elsevier and co-workers examined the coordination geometry of diimine Pd^0 alkene complexes.[35] They discovered that DAF with alkenes could adopt a $Pd^0(\kappa^1\text{-DAF})(\eta^2\text{-alkene})_2$ structure whereas canonical diimine ligands such as bpy and phen only formed $Pd^0(\kappa^2\text{-diimine})(\eta^2\text{-alkene})$. DAF may have access to an associative ligand substitution mechanism that assists alkene exchange on a Pd^0 center. Additionally, Elsevier's observations helps provide insight into why strongly chelating ligands fail to allow for catalytic turn over in the acetoxylation reaction. Additionally, the exchange between O_2 and alkene ligands on $Pd^0(\kappa^2\text{-diamine})$ complexes has been characterized as being thermoneutral which may also help explain why DAF allows for aerobic turn over.[36] A model in Scheme 6.3 presents the kinetically important aspects of the steady-state phase of the reaction.
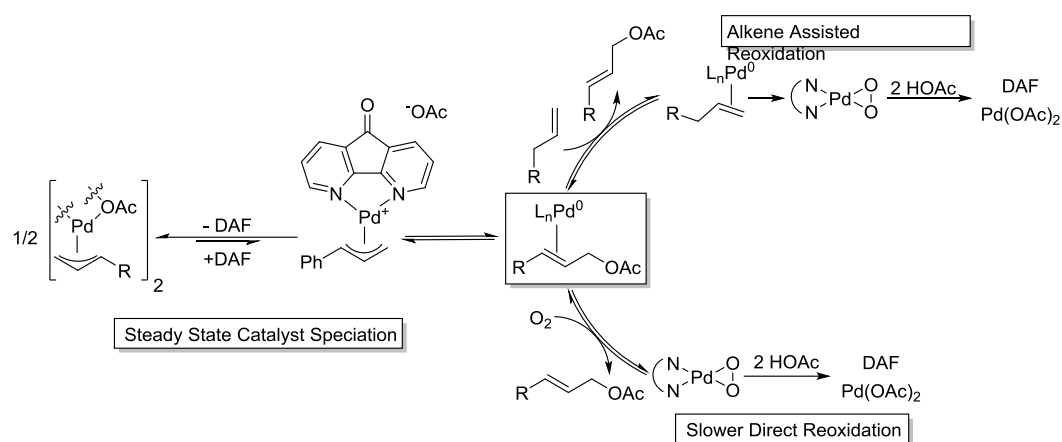
Scheme 6.3: Post-Burst Kinetic Model Highlighting Aspects that Affect the Observed Reaction Rate

6.3.4 Factors that Influence the Rate of the Reaction in the Steady State.

Multiple reaction components affect the reaction rate and a simple assignment of single rate determining step is not possible. In the burst phase of the reaction, C-H cleavage is the rate determining step however this is dependent on having a kinetically competent Pd^0 trap such as $Pd(OAc)_2$. The post-burst phase exhibits an O_2 dependence that is not a mass transport limited phenomena as well as a strong alkene dependence. Again, we believe that the alkene is helping to displace product and increase the available Pd^0 concentration in solution that can react with O_2. The reaction was much slower because O_2 is not as kinetically competent as $Pd(OAc)_2$. A Pd π-allyl resting state is consistent with the observed lack of a KIE in the the steady state regime as the catalyst and a function of O_2 concentration in solution. A unified kinetic model is presented in Scheme 6.4 that includes all of the kinetically relevant steps.
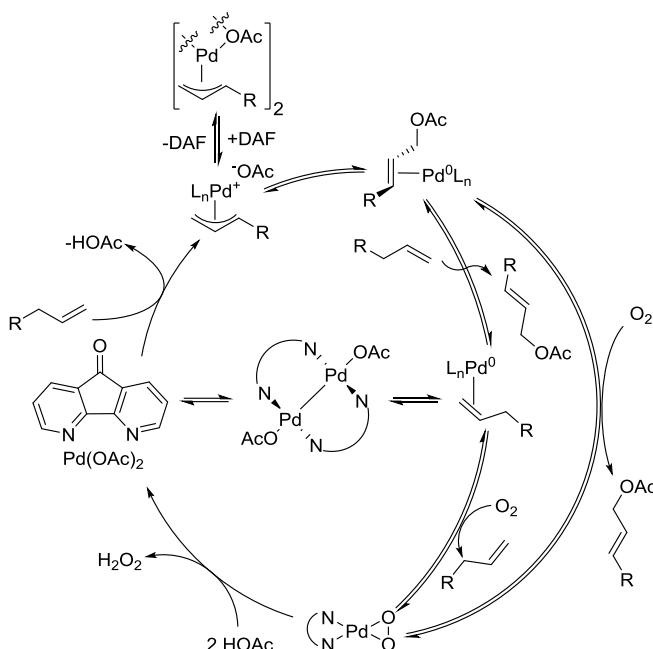
Scheme 6.4: Revised Acetoxylation Mechanism

6.3.5 Implications for Efficient Catalysis.

Pd^I formation is normally considered to be deleterious to catalysis in the cross-coupling literature and has been well characterized as such.[37] Ligand design has been instrumental in the development of more effective catalysts by mitigating Pd^I formation (Scheme 6.5). Hazari and co-workers had shown that NHC/Pd catalysts with appended allyl ligands used commonly for cross coupling readily undergo comproportionation under the reaction conditions and were able to minimize this, albeit not halt entirely, by introducing steric bulk such as a phenyl group on the allyl ligand.[33,38] Additionally, Schoenebeck and co-workers have shown that presence of Pd^I can be controlled by modulating steric bulk on phosphine ligands.[39] Even the X-type bridging ligand can have a dramatic effect on stabilization of Pd^I formation as chloride and bromides are much less stable than iodide.[40] Ligands present an opportunity to modulate catalyst activity and pyridyl ligand design continues to be the direction of investigation in our laboratory.
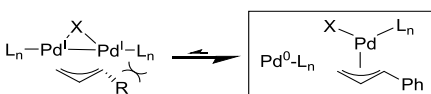
Scheme 6.5: Summary of Ligand Modulated Pd^I Disproportionation in Cross Coupling

The observation of rampant Pd[I] formation in the acetoxylation reaction helps provide an explanation for why reactions that proceed via reductive elimination are more problematic in aerobic catalysis than reactions that proceed via β-hydride elimination. Pd-catalyzed oxidation reactions that proceed by reductive elimination require stoichiometric oxidants such as BQ, Cu^{2+} or Ag^+ and Lewis Acid additives such as Pb^{2+} and Zn^{2+}. The formation of heterobimetallic structures have been proposed to be beneficial in oxidative catalysis while other examples inhibit catalysis.[41] Additionally, chemical oxidants are able to be dissolved in higher concentrations than can be achieved with O_2 as dissolving O_2 to comparable concentrations is hazardous and technically challenging.

Controlling Pd π-allyl speciation is important for performing selective substrate oxidation. Dimeric Pd π-allyls have been observed to be off-cycle species and erode selectivity in diastereoselective reductive elimination reactions. In particular, arresting the dimerization of Pd π-allyls has been observed to be important in controlling diastereoselective reductive elimination in the 1,4-diacetoxylation of dienes.[42] Neutral and cationic Pd π-allyls have also been previously observed to have different properties in stoichiometric reductive elimination studies.[43] Future efforts will focus on understanding the principles of reductive elimination from Pd π-allyls derived from C-H activation to perform effective catalyst controlled regioselective and diastereoselective aerobic Pd catalysis.

6.4 Conclusion.

This work has characterized the many mechanistic features of the DAF promoted Pd-catalyzed aerobic acetoxylation reaction. The reaction two-phase time course was kinetically analyzed to reveal a change in rate determining step. Operando X-ray absorption and NMR spectroscopy were utilized to characterize the evolution of the Pd catalyst over the reaction time course. New insights into the factors that affect catalyst speciation as well as the challenges of promoting reductive elimination in the paradigm of aerobic Pd-catalysis were presented. These insights will assist in catalyst design in the future and provide a foundation for designing systems that control region- and diastereoselectivity in the field of Pd-catalyzed allylic C-H functionalization.

6.5 Acknowledgements.

1. (a) Bäckvall, J. E. *Modern Oxidation Methods*, Wiley-VCH, Weinheim, 2004. (b) M. Weber, M. Weber, M. Kleine-Boymann, in *Ullmann's Encyclopedia of Industrial Chemistry*, Wiley-VCH Verlag GmbH & Co. KGaA, 2000, see chapter on Oxidations (c) Caron, S.; Dugger, R. W.; Ruggeri, S. G.; Ragan, J. A.; Ripin, D. H. B., *Chem. Rev.*, **2006**, *106*, 2943 – 2989

2. (a) Stahl, S. S. *Angew. Chem. Int. Ed.* **2004**, *43*, 3400 – 3420. (b) Stahl, S. S.; Alsters, P. L. *Liquid Phase Aerobic Oxidation Catalysis: Industrial Applications and Academic Perspectives*, John Wiley & Sons, 2016.

3. Cornell, C. N.; Sigman, M. S., *Inorg. Chem.* **2007**, *46*, 1903 – 1909.

4. (a) Wickens, Z. K.; Guzman, P. E.; Grubbs, R.H. *Angew. Chem. Int. Ed.* **2014**, *54*, 236-240. See also reviews: (b) Muzart, J., *Tetrahedron*, **2007**, *63,* 7505-7521. (c) Dong, J. J.; Browne, W. R.; Feringa, B. L., *Angew. Chem. Int. Ed.* **2015**, *54*, 734-744.

5. See reference 3 and (a) Takacs, J. M.; Jiang, X.-T., *Curr. Org. Chem.* **2003**, *7*, 369-396. (b) McDonald, R. I.; Liu, G.; Stahl, S. S. *Chem. Rev.* **2011**, *111*, 2981-3019.

6. (a) M. Weber, M. Weber, M. Kleine-Boymann, in *Ullmann's Encyclopedia of Industrial Chemistry*, Wiley-VCH Verlag GmbH & Co. KGaA, 2000, See chapter on Acetaldehyde for Wacker Process (b) Takacs, J. M.; Jiang, X.-T., *Curr. Org. Chem.* **2003**, *7*, 369 – 396.

7. (a) Engle, K. M.; Wang, D.-H.; Yu, J.-Q., *J. Am. Chem. Soc.*, **2010**, *132*, 14137-14151. (b) Le Bras, J.; Muzart, J. Chem. Rev. **2011**, *111*, 1170 - 1214. (c) Zheng, C.; Wang, D.; Stahl, S. S. *J. Am. Chem. Soc.* **2012**, *134*, 16496-16499. (d) Zheng, C.; Stahl, S. S. *Chem. Commun.* **2015**, *51*, 12771–12774. (e) Ying, C.-H.; Yan, S.-B.; Duan, W.-L., *Org. Lett.* **2014**, *16*, 500-503. (f) Odell, L. R.; Sävmarker, J.; Lindh, J.; Nilsson, P.; Larhed, M., *Comp. Org. Syn. II*, **2014**, *7*, 492-537.

8. (a) Nishimura, T.; Onoue, T.; Ohe, K.; Uemura, S., *Tetrahedron Lett.* **1998**, *39*, 6011 - 6014. (b) Nishimura, T.; Onoue, T.; Ohe, K.; Uemura, S. *J. Org. Chem.* **1999**, *64*, 6750-6755. (c) Jensen, D. R.; Pugsley, J. S.; Sigman, M. S., *J. Am. Chem. Soc.*, **2001**, *123*, 7475-7476 (d) Schultz, M. J.; Park, C. C.; Sigman, M. S. *Chem. Commun.* **2002**, 3034-3035. (e) Jensen, D. R.; Schultz, M. J.; Mueller, J. A.; Sigman, M. S., *Angew. Chem. Int. Ed.* **2003**, *42*, 3810 – 3813 (f) Schultz, M. J.; Hamilton, S. S.; Jensen, D. R.; Sigman, M. S., *J. Org. Chem.*, **2005**, *70*, 3343-3352.

9. (a) Ferreira, E. M.; Stoltz, B. M., *J. Am. Chem. Soc.* **2001**, *123*, 7725-7726 (b) Jensen, D. R.; Sigman, M. S., *Org. Lett.*, **2003**, *5*, 63-65 (c) Mandal, S. K.; Sigman, M. S., *J. Org. Chem.* **2003**, *68*, 7535-7537. (d) Bagdanoff, J. T.; Stoltz, B. M., *Angew. Chem. Int. Ed.* **2004**, *43*, 353-357. (e) Caspi, D. D.; Ebner, D. C.; Bagdanoff, J. T.; Stoltz, B. M., *Adv. Synth. Catal.* **2004**, *346*, 185 - 189.

10. (a) Campbell, A. N.; Stahl, S. S. *Acc. Chem. Res.* **2012**, *45*, 851-863. (b) Mitsudome, T.; Umetani, T.; Nosaka, N.; Mori, K.; Mizugaki, T.; Ebitani, K.; Kaneda, K., *Angew. Chem. Int. Ed.* **2006**, *45*, 481-485.

11. Campbell, A. N.; White, P. B.; Guzei, I. A.; Stahl S. S., *J. Am. Chem. Soc.* **2010**, *132*, 15116-15119.

12. (a) Pilarski L. T.; Selander, N.; Bose, D.; Szabó, K. J., *Org. Lett.*, **2009**, *11*, 5518-5521. (b) Alam, R.; Pilarski L. T.; Pershagen, E.; Szabó, K. J., *J. Am. Chem. Soc.*, **2012**, *134*, 8778-8781.

13. (a) Pilarski L. T.; Janson, P. G.; Szabó, K. J., *J. Org. Chem.*, **2011**, *76*, 1503-1506. (b) Sharma, A.; Hartwig, J. F., *J. Am. Chem. Soc.*, **2013**, *135*, 17983-17989.

14. (a) Chen, M. S.; White, M. C., *J. Am. Chem. Soc.,* **2004**, *126*, 1346 - 1347. (b) Chen, M. S.; Prabagaran, N.; Labenz, N. A.; White, M. C., *J. Am. Chem. Soc.* **2005,** *127*, 6970-6971. (c) Fraunhoffer, K. J.; Prabagaran, N.; Sirois, L. E.; White, M. C., *J. Am. Chem. Soc.*, **2006**, *128*, 9032 – 9033. (d) Covell, D.

J.; White, M. C., *Angew. Chem. Int. Ed.*, **2008,** *47*, 6448- 6451. (e) Stang, E. M.; White, M. C., *Nat. Chem.,* **2009**, *1*, 547-551. (f) Lin, B.-L.; Labinger, J. A.; Bercaw, J. E., *Can. J. Chem.* **2009**, *87*, 264-271. (g) Thiery, E.; Aouf, C.; Belloy, J.; Harakat, D.; Le Bras, J.; Muzart, J., *J. Org. Chem.*, **2009**, *75*, 1771-1774. (h) Kondo, H.; Yu, F.; Yamaguchi, J.; Liu, G.; Itami, K., *Org. Lett.*, **2014**, *16*, 4212-4215. (i) Malik, H. A.; Taylor, B. L. H.; Kerrigan, J. R.; Grob, J. E.; Houk, K. N.; Du Bois, J.; Hamann, L. G.; Patterson, A. W., *Chem. Sci.*, **2014**, *5*, 2352-2361.

15. Diao, T.; Stahl, S. S. *Polyhedron* **2014**, *84*, 96-102.

16. Piera, J.; Piera, J.; Bäckvall, J., *Angew. Chem. Int. Ed.*, **2008**, *47*, 3506-3523.

17. White, P. B.; Jaworski, J. N.; Fry, C. G.; Dolinar, B. S.; Guzei, I. A.; Stahl, S. S., *J. Am. Chem. Soc.* **2016**, 138, 4869-4880.

18. White, P. B.; Jaworski, J. N.; Geyunjian, H. Z.; Stahl, S. S., *ACS Catal.* **2016**, *6*, 3340-3348.

19. High yields of product formation (>40% yield) could not be obtained at 60 °C which is the previously reported optimized reaction temperature and kinetic investigations were generally performed at 80 °C. Peroxides have been reported to work with DAF to promote catalyst turn-over and an old bottle 1,4-dioxane with contaminated dioxanes was likely used.

20. See Chapter 5 and Jaworski, J. N.; McCann, S. D.; Guzei, I. A.; Stahl, S. S., *Angew. Int. Chem. Ed.*, **2017**, Accepted..

21. (a) Beach, N. J.; Knapp, S. M. M.; Landis, C. R., *Rev. Sci. Instrum.*, **2015**, *86*, 104101 (b) Chotchatchawankul, S., Mechanistic Studies of Rh(diphosphine)-Catalyzed Methanol Reductive Carbonylation, Dissertation, University of Wisconsin - Madison. Madison, WI, 2015.

22. Osterberg, P. M.; Niemeier, J. K.; Welch, C. J.; Hawkins, J. M.; Martinelli, J. R.; Johnson, T. E.; Root, T. W; Stahl, S. S. *Org. Process Res. Dev.* **2015**, *19*, 1537-1543.

23. Knapp, S. M. M.; Shaner, S. E.; Kim, D.; Shopov, D. Y.; Tendler, J. A.; Pudalov, D. M.; Chianese, A. R., *Organometallics* **2014**, *33*, 473-484

24. (a) Nelson, R. C.; Miller, J. T., *Catal. Sci. Technol.*, **2012**, *2*, 461-470 (b) Adrio, L. A.; Nguyen, B. N.; Guilera, G.; Livingston, A. G.; Hii, K. K., *Catal. Sci. Technol.*, **2012**, *2*, 316–323 (c) Sherborne, G. J.; Nguyen, B. N., *Chem. Cent. J.,* **2015**, 9:37.

25. (a) Evans, J.; O'Neill, L.; Kambhampati, V. L.; Rayner, G.; Turin, S.; Genge, A.; Dent, A. J.; Neisius, T., *Dalton Trans.* **2002**, 2207-2212. (b) Tromp, M.; Sietsma, J. R. A.; van Bokhoven, J. A.; van Strijdonck, G. P. F.; van Haaren, R. J.; van der Eerden, A. M. J.; van Leeuwen, P. W. N. M; Koningsberger, D. C., *Chem. Commun.* **2003**, 128-129. (c) Fiddy, S. G.; Evans, J.; Newton, M. A.; Neisius, T.; Tooze, R. P.; Oldman, R., *Chem. Commun.*, **2003**, 2682-2683. (d) Fiddy, S. G.; Evans, J.; Neisius, T.; Newton, M. A.; Tsoureas, N.; Tulloch, A. A. D.; Danopoulos, A. A., *Chem. Eur. J.* **2007**, *13*, 3652-3659. (e) Ellis, P. J.; Fairlamb, I. J. S.; Hackett, S. F. J.; Wilson, K.; Lee, A. F., *Angew. Chem. Int. Ed.* **2010**, *49*, 1820-1824.

26. For a reactor with similar capabilities, see Bauer, M.; Heusel, G.; Mangold, S.; Bertagnolli, H., *J. Synchrotron Rad.,* **2010**, *17*, 273-279.

27. Interesting to note is that the edge at 11 minutes does not overlay exactly with the [Pd^{I}(DAF)OAc)]$_2$ (**2**) reference. The time point at 11 minutes is the point at which the edge most closely resembles that of reference (**2**) and has the lowest edge energy. A linear combination of [Pd^{II}(DAF)(cinnamyl)]BF$_4$ (**5**) and (**2**) is provides a reasonable fit (both of the raw edge and X-space) where approximately ~70% (**2**) and ~30% (**5**) are present. Incorporation of DAF/Pd(OAc)$_2$ (**1**) and (**4**) do not provide reasonable fits.

28. Halogenated solvents were avoided as they had been previously characterized to decompose Pd^{I}. See reference 20.

29. NMR shows similar behavior but Pd^{I} appears to be lower in quantity likely because of the higher dissolved O$_2$ in solution from the reaction being performed at 3.2 atm of O$_2$.

30. (a) Hazari, N.; Hruszkewycz, D. P., *Chem. Soc. Rev.*, **2015**, *45*, 2871-2899 (b) Bonney, K. J.; Schoenebeck, F., *Chem. Soc. Rev.*, **2014**, *43*, 6609-6638.

31. (a) Engelin, C.; Jensen, T.; Rodriguez-Rodriguez, S.; Fristrup, P., *ACS Catal.* **2013,** *3*, 294-302. (b) Gómez-Gallego, M.; Sierra, M. A. *Chemical Rev.* **2011**, *111*, 4857-4963.

32. Hruszkewycz, D. P.; Balcells, D.; Guard, L. M.; Hazari, N.; Tilset, M., *J. Am. Chem. Soc.* **2014**, *136*, 7300-7316.

33. (a) Melvin, P. R.; Balcells, D.; Hazari, N.; Nova, A., *ACS Catal.*, **2015**, *5*, 5596-5606. (b) Melvin, P. R.; Nova, A.; Balcells, D.; Dai, W.; Hazari, N.; Hruszkewycz, D. P.; Shah, H. P.; Tudge, M. T., *ACS Catal.*, **2015**, *5*, 3680 - 3688. (c) Hruszkewycz, D. P.; Guard, L. M.; Balcells, D.; Feldman, N.; Hazari, N.; Tilset, M., *Organometallics* **2015**, *34*, 381-394.

34. For an example of a mass-transport limited aerobic Pd-catalyzed reaction see: Steinhoff, B. A.; Stahl, S. S. *J. Am. Chem. Soc.* **2006**, *128*, 4348-4355.

35. Klein, R. A.; Witte, P.; van Belzen, R.; Fraanje, J.; Goubitz, K.; Numan, M.; Schenk, H.; Ernsting, J. M.; Elsevier, C. J., *Eur. J. Inorg. Chem.* **1998,** 319-330.

36. Popp, B. V.; Morales, C. M.; Landis, C. R.; Stahl, S. S. *Inorg. Chem.* **2010**, 49, 8200-8207.

37. See reference 30, 35 and the following: (a) Bonney, K. J.; Proutierea, F.; Schoenebeck, F., *Chem. Sci.*, **2013**, *4*, 4434-4439 (b) Proutiere, F.; Aufiero, M.; Schoenebeck, F., *J. Am. Chem. Soc.* **2012**, *134*, 606-612.

38. (a) Melvin, P. R.; Balcells, D.; Hazari, N.; Nova, A., *ACS Catal.*, **2015**, *5*, 5596-5606. (b) Melvin, P. R.; Nova, A.; Balcells, D.; Dai, W.; Hazari, N.; Hruszkewycz, D. P.; Shah, H. P.; Tudge, M. T., *ACS Catal.*, **2015**, *5*, 3680-3688. (c) Hruszkewycz, D. P.; Guard, L. M.; Balcells, D.; Feldman, N.; Hazari, N.; Tilset, M., *Organometallics* **2015**, *34*, 381-394.

39. Proutiere, F.; Lyngvi, E.; Aufiero, M.; Sanhueza, I. A.; Schoenebeck, F., *Organometallics* **2014**, *33*, 6879-6884.

40. (a) Durà-Vilà, V.; Mingos, D. M. P.; Vilar, R.; White, A. J. P.; Williams, D. J., *Chem. Commun.* **2000**, 1525-1526. (b) Proutiere, F.; Aufiero, M.; Schoenebeck, F., J. Am. Chem.Soc. **2012**, *134*, 606-612. (c) Yin, G.; Kalvet, I.; Schoenebeck, F., *Angew. Chem. Int. Ed.* **2015**, *54*, 6809-6813.

41. (a) Goel, A. B.; Throckmorton, P. E.; Grimm, R. A., *Inorg. Chim. Acta,* **1986**, *117*, L15-L17 (b) Goel, A. B.; *Inorg. Chim. Acta,* **1986**, *121*, L11-L13. (c) Goel, A. B., *Inorg. Chim. Acta,* **1987**, *129*, L31-L32 (d) Aufiero, M.; Proutiere, F.; Schoenebeck, F., *Angew. Chem. Int. Ed.* **2012**, *51*, 7226 –7230. (e) Yang, Y.-F.; Cheng, G.-J.; Liu, P.; Leow, D.; Sun, T.-Y.; Chen, P.; Zhang, X.; Yu, J.-Q.; Wu, Y.-D.; Houk, K. N., *J. Am. Chem. Soc.* **2014**, 136, 344−355. (f) Bock, K.; Feil, J. E.; Karaghiosoff, K.; Koszinowski, K., *Chem. Eur. J.,* **2015**, *21*, 5548-5560.

42. (a) Grennberg, H.; Gogoll, A.; Bäckvall, J.-E., *J. Org. Chem.*, **1991**, *56*, 5808-5811. (b) Eastgate, M. D.; Buono, F. G., *Angew. Chem. Int. Ed.* **2009**, *48*, 5958-5961. (c) Zheng, B.; Schmidt, M. A.; Eastgate, M. D., *J. Org. Chem.* **2016**, *81*, 3112-3118.

43. (a) Bäckvall, J.-E.; Nordberg, R. E.; Wilhelm, D., *J. Am. Chem. Soc.,* **1985**, *107*, 6892 − 6898. (b) Vitagliano, A.; Åkermark, B.; Hansson, S., *Organometallics,* **1991**, *10*, 2592 − 2599.

Appendix A:Supporting Information for Chapter 3.

A1. General Experimental Considerations.

All commercially available compounds were used as received. $CDCl_3$ for NMR spectroscopy was filtered through dry K_2CO_3 to remove residual HCl prior to use. All samples were prepared in a teflon-capped scintillation vial and placed in a dark location a day in advance to allow the species to equilibrate prior to data acquisition. ^{1}H and ^{15}N NMR spectra were recorded on a Varian INOVA 600 MHz or Bruker Avance-500 spectrometer. ^{1}H NMR chemical shifts are reported in parts per million relative to internal TMS (0.00 ppm) in $CDCl_3$. ^{15}N NMR chemical shifts are reported in parts per million and absolute referenced[1] using the ^{1}H spectrum to liquid ammonia (0.00 ppm). In cases where spectral overlap occurred, integrations were obtained by using line-fitting routines in the MestReNova v. 8.02 software package. The sample temperature was calibrated with an external 4% MeOH in MeOD-d_3 reference standard. The pw90 and longest T_1 values were computed from the pw360 and inversion recovery experiments, respectively, after each temperature change. All standard ^{1}H spectra were recorded quantitatively (recycle delay $\geq 5*T_1$) and integrals referenced to an internal standard (1,3,5-trimethoxybenzene). For species **A-F**, selective TOCSY and ROESY experiments were used as implemented in Varian ChemPack 3.1 and were performed using SEDUCE shaped pulses with spinlock frequencies of 8.5 kHz and 5.4 kHz, respectively. For species **G-L**, the standard selrogp pulse program with a spinlock of 2.78 kHz in the TopSpin 3.1 library was used for ROESY experiments. Varian pulse programs for NOESY and TOCSY with spinlock of 8.90 kHz from ChemPack 3.1 were ported over for use on the Bruker spectrometer. ^{1}H-^{15}N HMBC uniformly have dof = 250 ppm.[2] Two-times linear prediction in F1 was applied to all 2D HSQC and HMBC spectra.

Crystals of complexes **A**, **B**, **E**, **G and H** were grown by vapor diffusion of pentane or hexane into 20-40 mM $CDCl_3$ solutions of $Pd(OAc)_2$ with various quantities of ligand (**A**: 0.5 equiv DAF, **B**: 1.0 equiv DAF, **E**: 6 equiv, **G**: 0.5 equiv Me_2DAF, **H**: 1 eq of Me_2DAF). Optimal crystals were grown in a room held at a constant 4 °C. Complexes **A, G and H** produced a nearly quantitative amount of crystals whereas **B** and **E** were significantly more challenging to grow and produced few crystals. Crystals of complexes **I** and **J** were crystallized in solutions of 1:1 TFAH and $CDCl_3$ using 0.5 equiv DAF and 1.0 eq DAF respectively relative to $Pd(OAc)_2$. A crystal of complex **L** was obtained from a 1:1 mixture of $Pd(OPiv)_2$ and DAF that was equilibrated for 5 days at room temperature and grown from vapor diffusion of pentane overnight. Crystals of complex **M** were obtained by reacting $Pd(OAc)_2$ with 2 equivalents of perfluorobenzoic acid and crystallized out of an 11 mM solution over two days in an NMR tube. The details of the X-ray data collection can be found below for each of the complexes.

A2. General Computational Considerations.

All computations were performed with the Gaussian 09 program[3] using resources provided by University of Wisconsin–Madison Chemistry Department. Spin-restricted density functional theory (DFT) calculations were performed with the hybrid density functional, rB3LYP.[4,5] A combination of the Stuttgart RSC 1997 ECP/triple-ζ basis[6] for Pd and the all-electron 6-31+G(d) basis set for all other atoms was used for gas-phase geometry optimizations and normal mode analyses. Full geometry optimizations were carried out in internal coordinates using the default Berny algorithm. Frequency calculations were performed at the optimized geometries to confirm that each geometry had the appropriate number of imaginary frequencies: zero for minima or one for transition states. The imaginary frequency identifying a saddle-point was visually inspected for the proper motion.

At the calculated stationary points, solvation-corrected single-point total energy calculations were carried out with the Pd basis detailed above and the 6-311+G (d,p) basis on all other atoms with electrostatic

and non-electrostatic solvation effects evaluated using the polarizable-continuum model (PCM). The solvation cavity was generated using UFF radii, explicitly treating hydrogen atoms, and the radii were scaled by a factor of 1.2. The solvent chosen was chloroform.

A3. Supporting NMR Spectra

A3.1 1D NOESY vs 1D ROESY Discussion

1D NOESY experiments involve a selective inversion pulse followed by a mixing period where the NOEs build up. During detection, resonances that undergo chemical exchange with the selected peak appear with the same phase as the selected peak while resonances with NOEs appear with opposite phase for compounds in the fast motion limit. A disadvantage of the 1D NOESY experiment is that the intensity and sign of the NOE is sensitive to molecular size, sample temperature and field strength. These parameters are manifested in a $\log(\omega_0\tau_c)$ term where ω_0 is the main field strength and τ_c is molecular correlation time. τ_c is approximately the inverse of the molecular tumbling frequency and becomes larger as the size of the molecule increases or the temperature decreases. Therefore, at a given $\log(\omega_0\tau_c)$, the value of an NOE decreases, crosses through zero and becomes negative, or stated more specifically, the same phase as the irradiated peak. These negative NOEs become indistinguishable, without perofmring other experiments (e. g., at different tempeartures), from fast chemical exchange and therefore are unreliable as indicators as NOE in exchanging systems.

The ROESY, or rotating-frame NOESY, experiment avoids this problem by applying a spinlock in the rotating frame, which substitutes ω_0 with ω_1, where ω_1 is the magnetic field strength of the resulting spinlock rf. ω_1 is many orders of magnitude smaller than ω_0 and moves the $\log(\omega_0\tau_c)$ term toward the origin. This results in through-space interactions (ROEs) always appearing with the opposite phase as the selected peak and therefore always distinguishable from chemical exchange. However, ROESY experiments suffer from more artifacts and smaller possible mix times than the corresponding NOESY experiment due to the spinlock.

All values are in ppm

Assignment		*Ortho*	*Meta*	*Para*	^{15}N *Resonance*	*OAc*
A	**a⁰**	10.58	7.80	8.31	203.7	1.78, 2.04, (2.05)
B	**b¹**	10.13	7.45	8.11	189.3	1.87, 1.95
	b²	9.56	7.72	8.23	304.6	
C	**c¹**	10.12	7.37	8.00	203.7	1.85
	c²	9.58	7.74	8.17	304.3	
D	**d¹**	9.96	7.59	8.16	206.3	1.66
	d²	9.11	7.63	8.19	309.3	
E	**e¹**	9.85	7.63	8.16	207.1	1.52
	e²	9.41	7.65	8.15	306.7	
F	**f⁰**	8.66	7.93	8.66	213.3	2.27
G	**g⁰**	10.50	7.60	7.96	199.4	2.04, 2.01, 1.74
H	**h⁰**	7.98	7.74	7.94	209.7	2.16
I	**i⁰**	10.16	8.01	8.49	197.27	--
J	**j⁰**	8.01	7.74	8.35	198.7	--
K	**k⁰**	--	8.41	7.77	--	--
L	**l⁰**	9.56	7.70	8.22	216.3	0.54 (OPiv)

Table A 1: Compilation of all ^1H and ^{15}N chemical shifts for A-L obtained using TOCSY, NOESY, ^1H-^{13}C HSQC, ^1H-^{13}C HMBC, ROESY and ^1H-^{15}N HMBC experiments. The acetate resonance for A given in parentheses is inferred from comparing relative integrations of the acetate region. Species A-F chemical shifts reported at -45 °C. Species G-L reported at 24 °C[1]

---

[1] Table A-1 is a compilation of chemical shifts observed by PBW and JNJ

A3.2   TOCSY Spectra of A–E2

Structure **A**
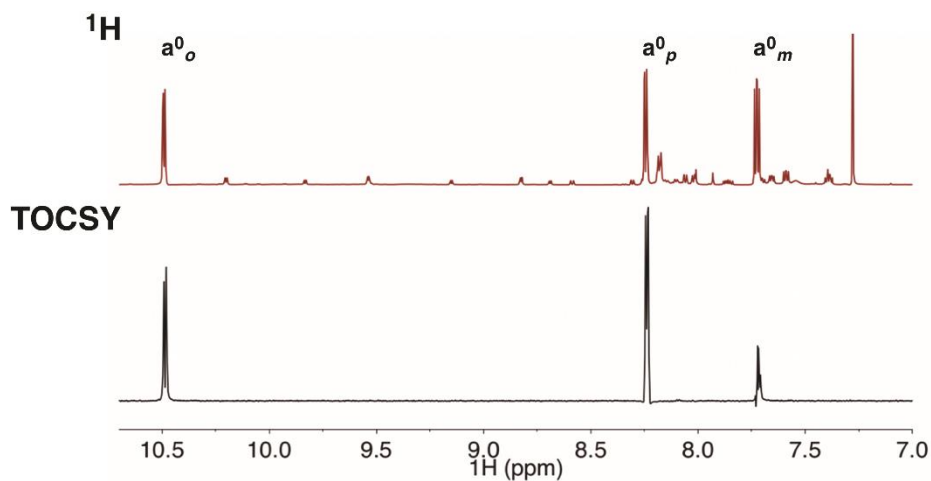
Figure A 1: ^{1}H 1D TOCSY spectrum of 0.5 equiv DAF at 12 °C. ns = 8, d1 = 3.57 s, 8.5 kHz spinlock, mix = 0.03 s. The resonance a^0_o was selected.

Structure **B**
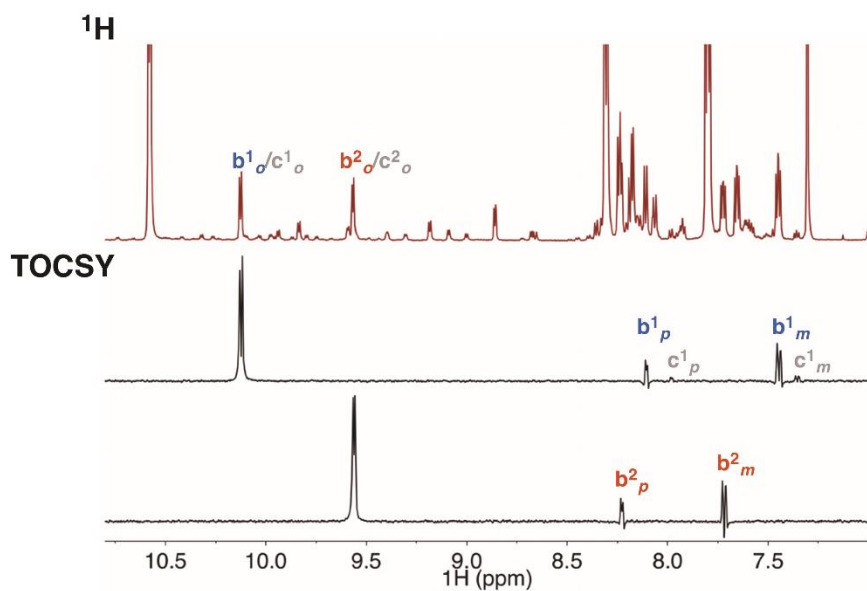
Figure A 2: ^{1}H 1D TOCSY spectrum of 0.5 equiv DAF at -45 °C. ns = 8, d1 = 3.57 s, 8.5 kHz spinlock, mix = 0.03 s. The resonances b^1_o (middle) and b^2_o (bottom) were selected in order to determine the chemical shift of the meta and para protons for

[2] All data pertaining to DAF/Pd(OAc)$_2$ was obtained independently by PBW

each ring. Due to the significant overlap of b^1_o and c^1_o, small amounts of the meta and para protons for C are observed in the TOCSY.

Structures **C–E**
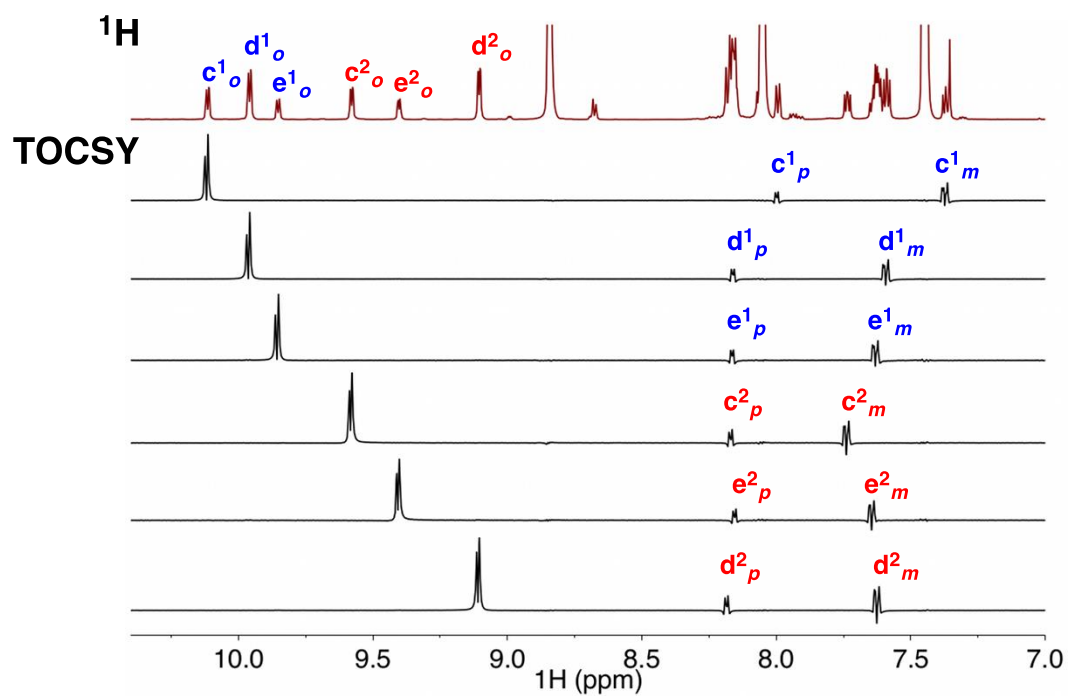
Figure A 3: ^{1}H 1D TOCSY spectrum of 6 equiv DAF at -45 °C. ns = 8, d1 = 3.57 s, 8.5 kHz spinlock, mix = 0.03 s. Each resonance from c^1_o–e^2_o was selected in order to determine the chemical shift of the meta and para protons, which exhibit large amounts of chemical shift overlap in the ^{1}H spectrum.

A3.3 1D ROESY at 0.5 Equiv of DAF[2]
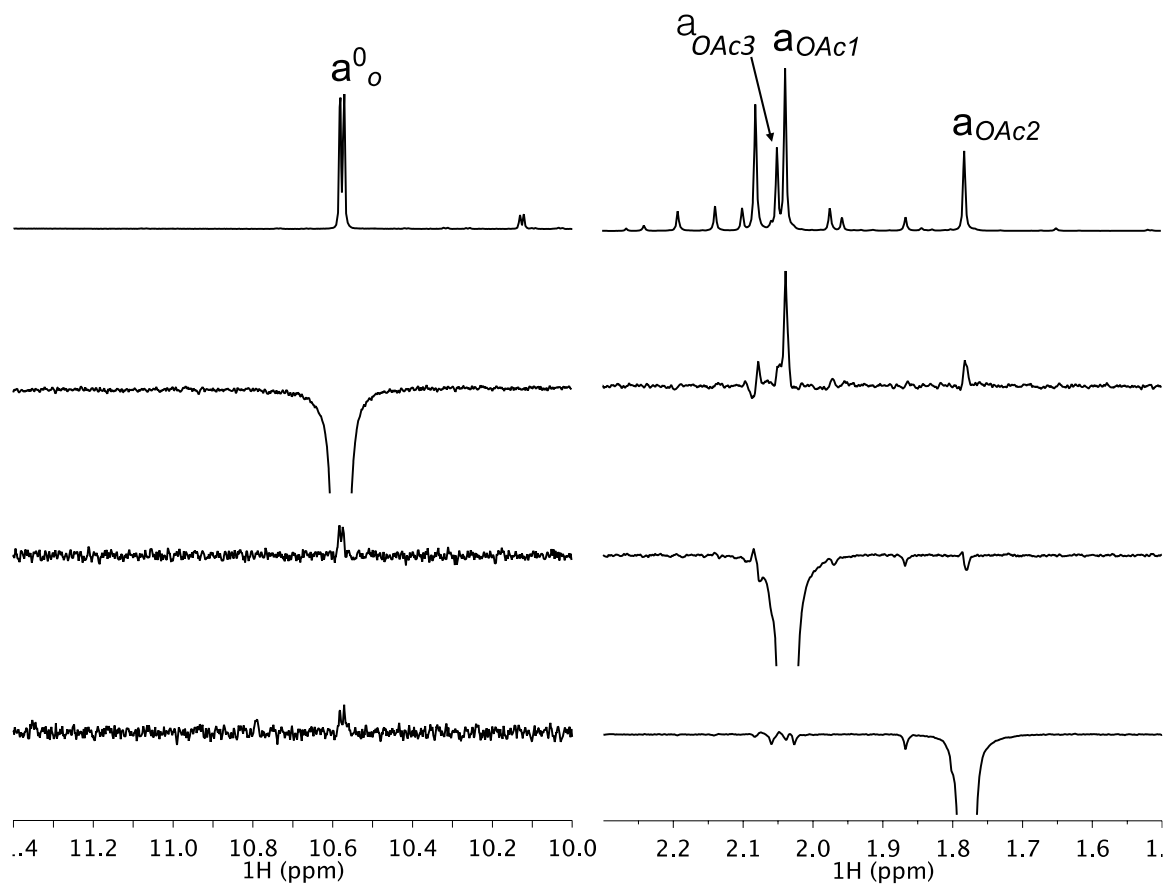
Figure A 4: ^{1}H-^{1}H 1D ROESY spectra of A at 0.5 equiv DAF at -45 °C. ns = 128, d1 = 6.3 s, 5.4 kHz spinlock, mix = 0.8 s. The extra acetate resonances represent the unobserved, by 1D ROESY, OAc resonance, free Pd(OAc)$_2$ and other minor DAF-Pd(OAc)$_2$ species.

1D & 2D ROESY at 1 Equiv of DAF
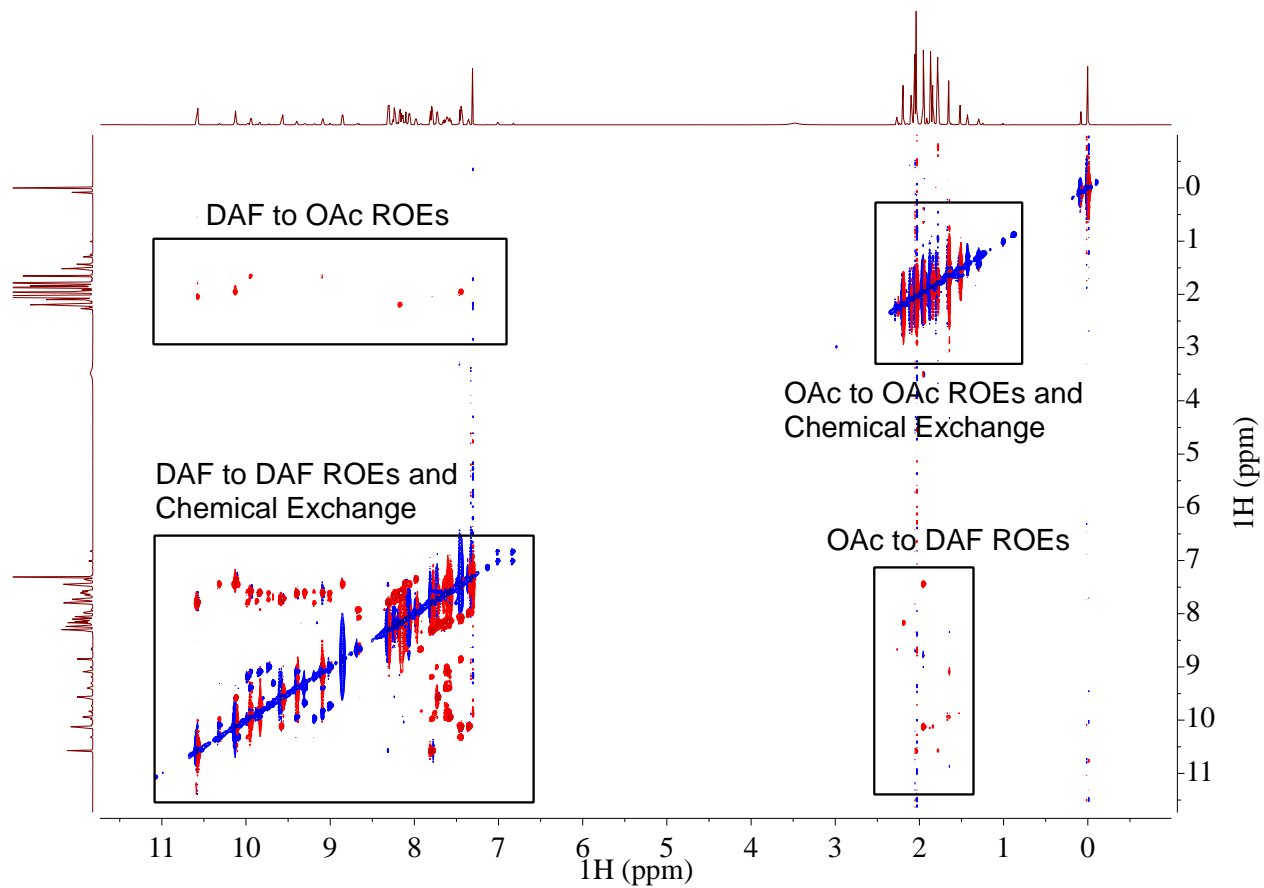
Figure A 5: ^{1}H-^{1}H ROESY spectrum of 1 equiv DAF at -45 °C. ns = 48, d1 = 6.3 s, ni = 200, sw(f1) = sw(f2) = 12.7 ppm, 5.3 kHz spinlock, mix = 0.8 s.

Zoomed-In Regions of the 2D ROESY Spectrum at 1 Equiv DAF
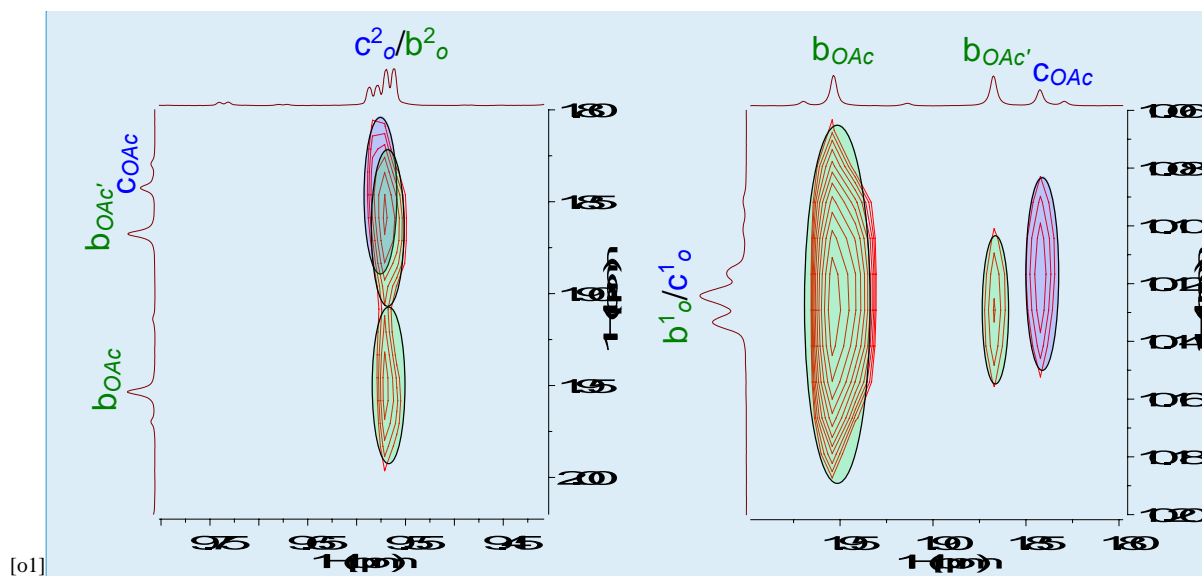
Figure A 6: ^{1}H-^{1}H 2D ROESY at 1 Equiv of DAF. Species B has two acetate cross-peaks. 1D ROESY Experiments on Observed

Acetate Resonances
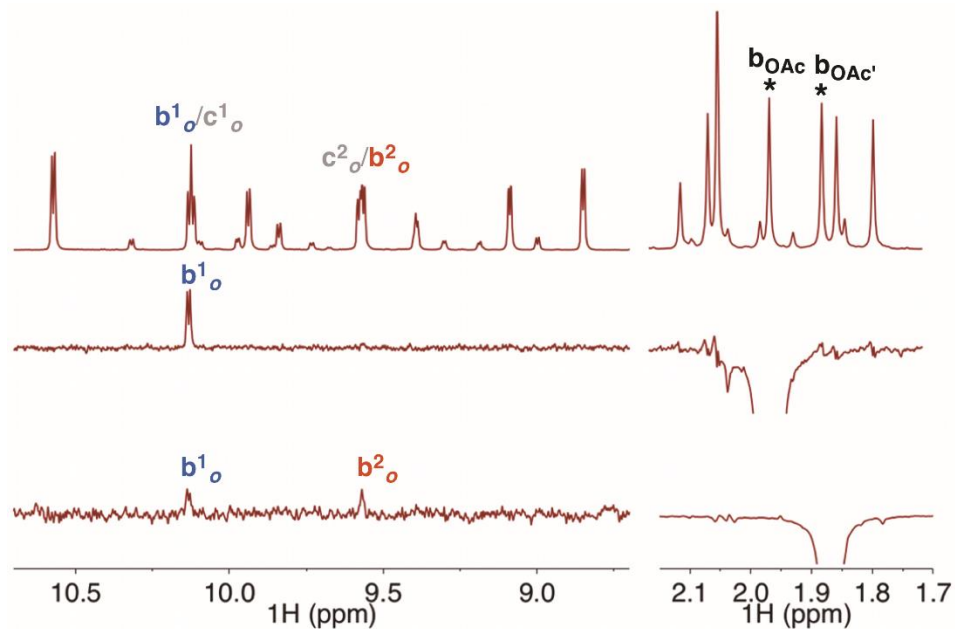
Figure A 7: Stacked 1D ROESY experiments selecting b_{OAc} and $b_{OAc'}$. The " * " indicates which peaks were irradiated. Through-

space interactions are revealed between b_{OAc}/$b_{OAc'}$ and b^1_o/b^2_o in the spectra. ns = 512 (middle) and 1024 (bottom), d1 = 6.3 s, 5.4

kHz spinlock, mix = 0.8 s.

A3.4 1D ROESY Experiments on $c^1_o - d^1_o$ and $f^0_o/{}_p{}^2$
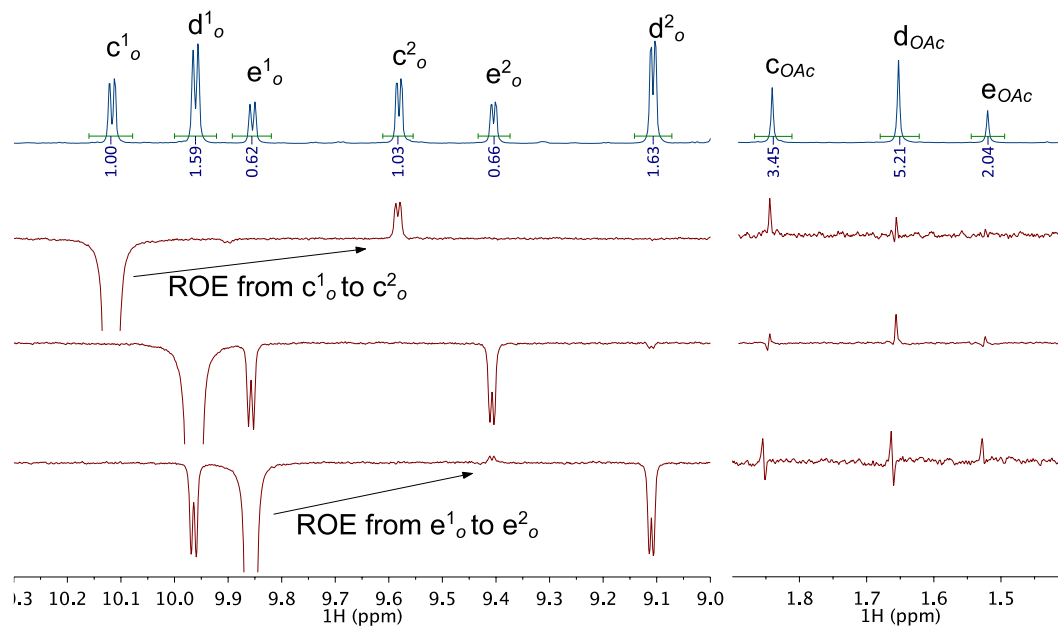
Figure A 8: Stacked 1D ROESY experiments selecting $c^1_o - e^1_o$. Nearby OAc residues are identified for each complex C − E. Through-space interactions are revealed between c^1_o/c^2_o and e^1_o/e^2_o, and provide insight into the orientation of the ligands. ns = 40, d1 = 10 s, 5.4 kHz spinlock, mix = 0.6 s.

Build-Up Curves for $c_{OAc} - e_{OAC}$
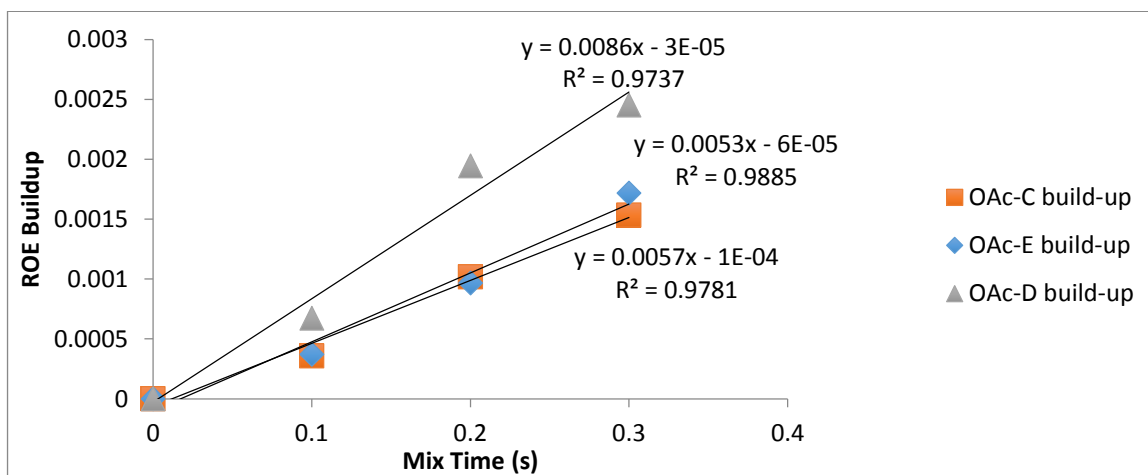
Figure A 9: ROE build-up curves for $c_{OAc} - e_{OAc}$. These confirm that the positive peaks amidst the artifacts in A8 are indeed ROEs and not artifacts themselves.

1D ROESY of $f^0_{o/p}$
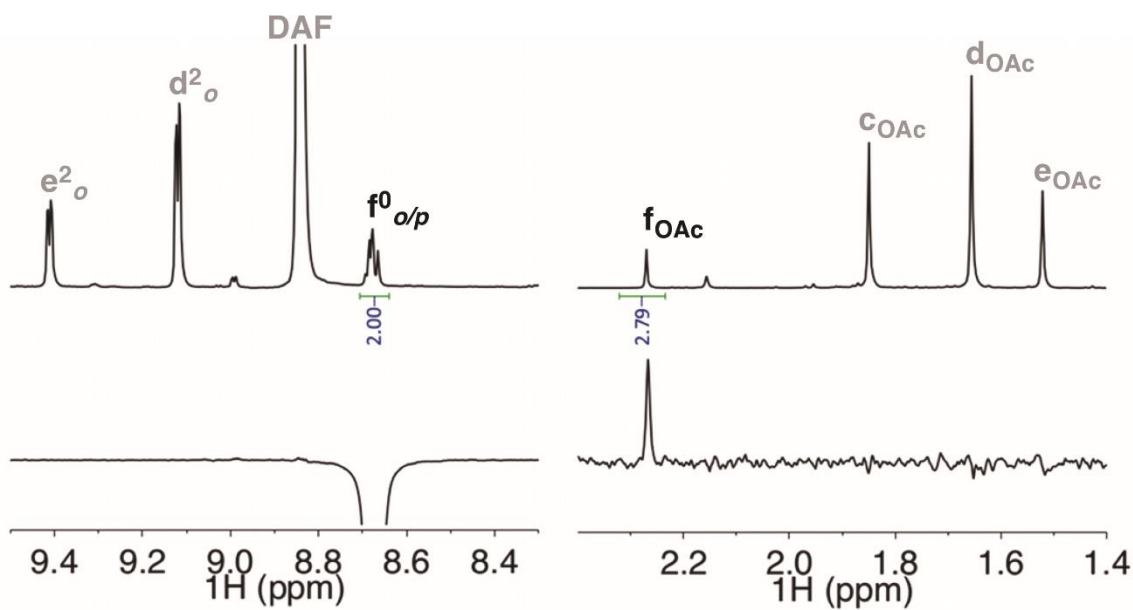
Figure A 10: 1D ROESY experiment selecting $f^0_{o/p}$. ns = 40, d1 = 10 s, 5.4 kHz spinlock, mix = 0.6 s.

A3.5 Measurement of ΔG‡exchange for D and E by Lineshape Analysis[2]
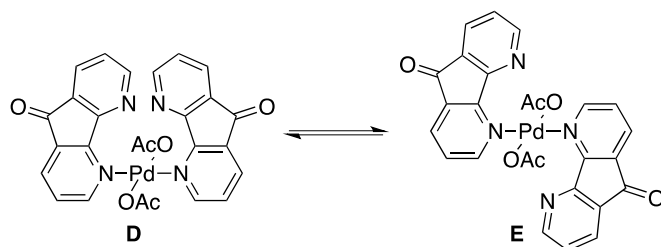
Variable Temperature Spectra
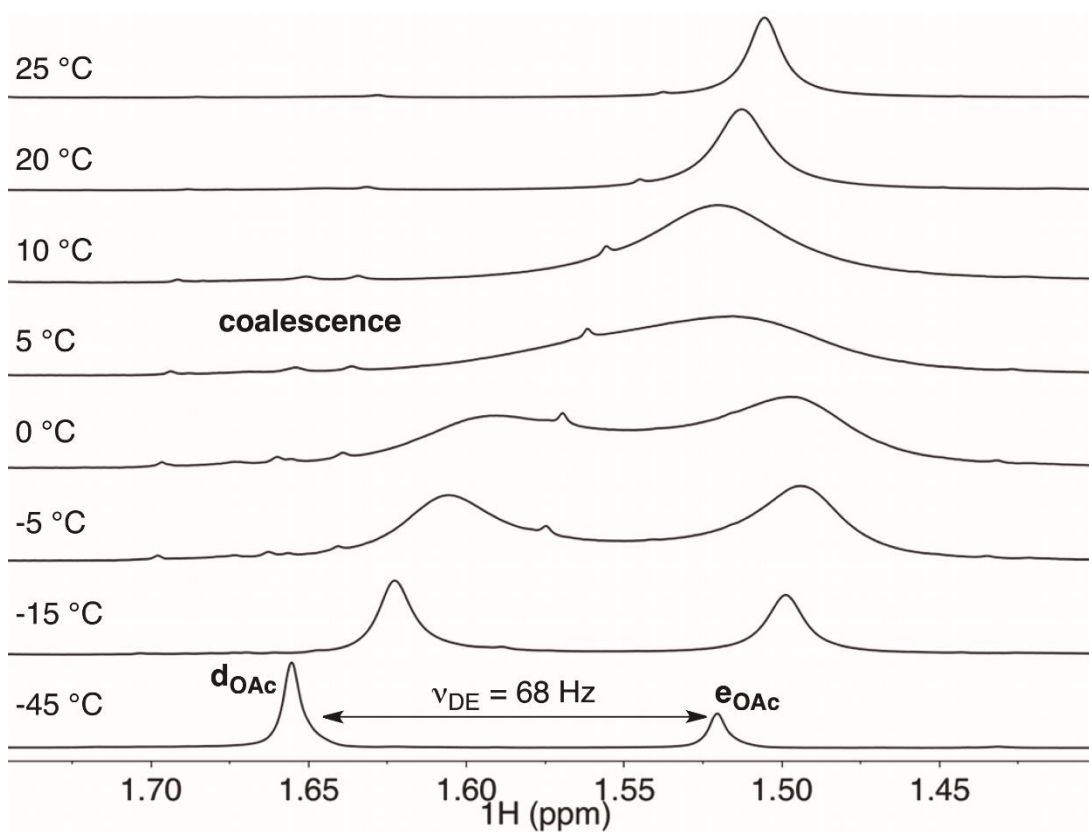
Figure A 11: Variable-temperature spectra of a CDCl₃ solution of 6:1 DAF:Pd(OAc)₂. The spectral window is focused on the acetate resonances of D and E (d_{OAc} and e_{OAc}). These peaks were chosen for lineshape analysis due to their simple singlet nature. The resonances are sharp at -45 °C and progressively broaden until ~5 °C at which point they coalesce. This single broad peak progressively narrows at higher temperatures. ¹H: ns = 8, d1 = 20 s, ds =2.

Determining Rate Constants of Exchange from Line Shape Analysis

The rate constants of chemical exchange between **D** and **E** were determined by lineshape analysis of the above spectra. The width at half-height was obtained from performing line-fitting routines on the peaks. Three sets of equations were used to extract out the rate constants below, at and above the coalescence point for the two acetate resonances[7] (eq 1-3).

Below coalescence:

$$k = \pi(\nu - \nu_{ref,\mathbf{D}}) \quad (1)$$

where ν and $\nu_{ref,\mathbf{D}}$ are the line-widths at half-height for $\mathbf{d_{OAc}}$ at a given temperature and -45 °C, respectively.

At Coalescence: $k = (\pi/\sqrt{2})\nu_{\mathbf{DE}} \quad (2)$

where $\nu_{\mathbf{DE}}$ is the difference in frequency between $\mathbf{d_{OAc}}$ and $\mathbf{e_{OAc}}$ at -45 °C

Above Coalescence:

$$k = (\pi \, \nu_{\mathbf{DE}}^2)/(2(\nu - \nu_{ref,\mathbf{D}})) \quad (3)$$

The rate constant for the exchange process at room temperature was determined to be 1967 s^{-1}, which corresponds to a $\mathbf{\Delta G^{\ddagger}} = 13$ kcal/mol. The rate constants at each temperature were used to construct an Eyring plot to test the quality of the analysis and provide an error for the room temperature measurement.
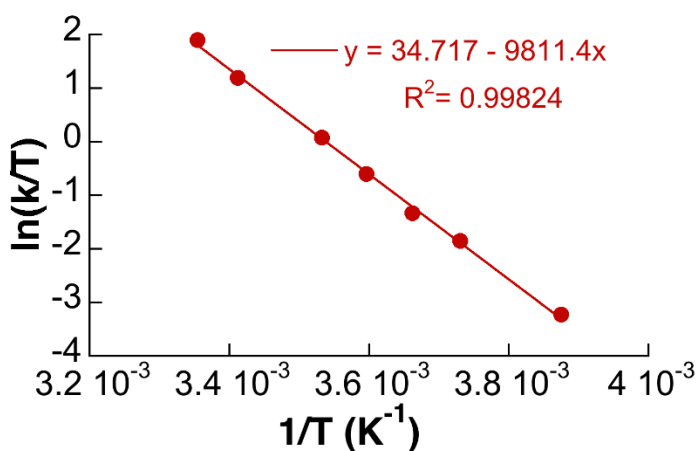
Figure A 12: Eyring plot of the temperature-dependent rate constants obtained for exchange between D and E.

A3.6 ^{1}H-^{15}N HMBC Spectra at 0.5, 1 and 6 Equiv of DAF Relative to Pd(OAc)$_2$[2]

0.5 Equiv DAF
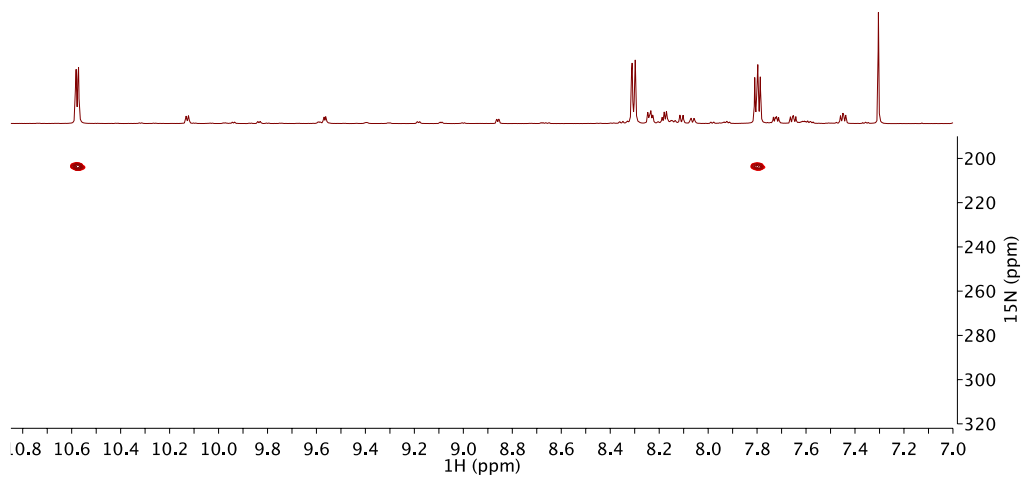
Figure A 13: ^{1}H-^{15}N HMBC spectrum of 1:2 DAF:Pd(OAc)$_2$ at -45 °C. ns = 16, ni = 256, d1 = 4 s, sw(f1) = 250 ppm, ^{1}J$_{NH}$ = 100 Hz and ^{n}J$_{NH}$ = 8 Hz. Cosine-squared window functions were applied in the f1 and f2 dimensions.

1 Equiv of DAF
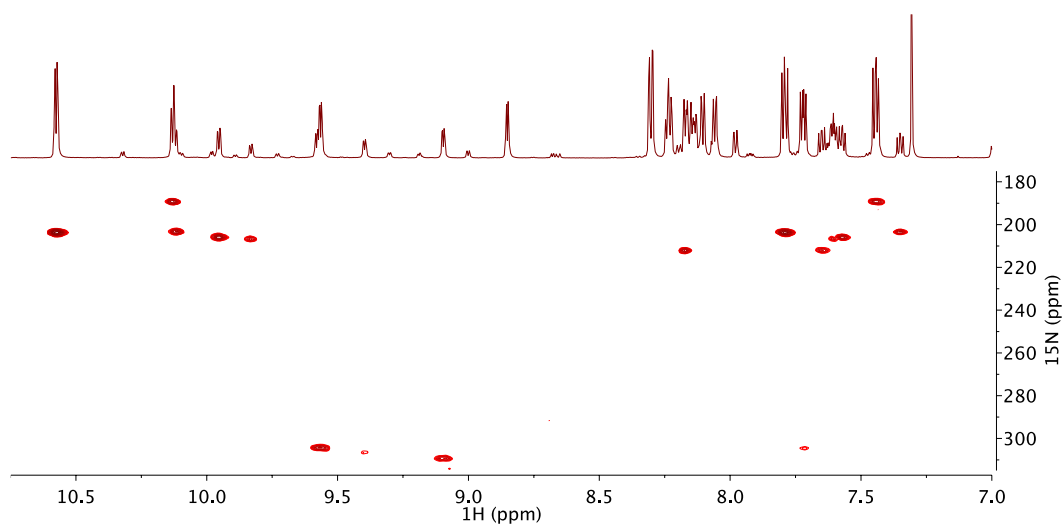
Figure A 14: ^{1}H-^{15}N HMBC spectrum of 1:1 DAF:Pd(OAc)$_2$ at -45 °C. ns = 32, ni = 256, d1 = 4 s, sw(f1) = 250 ppm, ^{1}J$_{NH}$ = 100 Hz and ^{n}J$_{NH}$ = 8 Hz. Cosine-squared window functions were applied in the f1 and f2 dimensions.

6 Equiv of DAF
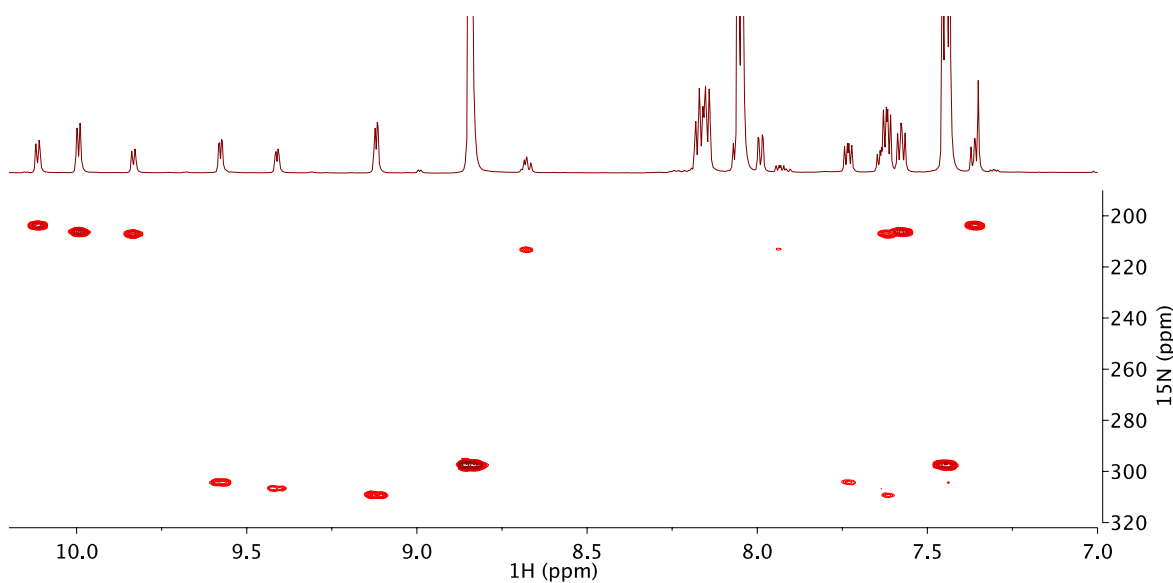
Figure A 15: ^{1}H-^{15}N HMBC spectrum of 6:1 DAF:Pd(OAc)$_2$ at -45 °C. ns = 32, ni = 256, d1 = 4 s, sw(f1) = 250 ppm, ^{1}J$_{NH}$ = 100 Hz and ^{n}J$_{NH}$ = 8 Hz. Cosine-squared window functions were applied in the f1 and f2 dimensions.

A3.7 Array of Temperature and 1D TOCSY Spectra of f$_{o/p}$ ^{2}
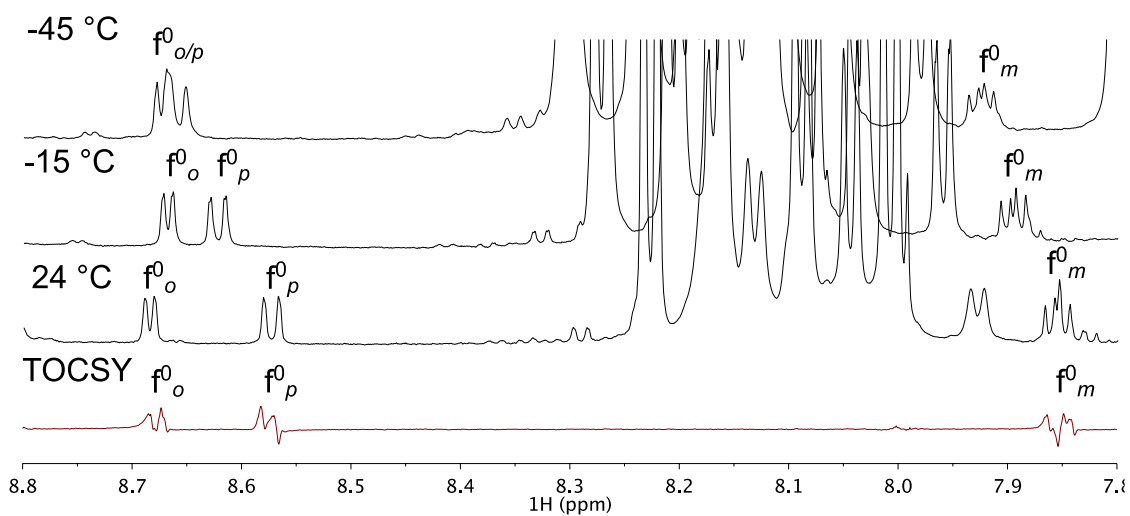
Figure A 16: ^{1}H 1D spectra at -45, -15 and 24 °C (top three spectra) and ^{1}H 1D TOCSY at 24 °C. ^{1}H 1D: ns = 16, ds = 2, d1 = 20 s; ^{1}H 1D TOCSY: ns = 8, ds = 4, d1 = 7 s, mix = 60 ms. The f^0_o proton was selected in the 1D TOCSY experiment.

A3.8 ^{1}H-^{13}C HSQC Spectrum of Species $f_{o/p}$ at -45 °C[2]

Complete ortho Proton Region
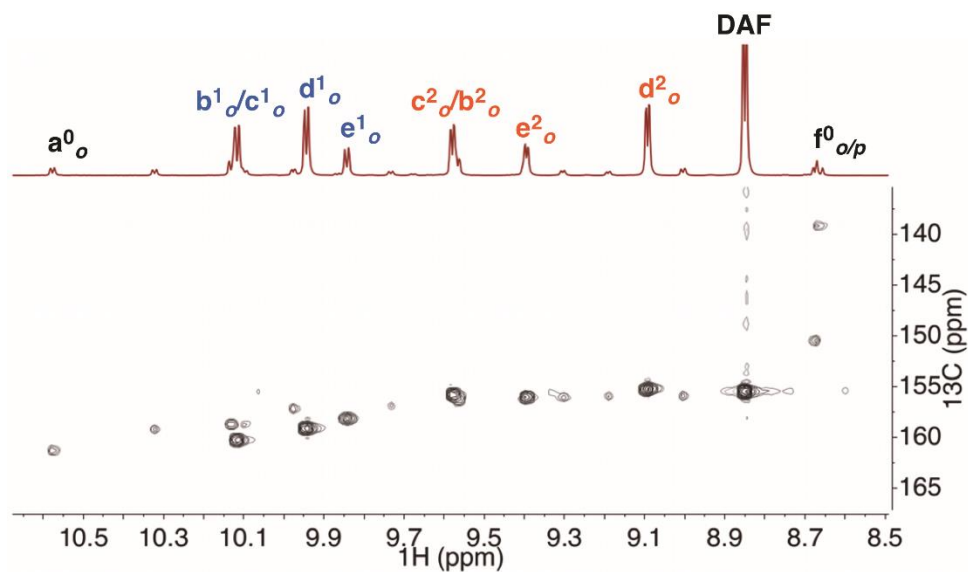
Figure A 17: ^{1}H-^{13}C HSQC spectrum of 2:1 DAF:Pd(OAc)$_2$ -45 °C. ns = 4, ni = 256, d1 = 3.57 s, dof = 100 ppm, sw(f1) = 200 ppm, ^{1}J$_{CH}$ = 170 Hz. Cosine-squared window functions were applied in both the f1 and f2 dimensions.

Zoom-In of $\mathbf{f_{o/p}}$ Region from S15
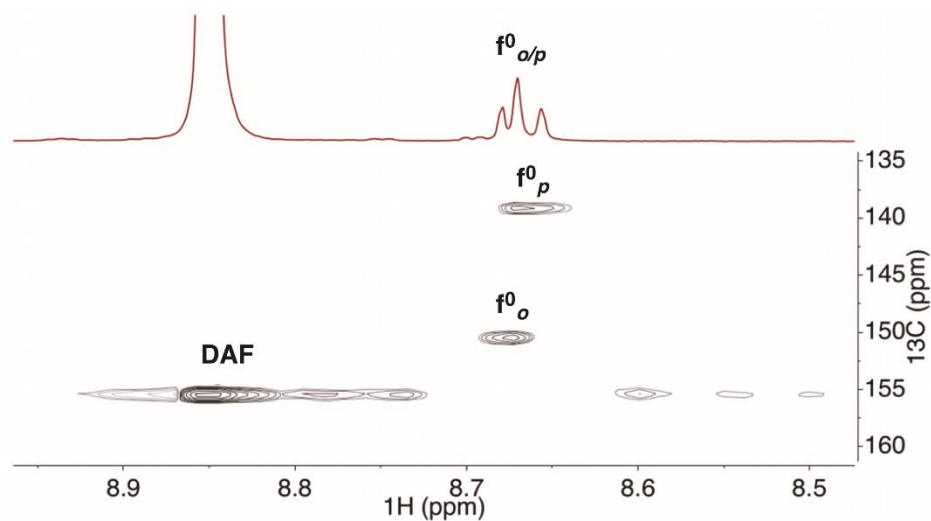
Figure A 18: Expansion of the ^{1}H-^{13}C HSQC spectrum in Fig. S18 of the $f_{o/p}$ region at -45 °C. The ^{1}H peak $f_{o/p}$ clearly consisted of two well-resolved ^{1}H and ^{13}C cross-peaks. The more downfield ^{1}H resonance of $f_{o/p}$ was assigned to f_o since the corresponding ^{13}C chemical shift was closer to the ^{13}C chemical shift of the ortho carbon of free DAF. The free DAF carbon exhibits t$_2$ noise along its carbon cross-peak.

A3.9 NMR Characterization Me$_2$DAF Ligated Pd(OAc)$_2$ Species G and H[3]
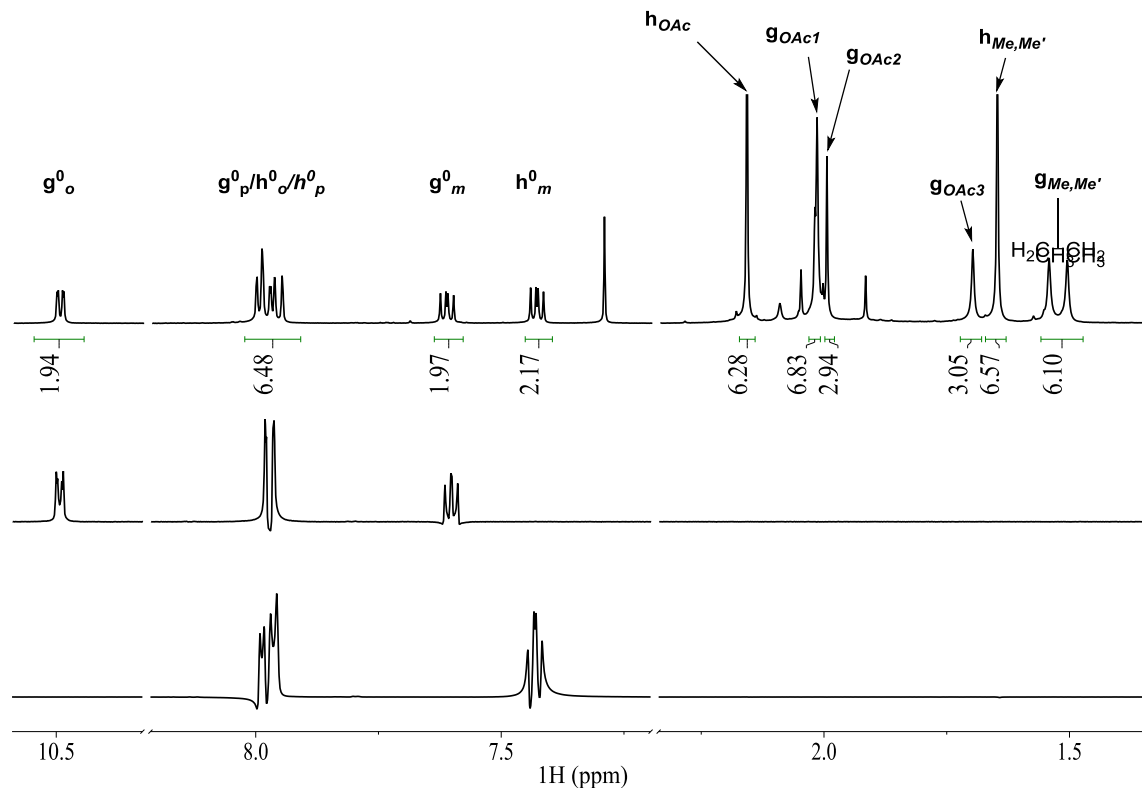
Figure A 19: Stacked plot of 1D ^{1}H spectrum (top) of 0.5:1 Me$_2$DAF:Pd(OAc)$_2$, and 1D ^{1}H TOCSY selected 10.50 ppm (middle) and 7.42 ppm (bottom). The ^{1}H 1D TOCSY spectrum selected at 10.50 ppm clearly illustrates a symmetrical DAF species for species G. The ^{1}H 1D TOCSY spectrum selected at 7.42 ppm shows all aromatic peaks belong to one symmetrical DAF species, species H, with the chemical shifts for h^0_o and h^0_p nearly overlapping. ^{1}H 1D TOCSY were acquired at 24 °C, ns = 8, d1 = 1 s, mix = 0.08 s.

---

[3] All data pertaining to Me$_2$DAF/Pd(OAc)$_2$ species was collected independently by JNJ
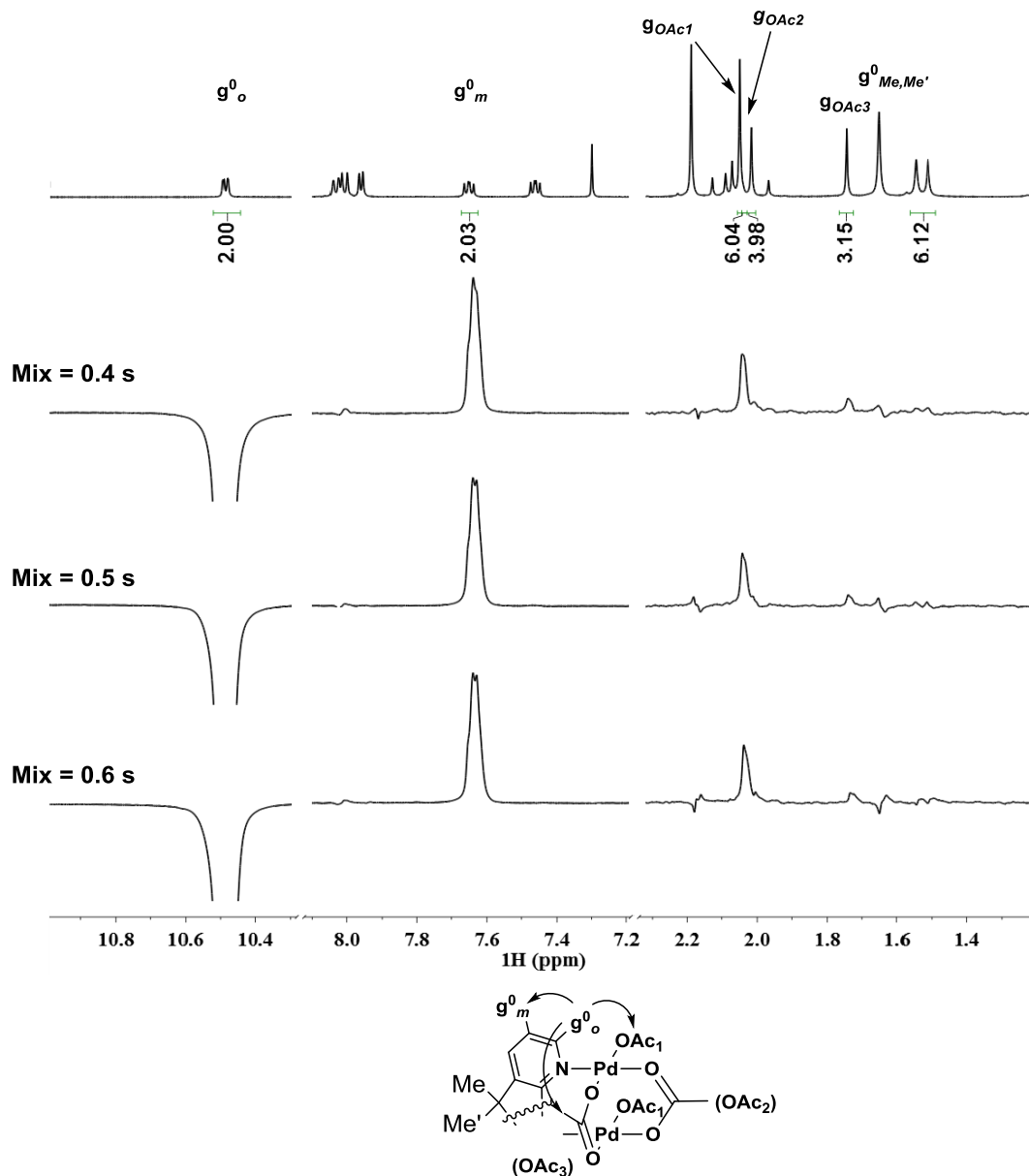
Figure A 20: Stacked 1D ROESY spectra with arrayed mix times for g^0_o at -45 °C. Through-space interactions are revealed between g^0_o and g^0_m, g_{OAc1}, g_{OAc3}. This provides insight into the orientation of the ligands. ns = 1024, d1 = 3 s, 2.78 kHz spinlock, mix = 0.4, 0.5, 0.6 s.
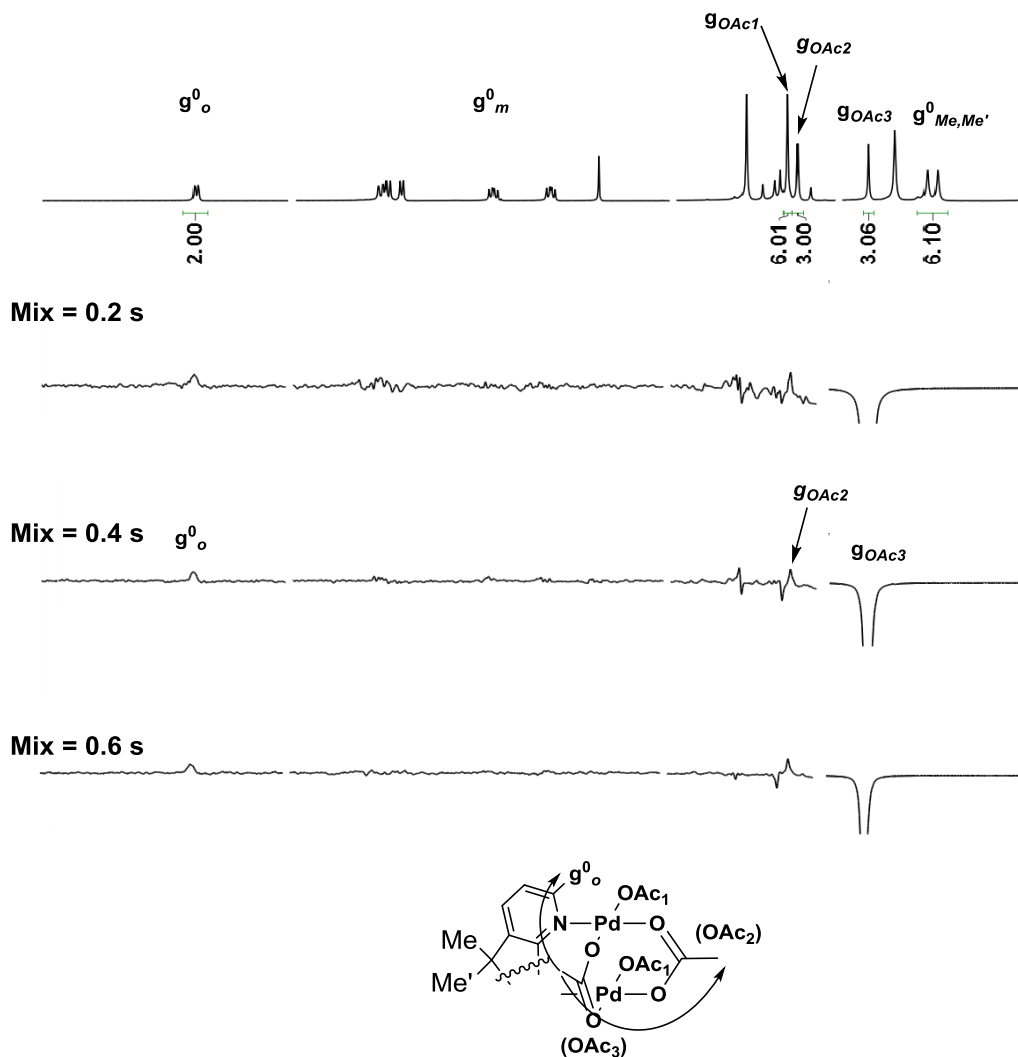
Figure A 21: Stacked 1D ROESY spectra with arrayed mix times of 0.2, 0.4 and 0.6 s (top to bottom) of g_{OAc3}. Through-space interactions are revealed between g_{OAc3} and g^0_o, g_{OAc2}. This provides insight into the orientation of the acetates. ns = 1024, d1 = 3 s, 2.78 kHz spinlock, mix = 0.2, 0.4, 0.6 s.
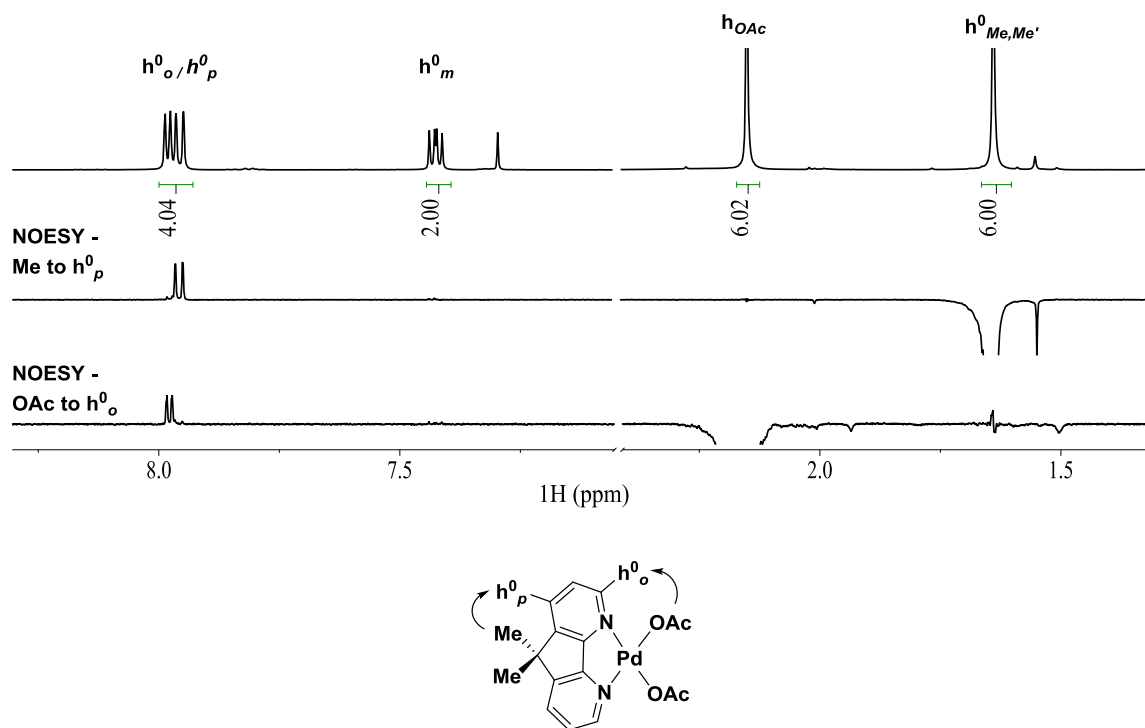
Figure A 22: Stacked plot of 1D ^{1}H spectrum (top) of 1:1 1:1 Me$_2$DAF:Pd(OAc)$_2$ and 1D ^{1}H NOESY spectra selected at from 1.65 ppm (middle) and NOESY from 2.14 ppm (bottom). Observed NOE from the peak at 2.14 ppm to h^0_o identifies that the peak is h$^0_{OAc}$ at 2.14. The NOE from 1.65 ppm to 7.95 ppm to h^0_p identifies the h$^0_{Me,Me'}$ peak for the symmetric gem-dimethyl group on the backbone of the ligand. ^{1}H-^{1}H 1D NOESY spectra 1:1 of Me$_2$DAF:Pd(OAc)$_2$ at 24 °C. ns = 64, d1 = 4 s, mix = 0.5 s.
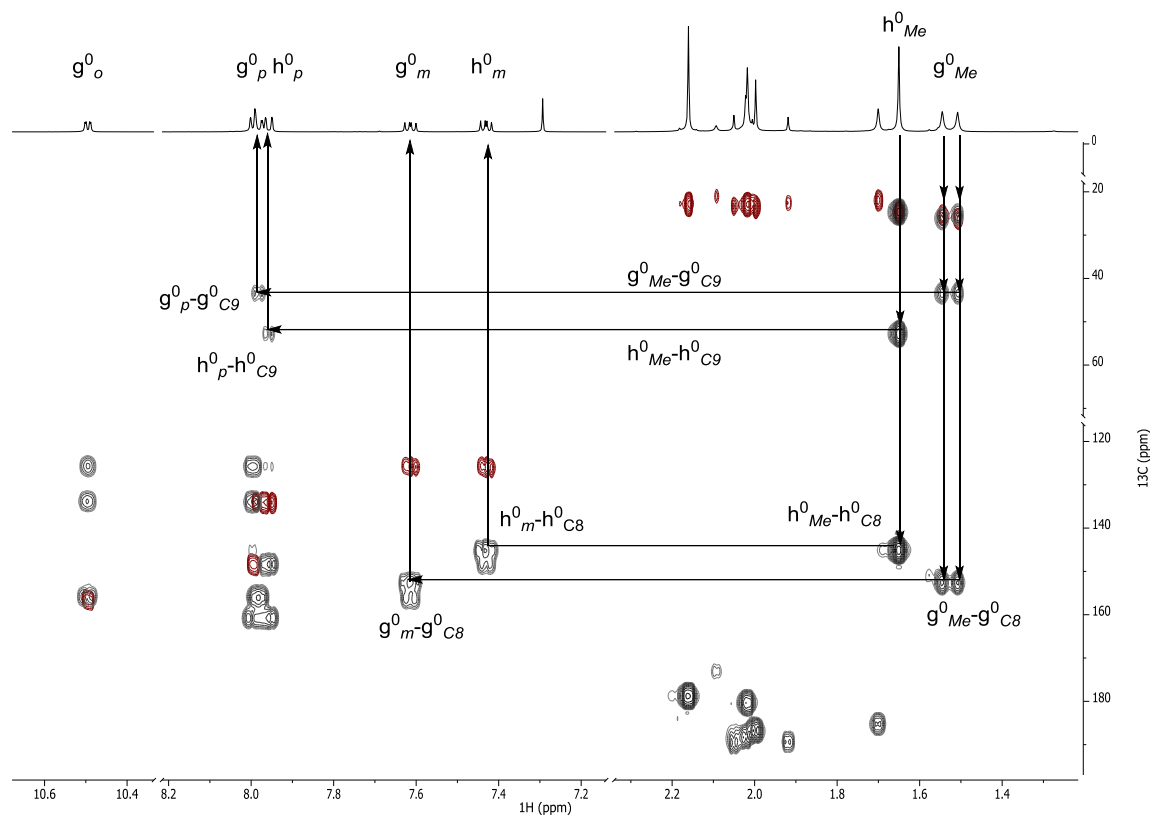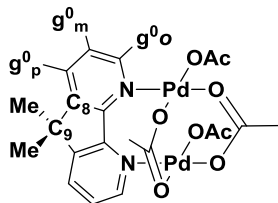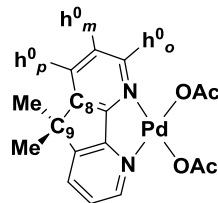
Figure A 23: Overlaid ^1H-^{13}C HSQC (red) and ^1H-^{13}C HMBC (grey) spectra of 0.5:1 Me$_2$DAF:Pd(OAc)$_2$ at 24 °C. 3-bond ^1H-^{13}C coupling shows methyl peaks at 1.54 and 1.51 ppm correspond to structure G by correlating the g^0_p to tertiary carbon g^0_{C9} and g^0_m to tertiary carbon g^0_{C8}. These two methyl groups are desymmetrized. 3-bond coupling from the peak at 1.65 ppm correlates h^0_p to h^0_{C9} and h^0_m to h^0_{C8}. HSQC: ns = 4, ni = 256, d1 = 4 s, sw(f1) = 200 ppm, $^1J_{CH}$ = 170 Hz. HMBC: ns = 8, ni = 256, sw(f1) = 210 ppm, $^1J_{CH}$ = 170 Hz. Cosine-bell window functions were applied in both the f1 and f2 dimensions.
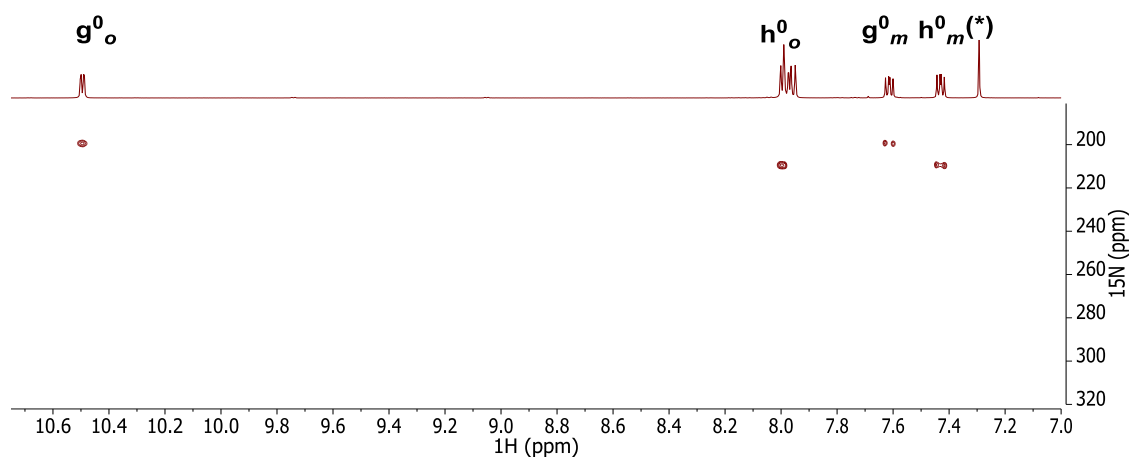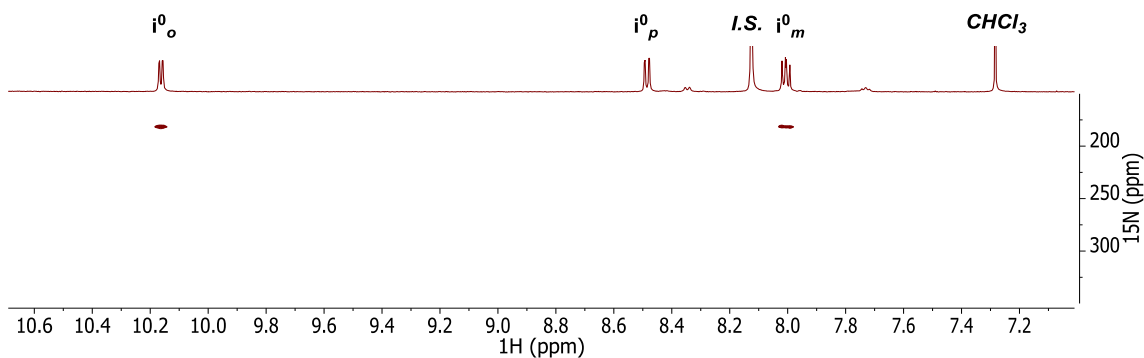
Figure A 24: ^{1}H-^{15}N HMBC spectrum of 0.5:1 Me$_2$DAF:Pd(OAc)$_2$ at 24 °C. Both species G and H are observed and have similar ^{15}N chemical shifts. ns = 16, ni = 128, d1 = 4 s, sw(f1) = 200 ppm, ^{1}J$_{NH}$ = 100 Hz and ^{n}J$_{NH}$ = 8 Hz. Cosine-squared window functions were applied in the f1 and f2 dimensions. (*) designates the CHCl$_3$ peak.

A3.10 NMR Characterization of DAF Ligated Pd(TFA)$_2$ Species I, J and K[4]
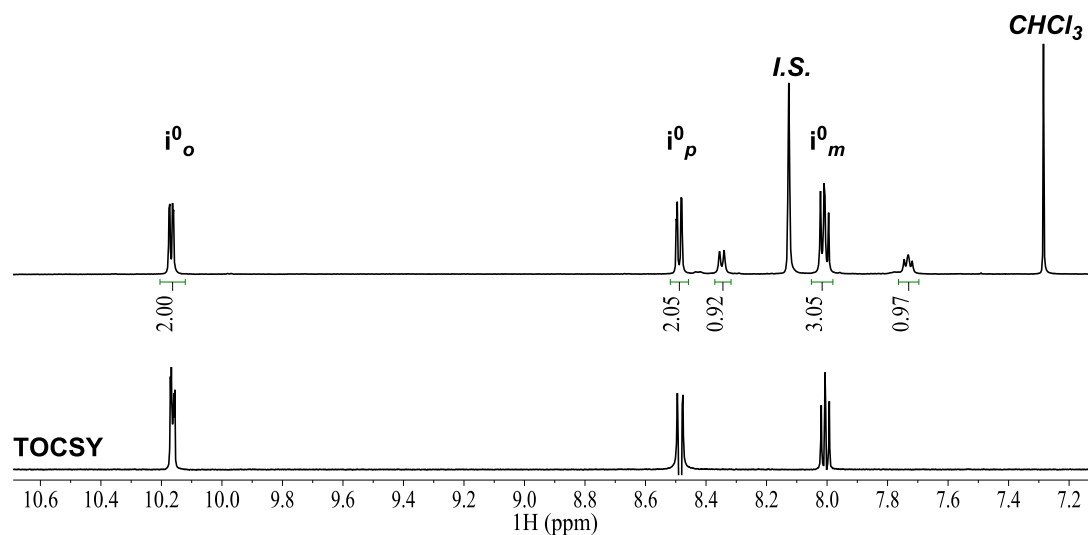
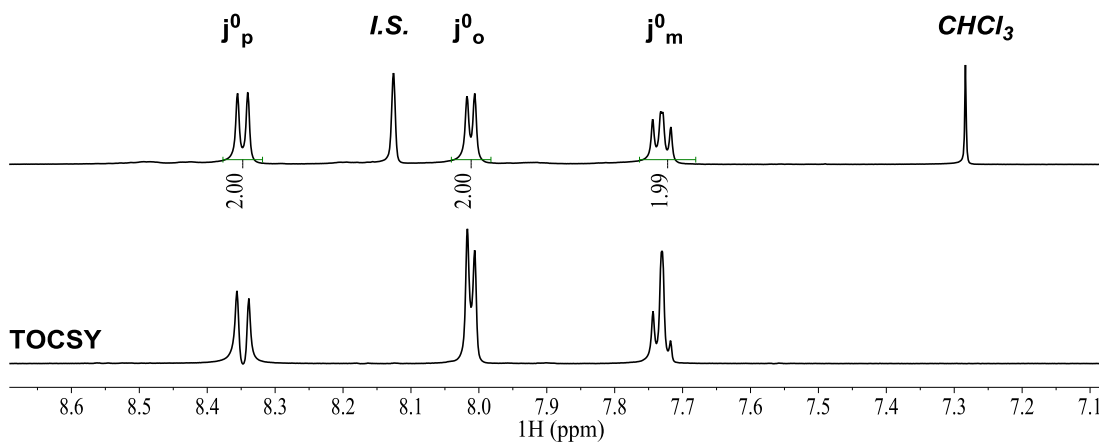**Figure A 25**: Stacked plot of ^{1}H 1D and TOCSY spectra of 0.5:1 DAF:Pd(TFA)$_2$ at 24 °C in a 6.58 M solution of TFAH in CDCl$_3$ (1:1 mixture of CDCl$_3$:TFAH). Irradiating peak at 8.01 ppm for TOCSY. Protons j^0_p and j^0_o are assigned based on ^{1}H-^{15}N HMBC (Figure A 26 below). Internal standard (I.S.) is 1,3,5-tris(trifluoromethyl)benzene. ^{1}H 1D TOCSY 24 °C with ns = 16, d1 = 3 s, mix = 0.06 s.


[4] All data pertaining to DAF/Pd(TFA)$_2$ species was independently obtained by JNJ

Figure A 26: ^{1}H-^{15}N HMBC spectrum of 0.25:1 DAF:Pd(OAc)$_2$ at 24 °C in a 6.58 M solution of TFAH in CDCl$_3$ (1:1 mixture of CDCl$_3$:TFAH). Internal standard (I.S.) is 1,3,5-tris(trifluoromethyl)benzene. ns = 32, ni = 256, d1 = 2 s, sw(f1) = 200 ppm, ^{1}J$_{NH}$ = 100 Hz and ^{n}J$_{NH}$ = 8 Hz. Cosine-squared window functions were applied in the f1 and f2 dimensions.

Figure A 27: Stacked plot of ^{1}H 1D and TOCSY spectra of 1:1 DAF:Pd(TFA)$_2$ at 24 °C in a 6.58 M solution of TFAH in CDCl$_3$ (1:1 mixture of CDCl$_3$:TFAH). Internal standard (I.S.) is 1,3,5-tris(trifluoromethyl)benzene. The selected peak was 8.01 ppm for for the 1D TOCSY. All protons j^0$_p$, j^0$_o$ and j^0$_m$ are assigned based on this data combined with the ^{1}H-^{15}N HMBC spectrum (Figure A 28 below). ^{1}H 1D TOCSY spectrum: ns = 16, d1 = 3 s, mix = 0.06 s.
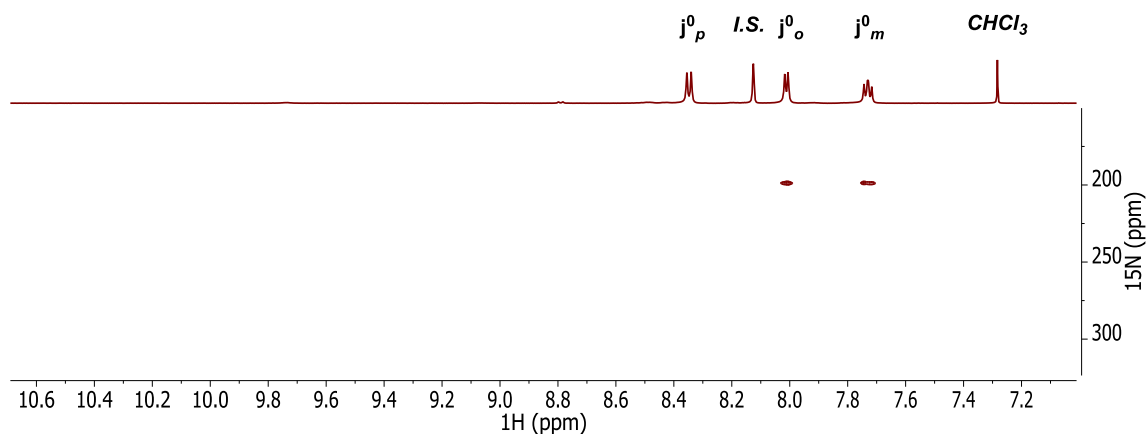
Figure A 28: ^{1}H-^{15}N HMBC spectrum of 1:1 DAF:Pd(TFA)$_2$ at 24 °C in a 6.58 M solution of TFAH in CDCl$_3$ (1:1 mixture of CDCl$_3$:TFAH). ns = 32, ni = 256, d1 = 2 s, sw(f1) = 200 ppm, ^{1}J$_{NH}$ = 100 Hz and ^{n}J$_{NH}$ = 8 Hz. Cosine-squared window functions were applied in the f1 and f2 dimensions.
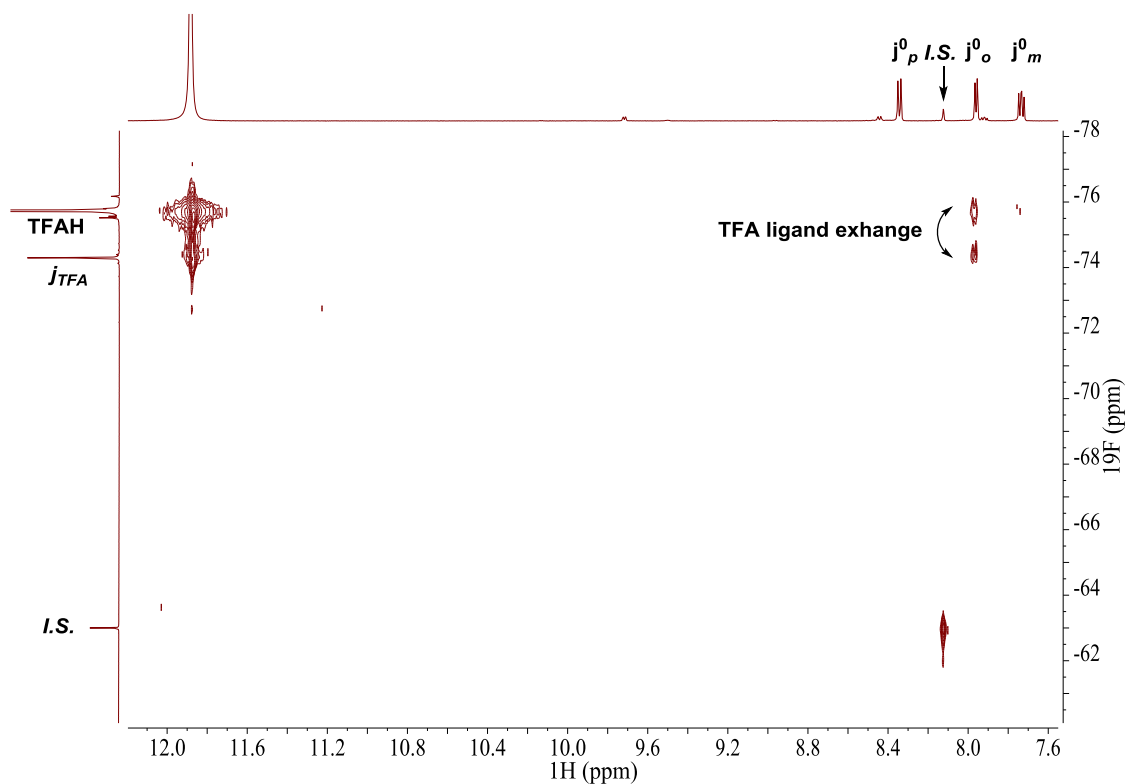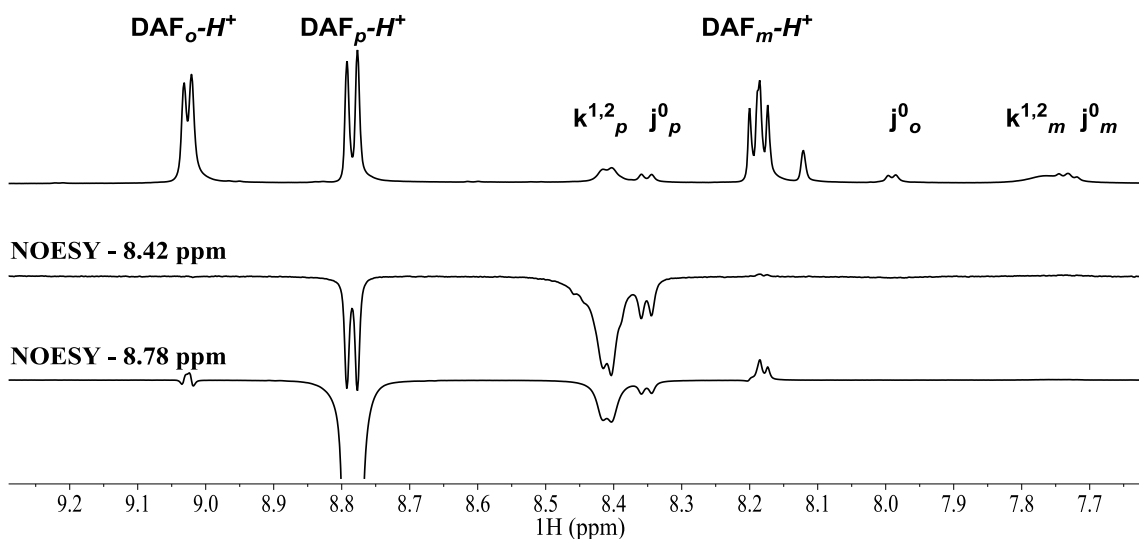

Figure A 29: ^{1}H-^{19}F 2D HOESY spectrum of 1:1 DAF:Pd(TFA)$_2$ at -20 °C in a 0.18 M solution of TFAH in CDCl$_3$.(1:1 mixture of CDCl$_3$:TFAH) ns = 16, ni = 128, d1 = 4 s, dof = -70 ppm, sw(f1) = 30.0 ppm, mix = 0.3 s. Cosine-squared window functions were applied in the f1 and f2 dimensions.

Figure A 30: Stacked plot of [1]H 1D and NOESY spectra of 6:1 DAF:Pd(TFA)$_2$ at 24 °C in a 6.58 M solution of TFAH in CDCl$_3$ (1:1 mixture of CDCl$_3$:TFAH). The K species grows in and becomes the dominant DAF ligated Pd species with stoichiometry of 2:1 DAF:Pd. [1]H 1D TOCSY of 6:1 DAF:Pd(TFA)$_2$ at 24 °C. ns = 64, d1 = 3 s, mix = 0.06 s.
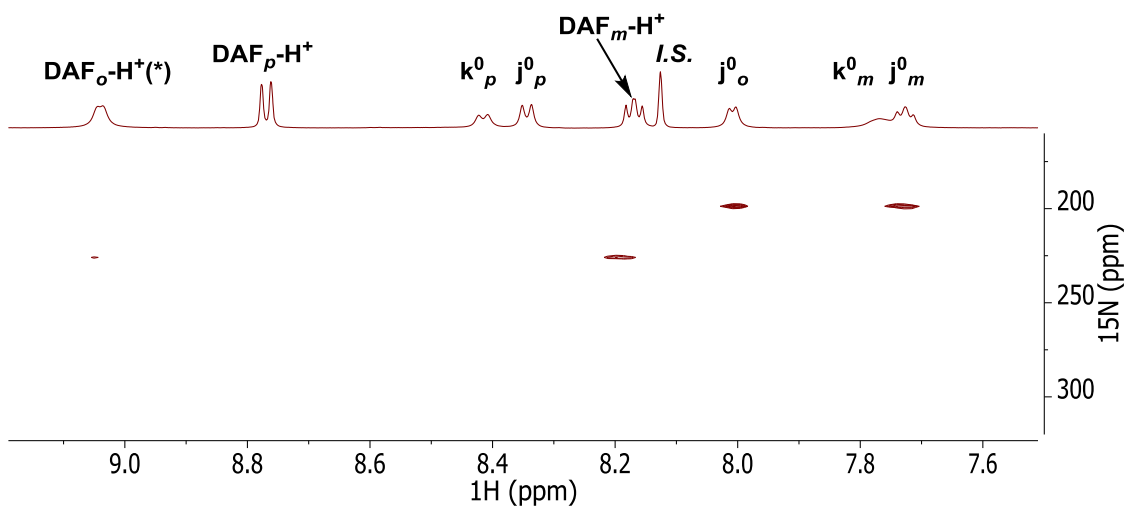
Figure A 31: ^{1}H-^{15}N HMBC spectrum of 2:1 DAF:Pd(TFA)$_2$ at 24 °C in a 6.58 M solution of TFAH in CDCl$_3$ (1:1 mixture of CDCl$_3$:TFAH). ns = 32, ni = 256, d1 = 2 s, sw(f1) = 200 ppm, $^1J_{NH}$ = 100 Hz and $^nJ_{NH}$ = 8 Hz. Cosine-squared window functions were applied in the f1 and f2 dimensions. The ^{15}N chemical shift of 225.9 ppm is consistent with protonated free ligand. No ^{15}N chemical shift is observed for species K.
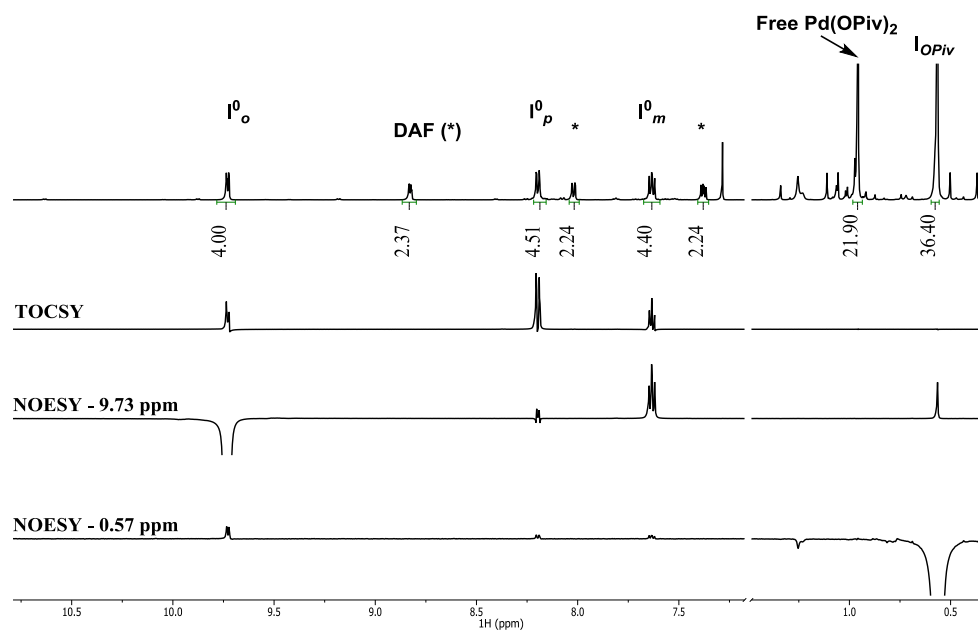
A3.11 NMR Characterization of Species L – DAF$_2$Pd$_2$(OPiv)$_4$ Species[5]

Figure A 32: Stacked plot of ^{1}H 1D, TOCSY, NOESY spectra of 1:1 DAF:Pd(OPiv)$_2$ at 24 °C in a 40 mM solution of CDCl$_3$. The L species grows in and dominants the spectra. Samples were equilibrated for five days. ^{1}H 1D TOCSY selected at 9.73 ppm: ns = 16, d1 = 1 s, 8.9 kHz spinlock, mix = 0.09 s. ^{1}H 1D NOESY ns = 800, d1 = 3s, mix = 0.50s.
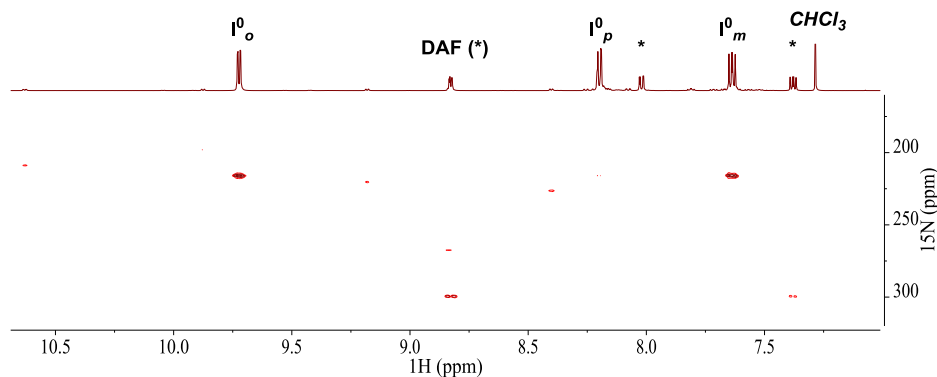
Figure A 33: ^{1}H-^{15}N HMBC spectrum of a 1:1 DAF:Pd(OPiv)$_2$ sample at 24 °C equilibrated for 5 days. Dimeric species L dominants the spectrum and gives a bound ^{15}N chemical shift at 216.3 ppm, but other species are present in small amounts in addition to free ligand. ns = 32, ni = 256, d1 = 4 s, sw(f1) = 200 ppm, ^{1}J$_{NH}$ = 100 Hz and ^{n}J$_{NH}$ = 8 Hz. Cosine-squared window functions were applied in the f1 and f2 dimensions.

---

[5] All data pertaining to DAF/Pd(OPiv)$_2$ speciation was collected by JNJ

Table S1 – Summary of DAF Pd(II) data

	Complex	N-N Distance	*a* Angle (°)	Pd-Pd Distance	Pd-N Distance	^{15}N d (ppm)
k²	DAF/Pd(TFA)$_2$ - **J**	2.760	60.1	2.049	2.049	197.2
	Me$_2$DAF/Pd(OAc)$_2$ - **H**	2.778	61.3	2.064	2.064	209.6
	DAF-PdCl$_2$[a]	2.783	61.1	2.085	2.085	--
	DAF Ligand[b]	**3.063**	**72.5**	--	--	299.4
	Me$_2$DAF Ligand[c]	**3.067**	**73.0**	--	--	298.6
m	DAF/Pd$_2$(OAc)$_4$	3.301	83.3	2.730	1.999	203.7
	Me$_2$DAF/Pd$_2$(OAc)$_4$ - **G**	3.291	83.4	2.726	2.001	199.4
	DAF/Pd$_2$(TFA)$_4$ - **I**	3.324	84.6	2.754	1.989	198.7
	DAF$_2$Pd$_2$(OPiv)$_4$ - **L**	3.235	81.0	2.803	2.027	214.4
	DAF$_2$Pd$_2$(BzF$_5$)$_2$ - **M**	3.237	81.4	2.779	2.023	--
k¹	DAF$_2$Pd$_2$(OAc)$_2$ - **B**	3.112	75.1	2.983	1.987	189.3/304.6
	DAF$_2$Pd(OAc)$_2$ - **E**	3.097	74.4	--	2.015	207.1/306.7

[a] Xu, Z.-G.; Liu, H.-Y.; Zhan, Q.-G.; Chen, J.; Xu, M.-J., Acta Crystallogr., Sec. E 2009, 65, m1166
[b] Fun, H.-K.; Sivakumar, K.; Zhu, D.-R.; You, X.-Z. *Acta Cryst.* 1995, C51, 2076-2078
[c] see supporting information below for Me2DAF

Table A 2: Summary of DAF Pd^{II} Species Data. Species A-F chemical shifts reported at -45 °C. Species G-L reported at 24 °C.

A4. X-ray Crystal Data for G, H, I, J, L, M, and Free Me$_2$DAF

All data this this section was obtained by crystals grown by JNJ and the data was obtained and analyzed by

Brian Dolinar or Dr. Ilia Guzei.

A4.1 X-ray Structure of (μ-Me$_2$DAF)Pd$_2$(OAc)$_4$, Structure G

An orange-red crystal with approximate dimensions 0.166 x 0.119 x 0.067 mm^3 was selected under oil under ambient conditions and attached to the tip of a MiTeGen MicroMount©. The crystal was mounted in a stream of cold nitrogen at 100(1) K and centered in the X-ray beam by using a video camera.

The crystal evaluation and data collection were performed on a Bruker Quazar SMART APEXII diffractometer with Mo K$_\alpha$ (λ = 0.71073 Å) radiation and the diffractometer to crystal distance of 4.96 cm.

The initial cell constants were obtained from three series of ω scans at different starting angles. Each series consisted of 12 frames collected at intervals of 0.5° in a 6° range about ω with the exposure time of 10 seconds per frame. The reflections were successfully indexed by an automated indexing routine built in the APEXII program suite. The final cell constants were calculated from a set of 9800 strong reflections from the actual data collection.

The data were collected by using the full sphere data collection routine to survey the reciprocal space to the extent of a full sphere to a resolution of 0.70 Å. A total of 75418 data were harvested by collecting 6 sets of frames with 0.5° scans in ω and φ with exposure times of 20 sec per frame. These highly redundant datasets were corrected for Lorentz and polarization effects. The absorption correction was based on fitting a function to the empirical transmission surface as sampled by multiple equivalent measurements.[8]

Structure Solution and Refinement for G

The systematic absences in the diffraction data were uniquely consistent for the space group $P2_1/n$ hat yielded chemically reasonable and computationally stable results of refinement.[9,10,11]

A successful solution by the direct methods provided most non-hydrogen atoms from the *E*-map. The remaining non-hydrogen atoms were located in an alternating series of least-squares cycles and difference Fourier maps. All non-hydrogen atoms except for those of chloroform molecules C23B and C23C were refined with anisotropic displacement coefficients. All hydrogen atoms were included in the structure factor calculation at idealized positions and were allowed to ride on the neighboring atoms with relative isotropic displacement coefficients.

The asymmetric unit contains one molecule of the dipalladium complex shown in Figure 1 and 1.87 molecules of chloroform. Acetate ligand O7 of the dipalladium compound is disordered over two positions (major component: 55(3)%). Thermal parameter restraints and constraints were used in order to obtain a chemically reasonable and computationally stable refinement.

The chloroform molecules occupy two positions within the asymmetric unit. Chloroform molecule C22 is fully occupied and has two disordered components (major component: 58(3)%). Chloroform molecule C23 is partially occupied and has four disordered components (occupancies: 55.8(4)%, 20.8(2)%, 7.3(3)%, 3.07(16)%). Bond distance restraints and constraints as well as thermal parameter restraints and constraints were used on the disordered chloroform molecules in order to obtain a chemically reasonable and computationally stable refinement.

The final least-squares refinement of 492 parameters against 7433 data resulted in residuals R (based on F^2 for $I \geq 2\sigma$) and wR (based on F^2 for all data) of 0.0197 and 0.0495, respectively. The final difference Fourier map was featureless.

Summary Crystal Data for C$_{21}$H$_{24}$N$_2$O$_8$Pd$_2$,1.87CHCl$_3$ (M =868.24): monoclinic, space group P2$_1$/n (no. 14), a = 11.337(4) Å, b = 20.912(8) Å, c = 13.689(5) Å, β = 97.432(16)°, V = 3218(2) Å^3, Z = 4, T = 100.0 K, μ(Mo Kα) = 1.628 mm^{-1}, *Dcalc* = 1.792 g/mm^3, 75418 reflections measured (3.578 $\leq$ 2Θ $\leq$ 55.132), 7433 unique (R_{int} = 0.0402) which were used in all calculations. The final R_1 was 0.0197 (I > 2σ(I)) and wR_2 was 0.0495 (all data).
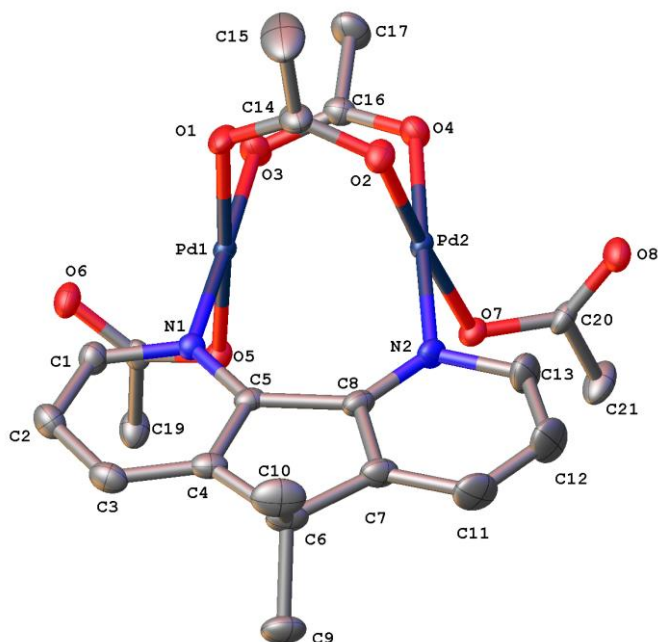
Figure A 34: The palladium complex of G. All atoms are drawn as 50% thermal ellipsoids. All disordered parts and H atoms are omitted for clarity.
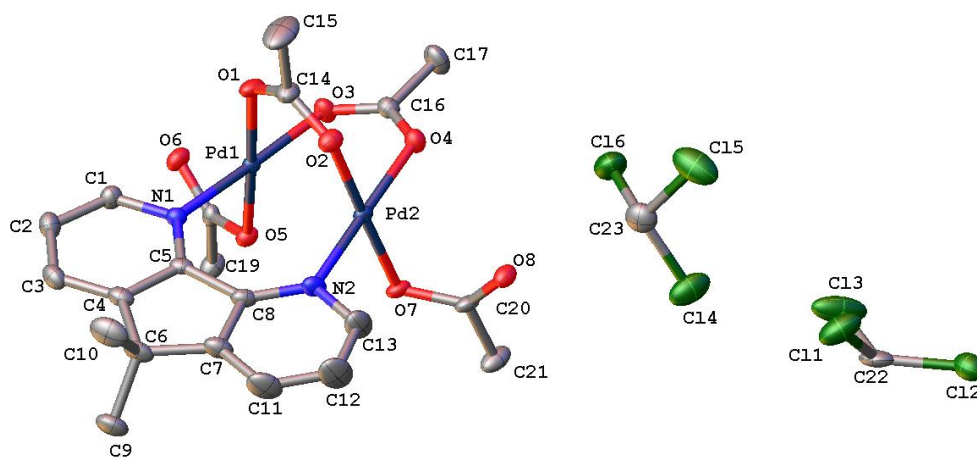
Figure A 35: The asymmetric unit of G. All atoms are drawn as 50% thermal ellipsoids. All disordered parts and H atoms are omitted for clarity. Chloroform molecule C23 is partially occupied (87%).
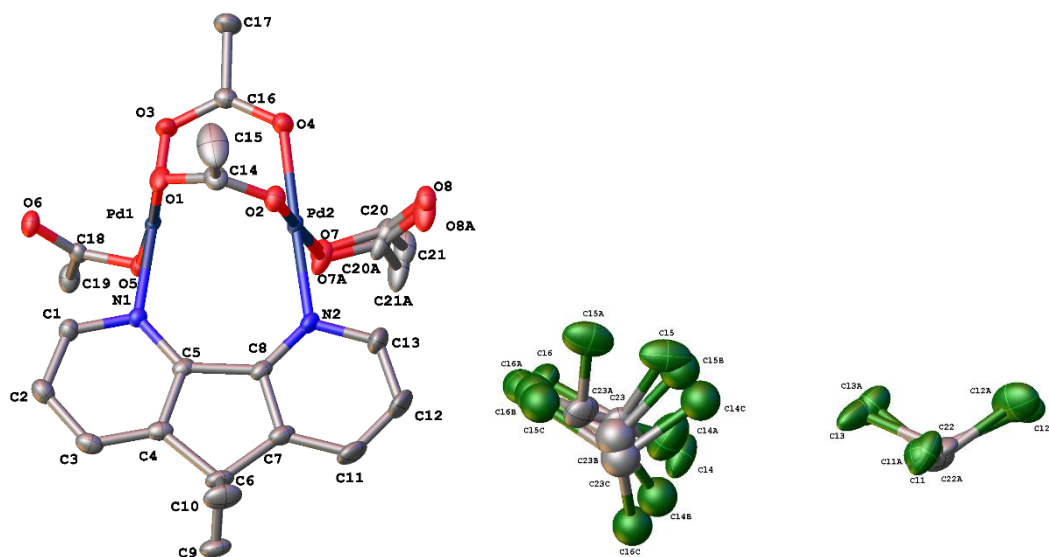
Figure A 36: The asymmetric unit of G including all disordered parts. All atoms are drawn with 50% probability ellipsoids. All H atoms are omitted for clarity.

Table A 3: Crystal data and structure refinement for G

Identification code	Stahl191
Empirical formula	$C_{21}H_{24}N_2O_8Pd_2$, 1.87$CHCl_3$
Formula weight	868.24
Temperature/K	100(1)
Crystal system	monoclinic
Space group	$P2_1/n$
a/Å	11.337(4)
b/Å	20.912(8)
c/Å	13.689(5)
α/°	90
β/°	97.432(16)
γ/°	90
Volume/Å^3	3218(2)
Z	4
ρ_{calc}mg/mm^3	1.792
m/mm^{-1}	1.628
F(000)	1713.0
Crystal size/mm^3	$0.166 \times 0.119 \times 0.067$
Radiation	Mo Kα (λ = 0.71073)
2Θ range for data collection	3.578 to 55.132°
Index ranges	$-14 \leq h \leq 14$, $-27 \leq k \leq 27$, $-17 \leq l \leq 17$
Reflections collected	75418
Independent reflections	7433[R(int) = 0.0402]
Data/restraints/parameters	7433/132/492
Goodness-of-fit on F^2	1.071
Final R indexes [I>=2σ (I)]	R_1 = 0.0197, wR_2 = 0.0477
Final R indexes [all data]	R_1 = 0.0226, wR_2 = 0.0495
Largest diff. peak/hole / e Å^{-3}	0.72/-0.54

A4.2 X-ray Structure of (κ^2-Me$_2$DAF)Pd(OAc)$_2$, Structure H

A yellow crystal with approximate dimensions 0.356 x 0.176 x 0.106 mm^3 was selected under oil under ambient conditions and attached to the tip of a MiTeGen MicroMount©. The crystal was mounted in a stream of cold nitrogen at 100(1) K and centered in the X-ray beam by using a video camera.

The crystal evaluation and data collection were performed on a Bruker SMART APEXII diffractometer with Cu K$_\alpha$ (λ = 1.54178 Å) radiation and the diffractometer to crystal distance of 4.03 cm.

The initial cell constants were obtained from three series of ω scans at different starting angles. Each series consisted of 41 frames collected at intervals of 0.6° in a 25° range about ω with the exposure time of 10 seconds per frame. The reflections were successfully indexed by an automated indexing routine built in the APEXII program. The final cell constants were calculated from a set of 9802 strong reflections from the actual data collection.

The data were collected by using the full sphere data collection routine to survey the reciprocal space to the extent of a full sphere to a resolution of 0.82 Å. A total of 34816 data were harvested by collecting 16 sets of frames with 0.65° scans in ω and φ with an exposure time 15-30 sec per frame. These highly redundant datasets were corrected for Lorentz and polarization effects. The absorption correction was based on fitting a function to the empirical transmission surface as sampled by multiple equivalent measurements.[8]

Structure Solution and Refinement for H

The systematic absences in the diffraction data were uniquely consistent for the space group $P2_1/n$ that yielded chemically reasonable and computationally stable results of refinement.[9,10,11]

A successful solution by the direct methods provided most non-hydrogen atoms from the *E*-map. The remaining non-hydrogen atoms were located in an alternating series of least-squares cycles and difference Fourier maps. All non-hydrogen atoms were refined with anisotropic displacement coefficients. All hydrogen atoms were included in the structure factor calculation at idealized positions and were allowed to ride on the neighboring atoms with relative isotropic displacement coefficients.

The asymmetric unit contains one molecule of the palladium complex shown in Figure 1 and 1.47 molecules of chloroform. Acetate ligand O3 of the palladium complex is disordered over two positions (major component: 57(4)%). Bond distance and thermal parameter restraints were used on the disordered acetate to ensure a chemically reasonable and computationally stable refinement.

The chloroform molecules occupy two positions within the asymmetric unit. Chloroform molecule C18 is fully occupied and has disordered components (major component: 53.0(2)%). Chloroform molecule C19 is partially occupied (47.2(2)%) and is disordered over a crystallographic inversion center. Bond distance restraints were used on the disordered chloroform molecules in order to obtain a chemically reasonable and computationally stable refinement.

The final least-squares refinement of 369 parameters against 4400 data resulted in residuals *R* (based on F^2 for $I \geq 2\sigma$) and *wR* (based on F^2 for all data) of 0.0247 and 0.0724, respectively.

Summary Crystal Data for C$_{17}$H$_{18}$N$_2$O$_4$Pd 1.47CHCl$_3$ (*M* =596.65): monoclinic, space group $P2_1/n$ (no. 14), a = 10.376(3) Å, b = 12.988(2) Å, c = 17.735(3) Å, β = 101.520(14)°, V = 2341.8(8) Å^3, Z = 4, T = 100.0 K, μ(Cu Kα) = 11.278 mm^{-1}, *Dcalc* = 1.692 g/mm^3, 34816 reflections measured (8.5 ≤ 2Θ ≤ 140.108), 4400 unique (R_{int} = 0.0219) which were used in all calculations. The final R_1 was 0.0247 (I > 2σ(I)) and wR_2 was 0.0724 (all data).
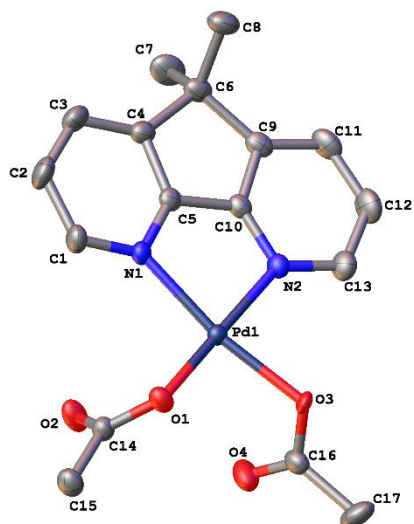
Figure A 37: The palladium complex of H. All atoms are drawn as 50% thermal probability ellipsoids. All H atoms and disordered components are omitted for clarity.
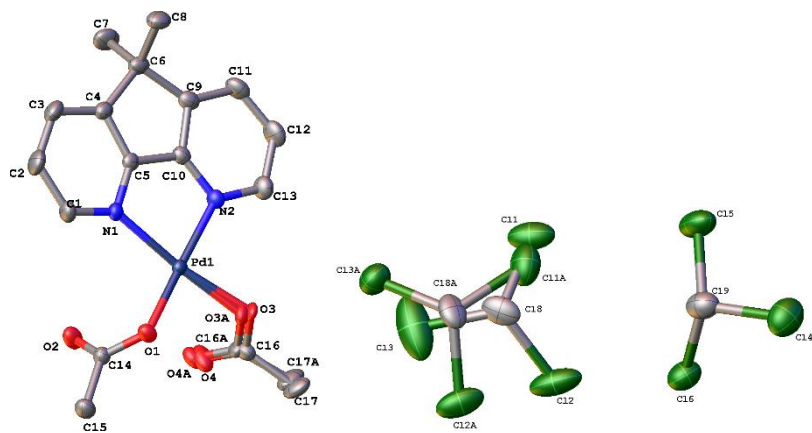
Figure A 38: The asymmetric unit of H showing all disordered parts. All atoms are drawn as 50% thermal probability ellipsoids. All H atoms are omitted for clarity. Chloroform molecule C19 is partially occupied (47.2(2)%).

Table A 4: Crystal data and structure refinement for H

Identification code	Stahl190
Empirical formula	$C_{17}H_{18}N_2O_4Pd$, $1.47CHCl_3$
Formula weight	596.65
Temperature/K	100(1)
Crystal system	monoclinic
Space group	$P2_1/n$
a/Å	10.376(3)
b/Å	12.988(2)
c/Å	17.735(3)
α/°	90
β/°	101.520(14)
γ/°	90
Volume/Å^3	2341.8(8)
Z	4
ρ_{calc} mg/mm^3	1.692
μ/mm^{-1}	11.278
F(000)	1190.0
Crystal size/mm^3	$0.356 \times 0.176 \times 0.106$
Radiation	Cu Kα (λ = 1.54178)
2Θ range for data collection	8.5 to 140.108°
Index ranges	$-12 \leq h \leq 12$, $-15 \leq k \leq 15$, $-21 \leq l \leq 21$
Reflections collected	34816
Independent reflections	4400[R(int) = 0.0219]
Data/restraints/parameters	4400/138/369
Goodness-of-fit on F^2	1.176
Final R indexes [I>=2σ (I)]	$R_1 = 0.0247$, $wR_2 = 0.0719$
Final R indexes [all data]	$R_1 = 0.0253$, $wR_2 = 0.0723$
Largest diff. peak/hole / e Å^{-3}	1.02/-0.38

A4.3 X-ray Structure of (μ-DAF)Pd$_2$(TFA)$_4$, Structure I

A red-orange crystal with approximate dimensions 0.2 x 0.1 x 0.1 mm^3 was selected under oil under ambient conditions and attached to the tip of a MiTeGen MicroMount©. The crystal was mounted in a stream of cold nitrogen at 200(1) K and centered in the X-ray beam by using a video camera.

The crystal evaluation and data collection were performed on a Bruker SMART APEXII diffractometer with Cu K$_\alpha$ (λ = 1.54178 Å) radiation and the diffractometer to crystal distance of 4.03 cm.

The initial cell constants were obtained from three series of ω scans at different starting angles. Each series consisted of 41 frames collected at intervals of 0.6° in a 25° range about ω with the exposure time of 10 seconds per frame. The reflections were successfully indexed by an automated indexing routine built in the APEXII program. The final cell constants were calculated from a set of 9893 strong reflections from the actual data collection.

The data were collected by using the full sphere data collection routine to survey the reciprocal space to the extent of a full sphere to a resolution of 0.82 Å. A total of 56440 data were harvested by collecting 15 sets of frames with 0.5° scans in ω and φ with an exposure time 10-20 sec per frame. These highly redundant datasets were corrected for Lorentz and polarization effects. The absorption correction was based on fitting a function to the empirical transmission surface as sampled by multiple equivalent measurements.[8]

Structure Solution and Refinement

The systematic absences in the diffraction data were uniquely consistent for the space group *P*2$_1$/*n* that yielded chemically reasonable and computationally stable results of refinement.[9,10,12]

A successful solution by the direct methods provided most non-hydrogen atoms from the *E*-map. The remaining non-hydrogen atoms were located in an alternating series of least-squares cycles and difference Fourier maps. All non-hydrogen atoms (except the minor component of the disordered trifluoroacetic acid C3sa) were refined with anisotropic displacement coefficients. All hydrogen atoms were included in the structure factor calculation at idealized positions and were allowed to ride on the neighboring atoms with relative isotropic displacement coefficients.

The asymmetric unit consists of one molecule of the dipalladium complex shown in (Figure A 39) as well as two molecules of trifluoroacetic acid. All CF$_3$ groups exhibit positional disorder as follows.

CF$_3$ groups F1 (3 components, occupancies: 57.2(3)%, 32.3(3)%, 10.5(3)%), F4 (2 components, major component: 56.4(14)%), F7 (2 components, major component: 60.2(10)%) and F10 (3 components, occupancies: 59.3(3)%, 21.4(3)%, 129.3(3)%) of the trifluoroacetate ligands on the dipalladium complex exhibit positional disorder. Bond distance restraints and constraints as well as thermal parameter restraints were used to facilitate a chemically reasonable and computationally stable refinement.

Trifluoroacetic acid molecules F1SA (major component: 72.0(6)%) and F4SA (major component: 60.3(8)%) exhibit positional disorder and were modeled with an idealized geometry. Thermal parameter restraints and geometrical restraints were used to achieve a chemically reasonable and computationally stable refinement.

The final least-squares refinement of 774 parameters against 6565 data resulted in residuals *R* (based on *F*^{2} for *I*≥2σ) and *wR* (based on *F*^{2} for all data) of 0.0360 and 0.1030, respectively.

Summary Crystal Data for C$_{23}$H$_8$F$_{18}$N$_2$O$_{13}$Pd$_2$ (*M* =1075.11 g/mol): monoclinic, space group P2$_1$/n (no. 14), *a* = 14.8547(16) Å, *b* = 16.258(3) Å, *c* = 15.2201(13) Å, *β* = 115.105(6)°, *V* = 3328.5(7) Å^3, *Z* = 4, *T* = 200 K, μ(CuKα) = 10.303 mm^{-1}, *Dcalc* = 2.145 g/cm^3, 56440 reflections measured (6.968° ≤ 2Θ ≤ 146.52°), 6565 unique (*R*$_{int}$ = 0.0380, R$_{sigma}$ = 0.0189) which were used in all calculations. The final *R*$_1$ was 0.0360 (I > 2σ(I)) and *wR*$_2$ was 0.1030 (all data).
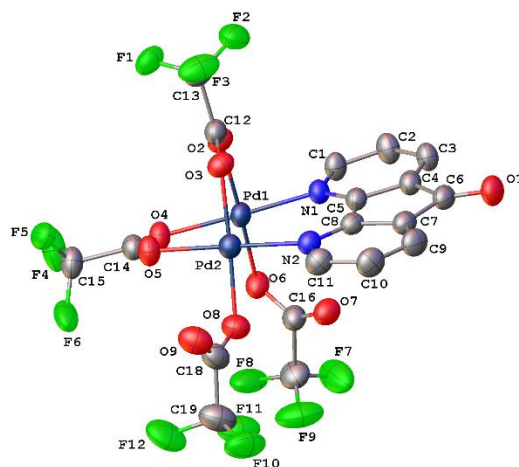
Figure A 39: A molecular drawing of the dipalladium complex of I shown with 50% probability ellipsoids. All H atoms and disordered components are omitted for clarity.
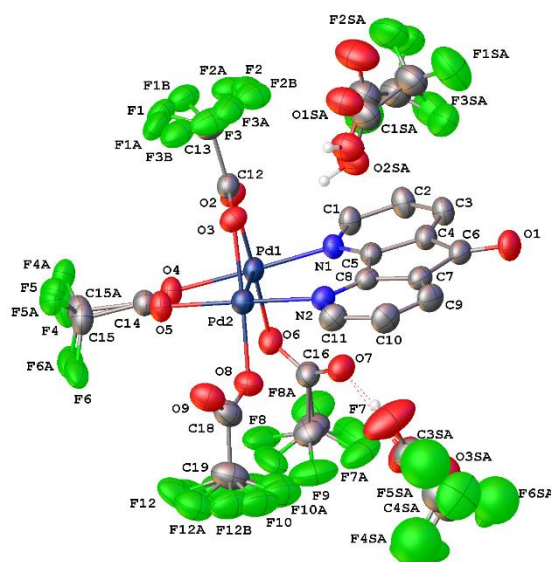
Figure A 40: The asymmetric unit of I including all disordered components. All atoms are drawn as 50% thermal probability ellipsoids. All H atoms except those on heteroatoms are omitted for clarity

Table A 5: Crystal data and structure refinement for Structure I.

Identification code	Stahl201
Empirical formula	$C_{23}H_8F_{18}N_2O_{13}Pd_2$
Formula weight	1075.11
Temperature/K	200
Crystal system	monoclinic
Space group	$P2_1/n$
a/Å	14.8547(16)
b/Å	16.258(3)
c/Å	15.2201(13)
$\alpha/°$	90
$\beta/°$	115.105(6)
$\gamma/°$	90
Volume/Å^3	3328.5(7)
Z	4
ρ_{calc}g/cm^3	2.145
μ/mm^{-1}	10.303
F(000)	2072.0
Crystal size/mm^3	$0.3 \times 0.1 \times 0.1$
Radiation	CuKα ($\lambda = 1.54178$)
2Θ range for data collection/°	6.968 to 146.52
Index ranges	$-18 \leq h \leq 18$, $-17 \leq k \leq 19$, $-17 \leq l \leq 18$
Reflections collected	56440
Independent reflections	6565 [$R_{int} = 0.0380$, $R_{sigma} = 0.0189$]
Data/restraints/parameters	6565/935/774
Goodness-of-fit on F^2	1.021
Final R indexes [I>=2σ (I)]	$R_1 = 0.0360$, $wR_2 = 0.0972$
Final R indexes [all data]	$R_1 = 0.0429$, $wR_2 = 0.1030$
Largest diff. peak/hole / e Å^{-3}	1.21/-0.57

A4.4 X-ray Structure of (κ^2-DAF)Pd(TFA)$_2$, Structure J

A yellow crystal with approximate dimensions 0.325 x 0.311 x 0.162 mm^3 was selected under oil under ambient conditions and attached to the tip of a MiTeGen MicroMount©. The crystal was mounted in a stream of cold nitrogen at 100(1) K and centered in the X-ray beam by using a video camera.

The crystal evaluation and data collection were performed on a Bruker SMART APEXII diffractometer with Cu K$_\alpha$ (λ = 1.54178 Å) radiation and the diffractometer to crystal distance of 4.03 cm.

The initial cell constants were obtained from three series of ω scans at different starting angles. Each series consisted of 35 frames collected at intervals of 0.7° in a 25° range about ω with the exposure time of 1 second per frame. The reflections were successfully indexed by an automated indexing routine built in the APEXII program. The final cell constants were calculated from a set of 9308 strong reflections from the actual data collection.

The data were collected by using the full sphere data collection routine to survey the reciprocal space to the extent of a full sphere to a resolution of 0.82 Å. A total of 21543 data were harvested by collecting 19 sets of frames with 0.6° scans in ω and φ with an exposure time 2-8 sec per frame. These highly redundant datasets were corrected for Lorentz and polarization effects. The absorption correction was based on fitting a function to the empirical transmission surface as sampled by multiple equivalent measurements.[8]

Structure Solution and Refinement for J

The systematic absences in the diffraction data were consistent for the space groups $P\bar{1}$ and $P1$. The structure was solved in both $P1$ and $P\bar{1}$. Only centrosymmetric space group $P\bar{1}$ yielded chemically reasonable and computationally stable results of refinement.[9,10,11]

A successful solution by the charge-flipping provided most non-hydrogen atoms from the E-map.[12] The remaining non-hydrogen atoms were located in an alternating series of least-squares cycles and difference Fourier maps. All non-hydrogen atoms were refined with anisotropic displacement coefficients. Hydrogen atoms H1S and H3S were located from the Fourier difference map and refined independently. All other hydrogen atoms were included in the structure factor calculation at idealized positions and were allowed to ride on the neighboring atoms with relative isotropic displacement coefficients.

There are two molecules of trifluoroacetic acid per molecule of Pd complex. These form hydrogen bonds with the trifluoroacetate groups on the Pd complex.

The final least-squares refinement of 396 parameters against 4678 data resulted in residuals R (based on F^2 for $I \geq 2\sigma$) and wR (based on F^2 for all data) of 0.0218 and 0.0571, respectively. The final difference Fourier map was featureless.

Summary Crystal Data for C$_{19}$H$_8$F$_{12}$N$_2$O$_9$Pd (M =742.67): triclinic, space group $P\bar{1}$ (no. 2), a = 11.0499(10) Å, b = 11.1974(9) Å, c = 11.2382(7) Å, α = 96.618(3)°, β = 114.186(3)°, γ = 99.355(5)°, V = 1225.77(16) Å^3, Z = 2, T = 100.0 K, μ(CuKα) = 7.501 mm^{-1}, $Dcalc$ = 2.012 g/mm^3, 21543 reflections measured (8.17 $\leq$ 2Θ $\leq$ 144.572), 4678 unique (R_{int} = 0.0234, R$_{sigma}$ = 0.0169) which were used in all calculations. The final R_1 was 0.0218 (I > 2σ(I)) and wR_2 was 0.0568 (all data).
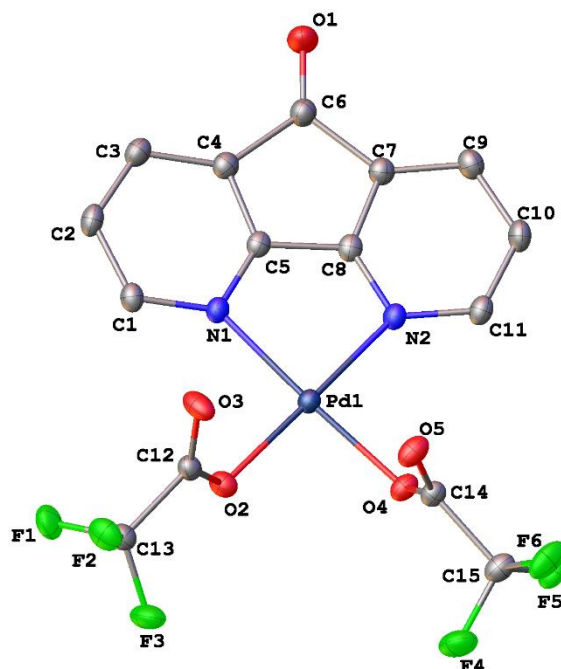
Figure A 41: A molecular drawing of J shown with 50% thermal probability ellipsoids. All H atoms and solvent molecules are omitted for clarity.
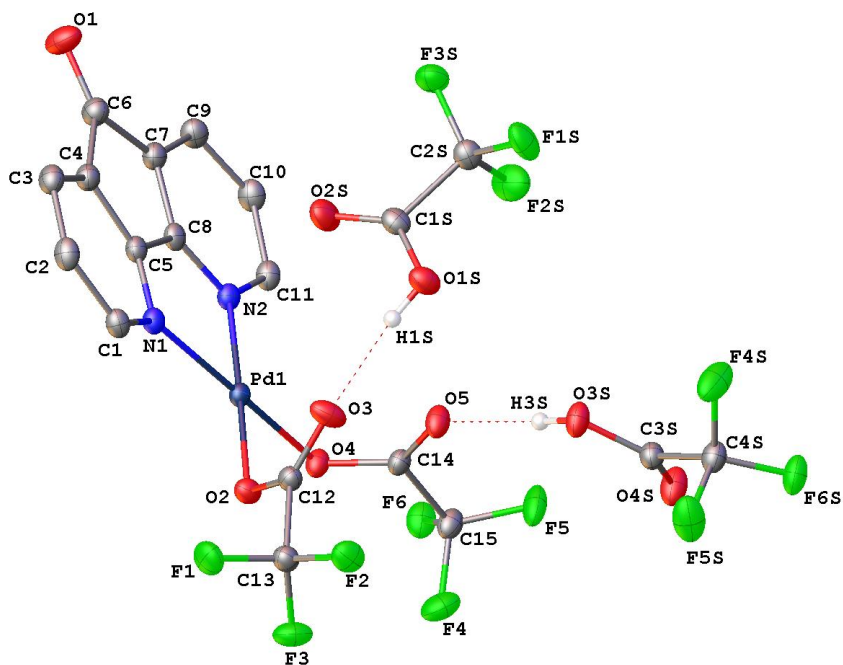
Figure A 42: The asymmetric unit of J. All atoms are drawn as 50% thermal probability ellipsoids. All H atoms except those on heteroatoms are omitted for clarity.

Table A 6: Crystal data and structure refinement for J.

Identification code	Stahl198
Empirical formula	$C_{15}H_6F_6N_2O_5Pd; 2(C_2F_3O_2H)$
Formula weight	742.67
Temperature/K	100(1)
Crystal system	triclinic
Space group	$P\bar{1}$
a/Å	11.0499(10)
b/Å	11.1974(9)
c/Å	11.2382(7)
α/°	96.618(3)
β/°	114.186(3)
γ/°	99.355(5)
Volume/Å^3	1225.77(16)
Z	2
ρ_{calc} mg/mm^3	2.012
μ/mm^{-1}	7.501
F(000)	724.0
Crystal size/mm^3	0.325 × 0.311 × 0.162
Radiation	CuKα (λ = 1.54178)
2Θ range for data collection	8.17 to 144.572°
Index ranges	-13 ≤ h ≤ 13, -13 ≤ k ≤ 12, -13 ≤ l ≤ 13
Reflections collected	21543
Independent reflections	4678 [R_{int} = 0.0234, R_{sigma} = 0.0169]
Data/restraints/parameters	4678/0/396
Goodness-of-fit on F^2	1.134
Final R indexes [I>=2σ (I)]	R_1 = 0.0218, wR_2 = 0.0568
Final R indexes [all data]	R_1 = 0.0218, wR_2 = 0.0568
Largest diff. peak/hole / e Å^{-3}	0.62/-0.50

A4.5 X-ray Structure of [(μ-DAF)Pd(κ^1-OPiv)$_2$]$_2$, Structure L

A red-orange crystal with approximate dimensions 0.258 x 0.192 x 0.097 mm^3 was selected under oil under ambient conditions and attached to the tip of a MiTeGen MicroMount©. The crystal was mounted in a stream of cold nitrogen at 100(1) K and centered in the X-ray beam by using a video camera.

The crystal evaluation and data collection were performed on a Bruker Quazar SMART APEXII diffractometer with Mo K$_α$ ($λ = 0.71073$ Å) radiation and the diffractometer to crystal distance of 4.96 cm.

The initial cell constants were obtained from three series of ω scans at different starting angles. Each series consisted of 12 frames collected at intervals of 0.5° in a 6° range about ω with the exposure time of 10 seconds per frame. The reflections were successfully indexed by an automated indexing routine built in the APEXII program suite. The final cell constants were calculated from a set of 9810 strong reflections from the actual data collection.

The data were collected by using the full sphere data collection routine to survey the reciprocal space to the extent of a full sphere to a resolution of 0.70 Å. A total of 72342 data were harvested by collecting 6 sets of frames with 0.5° scans in ω and φ with exposure times of 20 sec per frame. These highly redundant datasets were corrected for Lorentz and polarization effects. The absorption correction was based on fitting a function to the empirical transmission surface as sampled by multiple equivalent measurements.[8]

Structure Solution and Refinement for L

The systematic absences in the diffraction data were consistent for the space groups $P\bar{1}$ and $P1$. The E-statistics strongly suggested the centrosymmetric space group $P\bar{1}$ that yielded chemically reasonable and computationally stable results of refinement.[9,10,11]

A successful solution by the direct methods provided most non-hydrogen atoms from the E-map. The remaining non-hydrogen atoms were located in an alternating series of least-squares cycles and difference Fourier maps. All non-hydrogen atoms except those of chloroform molecule C45 were refined with anisotropic displacement coefficients. All hydrogen atoms were included in the structure factor calculation at idealized positions and were allowed to ride on the neighboring atoms with relative isotropic displacement coefficients.

The asymmetric unit consists of 1 molecule of the dipalladium complex shown in Figure 1 and three partially occupied molecules of chloroform (total: 1.53 molecules CHCl$_3$ per molecule dipalladium complex).

The pivalate ligands on the dipalladium complex each exhibit positional disorder. Ligand O1 was disordered over two positions (major component: 70.4(9)%) Ligand O3 was disordered over two positions (major component: 62.9(13)%) Ligand O5 was disordered over three positions (occupancies: 36.0(3)%, 33.6(3)%, 30.5(3)%). Ligand O7 was disordered over two positions (major component: 57.0(11)%). Bond distance and thermal parameter restraints were applied to the disordered ligands in order to obtain a chemically reasonable and computationally stable refinement.

Chloroform molecules C43 and C45 are disordered over an inversion center (occupancies: 47.3(4)%, 29.4(5)% per diapalldium molecule, respectively) Chloroform molecule C44 is disordered over three positions (occupancies: 44.9(10)%, 20.3(6)%, 11.2(6)% per dipalladium molecule) The chloroform molecules were refined with constrained geometries as well as thermal parameter restraints and constraints in order to obtain a chemically reasonable and computationally stable refinement.

The final least-squares refinement of 943 parameters against 15379 data resulted in residuals R (based on F^2 for $I \geq 2σ$) and wR (based on F^2 for all data) of 0.0653 and 0.1457, respectively. The final difference Fourier map contained several peaks between 2e$^-$/A^3 and 2.5 e$^-$/A^3 in the vicinity of the disordered ligands and solvents. These were interpreted as noise.

Crystal Data for C$_{43.54265}$H$_{49.54265}$Cl$_{4.62795}$N$_4$O$_{10}$Pd$_2$ (M =1165.78): triclinic, space group $P\bar{1}$ (no. 2), $a = 12.971(5)$ Å, $b = 13.996(4)$ Å, $c = 15.387(4)$ Å, $α = 73.854(17)°$, $β = 72.031(6)°$, $γ = 80.916(7)°$, $V = 2544.3(15)$ Å^3, $Z = 2$, $T = 100.0$ K, $μ$(MoKα) = 1.006 mm^{-1}, $Dcalc = 1.522$ g/mm^3, 72342 reflections measured (2.87 ≤ 2Θ ≤ 61.142), 15379 unique ($R_{int} = 0.0233$, R$_{sigma} = 0.0186$) which were used in all calculations. The final R_1 was 0.0653 (I > 2σ(I)) and wR_2 was 0.1457 (all data).
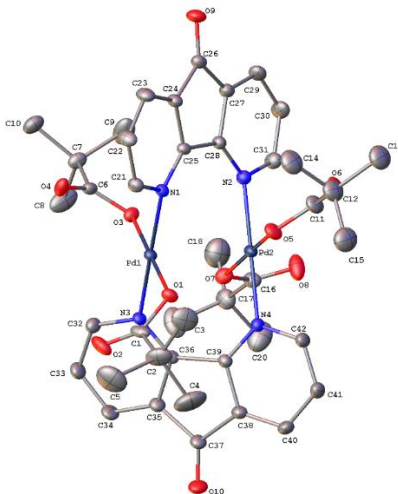
Figure A 43: A molecular drawing of the dipalladium complex of L. All atoms are drawn as 50% thermal probability ellipsoids. All H atoms and disordered components are omitted for clarity
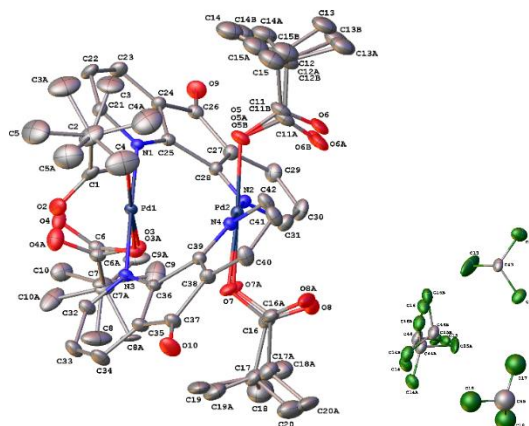
Figure A 44: The asymmetric unit of L showing all disordered components. All atoms are drawn as 50% thermal probability ellipsoids. All H atoms are omitted for clarity.

Table A 7: Crystal data and structure refinement for L.

Identification code	Stahl196
Empirical formula	$C_{42}H_{48}N_4O_{10}Pd_2$, 1.53($CHCl_3$)
Formula weight	1165.78
Temperature/K	100.0
Crystal system	triclinic
Space group	$P\bar{1}$
a/Å	12.971(5)
b/Å	13.996(4)
c/Å	15.387(4)
α/°	73.854(17)
β/°	72.031(6)
γ/°	80.916(7)
Volume/Å^3	2544.3(15)
Z	2
ρ_{calc} mg/mm^3	1.522
μ/mm^{-1}	1.006
F(000)	1179.0
Crystal size/mm^3	$0.258 \times 0.192 \times 0.097$
Radiation	MoKα (λ = 0.71073)
2Θ range for data collection	2.87 to 61.142°
Index ranges	$-18 \leq h \leq 18, -20 \leq k \leq 19, -21 \leq l \leq 21$
Reflections collected	72342
Independent reflections	15379 [R_{int} = 0.0233, R_{sigma} = 0.0186]
Data/restraints/parameters	15379/1524/949
Goodness-of-fit on F^2	1.287
Final R indexes [I>=2σ (I)]	R_1 = 0.0653, wR_2 = 0.1446
Final R indexes [all data]	R_1 = 0.0679, wR_2 = 0.1458
Largest diff. peak/hole / e Å^{-3}	2.25/-2.36

A4.6 X-ray Structure of [(μ-DAF)Pd(κ^1-O$_2$CC$_6$F$_5$)$_2$]$_2$, Structure M

An orange crystal with approximate dimensions 0.4 x 0.3 x 0.2 mm^3 was selected under oil under ambient conditions and attached to the tip of a MiTeGen MicroMount©. The crystal was mounted in a stream of cold nitrogen at 100(1) K and centered in the X-ray beam by using a video camera.

The crystal evaluation and data collection were performed on a Bruker Quazar SMART APEXII diffractometer with Mo K$_\alpha$ (λ = 0.71073 Å) radiation and the diffractometer to crystal distance of 4.96 cm.

The initial cell constants were obtained from three series of ω scans at different starting angles. Each series consisted of 12 frames collected at intervals of 0.5° in a 6° range about ω with the exposure time of 10 seconds per frame. The reflections were successfully indexed by an automated indexing routine built in the APEXII program suite. The final cell constants were calculated from a set of 9995 strong reflections from the actual data collection.

The data were collected by using the full sphere data collection routine to survey the reciprocal space to the extent of a full sphere to a resolution of 0.80 Å. A total of 67717 data were harvested by collecting 4 sets of frames with 0.5° scans in ω and φ with exposure times of 120 sec per frame. These highly redundant datasets were corrected for Lorentz and polarization effects. The absorption correction was based on fitting a function to the empirical transmission surface as sampled by multiple equivalent measurements.[8]
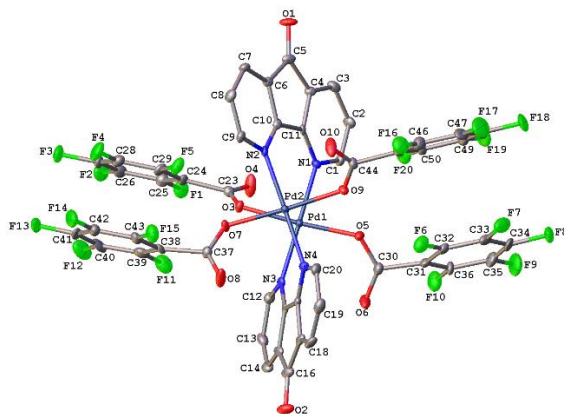
Structure Solution and Refinement

The systematic absences in the diffraction data were consistent for the space groups *P*2/*c* and *Pc*. The *E*-statistics strongly suggested the centrosymmetric space group *P*2/*c* that yielded chemically reasonable and computationally stable results of refinement.[9,10,11]

A successful solution by the direct methods provided most non-hydrogen atoms from the *E*-map. The remaining non-hydrogen atoms were located in an alternating series of least-squares cycles and difference Fourier maps. All non-hydrogen atoms were refined with anisotropic displacement coefficients. All hydrogen atoms were included in the structure factor calculation at idealized positions and were allowed to ride on the neighboring atoms with relative isotropic displacement coefficients.

The only crystal large enough for the single-crystal X-ray diffraction experiment proved to be a pseudo-merohedral twin with a 35.68(7)% second component contribution. The twin components are related by a 180° rotation about [201].

The final least-squares refinement of 776 parameters against 9752 data resulted in residuals *R* (based on F^2 for *I*≥2σ) and *wR* (based on F^2 for all data) of 0.0344 and 0.0722, respectively. The final difference Fourier map was featureless.

Summary Crystal Data for C$_{50}$H$_{12}$F$_{20}$N$_4$O$_{10}$Pd$_2$ (*M* =1421.44): monoclinic, space group P2/c (no. 13), *a* = 24.5357(10) Å, *b* = 8.7047(4) Å, *c* = 26.4314(10) Å, *β* = 122.616(2)°, *V* = 4754.9(4) Å^3, *Z* = 4, *T* = 99.99 K, μ(MoKα) = 0.903 mm^{-1}, *Dcalc* = 1.986 g/mm^3, 67717 reflections measured (3.082 ≤ 2Θ ≤ 52.832), 9752 unique (*R*$_{int}$ = 0.0748, R$_{sigma}$ = 0.0450) which were used in all calculations. The final *R*$_1$ was 0.0344 (I > 2σ(I)) and *wR*$_2$ was 0.0722 (all data).

Figure A 45: A molecular drawing of Structure M shown with 40% probability ellipsoids. All H atoms are omitted.

Table A 8: Crystal data and structure refinement for M.

Identification code	stahl197
Empirical formula	$C_{50}H_{12}F_{20}N_4O_{10}Pd_2$
Formula weight	1421.44
Temperature/K	99.99
Crystal system	monoclinic
Space group	P2/c
a/Å	24.5357(10)
b/Å	8.7047(4)
c/Å	26.4314(10)
α/°	90
β/°	122.616(2)
γ/°	90
Volume/Å^3	4754.9(4)
Z	4
ρ_{calc}mg/mm^3	1.986
m/mm^{-1}	0.903
F(000)	2768.0
Crystal size/mm^3	$0.4 \times 0.3 \times 0.2$
Radiation	MoKα (λ = 0.71073)
2Θ range for data collection	3.082 to 52.832°
Index ranges	-30 ≤ h ≤ 30, -10 ≤ k ≤ 10, -33 ≤ l ≤ 33
Reflections collected	67717
Independent reflections	9752 [R_{int} = 0.0748, R_{sigma} = 0.0450]
Data/restraints/parameters	9752/0/776
Goodness-of-fit on F^2	1.025
Final R indexes [I>=2σ (I)]	R_1 = 0.0344, wR_2 = 0.0660
Final R indexes [all data]	R_1 = 0.0521, wR_2 = 0.0722
Largest diff. peak/hole / e Å^{-3}	0.68/-0.67

A4.7 Me₂DAF Free Ligand

A colorless crystal with approximate dimensions 0.5 x 0.4 x 0.4 mm³ was selected under oil under ambient conditions and attached to the tip of a MiTeGen MicroMount©. The crystal was mounted in a stream of cold nitrogen at 100(1) K and centered in the X-ray beam by using a video camera.

The crystal evaluation and data collection were performed on a Bruker SMART APEXII diffractometer with Cu K_α ($\lambda = 1.54178$ Å) radiation and the diffractometer to crystal distance of 4.03 cm.

The initial cell constants were obtained from three series of ω scans at different starting angles. Each series consisted of 35 frames collected at intervals of 0.6° in a 25° range about ω with the exposure time of 1 second per frame. The reflections were successfully indexed by an automated indexing routine built in the APEXII program. The final cell constants were calculated from a set of 9835 strong reflections from the actual data collection.

The data were collected by using the full sphere data collection routine to survey the reciprocal space to the extent of a full sphere to a resolution of 0.8 Å. A total of 51177 data were harvested by collecting 13 sets of frames with 0.7° scans in ω and φ with an exposure time 1-2 sec per frame. These highly redundant datasets were corrected for Lorentz and polarization effects. The absorption correction was based on fitting a function to the empirical transmission surface as sampled by multiple equivalent measurements.[8]

Structure Solution and Refinement

The systematic absences in the diffraction data were uniquely consistent for the space group *Pbca* that yielded chemically reasonable and computationally stable results of refinement.[9,10,11]

A successful solution by the direct methods provided most non-hydrogen atoms from the *E*-map. The remaining non-hydrogen atoms were located in an alternating series of least-squares cycles and difference Fourier maps. All non-hydrogen atoms were refined with anisotropic displacement coefficients. All hydrogen atoms were included in the structure factor calculation at idealized positions and were allowed to ride on the neighboring atoms with relative isotropic displacement coefficients.
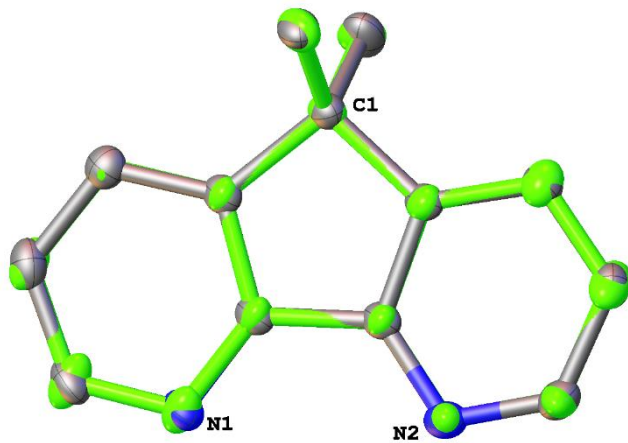
There are two symmetry independent molecules in the asymmetric unit with essentially identical geometries.

The final least-squares refinement of 275 parameters against 4225 data resulted in residuals R (based on F^2 for $I \geq 2\sigma$) and wR (based on F^2 for all data) of 0.0376 and 0.0950, respectively. The final difference Fourier map was featureless.

Summary Crystal Data for C13H12N2 (M =196.25): orthorhombic, space group Pbca (no. 61), a = 15.4073(9) Å, b = 13.5221(16) Å, c = 20.4502(16) Å, V = 4260.6(7) Å³, Z = 16, T = 100 K, μ(CuKα) = 0.572 mm⁻¹, Dcalc = 1.224 g/mm³, 51177 reflections measured (9.718 ≤ 2Θ ≤ 146.356), 4225 unique (Rint = 0.0355, Rsigma = 0.0140) which were used in all calculations. The final R1 was 0.0376 (I > 2σ(I)) and wR2 was 0.0950 (all data).
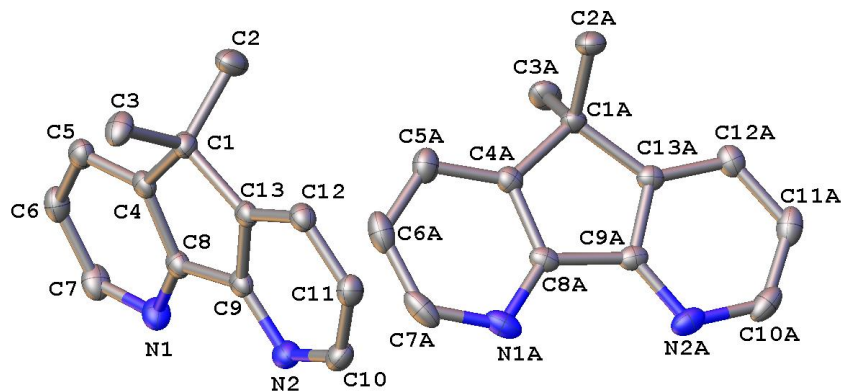
Figure A 46: A molecular drawing of Me₂DAF shown with 50% probability ellipsoids. All H atoms are omitted.

Figure A 47: The superposition of the two symmetry independent molecules of Me₂DAF shown with 50% probability ellipsoids.

All H atoms are omitted.

Table A 9: Crystal data and structure refinement for Me_2DAF.

Identification code	stahl195
Empirical formula	$C_{13}H_{12}N_2$
Formula weight	196.25
Temperature/K	100
Crystal system	orthorhombic
Space group	Pbca
a/Å	15.4073(9)
b/Å	13.5221(16)
c/Å	20.4502(16)
α/°	90
β/°	90
γ/°	90
Volume/Å^3	4260.6(7)
Z	16
ρ_{calc}mg/mm^3	1.224
m/mm^{-1}	0.572
F(000)	1664.0
Crystal size/mm^3	$0.5 \times 0.4 \times 0.4$
Radiation	CuKα (λ = 1.54178)
2Θ range for data collection	9.718 to 146.356°
Index ranges	$-19 \leq h \leq 19, -16 \leq k \leq 15, -25 \leq l \leq 24$
Reflections collected	51177
Independent reflections	4225 [R_{int} = 0.0355, R_{sigma} = 0.0140]
Data/restraints/parameters	4225/0/275
Goodness-of-fit on F^2	1.044
Final R indexes [I>=2σ (I)]	R_1 = 0.0376, wR_2 = 0.0923
Final R indexes [all data]	R_1 = 0.0410, wR_2 = 0.0950
Largest diff. peak/hole / e Å^{-3}	0.24/-0.24

1. Harris, R. K.; Becker, E. D.; Cabral de Menezes, S. M.; Granger, P.; Hoffman, R. E.; Zilm, K. W. *Pure Appl. Chem.* **2008**, *80*, 59.

2. We use VNMR parameter labels thoughout, where the TopSpin equivalents are: nt≡ns, ni≡td1, tof≡o1, dof≡o2, etc.

3. Gaussian 09, Revision C.01, Frisch, M. J.; Trucks, G. W.; Schlegel, H. B.; Scuseria, G. E.; Robb, M. A.; Cheeseman, J. R.; Scalmani, G.; Barone, V.; Mennucci, B.; Petersson, G. A.; Nakatsuji, H.; Caricato, M.; Li, X.; Hratchian, H. P.; Izmaylov, A. F.; Bloino, J.; Zheng, G.; Sonnenberg, J. L.; Hada, M.; Ehara, M.; Toyota, K.; Fukuda, R.; Hasegawa, J.; Ishida, M.; Nakajima, T.; Honda, Y.; Kitao, O.; Nakai, H.; Vreven, T.; Montgomery, J. A. Jr.; Peralta, J. E.; Ogliaro, F.; Bearpark, M.; Heyd, J. J.; Brothers, E.;Kudin, K. N.; Staroverov, V. N.; Keith, T.; Kobayashi, R.; Normand, J.; Raghavachari, K.; Rendell, A.; Burant, J. C.; Iyengar, S. S.; Tomasi, J.; Cossi, M.; Rega, N.; Millam, J. M.; Klene, M.; Knox, J. E.; Cross, J. B.; Bakken, V.; Adamo, C.; Jaramillo, J.; Gomperts, R.; Stratmann, R. E.; Yazyev, O.; Austin, A. J.; Cammi, R.; Pomelli, C.; Ochterski, J. W.; Martin, R. L.; Morokuma, K.; Zakrzewski, V. G.; Voth, G. A.; Salvador, P.; Dannenberg, J. J.; Dapprich, S.; Daniels, A. D.; Farkas, O.; Foresman, J. B.; Ortiz, J. V.; Cioslowski, J.; Fox, D. J. Gaussian, Inc., Wallingford CT, 2010.

4. Becke, A.D. *J. Chem. Phys.* **1993**, *98*, 1372.

5. Lee, C.; Yang, W.; Parr, R. G. *Phys. Rev. B* **1988**, *37*, 785.

6. a) Feller, D. *J. Comp. Chem.*, **1996**, *17*, 1571-1586. b) Schuchardt, K.L.; Didier, B.T.; Elsethagen, T.; Sun, L.; Gurumoorthi, V.; Chase, J.; Li, J.; and Windus, T.L. *J. Chem. Inf. Model*. **2007**, *47*, 1045.

7. See, for example, Gunther, H. in *NMR Spectroscopy: Basic Principles, Concepts, and Applicaitons in Chemistry*, 2nd ed., Wiley, 1995, pp 343.

8. Bruker-AXS. (2007-2013) APEX2 (Ver. 2013.2-0), SADABS (2012-1), and SAINT+ (Ver. 8.30C) Software Reference Manuals. Bruker-AXS, Madison, Wisconsin, USA.

9. Sheldrick, G. M. (2008) SHELXL. *Acta Cryst.* **A64**, 112-122.

10. Dolomanov, O.V.; Bourhis, L.J.; Gildea, R.J.; Howard, J.A.K.; Puschmann, H. "OLEX2: a complete structure solution, refinement and analysis program". *J. Appl. Cryst.* **2009**, *42*, *339-341*.

11. Guzei, I.A. (2013). Internal laboratory computer programs Gn

12. Bourhis, L. J.; Dolomanov, O. V.; Gildea, R. J.; Howard, J. A. K.; Puschmann, H. *Acta Cryst. A* **2015**, *A71*, 59.

Appendix B: Supporting Information for Chapter 4

B1. General Experimental Considerations

All commercially available compounds were used as received. c*is-N*-Tosyl-4-hexenylamide (**1**) was used from a previously reported synthesis.[1] Aerobic Pd-catalyzed transformations of **1** with various ancillary ligands were performed using a custom 48-well reaction apparatus that enabled reactions to be performed simultaneously under a constant pressure of O_2 (approx 1 atm) with controlled temperature and orbital agitation. Kinetic data were obtained by removing aliquots from a scaled-up reaction using an identical but larger-well reactor. The reactions or aliquots were filtered over a plug of silica, washed with EtOAc and the solvent was removed with a centrifugal evaporator. The yield was measured by ^{1}H NMR spectroscopy after addition of either trimethyl(phenyl)silane or 1,3,5-trimethoxybenzene as external standards to the crude evaporated mixture.

Synthesis and Characterization of Well-Defined Pd(N~N)(OAc)$_2$ Complexes[1]

Well-defined Pd(N~N)(OAc)$_2$ complexes were synthesized from a modification of a literature procedure.[2] A slight of excess of ligand (1.05 equiv) dissolved in minimal acetone was added to a concentrated solution of Pd(OAc)$_2$ in acetone. The mixture was stirred overnight during which the Pd(N~N)(OAc)$_2$ complex precipitated out of solution. The yellow precipitate was isolated by vacuum filtration, washed with acetone and dried under vacuum to afford the desired complex.

Pd(6,6'-Me$_2$bpy)(OAc)$_2$ (**5**) 90 mg, 65% yield, yellow precipitate. ^{1}H NMR (500 MHz, CDCl$_3$) δ 8.48 (d, *J* = 8.0 Hz, 2H), 7.91 (t, *J* = 7.9 Hz, 2H), 7.04 (d, *J* = 7.7 Hz, 2H), 2.71 (s, 6H), 2.02 (s, 6H).^{13}C NMR (126 MHz, CDCl$_3$) δ 178.01, 163.92, 157.42, 140.35, 126.56, 121.36, 24.32, 23.02.

Pd(2,9-Me$_2$Phen)(OAc)$_2$ (**6**) 118 mg, 85% yield, yellow precipitate. ^{1}H NMR (500 MHz, CDCl$_3$) δ 8.33 (d, *J* = 8.3 Hz, 2H), 7.84 (s, 2H), 7.47 (d, *J* = 8.3 Hz, 2H), 2.93 (s, 6H), 2.04 (s, 6H). ^{13}C NMR (126 MHz, CDCl$_3$) δ 178.76, 165.60, 147.73, 138.31, 128.09, 127.05, 126.32, 24.75, 23.05.

Pd(^{t}Bu$_2$bpy)(OAc)$_2$ (**7**) 121 mg, 87% yield, yellow precipitate. ^{1}H NMR (500 MHz, CDCl$_3$) δ 8.24 (d, *J* = 6.0 Hz, 2H), 7.83 (d, *J* = 2.0 Hz, 2H), 7.48 (dd, *J* = 6.1, 2.0 Hz, 2H), 2.13 (s, 6H), 1.42 (s, 18H). ^{13}C NMR (126 MHz, CDCl$_3$) δ 178.45, 165.13, 155.47, 149.95, 123.84, 118.41, 35.81, 30.29, 23.46.

B2. General NMR Spectroscopy Considerations.

Routine screening data were analyzed using an automated Bruker Av400 spectrometer equipped with an inverse BBFO+ probe. Characterization of well-defined Pd complexes was performed on a Bruker Av500 spectrometer equipped with a ^{13}C sensitive DCH LHe cryoprobe. Variable temperature and multidimensional spectra were recorded on a Varian INOVA 600 MHz spectrometer equipped with a HPX probe or Bruker Av500 spectrometer equipped with an inverse BBFO+ probe. ^{1}H NMR chemical shifts are reported in parts per million relative to internal TMS (0.00 ppm) in CDCl$_3$. ^{13}C and ^{15}N NMR chemical shifts are reported in parts per million and externally referenced to TMS from the ^{1}H spectrum. The ^{15}N chemical shifts is externally referenced to the ^{1}H spectrum and calibrated to liquid ammonia (at 0.00 ppm). The sample temperature was calibrated with an external 4% MeOH in MeOD-*d$_3$* reference standard. The pw90 and longest T_1 values were computed from the pw360 and inversion recovery experiments,

---

[1] Characterization performed by PBW

respectively, after each temperature change. All standard ^{1}H spectra were recorded quantitatively (recycle delay $\geq 5*T_1$) and integrals referenced to an internal standard (1,3,5-trimethoxybenzene). Selective TOCSY and ROESY experiments were used as implemented in Varian ChemPack 3.1 and were performed using SEDUCE shaped pulses with spinlock frequencies of 8.5 kHz and 5.4 kHz, respectively.

B3. General Computational Considerations.

All computations were performed with the Gaussian 09 program[3] using resources provided by University of Wisconsin–Madison Chemistry Department. Spin-restricted density functional theory (DFT) calculations were performed with the hybrid density functional, rB3LYP.[4,5] A combination of the Stuttgart RSC 1997 ECP/triple-ζ basis[6] for Pd and the all-electron 6-31+G(d) basis set for all other atoms was used for gas-phase geometry optimizations and normal mode analyses. Full geometry optimizations were carried out in internal coordinates using the default Berny algorithm. Frequency calculations were performed at the optimized geometries to confirm that each geometry had the appropriate number of imaginary frequencies: zero for minima or one for transition states. The imaginary frequency identifying a saddle-point was visually inspected for the proper motion.

At the calculated stationary points, solvation-corrected single-point total energy calculations were carried out with the Pd basis detailed above and the 6-311+G (d,p) basis on all other atoms with electrostatic and non-electrostatic solvation effects evaluated using the polarizable-continuum model (PCM). The solvation cavity was generated using UFF radii, explicitly treating hydrogen atoms, and the radii were scaled by a factor of 1.2. The solvent chosen was toluene.

B4. Determination of Amidopalladation Stereochemistry[2]
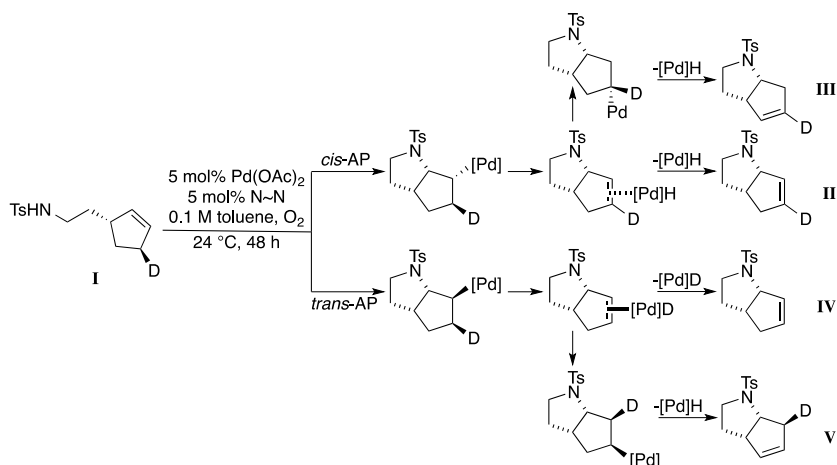
Figure B 1: Mechanistic origin for the observation of different alkene isomers with and without the deuterium label.

Reproduction of Chemical Shifts for **I**-**V**[7]

---

[2] Characterization performed by PBW

I ^{1}H NMR (CDCl$_3$) δ 7.76 (dt, J = 2.1, 9.0 Hz, 2H), 7.31 (dt, J = 2.1, 9.0 Hz, 2H), 5.71 (m, 1H), 5.56 (m, 1H), 4.58 (t, J = 6.0 Hz, 1H), 2.98 (dt, J = 6.6, 6.6 Hz, 2H), 2.65 (m, 1H), 2.44 (s, 3H), 2.28 (m, 1H), 1.98 (m, 1H), 1.63-1.38 (m, 2H), 1.32(m, 1H)

II ^{1}H NMR (CDCl$_3$) δ 7.73 (m, 2H), 7.33 (m, 2H), 5.81 (q, J = 2.1 Hz, 1H), 4.55 (dq, J = 2.1, 8.1 Hz, 1H), 3.37 (ddd,, J = 4.5, 6.9, 9.9 Hz, 1H), 3.06 (ddd, J = 6.6, 8.7, 9.9 Hz, 1H), 2.61 (m, 1H), 2.47 (m, 1H), 2.43 (s, 3H), 2.10 (dq, J = 2.1, 17.1 Hz, 1H), 1.83 (m, 1H), 1.51 (m, 1H)

III ^{1}H NMR (CDCl$_3$) δ 7.73 (m, 2H), 7.33 (m, 2H), 5.45 (q, J = 2.1 Hz, 1H), 4.18 (dt, J = 6.9, 4.2 Hz, 1H), 3.40-3.20 (m, 2H), 2.71 (m, 2H), 2.43 (s, 3H), 2.22 (m, 1H), 1.68-1.48 (m, 2H)

IV ^{1}H NMR (CDCl$_3$) δ 7.73 (m, 2H), 7.33 (m, 2H), 5.81 (m, 1H), 5.75 (m, 1H), 4.55 (dq, J = 2.1, 8.1 Hz, 1H), 3.37 (ddd,, J = 4.5, 6.9, 9.9 Hz, 1H), 3.06 (ddd, J = 6.6, 8.7, 9.9 Hz, 1H), 2.61 (m, 1H), 2.47 (m, 1H), 2.43 (s, 3H), 2.11 (dq, J = 2.1, 17.1Hz, 1H), 1.83 (m, 1H), 1.51 (m, 1H)

V ^{1}H NMR (CDCl$_3$) δ 7.73 (m, 2H), 7.33 (m, 2H), 5.72 (m, 1H), 5.45 (m, 1H), 4.18 (dt, J = 6.9, 4.2 Hz, 1H), 3.40-3.20 (m, 3H), 2.71 (m, 1H), 2.43 (s, 3H), 1.68-1.48 (m, 2H)

Spectra of Reaction Mixtures in CDCl$_3$
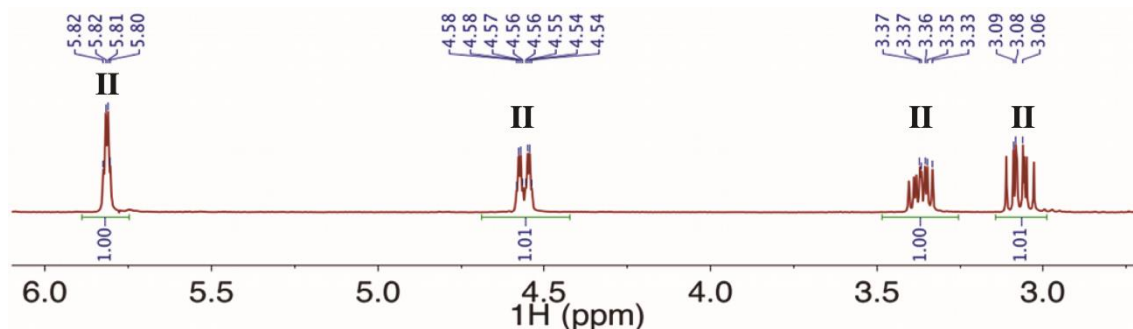
Figure B 2: ^{1}H NMR spectrum of the crude reaction mixture of Pd(OAc)$_2$/DAF with I. Only a single product (II) is observed and corresponds to a product from the cis-AP pathway. Ns = 16, ds = 2, d1 = 25 s.
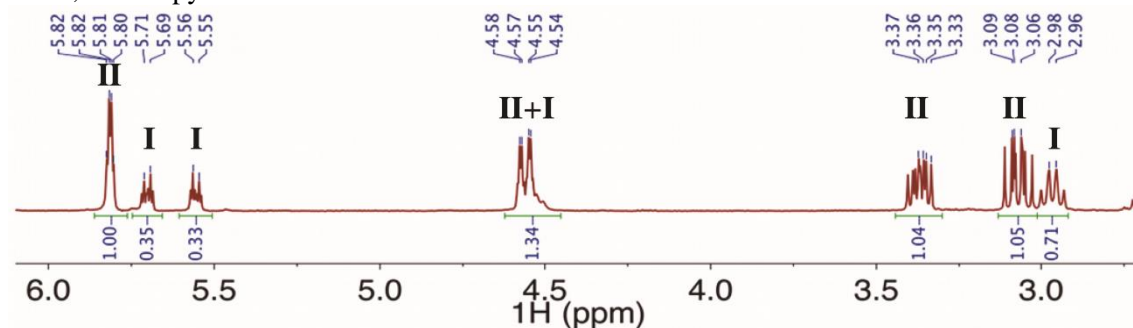
Figure B 3: ^{1}H NMR spectrum of the crude reaction mixture of Pd(OAc)$_2$/6,6'-Me$_2$bpy with I. Only a single product (II) is observed and corresponds to a product from the cis-AP pathway. Ns = 16, ds = 2, d1 = 25 s.

B5. Assessment of Bidentate Ligands on Oxidative Amidation - Experimental

B5.1 Experimental for Table 4.1[3]

Reactions were performed on a custom parallel 48 well reactor with orbital mixing at 50 rpm. Conditions were as follows: substrate (75 μmol, 0.1 M), Pd(OAc)$_2$ (3.75 μmol), O$_2$ (1 atm), toluene (0.75 mL), 50 °C, 24 h. Reactions were processed by filtering the mixture through silica, washing with EtOAc and removing the solvent by vacuum centrifugation. The resulting concentrate was dissolved in CDCl$_3$ containing an external standard (1,3,5-trimethoxybenzene) and analyzed by ^{1}H NMR spectroscopy.

B5.2 Kinetic Comparison of DAF, 9,9-Me$_2$DAF with Pd(OAc)$_2$ in Ox. Amidation
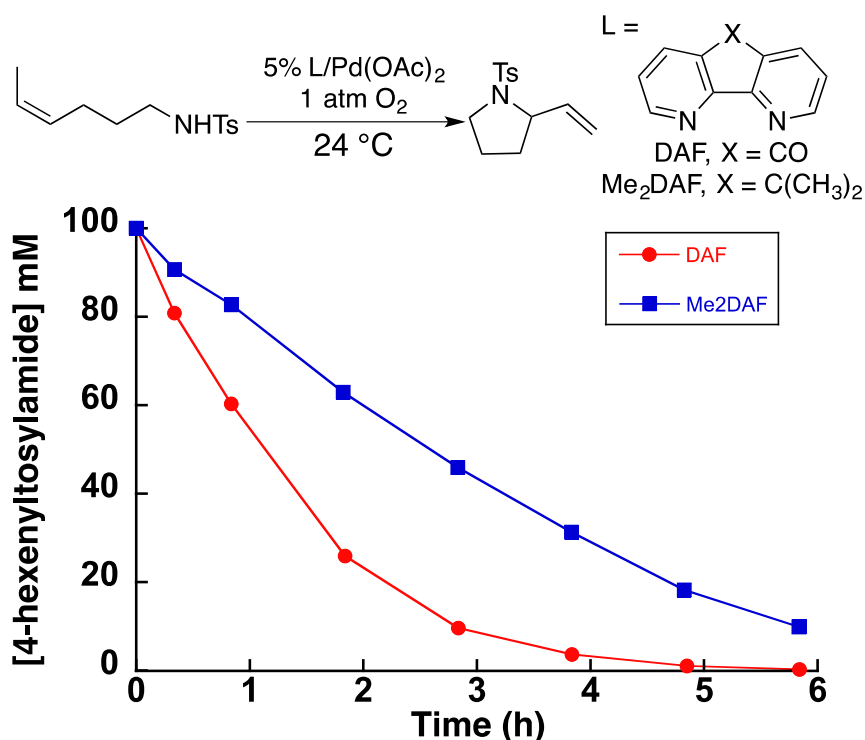
Figure B 4: Kinetic time courses of the oxidative cyclization of 1, 4-hexenyltosylamide with DAF and 9,9-Me$_2$DAF. Conditions:

5 mol % Pd(OAc)$_2$ (3.4 mg, 15 μmoles), 5 mol % ligand (DAF, 9,9-Me$_2$DAF), 1 (76 mg, 300 μmoles, 0.1 M), 24 °C, 1 atm O$_2$,

toluene (3 mL), int. std. = 1,3,5-trimethoxybenzene. The reaction was followed for 6 hours for with data collected approximately

every hour with the first time point at 20 minutes.[4]

---

[3] Table 4.1 is the combined work of PBW and JNJ

[4] DAF/Pd(OAc)$_2$, Me$_2$DAF/Pd(OAc)$_2$ rt data obtained independently by JNJ

B6. Pyridine Titration of Pd(N~N)(OAc)$_2$ Complexes

Increasing quantities of pyridine (0.5 equiv per 10 μL of a CDCl$_3$ stock solution) were added to solutions containing **4** and the well-defined complexes **5**-**7** (40 mM in CDCl$_3$, 0.5 mL). After every addition of pyridine, the sample was allowed to equilibrate at room temperature for 45 minutes prior to data acquisition. The speciation was monitored by ^{1}H NMR spectroscopy. Intermediate complexes were identified by comparing a given spectrum against free pyridine, Pd(py)$_2$(OAc)$_2$ and free bidentate ligand standards.

4,4'-^{t}Bu$_2$bpy[5]
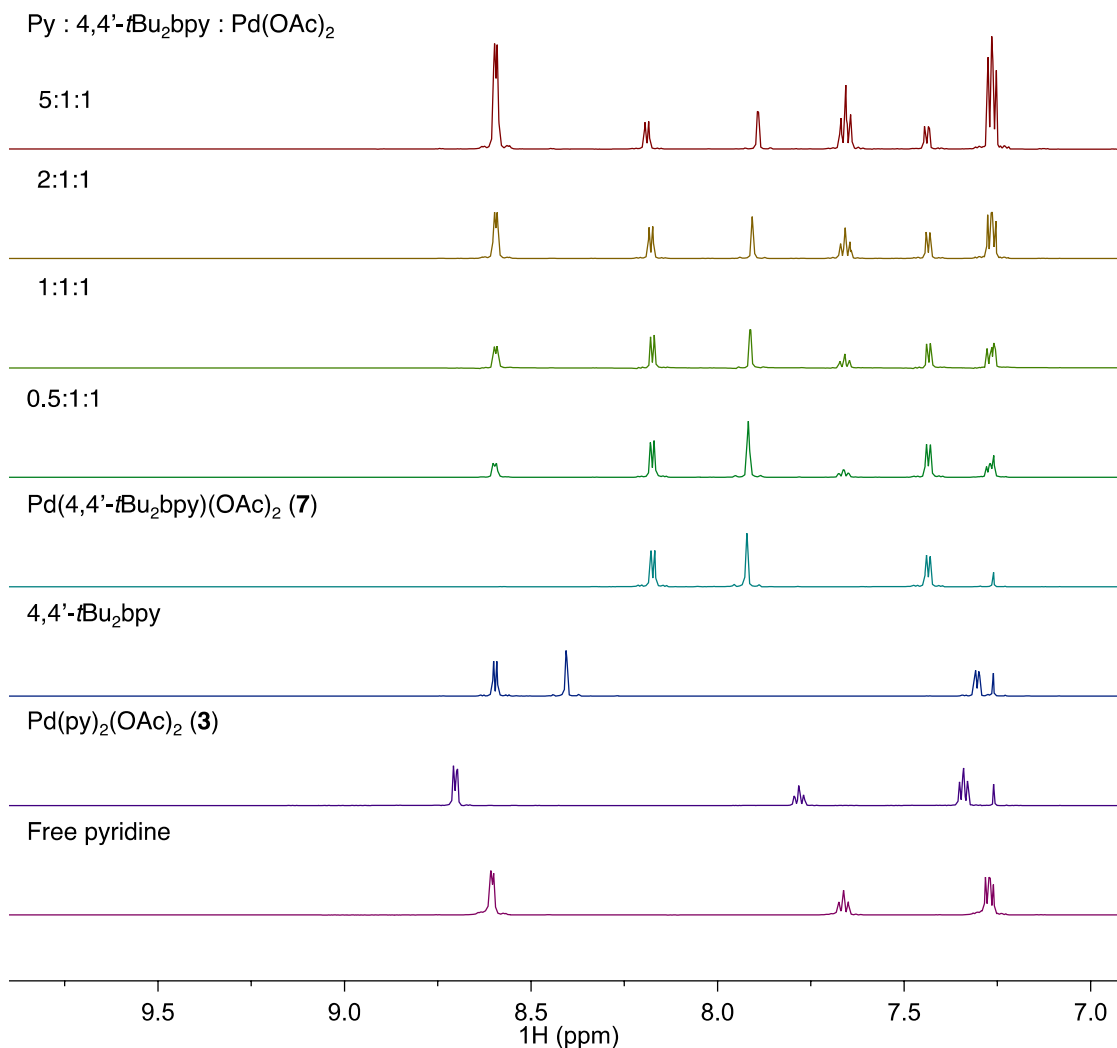
Figure B 5: Titration of pyridine into a CDCl$_3$ solution containing Pd(κ^2-4,4'-^{t}Bu$_2$bpy)(OAc)$_2$ (7) and 1,3,5-trimethoxybenzene as an internal standard. 7 is resistant to ligand dissociation and shows no sign of 4,4'-^{t}Bu$_2$bpy and Pd(pyridine)$_2$(OAc)$_2$ after 5 equivalents of pyridine have been added. ns = 8, ds = 2, d1 = 15.

---

[5] Characterization obtained by PBW, reproduced by JNJ

2,9-Me$_2$Phen[5]

Py : 2,9-Me$_2$Phen : Pd(OAc)$_2$

5:1:1

2:1:1

1:1:1

0.5:1:1

Pd(2,9-Me$_2$Phen)(OAc)$_2$ (**6**)

2,9-Me$_2$Phen

Pd(py)$_2$(OAc)$_2$

Free pyridine

9.5   9.0   8.5   8.0   7.5   7.0
1H (ppm)
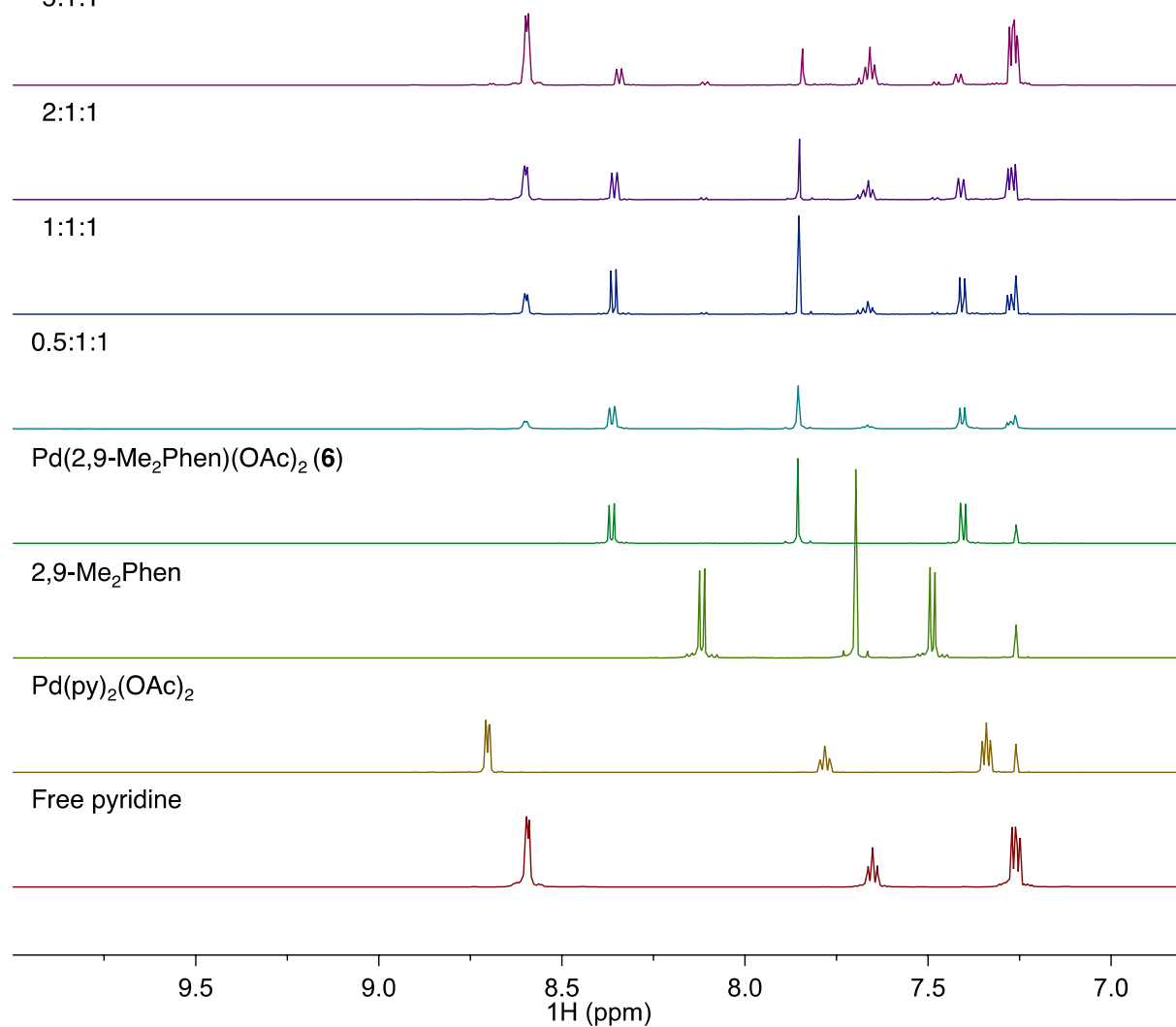
Figure B 6: Titration of pyridine into a CDCl$_3$ solution containing Pd(κ^2-2,9-Me$_2$Phen)(OAc)$_2$ (6) and 1,3,5-trimethoxybenzene as an internal standard. 6 is resistant to ligand dissociation and shows only trace amounts of 2,9-Me$_2$Phen and Pd(pyridine)$_2$(OAc)$_2$ after 5 equivalents of pyridine have been added. ns = 8, ds = 2, d1 = 15.

6,6'-Me$_2$bpy[5]

Py : 6,6'-Me$_2$bpy: Pd(OAc)$_2$

2:1:1

1:1:1

0.5:1:1

Pd(6,6'-Me$_2$bpy)(OAc)$_2$ (**5**)

6,6'-Me$_2$bpy

Pd(py)$_2$(OAc)$_2$

Free pyridine
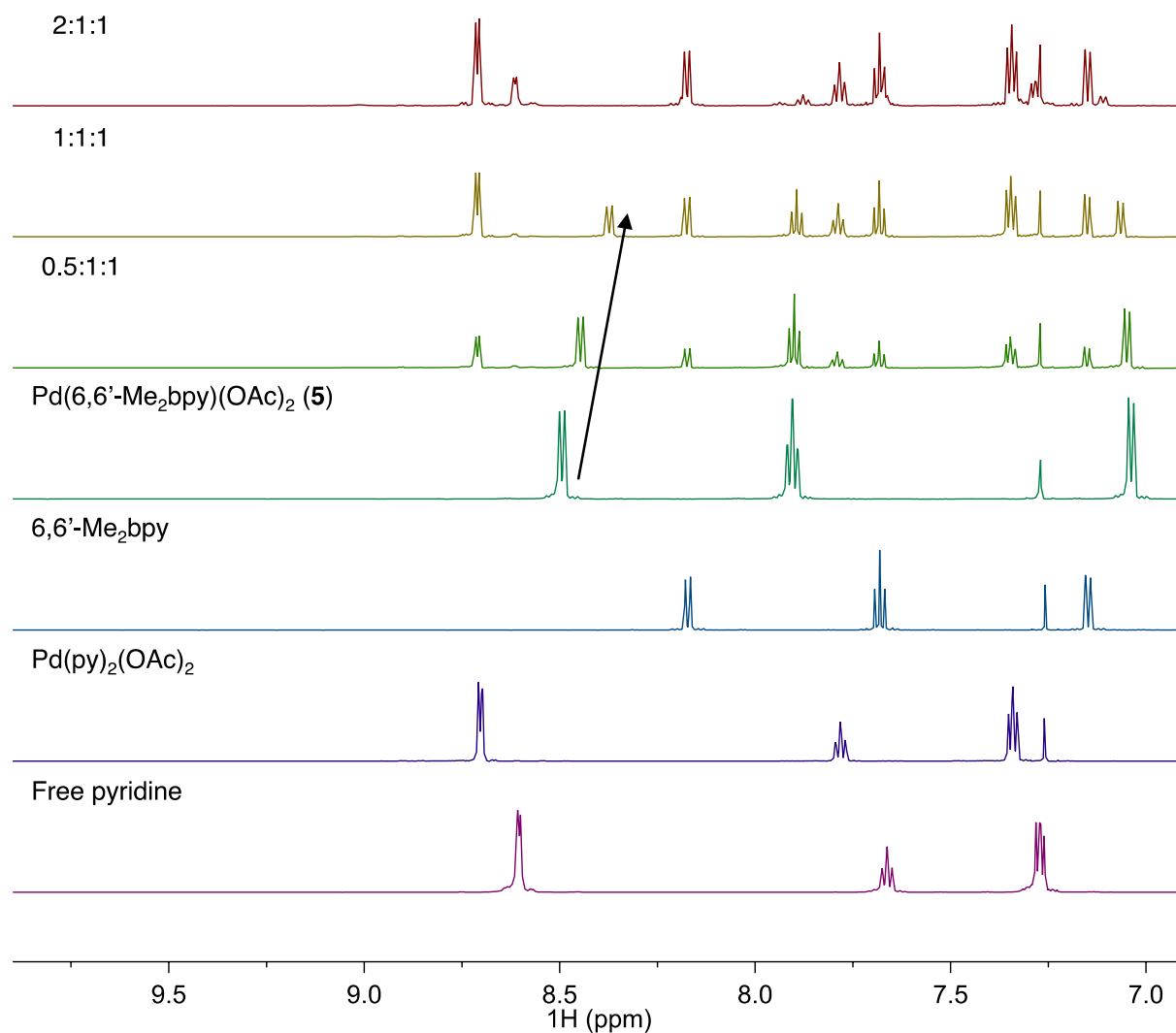
Figure B 7: Titration of pyridine into a CDCl$_3$ solution containing Pd(κ^2-6,6'-Me$_2$bpy)(OAc)$_2$ (5) and 1,3,5-trimethoxybenzene as an internal standard. Addition of pyridine results in the dissociation of 6,6'-Me$_2$bpy with concomitant formation of Pd(pyridine)$_2$(OAc)$_2$. Additionally, there is a change in the chemical shift of 5 signifying rapid exchange with a low-populated intermediate species that was later identified to be Pd(κ^1-6,6'-Me$_2$bpy)(pyridine)(OAc)$_2$ (9) (see below). After two equivalents of pyridine are added, nearly all the 6,6'-Me$_2$bpy ligand is dissociated and can be accounted for as Pd(pyridine)$_2$(OAc)$_2$. ns = 8, ds = 2, d1 = 15.
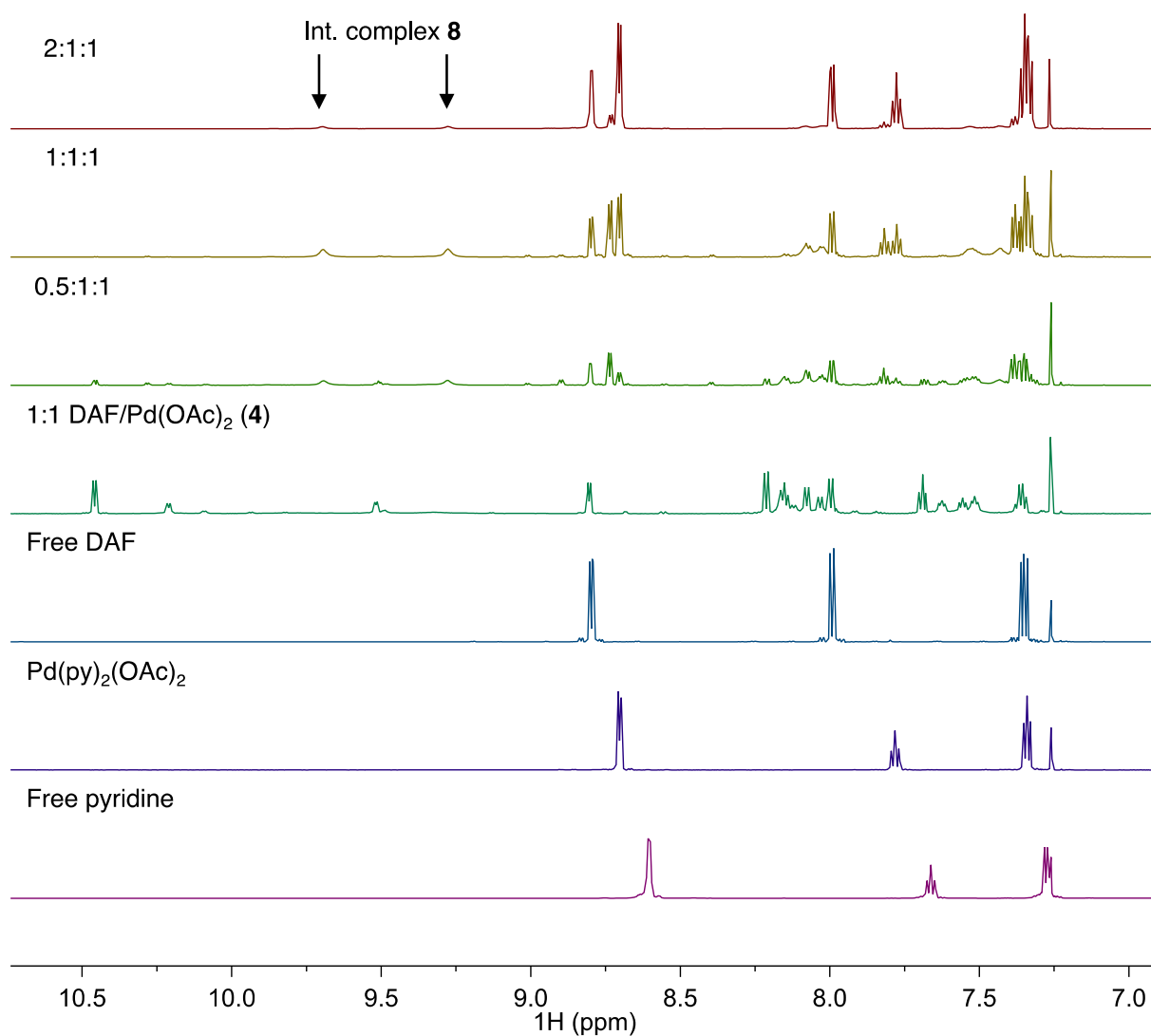
Figure B 8: Titration of pyridine into a CDCl3 solution at containing a 1:1 DAF:Pd(OAc)2 mixture and 1,3,5-trimethoxybenzene as an internal standard. In the absence of pyridine, multiple DAF-Pd(OAc)2 complexes are present, which have been characterized previously to be a mixture of monomeric and dimeric species.[8] Addition of pyridine results in the reduction of the species and appearance of Pd(κ^1-DAF)(pyridine)(OAc)2 (8). After two equivalents of pyridine are added, DAF ligand is dissociated and all of the Pd can be account for as Pd(pyridine)2(OAc)2. ns = 8, ds = 2, d1 = 15.

---

[6] Data obtained independently by JNJ

B7. Characterization of *trans*-Pd(κ¹-DAF)(py)(OAc)₂ (8) by NMR Spectroscopy. [7]
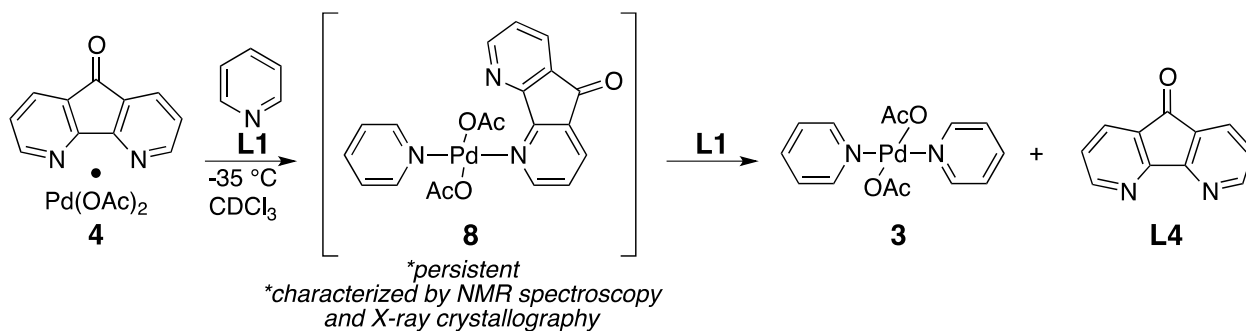
¹H 1D Spectrum at -35 °C
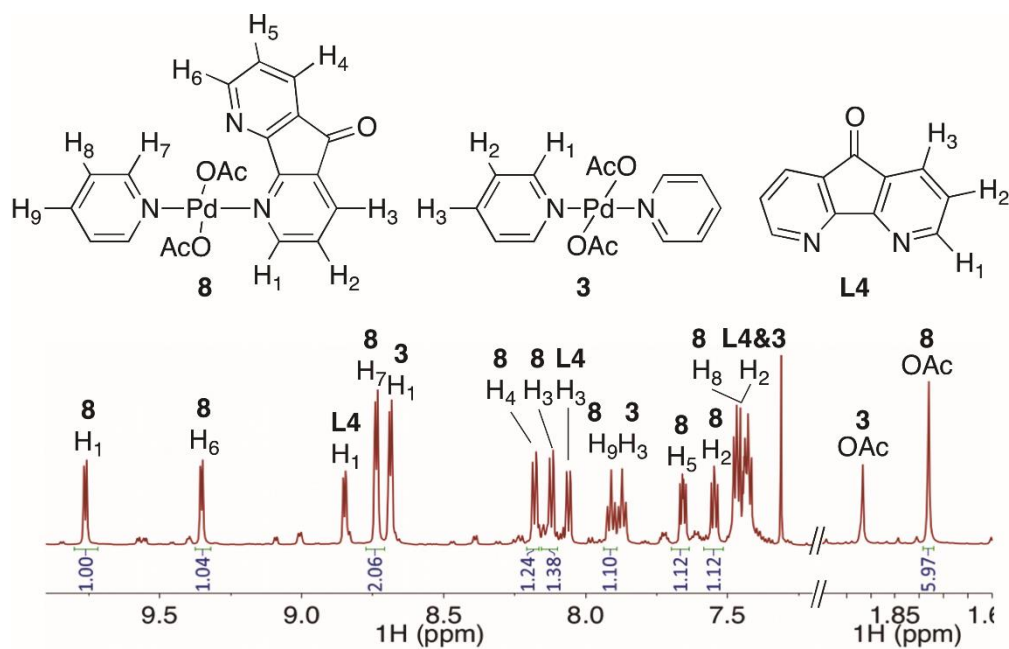
Figure B 9: ¹H 1D spectrum of a 1:1:1 DAF:pyridine:Pd(OAc)₂ mixture in CDCl₃ at -35 °C. The spectrum is split between the aromatic and aliphatic region to enhance visual resolution. ns = 4, ds = 2, d1 = 7.56 s.

---

[7] Data obtained independently by PBW

^{1}H 1D TOCSY Spectra at -35 °C
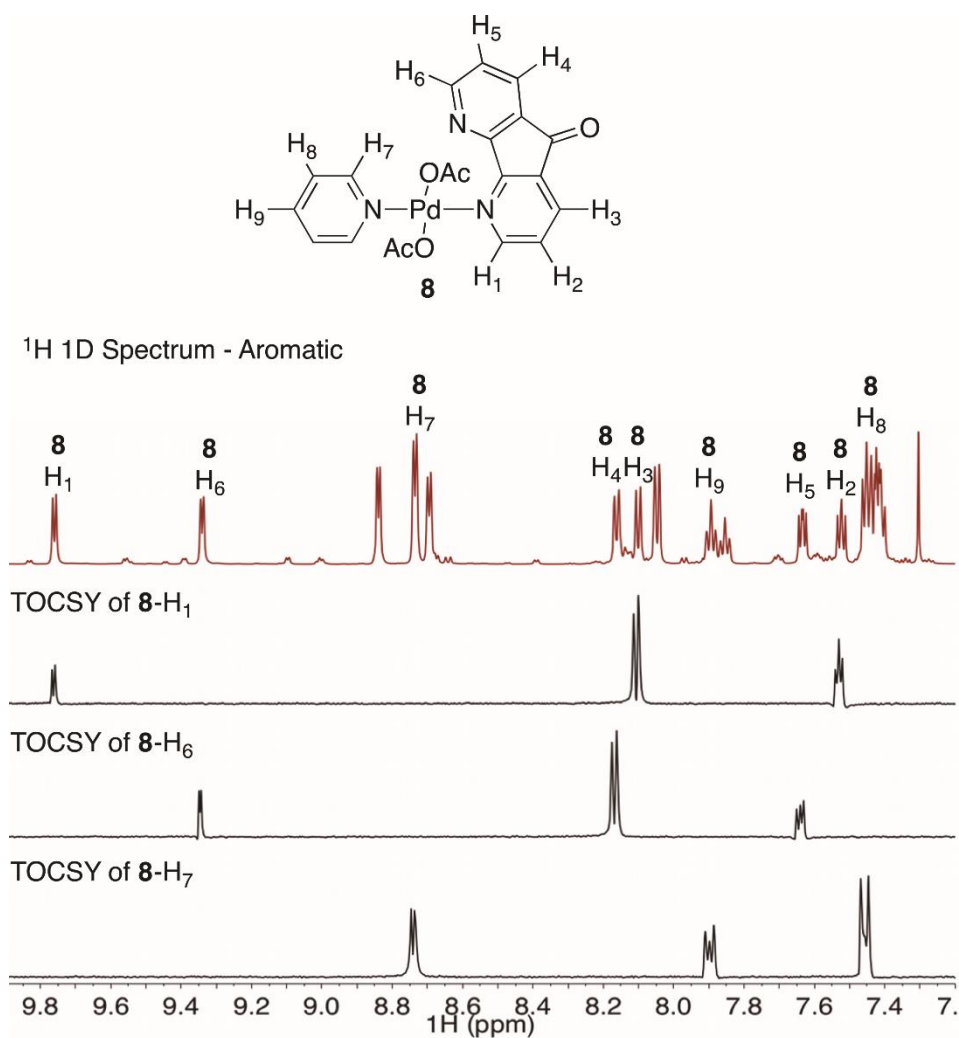
Figure B 10: ^{1}H 1D Spectrum (top) and 1D TOCSY spectra (bottom three) of a 1:1:1 DAF:pyridine:Pd(OAc)$_2$ mixture in CDCl$_3$ at -35 °C. ^{1}H 1D: ns = 4, ds = 2, d1 = 7.56 s; ^{1}H 1D TOCSY: These are slices extracted from an array of spectra with varying mix times for each proton. ns = 16, ds = 4, d1 = 2.52 s, 8.5 kHz spinlock, mix = 30 ms.

¹H 1D ROESY Spectra at -45 °C

Figure B 11: ¹H-¹H 1D ROESY Spectrum of **8**-H$_1$ (top), **8**-H$_6$ (middle) and **8**-H$_7$ (bottom) at -45 °C. Through-space interactions between both the DAF and pyridine ligand are observed as well as to the nearby acetate. These ROEs and integration confirm a stoichiometry consistent with a Pd(κ^1-DAF)(py)(OAc)$_2$ complex. ns = 128-256, d1 = 5.0 s, 5.4 kHz spinlock, mix = 0.3 s.

¹H-¹³C HSQC Spectrum at -35 °C
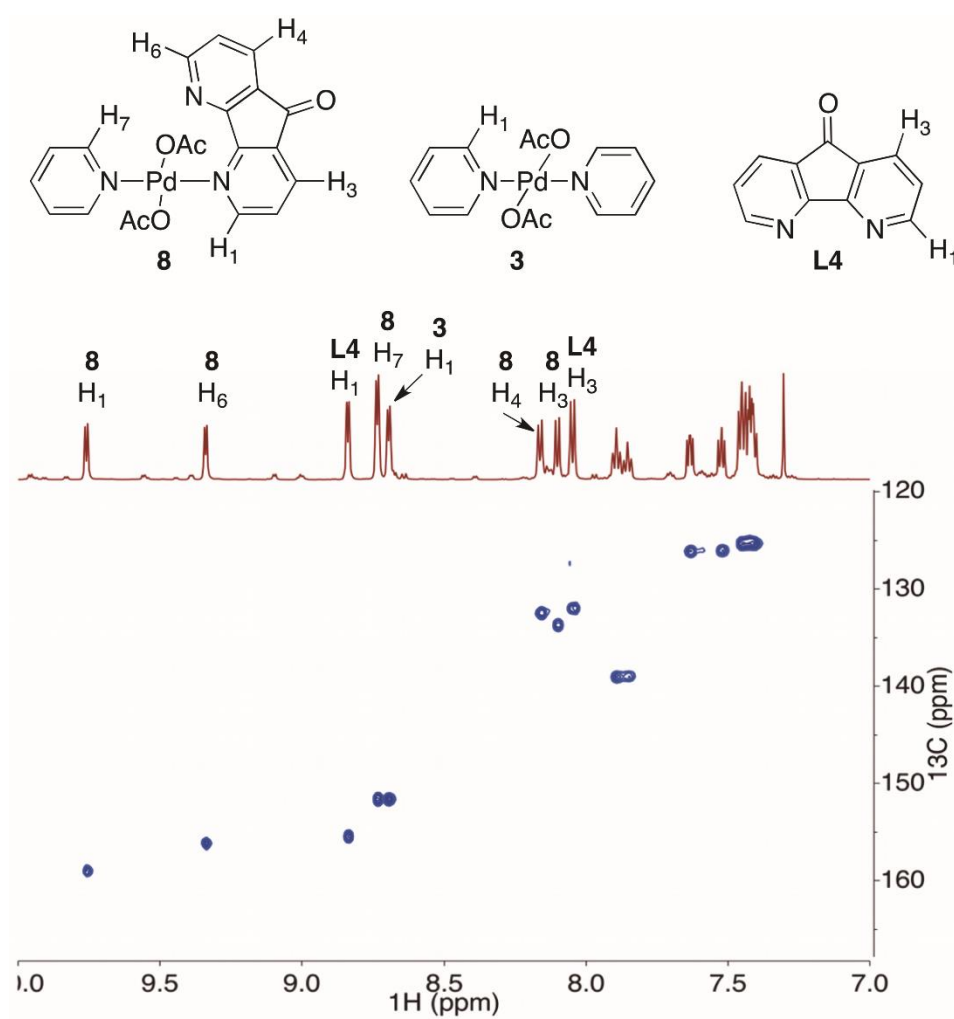
Figure B 12: ¹H-¹³C HSQC spectrum of a 1:1:1 DAF:pyridine:Pd(OAc)₂ mixture in CDCl₃ at -45 °C. ns = 8, ni = 128, d1 = 2.52 s, sw(f1) = 195 ppm, ¹J_{CH} = 170 Hz .

^{1}H-^{13}C HMBC Spectrum at -35 °C
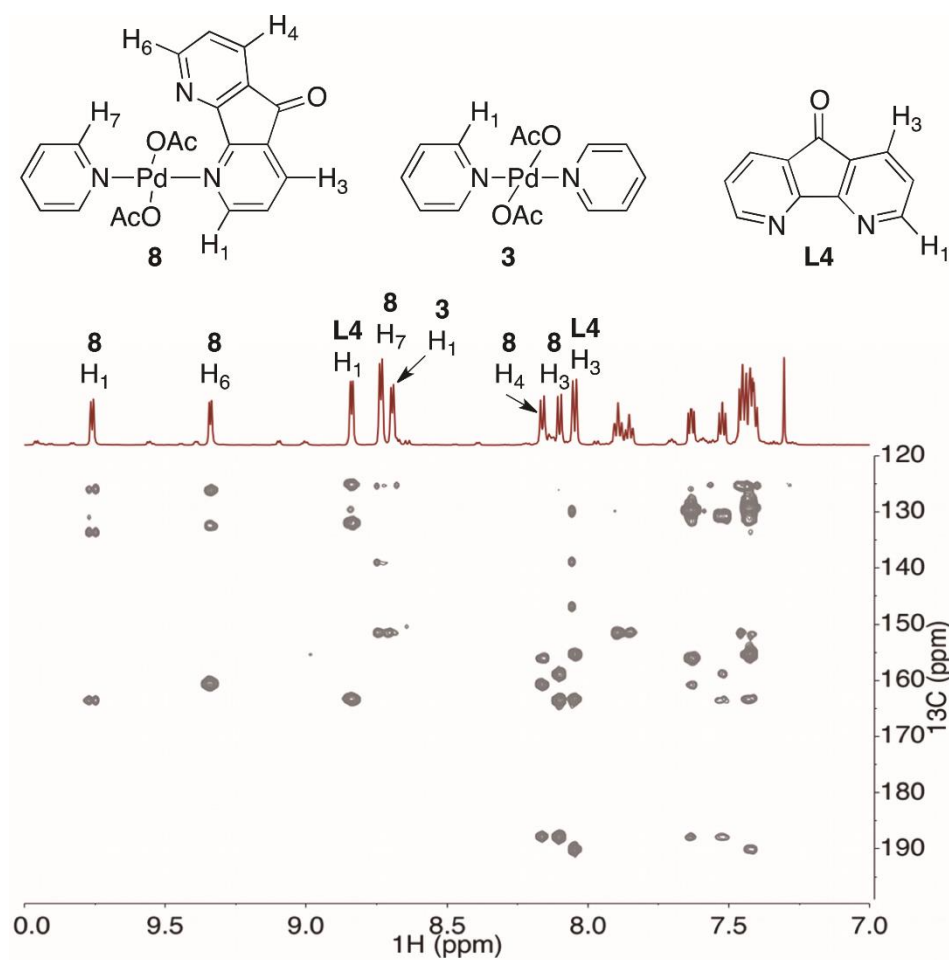
Figure B 13: ^{1}H-^{13}C HMBC spectrum of a 1:1:1 DAF:pyridine:Pd(OAc)$_2$ mixture in CDCl$_3$ at -45 °C. ns = 8, ni = 256, d1 = 2.52 s, sw(f1) = 195 ppm, $^nJ_{CH}$ = 3 Hz $^1J_{CH}$ = 170 Hz .

Interpretation of HSQC and HMBC Spectra
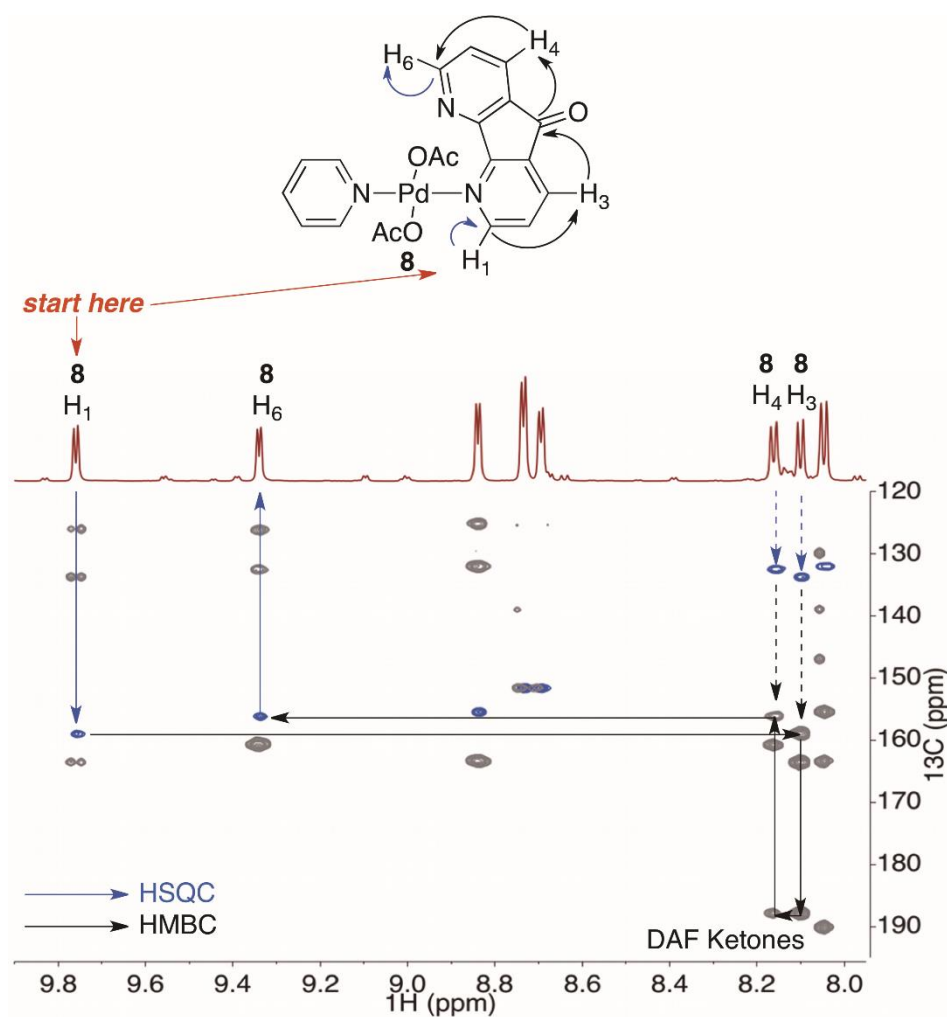
Figure B 14: Overlay of the ^1H-^{13}C HSQC and HMBC spectra to facilitate interpretation. The two resonances 8-H_1 and 8-H_6 belong to two chemically inequivalent pyridine rings that connect to the share same DAF carbonyl. This is suggestive of a k1-DAF complex.

¹H-¹⁵N HMBC Spectrum at -35 °C
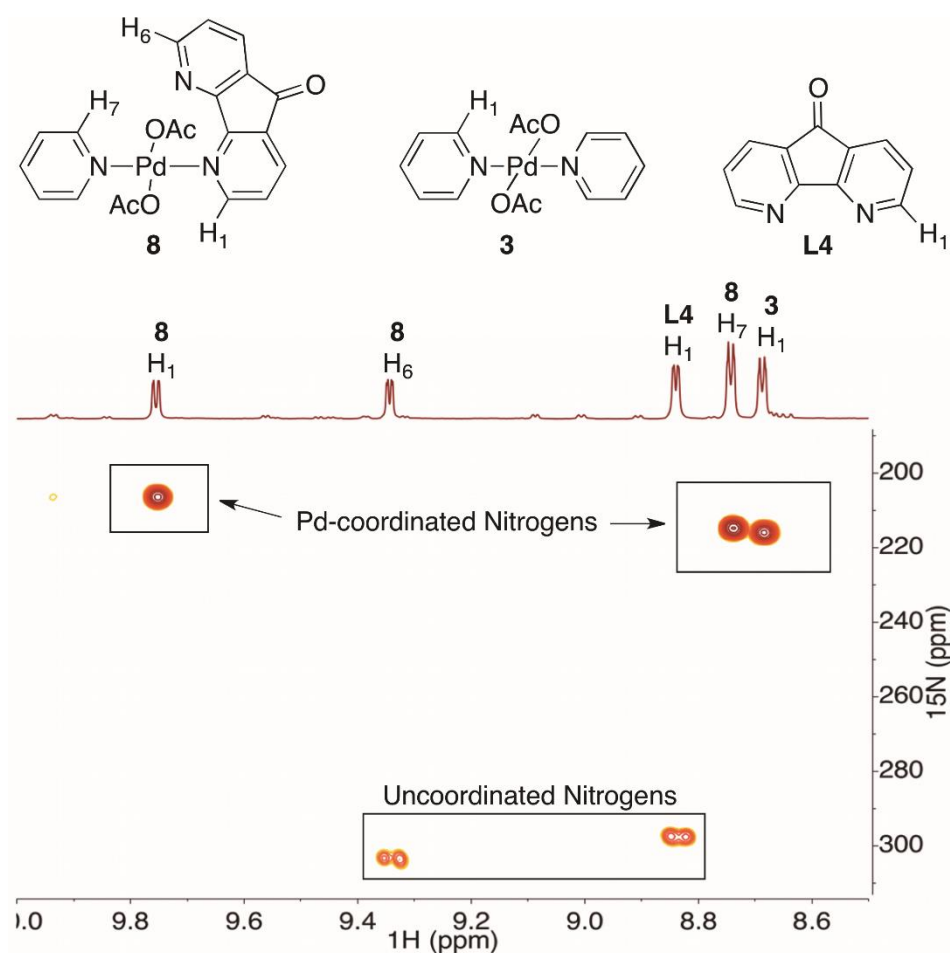
Figure B 15: ¹H-¹⁵N HMBC spectrum of a 1:1:1 DAF:pyridine:Pd(OAc)₂ mixture in CDCl₃ at -45 °C. The resonances near 200 ppm correspond to Pd-coordinated nitrogens while those around 300 ppm are uncoordinated nitrogens. This spectrum confirms that 8 consists of κ^1-DAF and pyridine ligand. ns = 24, ni = 256, d1 = 2.52 s, sw(f1) = 400 ppm, $^1J_{NH}$ = 100 Hz and $^nJ_{NH}$ = 8 Hz. Cosine-squared window functions were applied in the f1 and f2 dimensions.

B8. Characterization of *trans*-Pd(κ^1-6,6'-Me$_2$bpy)(py)(OAc)$_2$ (9) by NMR Spectroscopy[7]

^{1}H 1D EXSY and TOCSY Spectra at -70 °C
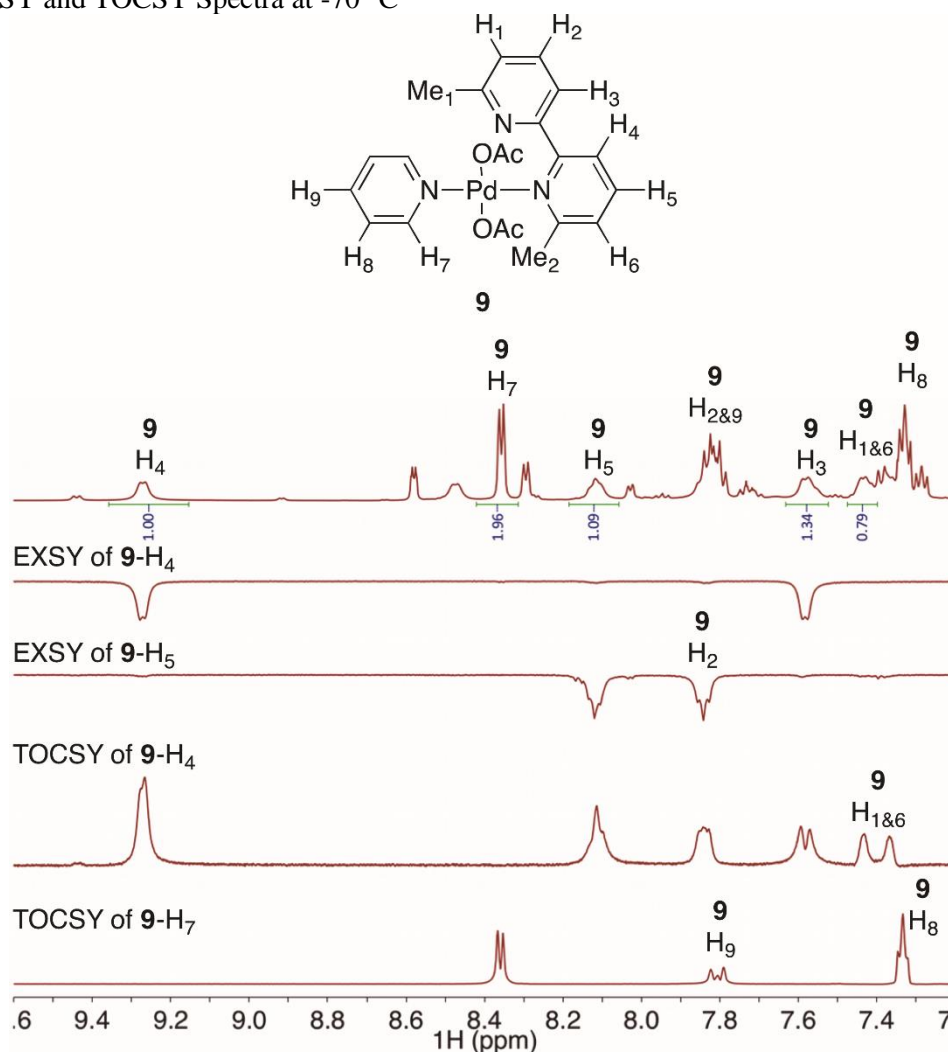
Figure B 16: ^{1}H 1D EXSY and TOCSY spectra of a 1:1 pyridine:Pd(6,6'-Me$_2$bpy)(OAc)$_2$ mixture in CD$_2$Cl$_2$ at -70 °C. The EXSY experiments identify exchange between 9-H$_4$ and 9-H$_3$ as well as 9-H$_5$ and 9-H$_2$. The TOCSY experiment of 9-H$_4$ reveal six resonances that are consistent with an asymmetrically coordinated 6,6'-Me$_2$bpy ligand. Furthermore, the lack of exchange within the pyridine ligand of 9 is evident from the TOCSY experiment of 9-H$_7$. ns = 16, ds = 4, d1 = 4 s, 8.5 kHz (TOCSY) and 5.4 kHz (EXSY) spinlock, mix =0.3 s (EXSY) and 0.06 s (TOCSY).

¹H 1D ROESY Spectra at -70 °C
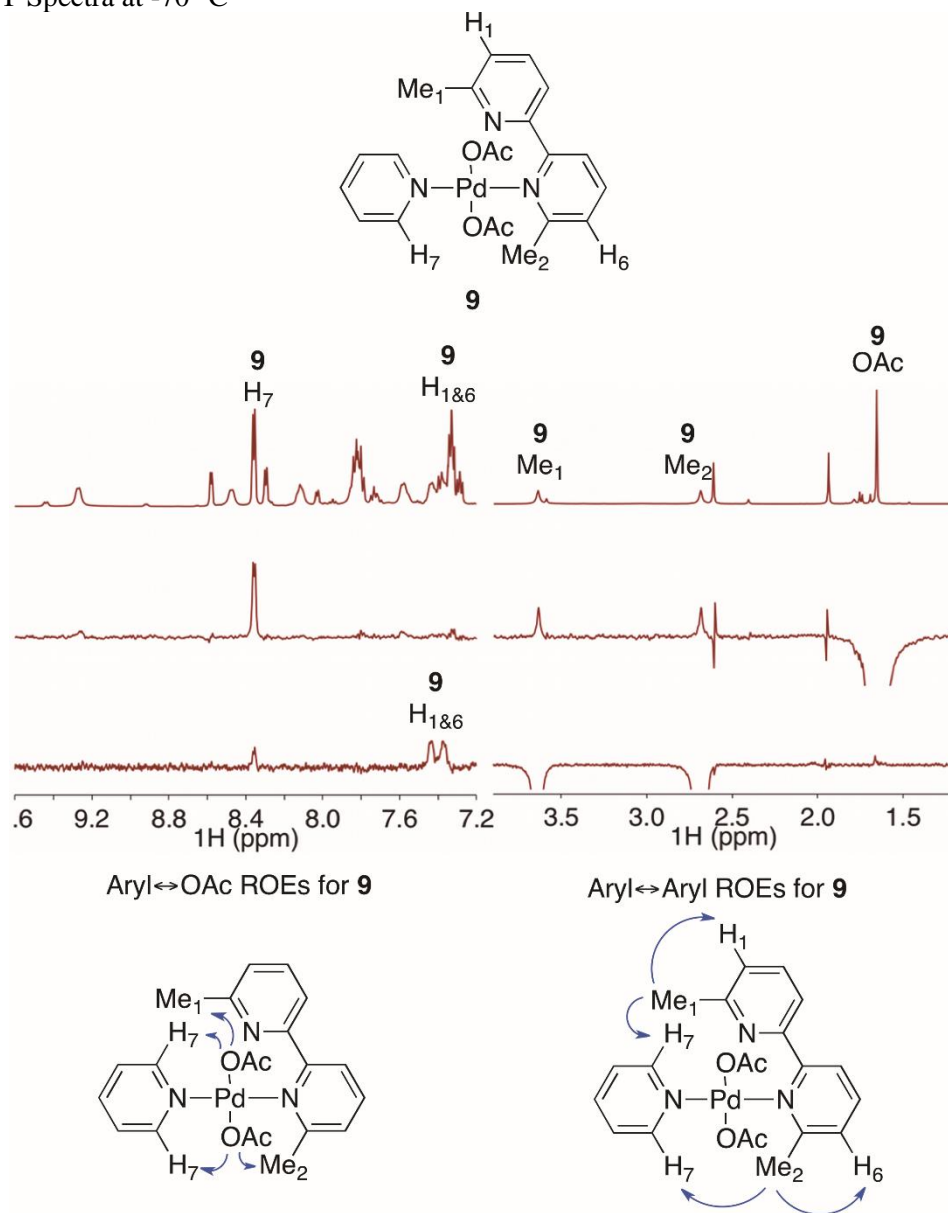
Figure B 17: ¹H 1D ROESY spectra of a 1:1 pyridine:Pd(6,6'-Me₂bpy)(OAc)₂ mixture in CD₂Cl₂ at -70 °C. Through-space interactions are evident between the 9-OAc residues and the methyl groups (9-Me₁ and 9-Me₂) of the 6,6'-Me₂bpy ligand as well as the pyridine ligand, 9-H₇ (middle). Additional through-space interactions are observed between 9-Me₁ and 9-Me₂ to 9-H₁, 9-H₆ and 9-H₇. These through-space and integrations of the corresponding resonances are consistent with a Pd(κ¹-6,6'-Me₂bpy)(pyridine)(OAc)₂. ns = 256, ds = 4, d1 = 7 s, 5.4 kHz spinlock, mix = 0.6 s.

Proposed Mechanism for Chemical Exchange[7]

The ROESY, TOCSY and EXSY data suggest that the intermediate species formed upon the addition of pyridine to Pd(6,6'-Me$_2$bpy)(OAc)$_2$ is the Pd(κ^1-6,6'-Me$_2$bpy)(pyridine)(OAc)$_2$ (**9**) complex. The 6,6'-Me$_2$bpy ligand has been shown by the EXSY experiments to engage in intramolecular chemical exchange in which the two pyridyl rings interconvert with each other. Additionally, the pyridine ligand of **9** appears sharp and the TOCSY experiment reveals an absence of chemical exchange. Therefore, the pyridine ligand experiences the same chemical environment regardless of intramolecular exchange process of the 6,6'-Me$_2$bpy ligand. A possible mechanism that satisfies these observations is an intramolecular ligand substitution in which the pyridyl rings of 6,6'-Me2bpy alternate between uncoordinated and coordinated to Pd. Evidence for this mechanism of exchange has been presented previously in the context of Pd(κ^1-DAF)$_2$(OAc)$_2$ complexes interconverting between different isomers.[8]
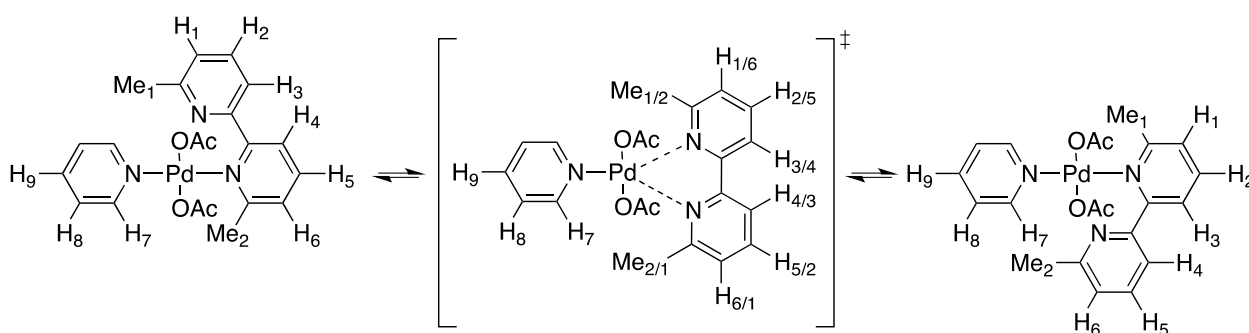
Scheme B 1: Proposed Mechanism for Chemical Exchange Between 9-H$_1$ and 9-H$_6$

B9. Crystal Structure Details for Pd(κ^1-Me$_2$DAF)(pyridine)(OAc)$_2$[8]
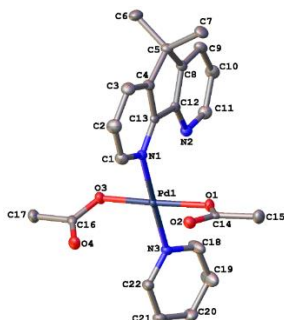
Figure B 18: A molecular drawing of Pd(κ^1-Me$_2$DAF)(pyridine)(OAc)$_2$ shown with 50% probability ellipsoids. All H atoms are

omitted.

Data Collection

A yellow crystal with approximate dimensions $0.321 \times 0.25 \times 0.078$ mm^3 was selected under oil under ambient conditions and attached to the tip of a MiTeGen MicroMount©. The crystal was mounted in a stream of cold nitrogen at 100(1) K and centered in the X-ray beam by using a video camera.

The crystal evaluation and data collection were performed on a Bruker Quazar SMART APEXII diffractometer with Mo K$_\alpha$ ($\lambda = 0.71073$ Å) radiation and the diffractometer to crystal distance of 4.96 cm.

The initial cell constants were obtained from three series of ω scans at different starting angles. Each series consisted of 12 frames collected at intervals of 0.5° in a 6° range about ω with the exposure time of 1 second per frame. The reflections were successfully indexed by an automated indexing routine built in the APEXII program suite. The final cell constants were calculated from a set of 6033 strong reflections from the actual data collection.

The data were collected by using the full sphere data collection routine to survey the reciprocal space to the extent of a full sphere to a resolution of 0.70 Å. A total of 19478 data were harvested by collecting 3 sets of frames with 0.5° scans in ω with exposure times of 2 sec per frame. These redundant datasets were corrected for Lorentz and polarization effects. The absorption correction was based on fitting a function to the empirical transmission surface as sampled by multiple equivalent measurements.[9]

Structure Solution and Refinement

The systematic absences in the diffraction data were uniquely consistent for the space group $P2_1/c$ that yielded chemically reasonable and computationally stable results of refinement.[10],[11],[12]

A successful solution by the direct methods provided most non-hydrogen atoms from the E-map. The remaining non-hydrogen atoms were located in an alternating series of least-squares cycles and difference Fourier maps. All non-hydrogen atoms were refined with anisotropic displacement coefficients. All hydrogen atoms were included in the structure factor calculation at idealized positions and were allowed to ride on the neighboring atoms with relative isotropic displacement coefficients.

The final least-squares refinement of 275 parameters against 6447 data resulted in residuals R (based on F^2 for $I \geq 2\sigma$) and wR (based on F^2 for all data) of 0.0301 and 0.0722, respectively. The final difference Fourier map had one noticeable peak (ca. 1.55e/Å^3) in the vicinity of the Pd atom and was considered noise.

Summary Crystal Data for C$_{22}$H$_{23}$N$_3$O$_4$Pd (M =499.83): monoclinic, space group P2$_1$/c (no. 14), $a =$ 12.472(6) Å, $b =$ 8.829(5) Å, $c =$ 19.260(8) Å, $\beta =$ 90.22(3)°, $V =$ 2120.8(19) Å^3, $Z =$ 4, $T =$ 100.0 K, μ(Mo Kα) = 0.908 mm^{-1}, $Dcalc =$ 1.565 g/mm^3, 19478 reflections measured (3.266 $\leq 2\Theta \leq$ 61.312), 6447 unique ($R_{int} =$ 0.0355) which were used in all calculations. The final R_1 was 0.0301 (I > 2σ(I)) and wR_2 was 0.0722 (all data).

---

[8] Crystals obtained independently by JNJ

Table B 1: Crystal data and structure refinement for Pd(κ^1-Me$_2$DAF)(pyridine)(OAc)$_2$

Identification code	stahl192
Empirical formula	$C_{22}H_{23}N_3O_4Pd$
Formula weight	499.83
Temperature/K	100.0
Crystal system	monoclinic
Space group	P2$_1$/c
a/Å	12.472(6)
b/Å	8.829(5)
c/Å	19.260(8)
α/°	90
β/°	90.22(3)
γ/°	90
Volume/Å^3	2120.8(19)
Z	4
ρ_{calc}mg/mm^3	1.565
m/mm^{-1}	0.908
F(000)	1016.0
Crystal size/mm^3	$0.321 \times 0.25 \times 0.078$
Radiation	Mo Kα (λ = 0.71073)
2Θ range for data collection	3.266 to 61.312°
Index ranges	$-17 \leq h \leq 9, -12 \leq k \leq 12, -26 \leq l \leq 26$
Reflections collected	19478
Independent reflections	6447[R(int) = 0.0355]
Data/restraints/parameters	6447/0/275
Goodness-of-fit on F^2	1.063
Final R indexes [I>=2σ (I)]	R$_1$ = 0.0301, wR$_2$ = 0.0681
Final R indexes [all data]	R$_1$ = 0.0410, wR$_2$ = 0.0722
Largest diff. peak/hole / e Å^{-3}	1.55/-0.62

1. McDonald, R. I.; White, P. B.; Weinstein, A. B.; Tam, C. P.; Stahl, S. S., *Org Lett* **2011,** *13*, 2830-2833.
2. Pearson, D. M.; Conley, N. R.; Waymouth, R. M., *Adv.Synth. Catal.* **2011,** *353*, 3007-3013.
3. Gaussian 09, Revision C.01, Frisch, M. J.; Trucks, G. W.; Schlegel, H. B.; Scuseria, G. E.; Robb, M. A.; Cheeseman, J. R.; Scalmani, G.; Barone, V.; Mennucci, B.; Petersson, G. A.; Nakatsuji, H.; Caricato, M.; Li, X.; Hratchian, H. P.; Izmaylov, A. F.; Bloino, J.; Zheng, G.; Sonnenberg, J. L.; Hada, M.; Ehara, M.; Toyota, K.; Fukuda, R.; Hasegawa, J.; Ishida, M.; Nakajima, T.; Honda, Y.; Kitao, O.; Nakai, H.; Vreven, T.; Montgomery, J. A. Jr.; Peralta, J. E.; Ogliaro, F.; Bearpark, M.; Heyd, J. J.; Brothers, E.;Kudin, K. N.; Staroverov, V. N.; Keith, T.; Kobayashi, R.; Normand, J.; Raghavachari, K.; Rendell, A.; Burant, J. C.; Iyengar, S. S.; Tomasi, J.; Cossi, M.; Rega, N.; Millam, J. M.; Klene, M.; Knox, J. E.; Cross, J. B.; Bakken, V.; Adamo, C.; Jaramillo, J.; Gomperts, R.; Stratmann, R. E.; Yazyev, O.; Austin, A. J.; Cammi, R.; Pomelli, C.; Ochterski, J. W.; Martin, R. L.; Morokuma, K.; Zakrzewski, V. G.; Voth, G. A.; Salvador, P.; Dannenberg, J. J.; Dapprich, S.; Daniels, A. D.; Farkas, O.; Foresman, J. B.; Ortiz, J. V.; Cioslowski, J.; Fox, D. J. Gaussian, Inc., Wallingford CT, 2010.
4. Becke, A.D. *J. Chem. Phys.* **1993**, *98*, 1372 –1377.
5. Lee, C.; Yang, W.; Parr, R. G. *Phys. Rev. B* **1988**, *37*, 785 – 789.
6. a) Feller, D. *J. Comp. Chem.*, **1996**, *17*(13), 1571-1586. b) Schuchardt, K.L.; Didier, B.T.; Elsethagen, T.; Sun, L.; Gurumoorthi, V.; Chase, J.; Li, J.; and Windus, T.L. *J. Chem. Inf. Model.*, **2007**, *47*(3), 1045-1052
7. Liu, G. S.; Stahl, S. S., *J. Am. Chem. Soc.* **2007,** *129*, 6328-6335.
8. White, P. B.; Jaworski, J. N.; Fry, C. G.; Dolinar, B. S.; Guzei, I. A.; Stahl, S. S. *J. Am. Chem. Soc. 138*, 4869-4880.
9. Bruker-AXS. (2007-2013) APEX2 (Ver. 2013.2-0), SADABS (2012-1), and SAINT+ (Ver. 8.30C) Software Reference Manuals. Bruker-AXS, Madison, Wisconsin, USA.
10. Sheldrick, G. M. (2008) SHELXL. *Acta Cryst.* **A64**, 112-122.
11. Guzei, I.A. (2013). Internal laboratory computer programs Gn.
12. Dolomanov, O.V.; Bourhis, L.J.; Gildea, R.J.; Howard, J.A.K.; Puschmann, H. "OLEX2: a complete structure solution, refinement and analysis program". *J. Appl. Cryst.* (2009) **42**, *339-341*.

Appendix C: Supporting Information for Chapter 5

C1. Materials and Methods

Allylbenzene, pyridine, EtOAc, AcOD-d_4, Pd(OAc)$_2$, 4,5-diazafluore-9-one (DAF) and NaOAc were purchased from Sigma Aldrich and used without additional purification. 1,4-Dioxane-d_8 was purchased from Cambridge Isotope Laboratories. (Z)-4-hexenyltosylamide was synthesized according to the literature.[1a] Inhibitor free 1,4-dioxane was purchased as anhydrous 99.8% and stored under an inert atmosphere as 1,4-dioxane is a peroxide forming solvent. Ultra pure toluene was obtained from a solvent purification system using columns of Al$_2$O$_3$ under argon. Aerobic Pd-catalyzed kinetic data was obtained using a custom 48-well reaction apparatus that enabled reactions to be performed under a constant atmosphere of O$_2$ (approx 1 atm) with controlled temperature and orbital agitation. Kinetic data for the aza-Wacker reaction was analyzed by using 1,3,5-trimethoxybenzene. 50-100 μL aliquots were quenched by filtered over a plug of silica and subsequently washed with EtOAc. The solvent was removed with a centrifugal evaporator and the yield was measured by ^{1}H NMR spectroscopy. Kinetic dependencies were obtained by monitoring O$_2$ gas consumption using six 25 mL round-bottom reaction vessels interfaced with pressure transducers.[1] Temperature and mixing was controlled by a large oil bath on top of a hot plate. Kinetic data for the acetoxylation reaction was analyzed by using PhNO$_2$ as an internal standard. 50 μL aliquots were quenched with a stock solution of 0.1 M pyridine in EtOAc and analyzed directly with gas-chromatography. NMR Characterization of was performed on a Bruker Avance-500 spectrometer equipped with BBFO+ probe. Stock solutions were made daily and with volumetric glassware cleaned and stored at room temperature. ^{1}H NMR chemical shifts are reported in part per million (ppm) relative to tetramethylsilane (TMS) ^{15}N chemical shifts are referenced externally to ^{1}H spectrum and calibrated to liquid ammonia (0.00 ppm). The sample temperature was calibrated with an external 4% MeOH in MeOD-d_3 reference. All spectra were recorded quantitatively (recycle delay of $\geq 5*T_1$). UV-visible time course experiments were performed using a Cary 60 UV-Vis spectrometer and a 2 mm cuvette at room temperature. Crystal diffraction data collected by University of Wisconsin, Madison X-ray Crystallography Center. Elemental data collection was performed by Robertson Microlit Laboratories.

C2. NMR Characterization of [Pd^I(μ-DAF)(OAc)]$_2$ in the Acetoxylation Reaction
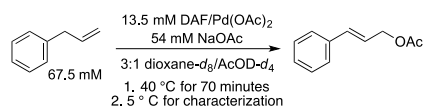
The formation of the Pd^I complex species was investigated by performing an acetoxylation experiment in a J-Young tube with 13.5 mM DAF/Pd(OAc)2, 54 mM NaOAc, 67.5 mM allylbenzene at 40 °C with 3.2 atm O$_2$ in a solvent mixture of 3:1 1,4-dioxane-d_8/AcOD-d_4. The DAF speciation and product formation was monitored to approximately 30% yield after 70 minutes. The reaction was then cooled in the spectrometer to 5 °C and the DAF speciation was rigorously characterized.

NMR Characterization of [(DAF)Pd^I(OAc)]$_2$ • xHOAc (**D** • xHOAc):
^{1}H NMR (500 MHz, 3:1 dioxane-d_8/AcOD-d_4, 5 °C 8.63 (dd, $^2J_{HH}$ = 5.8 Hz, $^3J_{HH}$ = 1.3 Hz, 4H, CH), 8.21 (dd, $^2J_{HH}$ = 7.5, $^3J_{HH}$ = 1.3 Hz, 4H), 7.54 (dd, $^2J_{HH}$ = 7.5, $^2J_{HH}$ = 5.8 Hz, 4H). ^{13}C (126 MHz, 3:1 dioxane-d_8/AcOD-d_4, 24 °C) 190.5, 167.8, 162.1, 136.9, 134.3, 130.5 ppm. ^{15}N (50.7 MHz, 3:1 dioxane-d_8/AcOD-d_4 5 °C) 217 ppm. (Acetate peaks not reported)
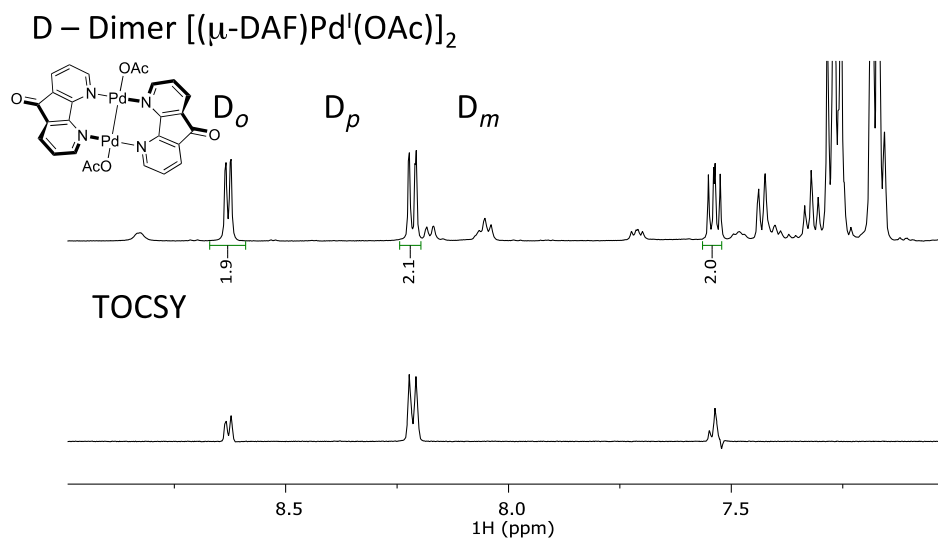
Figure C 1: TOCSY of o-CH of in situ formed [(DAF)Pd^I(OAc)]$_2$ • xHOAc. Irradiated 8.626 ppm. ns = 16, d1 = 1 s, pulse width = 12 s, mix = 0.08s, 5 °C
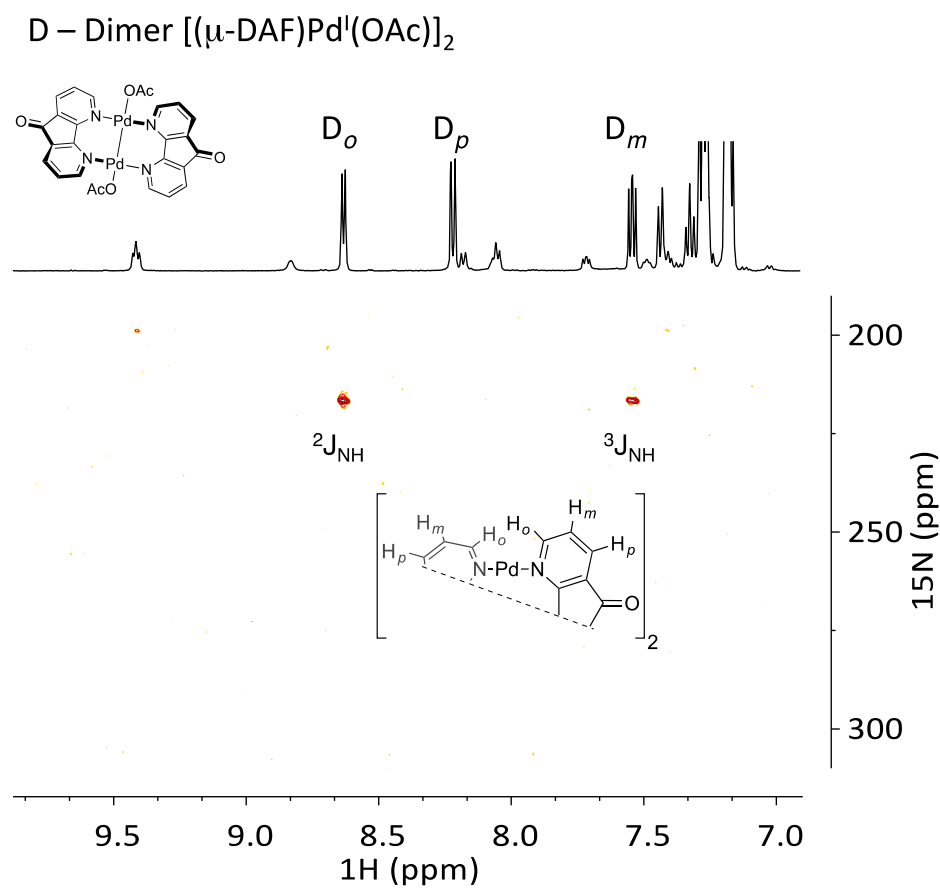
Figure C 2: ^{1}H-^{15}N HMBC of in situ formed [(DAF)Pd^I(OAc)]$_2$ • xHOAc at 5 °C. ns = 32, ni = 350 ppm, sw(f1) = 400 ppm, dof = 250 ppm, d1 = 4s, $^nJ_{HN}$ = 8 Hz.
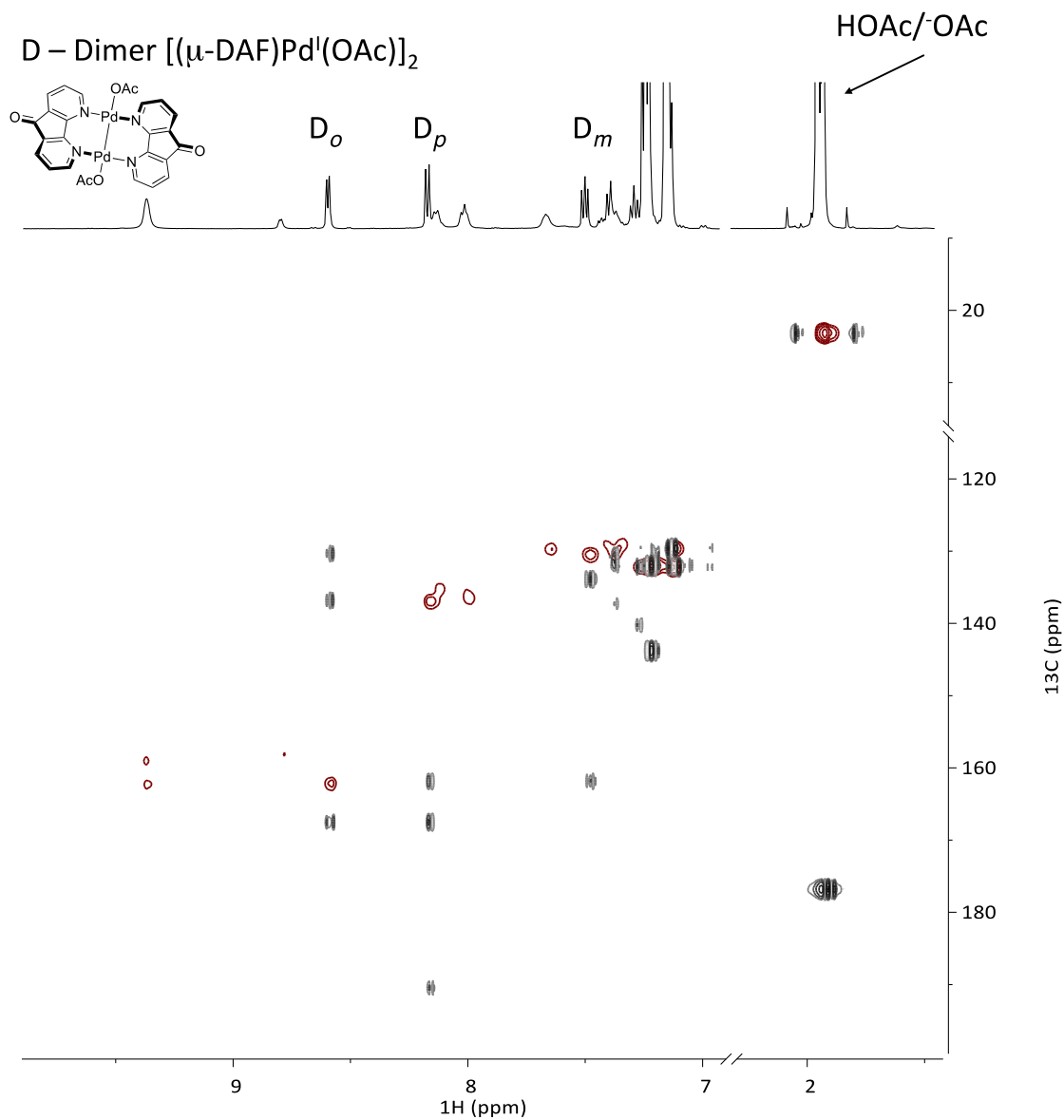
Figure C 3: ^{1}H-^{13}C HSQC and HMBC of in situ formed [(DAF)Pd^I(OAc)]$_2$ • xHOAc at 5 °C. Abbreviated overlay. HSQC (red): ns = 2, ni = 256, ds = 16, sw(f1) = 220 ppm, dof = 110 ppm, d1 = 1.5 s, $^1J_{CH}$ = 165 Hz. HMBC (grey): ns = 16, ni = 512, ds = 16, sw(f1) = 220 ppm, dof = 110 ppm, d1 = 2 s, $^1J_{CH}$ = 120 Hz, $^nJ_{CH}$ = 170 Hz.

C3. NMR Characterization of [Pd^I(μ-DAF)(OAc)]$_2$ in Amidation Reaction
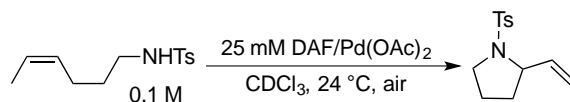
The reaction was performed in CDCl3 as to observe the Pd(I) species formed in situ at concentrations that gave adequate signal to noise. Reaction was performed at 24 °C under air by combined two stock solutions of substrate (0.2 M) and catalyst (50 mM) and injecting into the spectrometer at -35 °C within 5 minutes of mixing. The reaction turned from yellow to red within 1 minute of mixing. A single new DAF species was observed was and subsequently characterized by quantitative 1D 1H as well as 1H-15N HMBC, 1H-13C HSQC/HMBC. Analysis was possible by NMR with CDCl3 however after ~15 minutes at room temperature, degradation of the complex was observed as the complex does not seem to be indefinitely stable in CDCl3 as well as other halogenated solvents. There was two upfield 15N chemical shifts observed which we attribute to the chemical shift of the nitrogen of the tosylamide derived starting material and product, see Figure C7 below.

[(DAF)Pd^I(OAc)]$_2$ • 2HOAc: ^{1}H NMR (500 MHz, CDCl$_3$, -35 °C) 8.73 (dd, $^2J_{HH}$ = 5.8, $^3J_{HH}$ = 1.3 Hz, 4H), 8.13 (dd, $^2J_{HH}$ = 7.5, $^3J_{HH}$ = 1.3 Hz, 4H), 7.47 (dd, $^2J_{HH}$ = 7.5, $^2J_{HH}$ = 5.8 Hz, 4H), 1.90 (s, 12H). ^{13}C (126 MHz, CDCl$_3$, -35 °C) 186.7, 177.9, 163.2, 158.7, 133.5, 129.8, 126.9, 24.88. ^{15}N (50.7 MHz, CDCl$_3$, -35 °C) 219.40 ppm
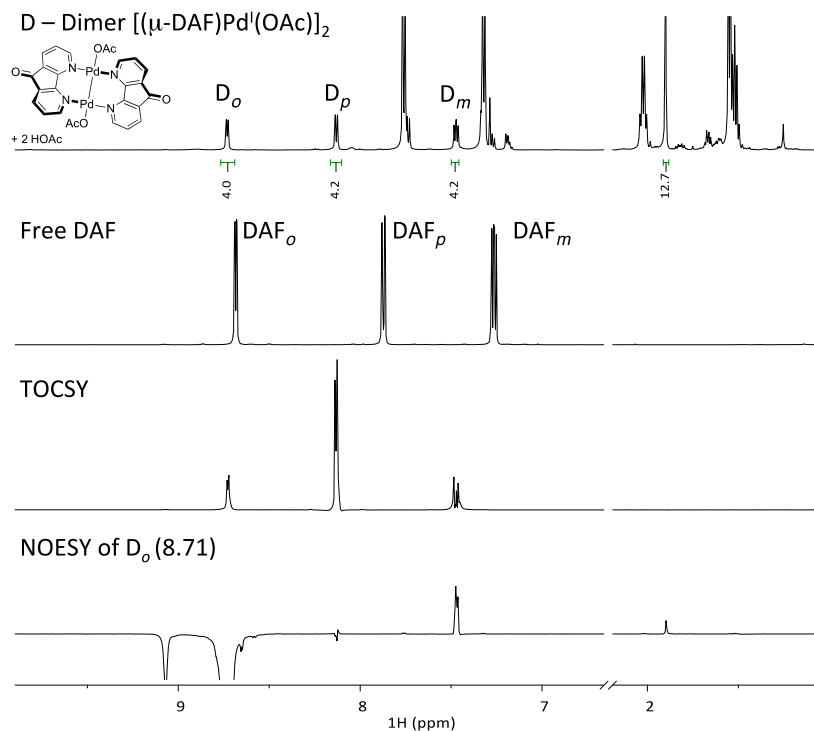
Figure C 4: Analysis of amidation reaction mixture with ^{1}H NMR, TOCSY and NOESY. Reaction was performed as above in CDCl$_3$ and analyzed at 0 °C. Free DAF included in stack plot for comparison. ^{1}H 1D TOCSY selected peak at 8.73 ppm, ns = 16, ds = 2, d1 = 1s, mix = 0.08s. ^{1}H 1D NOESY ns = 800, ds = 2, d1 = 3s, mix = 0.5s. NOE from o-CH of Pd(I) dimer synthesized in situ can be seen to the acetate. The integrations are 4:12 because there is free acetic acid present that is freely exchanging after reduction. This integration is because the catalyst used was DAF/Pd(OAc)$_2$.
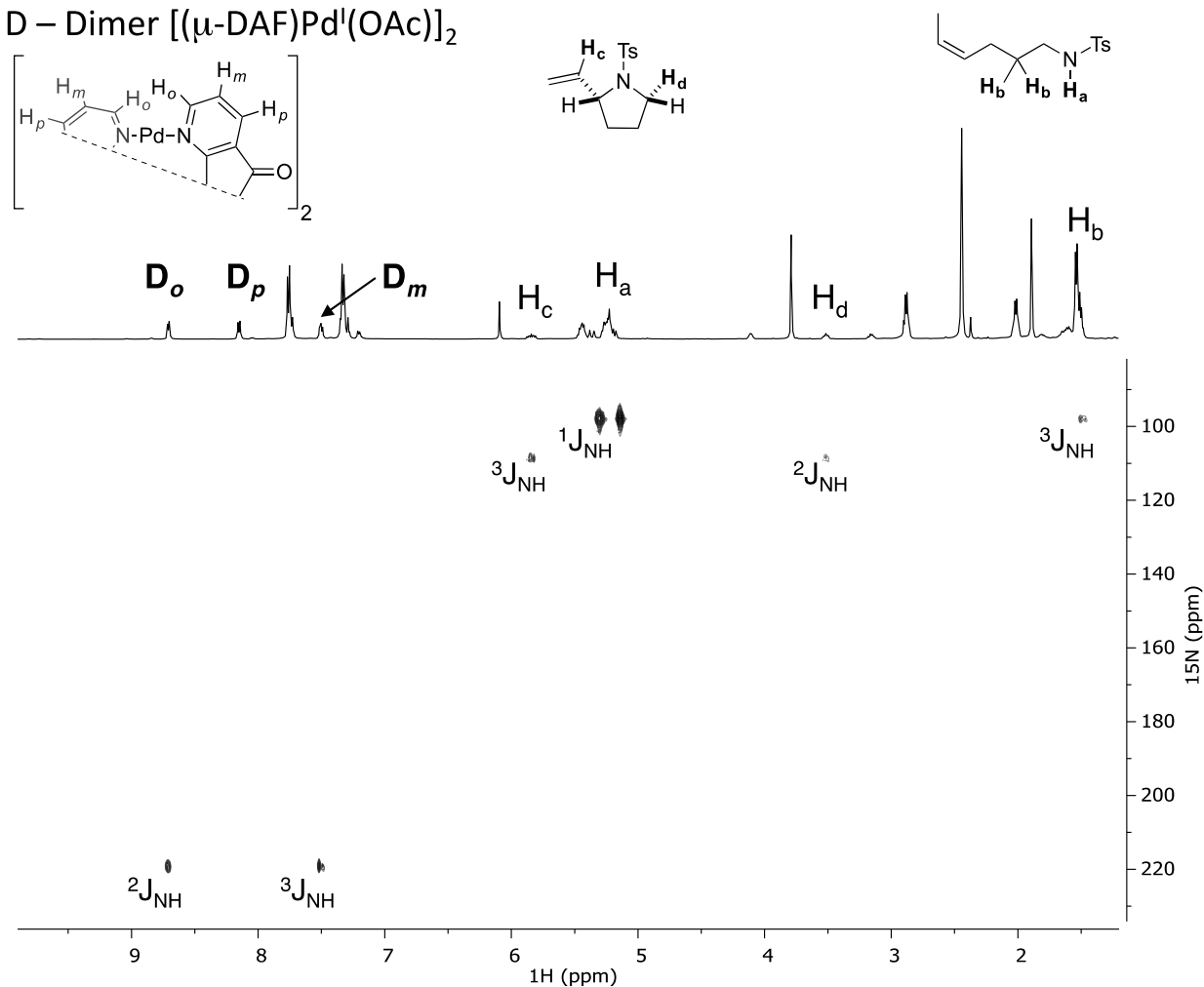
Figure C 5: ^{1}H-^{15}N HMBC of amidation reaction mixture at -35 °C. Analysis performed at -35 °C of reaction mixture from above. [(DAF)Pd^I(OAc)]$_2$-2HOAc (219.40 ppm), (Z)-4-hexenyltosylamide (98.24 ppm, ^{1}J$_{HN}$ = 83 Hz) and 1-tosyl-2-vinyl-pyrrolidine (108.72 ppm) all give diagnostic ^{15}N cross peaks. The ^{1}J$_{HN}$ for starting material is observed because of the high concentration (0.1 M) present in the solution. ns = 8, ni = 256 ppm, sw(f1) = 400 ppm, dof = 250 ppm, d1 = 3s, ^{n}J$_{HN}$ = 4 Hz.
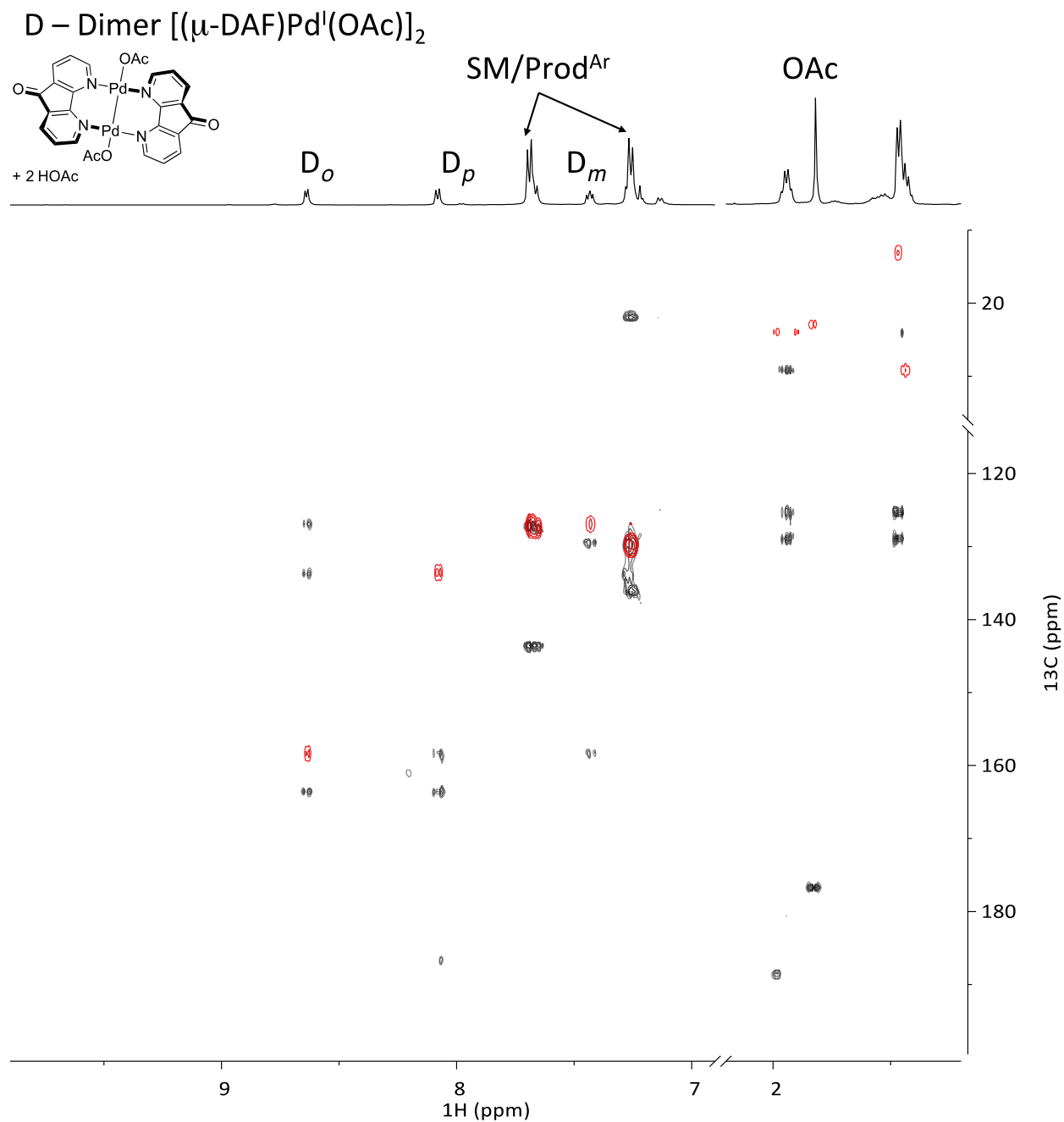
Figure C 6: ^{1}H-^{13}C HSQC and HMBC of amidation reaction mixture at - 0 °C. Abbreviated overlay. HSQC (red): ns = 8, ni = 256, ds = 16, sw(f1) = 250 ppm, dof = 125 ppm, d1 = 1.5 s, ^{1}J$_{CH}$ = 145 Hz. HMBC (grey): ns = 16, ni = 512, ds = 16, sw(f1) = 250 ppm, dof = 125 ppm, d1 = 1.5 s, ^{1}J$_{CH}$ = 120 Hz, ^{n}J$_{CH}$ = 170 Hz.

NMR Characterization (Z)-4-hexenyltosylamide. [1]H and ^{13}C matched that previously reported.[2,3]

^{1}H NMR (500 mHz, CDCl$_3$, 24 °C) 7.77 ppm (d, $^3J_{HH}$ = 8 Hz, 2H, CH), 7.33 (d, $^3J_{HH}$ = 8 Hz, d, CH), 5.48 ppm (m, 1H), 5.30 ppm (m, 1H), 4.38 (br s, 1H), 2.98 (q, $^3J_{HH}$ = 6.8 Hz, 2H, CH$_2$), 2.45 ppm (s, 3H), 2.05 ppm (q, $^3J_{HH}$ = 7.3 Hz. 2H, CH$_2$), 1.56 ppm (m, 5H, -CH$_3$, -CH$_2$-), [15]N (50.7 MHz, CDCl$_3$, 24 °C) 98.24 ppm ($^1J_{NH}$ = 84 Hz)
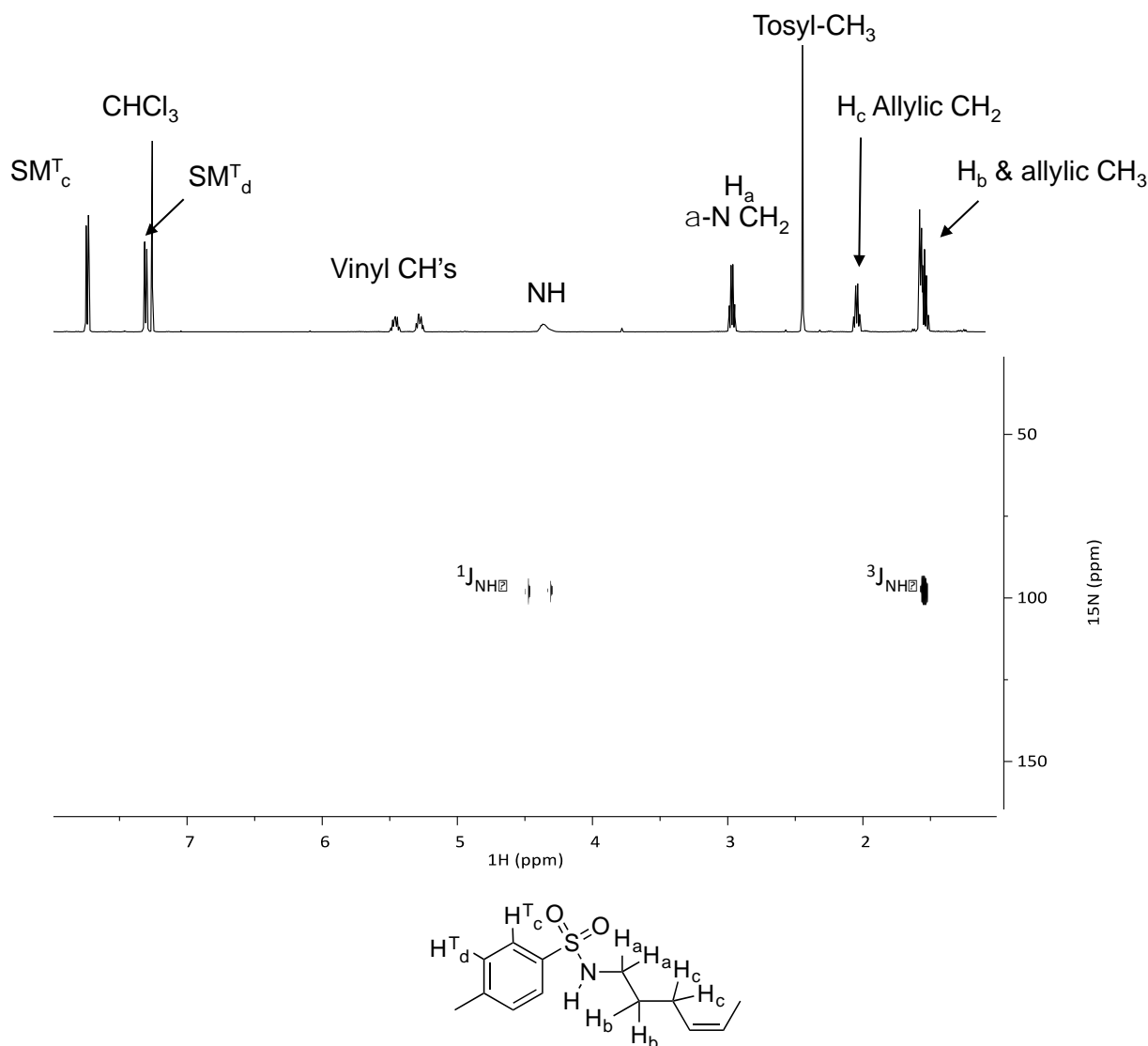
Figure C 7: ^{1}H-^{15}N HMBC of the starting material (Z)-4-Hexenyltosylamide. ns = 8, ni = 512, ds = 16, d1 = 3, sw(f1) = 400 ppm,

dof = 250 ppm

1-Tosyl-2-vinyl-pyrrolidine NMR Characterization of Product matched that reported in literature. A [15]N δ = 108.72 ppm was observed.[2]

C4. Independent Synthesis, Characterization of Pd(I) Dimer, [Pd^I(μ-DAF)(OAc)]$_2$
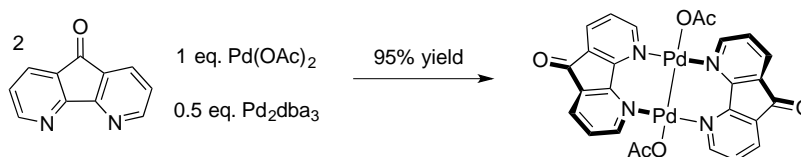
In a glovebox, 4,5-diazafluoren-9-one, (DAF, 2 eq, 73.2 mg, 0.4 mmol), Pd(OAc)$_2$ (1 eq, 44.8 mg, 0.2 mmol), and Pd$_2$dba$_3$ (0.5 eq, 91.5 mg, 0.1 mmol) were added to a 25 mL scintillation vial with stir bar. 20 mL of acetonitrile were added and mixed at room temperature. The solution changed from deep purple to red and cloudy after 5 minutes. After 4 hours, the reaction mixture was collected using a fine glass filter frit and washed several times with acetonitrile, benzene, chloroform and pentane. The compound was then dried *in vacuo* to give a 95% yield of [(DAF)Pd^I(OAc)]$_2$. The compound has had marginal solubility in CDCl$_3$ and was not indefinitely stable in halogenated solvents and so NMR characterization was performed at -35 °C. The compound readily decomposes in DMSO however and has negligible solubility in other solvents. The compound appears to be indefinitely stable on the bench top.

NMR characterization of Pd(I) Dimer, [(DAF)Pd^I(OAc)]$_2$: ^{1}H NMR (500 MHz, CDCl$_3$, -35 °C, TMS) 8.79 (dd, $^2J_{HH}$ = 6 Hz, $^3J_{HH}$ = 1.2 Hz, 4H), 8.14 (dd, $^2J_{HH}$ = 7.60 Hz, $^3J_{HH}$ = 1.3 Hz, 4H,), 7.50 (dd, $^2J_{HH}$ = 7.6 Hz, $^2J_{HH}$ = 5.0 Hz), 1.83 (s, 6H) 13C (126 MHz, CDCl$_3$, -35 °C) 158.62, 133.38, 126.75, 24.85, 163.46, 129.52, 186.61, 177.76 ^{15}N (50.7 MHz, CDCl$_3$, -35 °C) 220.74 ppm.

Elemental Analysis: Expected – 44.91% C, 2.61% H, 8.06% N; Experimental – 43.85%, 2.50% H, 7.62% N
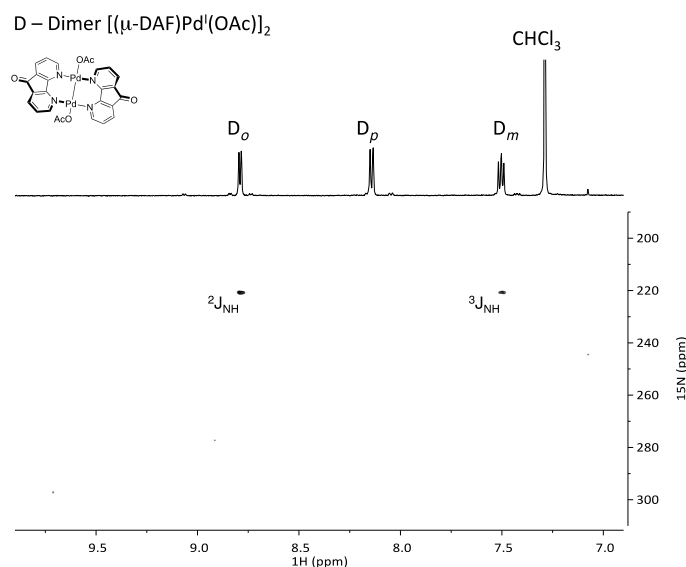
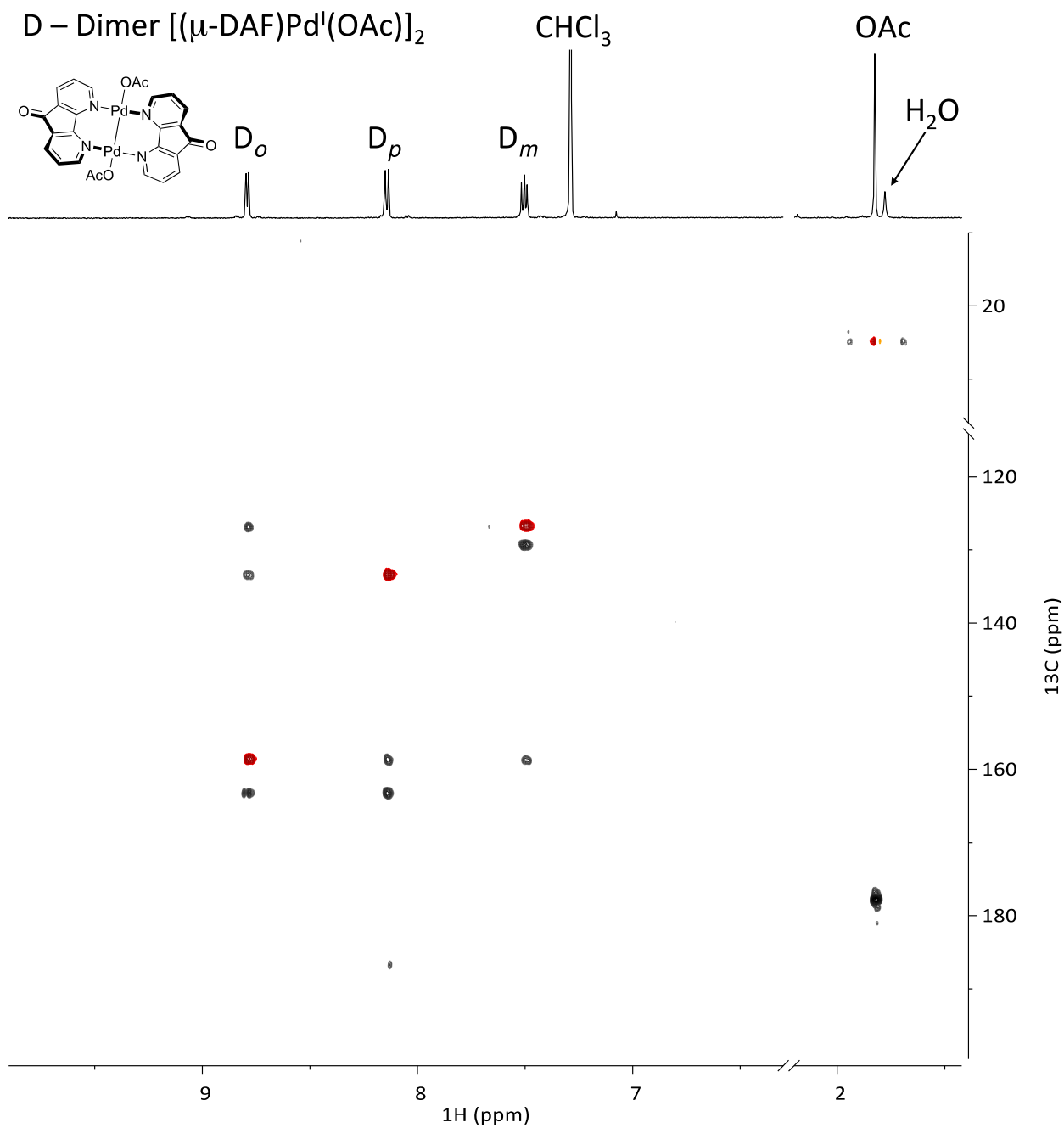**Figure C 8:** ^{1}H-^{15}N HMBC of [(DAF)Pd^I(OAc)]$_2$ at -35 °C. Cross peaks observed for the $^2J_{NH}$ and $^3J_{NH}$ at at 220.74 ppm. ns = 16, d1 = 3s, ni = 256, sw = 200, o1p = 250 ds = 16, $^nJ_{NH}$ = 7 Hz
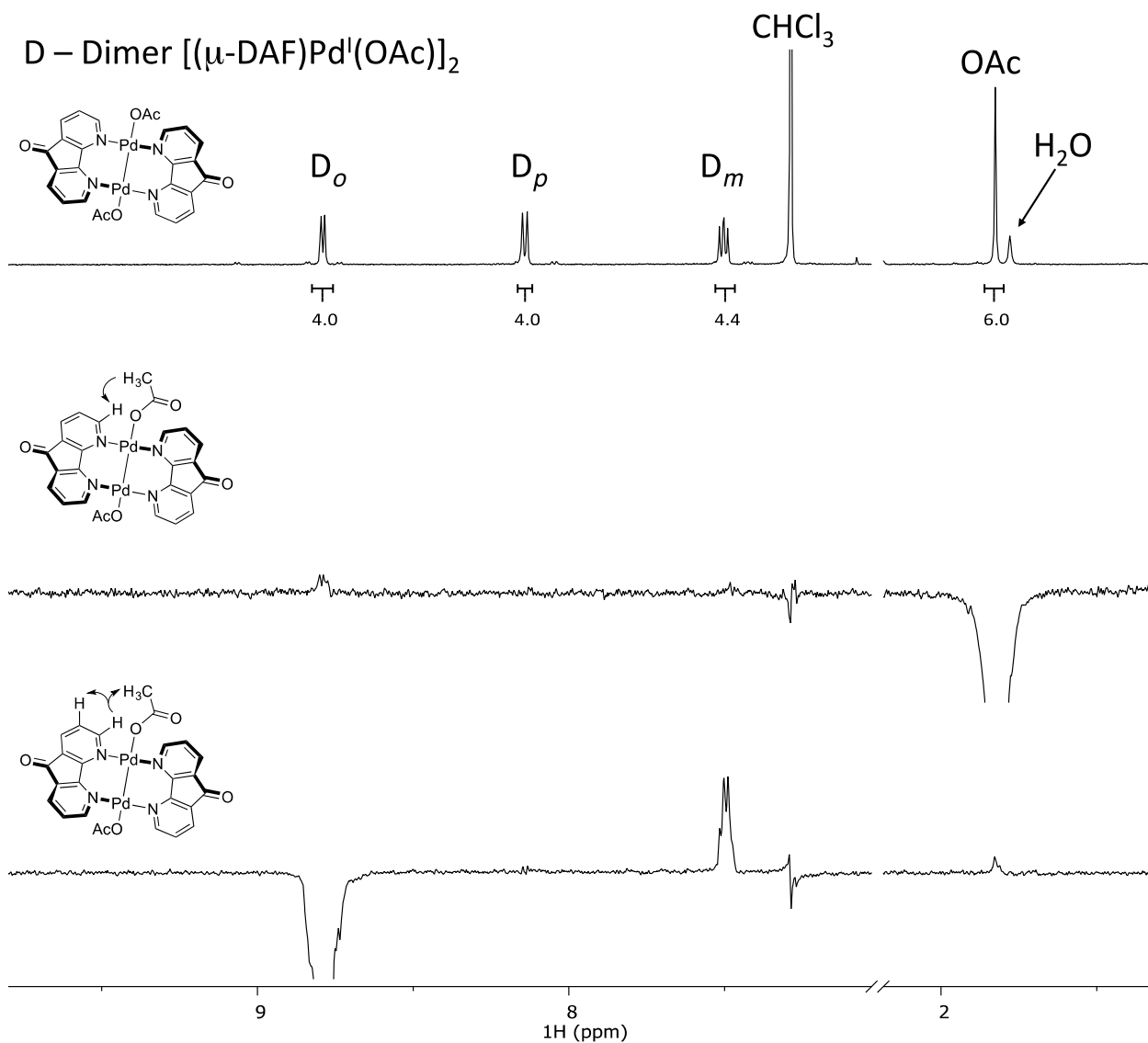
Figure C 9: ^{1}H-^{1}H 1D ROESY experiments between o-CH of DAF and acetate. D_o (8.76 ppm) and OAc (1.83 ppm) were selected. Through-space interactions are revealed between the D_o and D_m as well as D_o and OAc. ns = 1600, d1 = 3s, mix = 0.2 s, spinlock = 2.5 kHz.

Figure C 10: ¹H-¹³C HSQC and HMBC of [(DAF)Pdᴵ(OAc)]₂ at -35 °C. HSQC (red) ns = 8, ni = 512, ds = 16, sw(f1) = 250 ppm, dof = 125 ppm, d1 = 1.5 s, $^1J_{CH}$ = 145 Hz. HMBC (grey): ns = 24, ni = 256, ds = 16, sw(f1) = 250 ppm, dof = 125 ppm, d1 = 2 s, $^1J_{CH}$ = 120 Hz, $^nJ_{CH}$ = 170 Hz.

C5. UV-Vis Characterization of Pd Species In Solution

Initial UV-Vis experiments were performed on the amidation reaction and extinction coefficients were determined in toluene. DAF alone had two strong absorbances at 304 nm (ε = 6.35 ABS mM^{-1} cm^{-1}) and 317 nm (ε = 6.35 ABS mM^{-1} cm^{-1}). We attribute these two observed peaks to the excitation of an electron from degenerate orbitals of the pyridyl ring into the carbonyl π^* or the pyridyl $\pi -> \pi*$ their vibrational fine structure (see below). Pd(OAc)$_2$ gave a broad peak at 398 nm and an extinction coefficient of ε = 0.2782 ABS mM^{-1} cm^{-1}. We believe this transition corresponds to several metal-to-ligand charge transfers based on calculations (see below) and is consistent with what other investigators have observed and proposed.[4] A similar extinction coefficient of ε = 0.376 ABS mM^{-1} cm^{-1} for Pd(OAc)$_2$ in 3:1 AcOH/Dioxane was observed. Under catalytic conditions, the 398 nm Pd(OAc)$_2$ disappears under the enormous DAF peaks due to the small exctinction coefficient of Pd(OAc)$_2$ relative to the DAF. The DAF peaks are also off the scale under catalytic conditions. The peak dispersion between Pd^I and the DAF ligand enable it to be observed however an extinction coefficient could not be obtained for the Pd^I species due to its insolubility once crystallized.
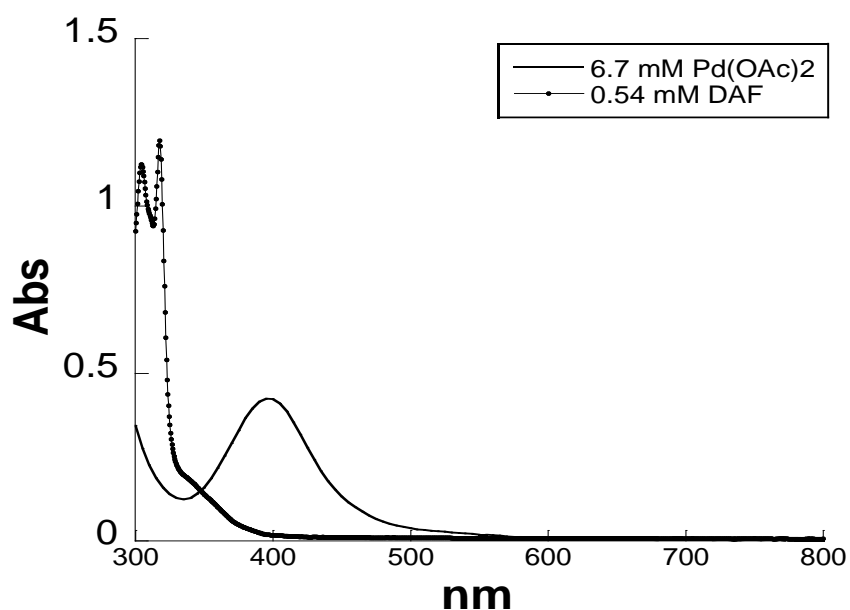
Figure C 11: Sample UV-Vis spectra of DAF and Pd(OAc)$_2$ in toluene.

An extinction coefficient for [Pd^I(μ-DAF)(OAc)]$_2$ was determined by using the independently synthesized compound ([Eq. (5)] in the manuscript). The maximum accessible concentration of the Pd^I complex in 3:1 dioxane/AcOH is 2.5 mM. Beer's Law behavior was observed for solutions of this complex below this concentration (**Figure C 12**).
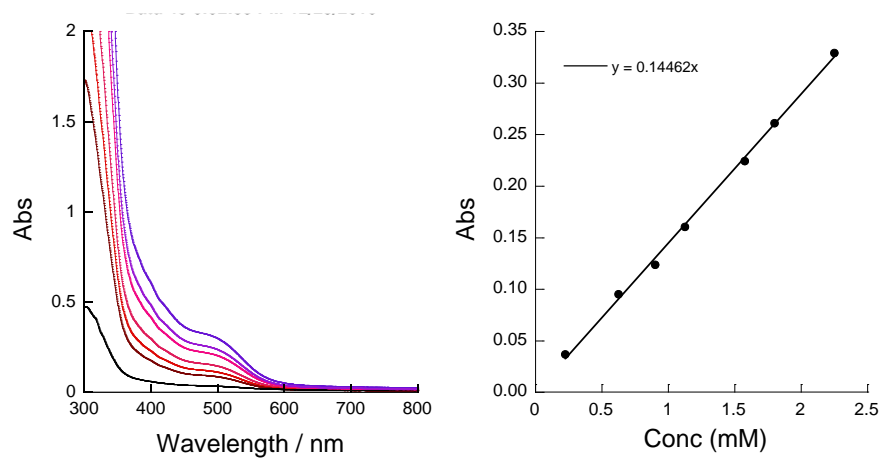
Figure C 12: Beer's Law Plot for UV-visible spectra of the Pd^I dimer [Pd^I(μ-DAF)(OAc)]$_2$ obtained in a quartz cell with 1 mm path length.

C6. Kinetic Competence of [Pd^I(μ-DAF)(OAc)]$_2$ versus DAF/Pd(OAc)$_2$

We found that the Pd^I dimer was soluble in pure acetic acid up to 17 mM which enabled a direct kinetic comparison with DAF/Pd(OAc)$_2$ in pure acetic acid. Initiating the reaction with Pd^I provided an initial rate that was similar to the post-burst rate when the reaction was initiated with DAF/Pd(OAc)$_2$.
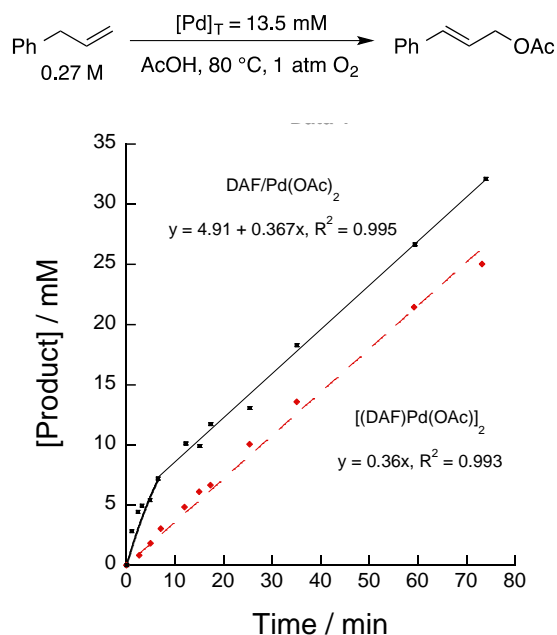
Figure C 13: Kinetic comparison of the DAF/Pd(OAc)$_2$ and [Pd^I(μ-DAF)(OAc)]$_2$ in the acetoxylation reaction 13.5 mM of DAF/Pd(OAc)$_2$ or 6.75 mM [Pd^I(μ-DAF)(OAc)]$_2$ was utilized to provide [Pd]$_T$ = 13.5 mM in each case.

C7. Reaction of [Pd^I(μ-DAF)(OAc)]$_2$ Dimer with O$_2$

A 3:1 Dioxane/AcOH solution with 2.5 mM [Pd^I(μ-DAF)(OAc)]$_2$ 54 mM NaOAc was subjected to an atmosphere of O$_2$ at 80 °C for two hours. The UV-vis spectrum was acquired prior to heating using a 1 mm quartz cuvette to give the characteristic absorbance at 475 nm. The UV-vis spectrum was then again recorded at 2 hours after a substantial color change was observed from red to yellow. The yellow solution provided an absorbance spectrum consistent of 5 mM DAF/Pd(OAc)$_2$.
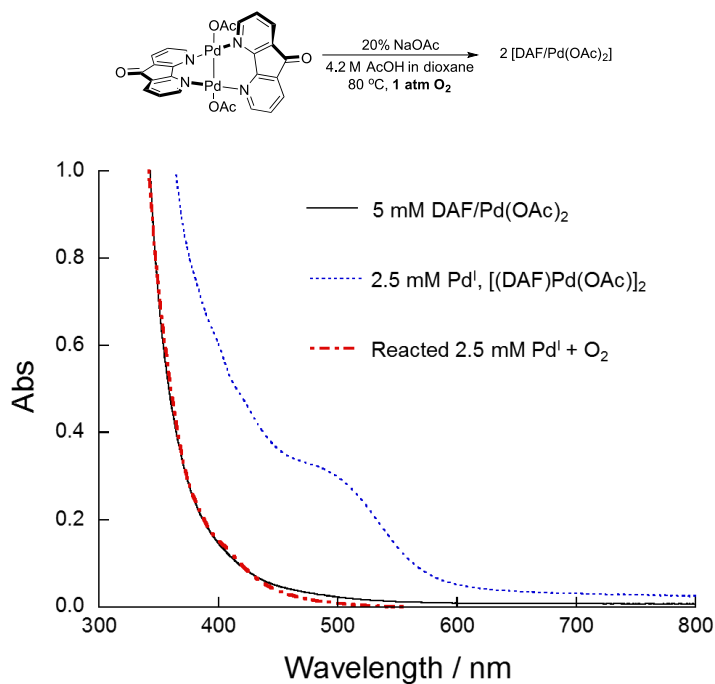
Figure C 14: UV-visible spectra of the Pd^I before and after subjection to aerobic oxidation conditions as well as compared to DAF/Pd(OAc)$_2$.

C8. Computational Details for UV-Vis Calculations

All geometries were fully optimized via density functional theory[5] using the CAM-B3LYP functional, LANL2TZ(f) basis set and effective core potential[6] for palladium and 6-31g(d) basis set for all other atoms using Gaussian09. [7] The nature of the stationary points were verified by computing analytical frequencies of all structures.[8] TD-DFT calculations were performed using the CAM-B3LYP functional at the optimized geometries, employing the same basis set for palladium and the 6-311G(2df,p) basis set for other atoms. The SMD continuum solvation model was used to model the effects of dioxane.[9] The computed epsilon value for complex ε = 988 ABS M^{-1} cm^{-1} was estimated by viewing the predicted UV-visible spectrum in Gaussview using a 1 cm^{-1} gaussian fit.

Key Computed UV-Visible Transitions
4,5-Diazafluoren-9-one
($\pi \rightarrow \pi^*$)
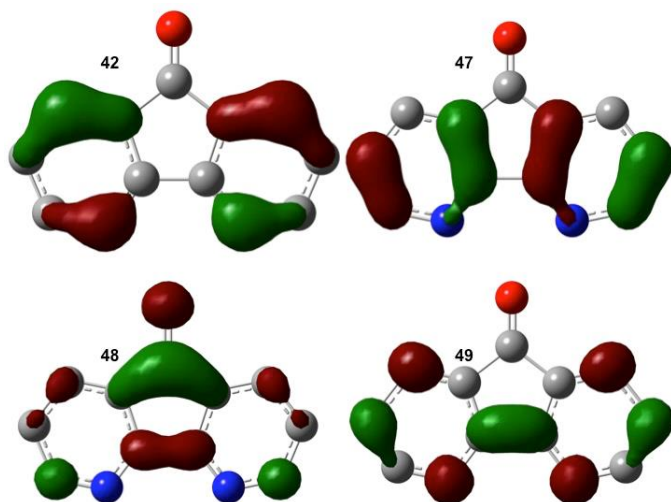Excited State 13: 1.000-A   4.6159 eV 268.60 nm f=0.2508 <S**2>=0.000

41A -> 50A	0.11144
42A -> 48A	**-0.28295**
47A -> 49A	**0.62216**
41B -> 50B	0.11144
42B -> 48B	**-0.28295**
47B -> 49B	**0.62216**

[Pd(OAc)$_2$]$_3$

3Pd(d(xy))→3Pd(d(x^2-y^2))

Excited State 18: 1.000-A   2.9586 eV 419.07 nm f=0.0037 <S**2>=0.000

    98A ->121A   -0.11284
    112A ->122A   0.22758
    113A ->123A   -0.22880
    116A ->123A   0.12643
    117A ->122A   -0.13917
    118A ->121A   0.49911
    98B ->121B   -0.11284
    112B ->122B   0.22758
    113B ->123B   -0.22880
    116B ->123B   0.12643
    117B ->122B   -0.13917
    118B ->121B   0.49911

Pd(d(xy))+2Pd(d(z^2))→Pd(d(x^2-y^2))
Pd(d(xy))+2Pd(d(z^2))→Pd(d(x^2-y^2))

Excited State 20: 1.000-A   3.0011 eV 413.13 nm f=0.0019 <S**2>=0.000

    99A ->121A   0.11212
    111A ->122A   0.14688
    111A ->123A   -0.15030
    113A ->121A   -0.12958
    114A ->121A   0.31370
    116A ->122A   -0.17408
    116A ->123A   0.14462
    117A ->121A   0.24926
    117A ->122A   0.15346
    117A ->123A   0.17030
    118A ->122A   -0.17238
    118A ->123A   0.18807
    99B ->121B   0.11212
    111B ->122B   0.14688
    111B ->123B   -0.15030
    113B ->121B   -0.12958
    114B ->121B   0.31370
    116B ->122B   -0.17408
    116B ->123B   0.14462
    117B ->121B   0.24926
    117B ->122B   0.15346
    117B ->123B   0.17030
    118B ->122B   -0.17238
    118B ->123B   0.18807

Pd(d(yz))+2Pd(d(z^2))→Pd(d(x^2-y^2))

Pd(d(xy))+Pd(d(yz))+Pd(d(z^2))→Pd(d(x^2-y^2))
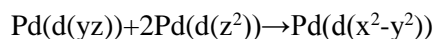
Excited State 21: 1.000-A   3.0039 eV 412.74 nm f=0.0020 <S**2>=0.000

100A ->121A	-0.11237
111A ->122A	0.13922
111A ->123A	0.13013
112A ->121A	-0.12620
115A ->121A	**0.31241**
116A ->121A	**-0.25488**
116A ->122A	0.15040
116A ->123A	0.17975
117A ->122A	0.17356
117A ->123A	-0.14205
118A ->122A	-0.17338
118A ->123A	-0.17104
100B ->121B	-0.11237
111B ->122B	0.13922
111B ->123B	0.13013
112B ->121B	-0.12620
115B ->121B	**0.31241**
116B ->121B	**-0.25488**
116B ->122B	0.15040
116B ->123B	0.17975
117B ->122B	0.17356
117B ->123B	-0.14205
118B ->122B	-0.17338
118B ->123B	-0.17104

2Pd(d(xz))+OAc(n)→Pd(d(x^2-y^2))

3Pd(d(xy))→2Pd(d(x^2-y^2))
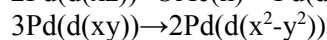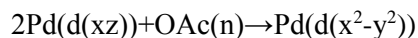
Excited State 23: 1.000-A   3.1104 eV 398.62 nm f=0.0014 <S**2>=0.000

102A ->121A	0.15244
111A ->122A	0.18872
112A ->121A	**0.25720**
112A ->122A	0.17758
112A ->123A	-0.11332
113A ->121A	0.19501
113A ->123A	0.17262
114A ->121A	0.14748
118A ->122A	**0.33095**
118A ->123A	-0.10285
120A ->123A	-0.10246
102B ->121B	0.15244
111B ->122B	0.18872
112B ->121B	**0.25720**
112B ->122B	0.17758
112B ->123B	-0.11332
113B ->121B	0.19501
113B ->123B	0.17262
114B ->121B	0.14748

118B ->122B   0.33095
  118B ->123B   -0.10285
  120B ->123B   -0.10246

$3Pd(d(yz))+OAc(n)\rightarrow 3Pd(d(x^2-y^2))$
$3Pd(d(xy))\rightarrow 2Pd(d(x^2-y^2))$
Excited State 24: 1.000-A   3.1127 eV 398.32 nm f=0.0013 <S**2>=0.000
  103A ->121A   -0.15241
  111A ->123A   0.21242
  112A ->121A   0.19018
  112A ->123A   -0.13357
  113A ->121A   -0.26077
  113A ->122A   0.15438
  113A ->123A   -0.12160
  115A ->121A   0.14070
  118A ->122A   0.10812
  118A ->123A   0.32910
  103B ->121B   -0.15241
  111B ->123B   0.21242
  112B ->121B   0.19018
  112B ->123B   -0.13357
  113B ->121B   -0.26077
  113B ->122B   0.15438
  113B ->123B   -0.12160
  115B ->121B   0.14070
  118B ->122B   0.10812
  118B ->123B   0.32910

$3Pd(d(z^2))\rightarrow 2Pd(d(x^2-y^2))$
$2Pd(d(z^2))\rightarrow 2Pd(d(x^2-y^2))$
Excited State 30: 1.000-A   4.7821 eV 259.27 nm f=0.0026 <S**2>=0.000
  118A ->121A   -0.18200
  119A ->122A   0.47376
  120A ->123A   0.47226
  118B ->121B   -0.18200
  119B ->122B   0.47376
  120B ->123B   0.47226

$2Pd(d(yz))+OAc(n)\rightarrow 3Pd(d(x^2-y^2))$
$3Pd(d(xy))\rightarrow 2Pd(d(x^2-y^2))$
Excited State 53: 1.000-A   5.5160 eV 224.77 nm f=0.0343 <S**2>=0.000
  106A ->121A   0.12218
  112A ->121A   0.39649
  114A ->121A   0.15611
  115A ->121A   0.17616
  115A ->123A   0.11814
  116A ->123A   -0.14935
  117A ->122A   -0.15775
  118A ->122A   -0.36522
 106B ->121B   0.12218
 **112B ->121B   0.39649**

```
114B ->121B      0.15611
115B ->121B      0.17616
115B ->123B      0.11814
116B ->123B     -0.14935
117B ->122B     -0.15775
118B ->122B     -0.36522
```

OAc(n)→3Pd(d(x^2-y^2))
3OAc(n)+3Pd(d(z^2))→ 2Pd(d(x^2-y^2))
 Excited State 70: 1.000-A   5.7802 eV 214.50 nm f=0.0386 <S**2>=0.000

```
104A ->123A      0.12390
106A ->121A      0.27475
107A ->121A      0.13525
109A ->123A     -0.27435
110A ->123A     -0.14023
111A ->122A     -0.21758
112A ->121A      0.12702
112A ->122A     -0.11190
112A ->123A      0.15782
113A ->122A     -0.15096
116A ->123A      0.14640
117A ->122A      0.13371
118A ->122A      0.18225
104B ->123B      0.12390
106B ->121B      0.27475
107B ->121B      0.13525
109B ->123B     -0.27435
110B ->123B     -0.14023
111B ->122B     -0.21758
112B ->121B      0.12702
112B ->122B     -0.11190
112B ->123B      0.15782
113B ->122B     -0.15096
116B ->123B      0.14640
117B ->122B      0.13371
118B ->122B      0.18225
```

106 109

112 113

114 115

116 117

118

119

120

121

122

123
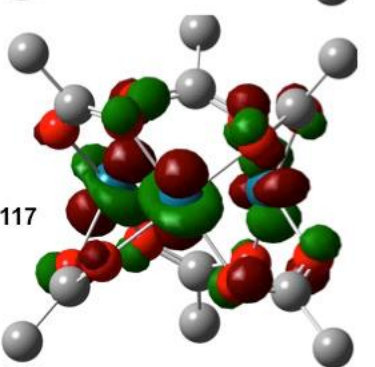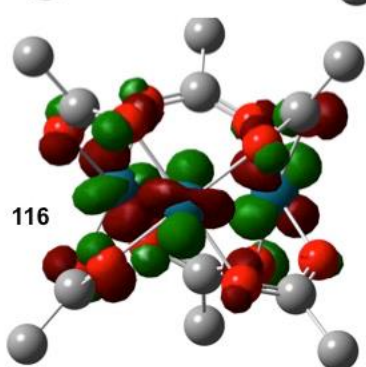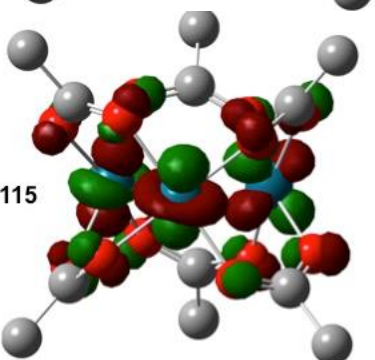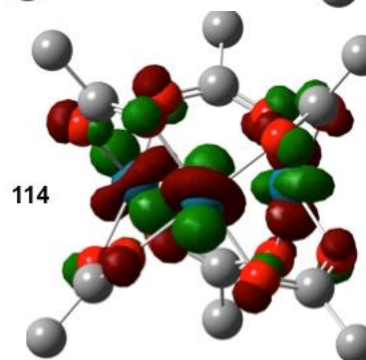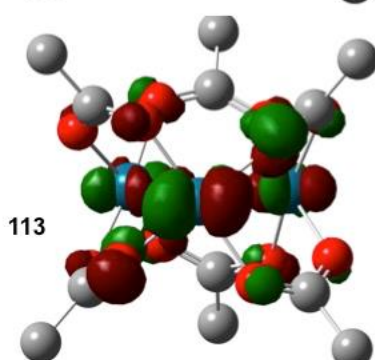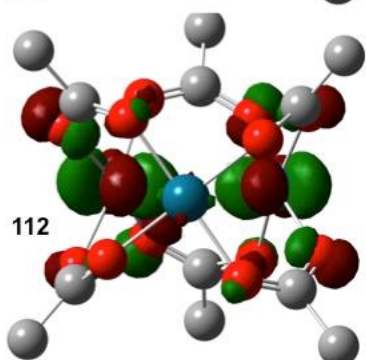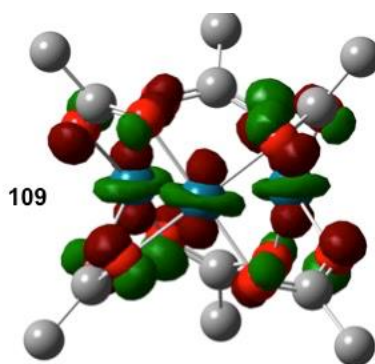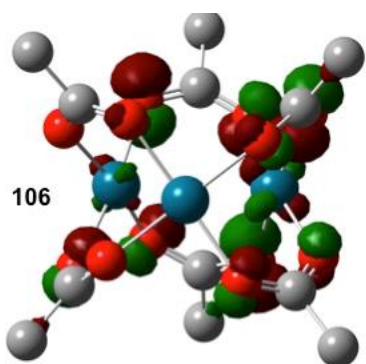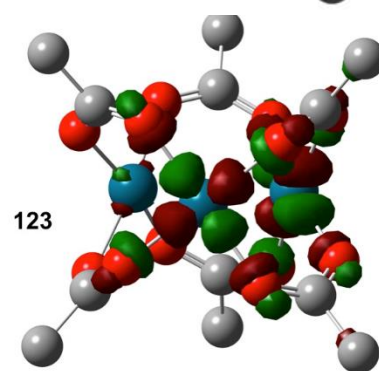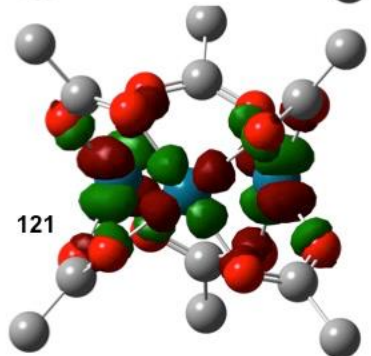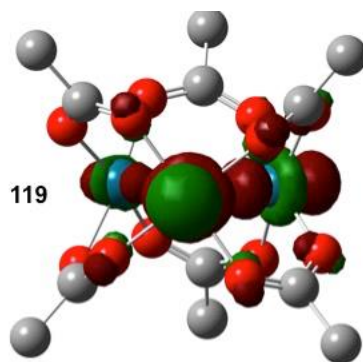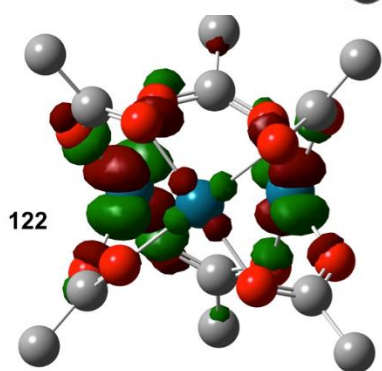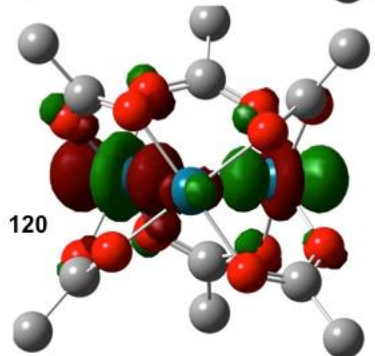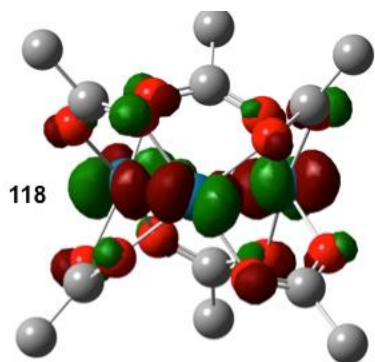
Pd(I) Dimer
Pd–Pd(□□→2DAF(π*)
Pd–Pd(□□→2DAF(π*)
Excited State 6: 1.000-A   2.4956 eV 496.81 nm f=0.0148 <S**2>=0.000
     140A -> 148A   -0.13591
     143A -> 144A   0.48994
     143A -> 147A   0.41459
     143A -> 148A   -0.15687
     140B -> 148B   -0.13591
     143B -> 144B   0.48994
     143B -> 147B   0.41459
     143B -> 148B   -0.15687

Pd–Pd(□□→2DAF(π*)
Pd–Pd(□□→2DAF(π*)
Excited State 17: 1.000-A   2.8889 eV 429.17 nm f=0.0228 <S**2>=0.000
     137A -> 148A   -0.16433
     140A -> 147A   -0.14596
     140A -> 148A   0.23787
     143A -> 144A   0.47453
     143A -> 147A   -0.27134
     143A -> 148A   0.23835
     137B -> 148B   -0.16433
     140B -> 147B   -0.14596
     140B -> 148B   0.23787
     143B -> 144B   0.47453
     143B -> 147B   -0.27134
     143B -> 148B   0.23835

$2Pd(d(z^2))+2OAc(n)\rightarrow DAF(C=O\pi^*)$
Pd–Pd(□□→2Pd(d(x^2-y^2))
Excited State 48: 1.000-A   3.6960 eV 335.45 nm f=0.0471 <S**2>=0.000
     135A -> 148A   -0.18128
     140A -> 144A   -0.23907
     140A -> 147A   -0.24622
     141A -> 145A   0.40325
     141A -> 146A   0.18909
     143A -> 148A   -0.25777
     135B -> 148B   -0.18128
     140B -> 144B   -0.23907
     140B -> 147B   -0.24622
     141B -> 145B   0.40325
     141B -> 146B   0.18909
     143B -> 148B   -0.25777

$2Pd(d(yz))\rightarrow 2DAF(\pi^*)$
$2Pd(d(z^2))+2OAc(n)\rightarrow 2DAF(\pi^*)$
Excited State 59: 1.000-A   3.8950 eV 318.32 nm f=0.0522 <S**2>=0.000
     130A -> 148A   -0.11943
     131A -> 148A   -0.10465
     135A -> 148A   0.18216

137A -> 147A   -0.11312
140A -> 144A   -0.24017
140A -> 147A   0.26326
141A -> 145A   0.21362
141A -> 146A   0.32366
143A -> 148A   0.22795
130B -> 148B   -0.11943
131B -> 148B   -0.10465
135B -> 148B   0.18216
137B -> 147B   -0.11312
140B -> 144B   -0.24017
140B -> 147B   0.26326
141B -> 145B   0.21362
141B -> 146B   0.32366
143B -> 148B   0.22795

2Pd(d(yz))→2DAF(π*)
2Pd(d(yz))→2Pd(d(x^2-y^2))
Excited State 75: 1.000-A   4.1543 eV 298.45 nm f=0.0780 <S**2>=0.000
135A -> 144A   -0.14554
135A -> 147A   -0.10409
135A -> 148A   -0.17117
137A -> 144A   0.11549
139A -> 144A   -0.11632
139A -> 147A   0.22917
140A -> 147A   0.35076
140A -> 148A   0.28218
142A -> 150A   -0.15974
143A -> 148A   -0.20773
135B -> 144B   -0.14554
135B -> 147B   -0.10409
135B -> 148B   -0.17117
137B -> 144B   0.11549
139B -> 144B   -0.11632
139B -> 147B   0.22917
140B -> 147B   0.35076
140B -> 148B   0.28218
142B -> 150B   -0.15974
143B -> 148B   -0.20773

Pd–Pd(□□→2DAF(π*)
2Pd(xy)+OAc(n)→2DAF(π*)
Excited State 78: 1.000-A   4.1799 eV 296.62 nm f=0.0697 <S**2>=0.000
133A -> 147A   -0.14752
135A -> 144A   -0.12808
136A -> 145A   -0.14089
136A -> 146A   0.14795
137A -> 144A   0.10276
139A -> 144A   -0.22890
139A -> 147A   0.38790
139A -> 148A   0.14354

140A -> 144A   0.10058
140A -> 147A   -0.17151
140A -> 148A   -0.15622
142A -> 150A   0.11159
143A -> 148A   0.12761
133B -> 147B   -0.14752
135B -> 144B   -0.12808
136B -> 145B   -0.14089
136B -> 146B   0.14795
137B -> 144B   0.10276
139B -> 144B   -0.22890
139B -> 147B   0.38790
139B -> 148B   0.14354
140B -> 144B   0.10058
140B -> 147B   -0.17151
140B -> 148B   -0.15622
142B -> 150B   0.11159
143B -> 148B   0.12761

$2Pd(xz)+OAc(n)\rightarrow 2DAF(\pi^*)$
$2Pd(z^2)+OAc(n)\rightarrow 2DAF(\pi^*)$
Excited State 88: 1.000-A   4.4024 eV 281.63 nm f=0.1741 <S**2>=0.000
    132A -> 146A   -0.10367
    134A -> 146A   -0.16132
    136A -> 145A   0.18574
    136A -> 146A   0.39158
    137A -> 144A   -0.15116
    138A -> 145A   0.38916
    138A -> 146A   0.18146
    132B -> 146B   -0.10367
    134B -> 146B   -0.16132
    136B -> 145B   0.18574
    136B -> 146B   0.39158
    137B -> 144B   -0.15116
    138B -> 145B   0.38916
    138B -> 146B   0.18146

$2Pd(z^2)+OAc(n)\rightarrow 2DAF(\pi^*)$
Excited State 93: 1.000-A   4.4449 eV 278.94 nm f=0.2121 <S**2>=0.000
    131A -> 147A   -0.13521
    132A -> 146A   0.16657
    133A -> 147A   0.10827
    134A -> 145A   -0.14558
    134A -> 146A   -0.19902
    135A -> 144A   0.18406
    135A -> 147A   -0.13946
    136A -> 146A   0.10335
    137A -> 144A   0.41357
    137A -> 147A   0.15313
    138A -> 146A   0.11395
    140A -> 144A   0.15126

131B -> 147B   -0.13521
132B -> 146B   0.16657
133B -> 147B   0.10827
134B -> 145B   -0.14558
134B -> 146B   -0.19902
135B -> 144B   0.18406
135B -> 147B   -0.13946
136B -> 146B   0.10335
137B -> 144B   0.41357
137B -> 147B   0.15313
138B -> 146B   0.11395
140B -> 144B   0.15126

$2Pd(xy)+OAc(n)\rightarrow 2DAF(\pi^*)$
$2Pd(z^2)+OAc(n)\rightarrow 2DAF(\pi^*)$
$2Pd(z^2)+OAc(n)\rightarrow 2DAF(\pi^*)$
$2Pd(z^2)+OAc(n)\rightarrow 2DAF(\pi^*)$

Excited State 99: 1.000-A   4.5182 eV 274.41 nm f=0.1997 <S**2>=0.000
   128A -> 145A   -0.11921
   132A -> 146A   -0.16346
   134A -> 145A   0.26286
   135A -> 144A   0.35454
   135A -> 147A   0.24976
   135A -> 148A   0.11909
   137A -> 144A   0.26693
   143A -> 148A   -0.13602
   128B -> 145B   -0.11921
   132B -> 146B   -0.16346
   134B -> 145B   0.26286
   135B -> 144B   0.35454
   135B -> 147B   0.24976
   135B -> 148B   0.11909
   137B -> 144B   0.26693
   143B -> 148B   -0.13602

$2Pd(z^2)+OAc(n)\rightarrow 2DAF(\pi^*)$
$2Pd(xz)+OAc(n)\rightarrow 2DAF(\pi^*)$
$2Pd(z^2)+OAc(n)\rightarrow 2DAF(\pi^*)$

Excited State 100: 1.000-A   4.5675 eV 271.45 nm f=0.0220 <S**2>=0.000
   131A -> 146A   0.12015
   132A -> 144A   -0.10437
   134A -> 144A   -0.15021
   134A -> 148A   -0.10655
   135A -> 145A   -0.27307
   136A -> 144A   -0.20365
   136A -> 147A   0.29687
   136A -> 148A   0.15437
   137A -> 146A   0.13183
   138A -> 144A   -0.10644

138A -> 147A   0.30394
131B -> 146B   0.12015
132B -> 144B   -0.10437
134B -> 144B   -0.15021
134B -> 148B   -0.10655
135B -> 145B   -0.27307
136B -> 144B   -0.20365
136B -> 147B   0.29687
136B -> 148B   0.15437
137B -> 146B   0.13183
138B -> 144B   -0.10644
138B -> 147B   0.30394

148
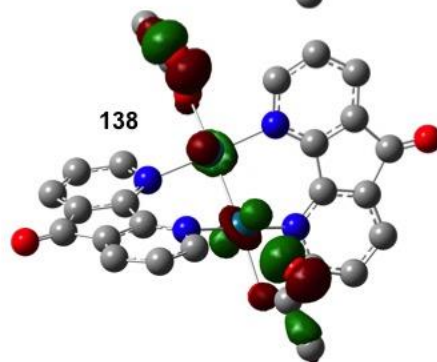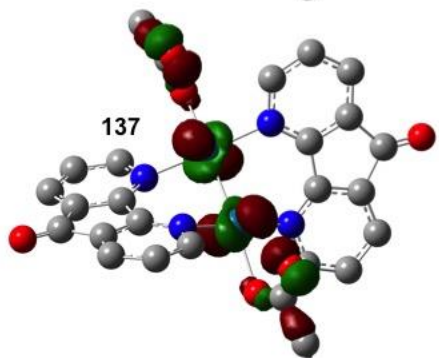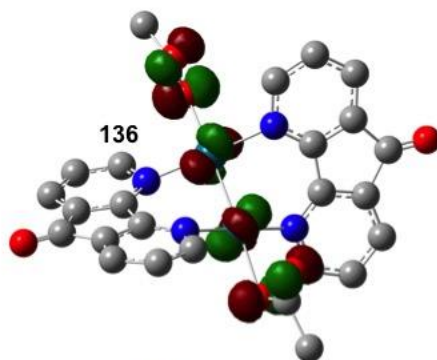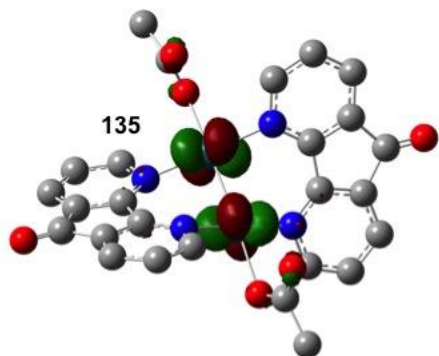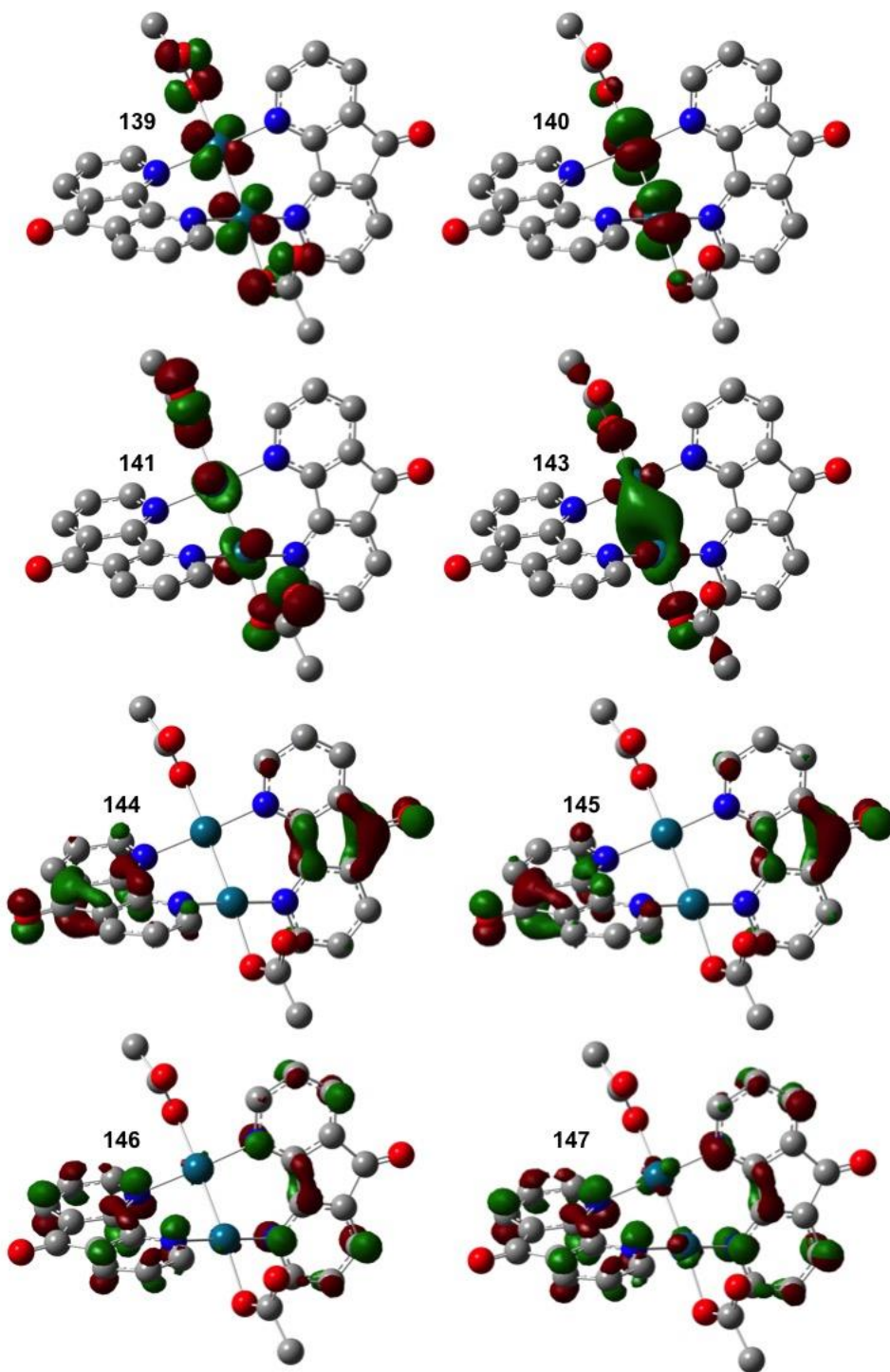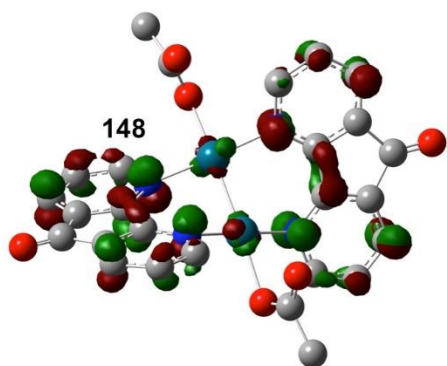
C9. Crystallographic Information for [Pd^I(μ-DAF)(OAc)]$_2$

Data Collection

A red crystal with approximate dimensions 0.19 x 0.18 x 0.04 mm^3 was selected under oil under ambient conditions and attached to the tip of a MiTeGen MicroMount©. The crystal was mounted in a stream of cold nitrogen at 100(1) K and centered in the X-ray beam by using a video camera.

The crystal evaluation and data collection were performed on a Bruker Quazar SMART APEXII diffractometer with Mo K$_α$ (λ = 0.71073 Å) radiation and the diffractometer to crystal distance of 4.96 cm. The initial cell constants were obtained from three series of ω scans at different starting angles. Each series consisted of 12 frames collected at intervals of 0.5° in a 6° range about ω with the exposure time of 15 seconds per frame. The reflections were successfully indexed by an automated indexing routine built in the APEXII program suite. The final cell constants were calculated from a set of 9931 strong reflections from the actual data collection.

The data were collected by using the full sphere data collection routine to survey the reciprocal space to the extent of a full sphere to a resolution of 0.80 Å. A total of 19730 data were harvested by collecting 5 sets of frames with 0.4° scans in ω and φ with exposure times of 40 sec per frame. These highly redundant datasets were corrected for Lorentz and polarization effects. The absorption correction was based on fitting a function to the empirical transmission surface as sampled by multiple equivalent measurements.[10]

Structure Solution and Refinement

The systematic absences in the diffraction data were consistent for the space groups *Cc* and *C2/c*. The *E*-statistics strongly suggested the centrosymmetric space group *C2/c* that yielded chemically reasonable and computationally stable results of refinement.[11]

A successful solution by the direct methods provided most non-hydrogen atoms from the *E*-map. The remaining non-hydrogen atoms were located in an alternating series of least-squares cycles and difference Fourier maps. All non-hydrogen atoms were refined with anisotropic displacement coefficients. All hydrogen atoms were included in the structure factor calculation at idealized positions and were allowed to ride on the neighboring atoms with relative isotropic displacement coefficients.

The only crystal large enough for the single-crystal X-ray diffraction experiment proved to be a non-merohedral twin with a minor (<10%) second component contribution. The twin components are related by a 179.9° rotation about direct axis [100]. The data were integrated and corrected for absorption as twinned followed by a separation of the data for the major component. The structure solution and refinement are based on the data for the major component only as if the data were acquired on a single crystal.

There are two molecules of acetic acid and one molecule of dioxane per dinuclear Pd complex in the lattice. The dinuclear Pd complex resides on a crystallographic 2-fold axis. The solvent dioxane occupies a crystallographic inversion center.

The final least-squares refinement of 238 parameters against 3635 data resulted in residuals R (based on F^2 for $I{\geq}2\sigma$) and wR (based on F^2 for all data) of 0.0260 and 0.0644, respectively. The final difference Fourier map was featureless.

Summary

Crystal Data for $C_{34}H_{34}N_4O_{12}Pd_2$ (M =903.45): monoclinic, space group C2/c (no. 15), a = 29.651(6) Å, b = 8.5945(17) Å, c = 13.903(3) Å, β = 90.11(5)°, V = 3543.0(13) Å^3, Z = 4, T = 99.95 K, μ(Mo Kα) = 1.084 mm^{-1}, $Dcalc$ = 1.694 g/mm^3, 19730 reflections measured (2.746 ≤ 2Θ ≤ 52.848), 3635 unique (R_{int} = .0387) which were used in all calculations. The final R_1 was 0.0260 (I > 2σ(I)) and wR_2 was 0.0644 (all data).
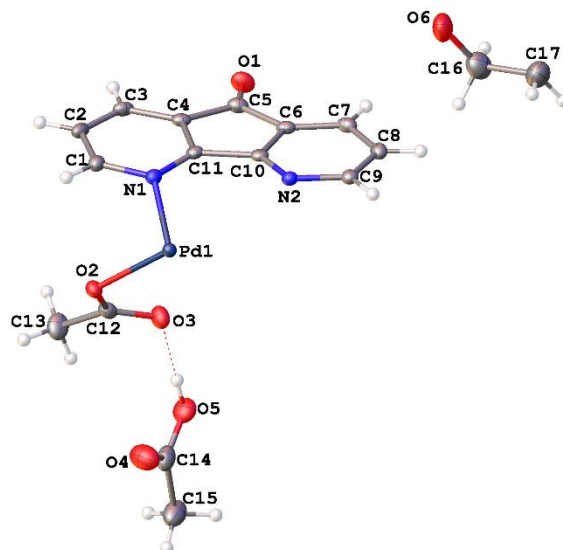
Figure C 15: A molecular drawing of the content of the asymmetric unit of [Pd(μ-DAF)(OAc)]₂ with solvent shown with 50%

probability ellipsoids.
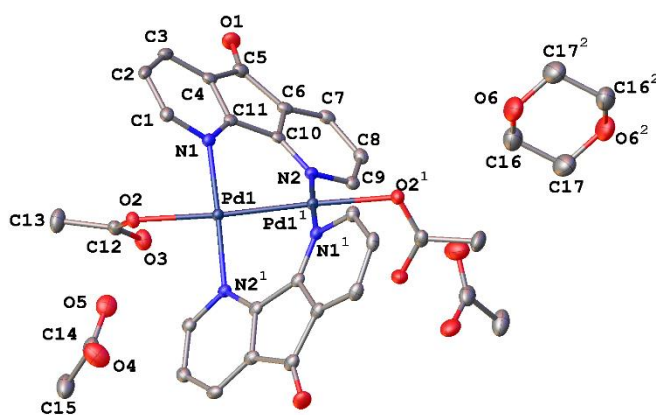
Figure C 16: A molecular drawing of [Pd(μ-DAF)(OAc)]₂ shown with 50% probability ellipsoids. All H atoms are omitted. Note

that there are two solvent molecules of acetic acid per Pd complex.

Table C 1: Crystal data and structure refinement for [(μ-DAF)Pd(OAc)]$_2$

Identification code	stahl189
Empirical formula	C$_{34}$H$_{34}$N$_4$O$_{12}$Pd$_2$
Formula weight	903.45
Temperature/K	99.95
Crystal system	monoclinic
Space group	C2/c
a/Å	29.651(6)
b/Å	8.5945(17)
c/Å	13.903(3)
α/°	90
β/°	90.11(5)
γ/°	90
Volume/Å^3	3543.0(13)
Z	4
ρ$_{calc}$mg/mm^3	1.694
m/mm^{-1}	1.084
F(000)	1816.0
Crystal size/mm^3	0.19 × 0.18 × 0.04
2Θ range for data collection	2.746 to 52.848°
Index ranges	-36 ≤ h ≤ 36, -10 ≤ k ≤ 10, -17 ≤ l ≤ 17
Reflections collected	19730
Independent reflections	3635[R(int) = .0387]
Data/restraints/parameters	3635/0/238
Goodness-of-fit on F^2	1.121
Final R indexes [I>=2σ (I)]	R$_1$ = 0.0260, wR$_2$ = 0.0632
Final R indexes [all data]	R$_1$ = 0.0284, wR$_2$ = 0.0644
Largest diff. peak/hole / e Å^{-3}	1.30/-0.54

1. (a) X. Ye, G. Liu, B. V. Popp, S. S. Stahl, *J. Org. Chem.*, **2011**, *76*, 1031-1044 (b) B. A. Steinhoff, I. A. Guzei, S. S. Stahl, *J. Am. Chem. Soc.* **2004**, *126*, 11268–11278 (c) B. A. Steinhoff, S. S. Stahl *Org. Lett.* **2002**, *4*, 4179–4181.
2. R. C. Larock, T. R. Hightower, L. A. Hasvold, K. P. Peterson, *J. Org. Chem.*, **1996**, *61*, 3584–3585
3. T. A. Cernak; T. H. Lambert, *J. Am. Chem. Soc.*, **2009**, 3124–3125
4. D. D. Kragten, R. A. van Santen, M. K. Crawford, W. D. Provine, J. J. Lerou, *Inorg. Chem.* **1999**, *38*, 331-339
5. (a) A. J. Cohen, N. C. Handy, *Mol. Phys.* **2001**, *99*, 607-615. (b) J. P. Perdew, K. Burke, M. Ernzerhof, *Phys. Rev. Lett.* **1996**, *77*, 3865-3868.
6. D. Feller, *J. Comp. Chem.* **1996**, *17*, 1571-1586.
7. M. J. Frisch, G. W. Trucks, H. B. Schlegel, G. E. Scuseria, M. A. Robb, J. R. Cheeseman, G. Scalmani, V. Barone, B. Mennucci, G. A. Petersson, H. Nakatsuji, M. Caricato, X. Li, H. P. Hratchian, A. F. Izmaylov, J. Bloino, G. Zheng, J. L. Sonnenberg, M. Hada, M. Ehara, K. Toyota, R. Fukuda, J. Hasegawa, M. Ishida, T. Nakajima, Y. Honda, O. Kitao, H. Nakai, T. Vreven, J. A. Montgomery, J. E. Peralta, F. Ogliaro, M. Bearpark, J. J. Heyd, E. Brothers, K. N. Kudin, V. N. Staroverov, R. Kobayashi, J. Normand, K. Raghavachari, A. Rendell, J. C. Burant, S. S. Iyengar, J. Tomasi, M. Cossi, N. Rega, J. M. Millam, M. Klene, J. E. Knox, J. B. Cross, V. Bakken, C. Adamo, J. Jaramillo, R. Gomperts, R. E. Stratmann, O. Yazyev, A. J. Austin, R. Cammi, C. Pomelli, J. W. Ochterski, R. L. Martin, K. Morokuma, V. G. Zakrzewski, G. A. Voth, P. Salvador, J. J. Dannenberg, S. Dapprich, A. D. Daniels, Ö. Farkas, J. B. Foresman, J. V. Ortiz, J. Cioslowski, D. J. Fox, *Gaussian 09, Revision D.01*; Gaussian, Inc.: Wallingford, CT, 2010
8. C. J. Cramer, *Essentials of Computational Chemistry: Theories and Models*; 2nd ed.; John Wiley & Sons: Chechester, 2004
9. A. V. Marenich, C. J. Cramer, D. G. Truhlar, *J. Phys. Chem. B* **2009**, *113*, 6378
10 Bruker-AXS. (2007-2013) APEX2 (Ver. 2013.2-0), SADABS (2012-1), and SAINT+ (Ver. 8.30C) Software Reference Manuals. Bruker-AXS, Madison, Wisconsin, USA.
11. (a) G. M. Sheldrick, (2008) SHELXL. *Acta Cryst.* **A64**, 112-122. (b) O. V. Dolomanov, L. J. Bourhis, R. J. Gildea, J. A. K. Howard, H. Puschmann, "OLEX2: a complete structure solution, refinement and analysis program". *J. Appl. Cryst.* (2009) **42**, *339-341*. (c) I. A. Guzei, (2013). Internal laboratory computer programs Gn.

Appendix D: Supporting Information for Chapter 6

D1. General Experimental Considerations

Solvents were purchased from Sigma Aldrich and used without purification. 1,4-dioxane was routinely used from Sure/Seal^{TM} bottles to avoid using peroxide contaminated solvent. Allylbenzene, cinnamyl acetate, Pd(OAc)$_2$, [Palladium(η^3-cinnamyl)Cl]$_2$, AgOAc, AgBF$_4$ and NaOAc-3H$_2$O were purchased from Sigma-Aldrich (Milwaukee, WI) and used without further purification. 4,5-diazafluoren-9-one (DAF) was purchasing from Oakwood Chemical (Estill, SC). Lithium aluminum deuteride was purchased from Cambridge Isotope Laboratories. Kinetic dependencies were obtained using an orbital mixer with an ambient atmosphere of O$_2$. Reaction aliquots were quenched with a 0.1 M solution of pyridine in EtOAc and analyzed gas-chromatography. Stock solutions were made fresh before every kinetic experiment as aged solutions gave irreproducible results. The initial rate the burst regime was determined from the first 3 minutes of the reaction, while the post-burst rates were determined in the linear regions of the time course from 13-30 minutes. Dependencies for the DAF and catalyst loadings were performed at 13.5 mM of Pd(OAc)$_2$ and 13.5 mM DAF/Pd(OAc)$_2$ respectively consistent with the published catalytic conditions.

D2. NMR Characterization of Na$^+$(κ^1-DAF)Pd(OAc)$_3$- Species

Evidence for formation of Na[Pd(κ^1-DAF)(κ^1-OAc)$_3$]. Initial investigations of the DAF/Pd(OAc)$_2$ catalyst mixture by NMR revealed the presence of mostly a single κ^1-DAF species. Six distinct ^{1}H chemical shifts of equal integration were observed and could be correlated to the same DAF ligand through ^{1}H-^{13}C HSQC/HMBC experiments (**Figure D 1**, **Figure D 2**). Further evidence for a κ^1 coordination mode can be seen in the ^{1}H-^{15}N HMBC where a bound N can be observed with ^{15}N δ = ~200 ppm and unbound N at ^{15}N δ = ~300 ppm (**Figure D 3**). We hypothesized that this was a palladate complex with the stoichiometry of 1:3 DAF to OAc ligands. To probe this hypothesis we titrated a stock solution of standard concentrations for the DAF/Pd(OAc)$_2$-catalyzed allylic oxidation ([DAF] = [Pd(OAc)$_2$ = 13.5 mM) with various amounts of NaOAc. The concentration of the κ^1-DAF species maximizes at approximately 13.5 mM at high NaOAc concentration (**Figure D 4**) which is consistent with quantitative formation of a monomolecular κ^1-DAF bound species. Representative spectra of the titration can be seen in **Figure D 5**. Attempts to crystallize this material resulted in substantial co-crystallization and/or precipitation of NaOAc from solution. Analogoues acetate salts were investigated and also exhibited similar behaviors with cesium providing the most well-resolved ^{1}H o-CH chemical shifts however crystallization attempts resulted crystallization of free DAF or CsOAc/Pd(OAc)$_2$ complexes.

Experimental: A stock solution of DAF and Pd(OAc)$_2$ ([DAF] = [Pd(OAc)$_2$] = 13.5 mM each) was prepared in 1,4-dioxane/AcOD-d_4 and 500 mL aliquots were added to various amounts of NaOAc. The mixtures were then sonicated until everything dissolved and transferred to a 5 mm NMR tube under ambient conditions and analyzed by NMR at 5° C.

^{1}H NMR (500 MHz, 5 °C, 3:1 1,4-Dioxane-d_8/AcOD-d_4) δ 9.34 (dd, J = 5.0, 1.4 Hz, 1H), 9.32 (dd, J = 5.9, 1.4 Hz, 1H), 8.12 (dd, J = 7.6, 1.6 Hz, 1H), 7.98 (dd, J = 7.6, 1.4 Hz, 1H), 7.65 (dd, J = 7.6, 5.0 Hz, 1H), 7.33 (dd, J = 7.6, 5.9 Hz, 1H) ppm. ^{13}C NMR (126 MHz, 5 °C, 3:1 1,4-Dioxane-d_8/AcOD-d_4) δ 187.28, 164.25, 160.40, 155.40, 158.32, 131.26, 132.54, 130.18, 131.65, 126.03, 125.29 ppm. ^{15}N NMR (50.7 MHz, 5 °C, 3:1 1,4-Dioxane-d_8/AcOD-d_4) 199.90, 305.90 ppm. Acetate characterization not reported due to excess acetic acid used in the solvent.
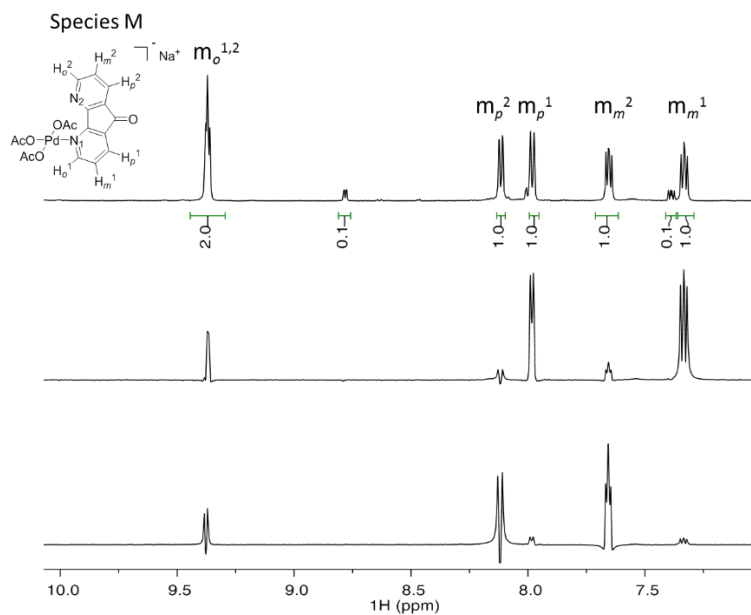
Figure D 1: Stacked spectra of a 1D ^{1}H and 1D ^{1}H TOCSY of κ^1-Species observed in 54 mM NaOAc, 13.5 mM DAF/Pd(OAc)$_2$.

Spectra recorded at 5 °C. NS = 16, d1 = 4s, mix = 0.08s.
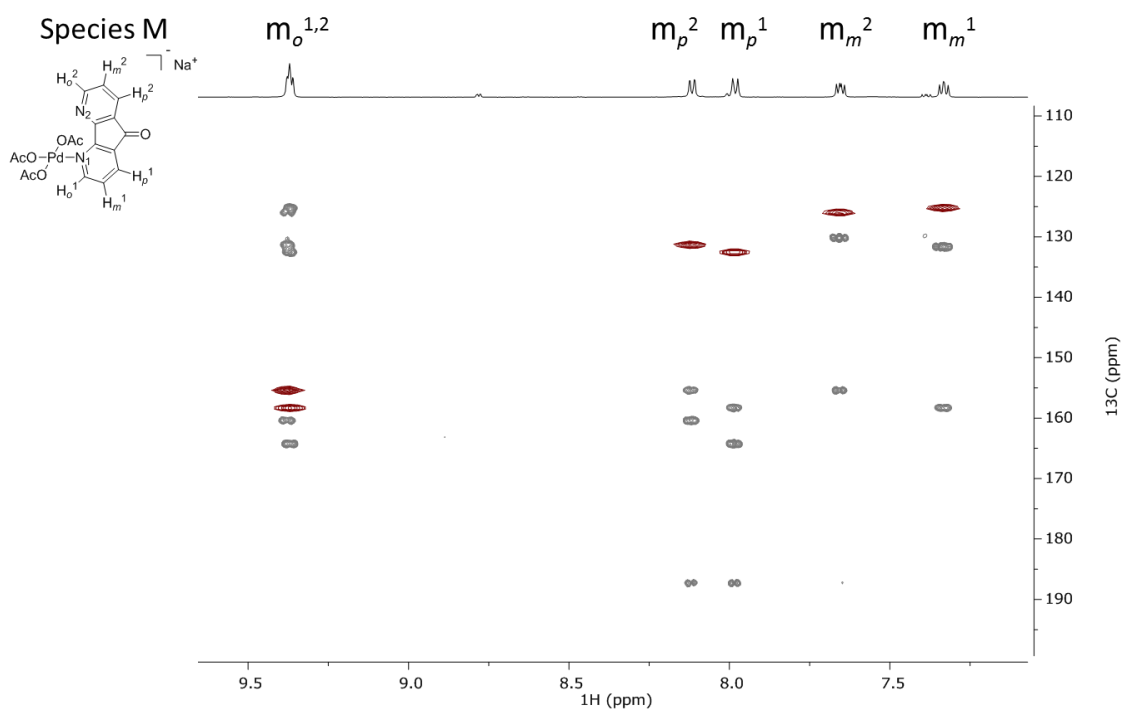
Figure D 2: Overlaid ^{1}H-^{13}C HSQC (red) and ^{1}H-^{13}C HMBC (grey) spectra of κ^1-Species observed in 54 mM NaOAc, 13.5 mM

DAF/Pd(OAc)$_2$ in 3:1 Dioxane/AcOH. 3-Bond coupling reveals that both pyridyl rings are connected to the same carbonyl carbon.

Spectra recorded at 5 °C. HSQC: NS = 4, d1 = 2s, ni = 512, sw = 225 ppm, o1p = 100 ppm, $^1J_{CH}$ = 165 Hz. HMBC: NS = 4, d1 =

2s, ni = 512, sw = 225 ppm, o1p = 100 ppm, $^2J_{CH}$ = 120 Hz, $^NJ_{CH}$ = 170 Hz.
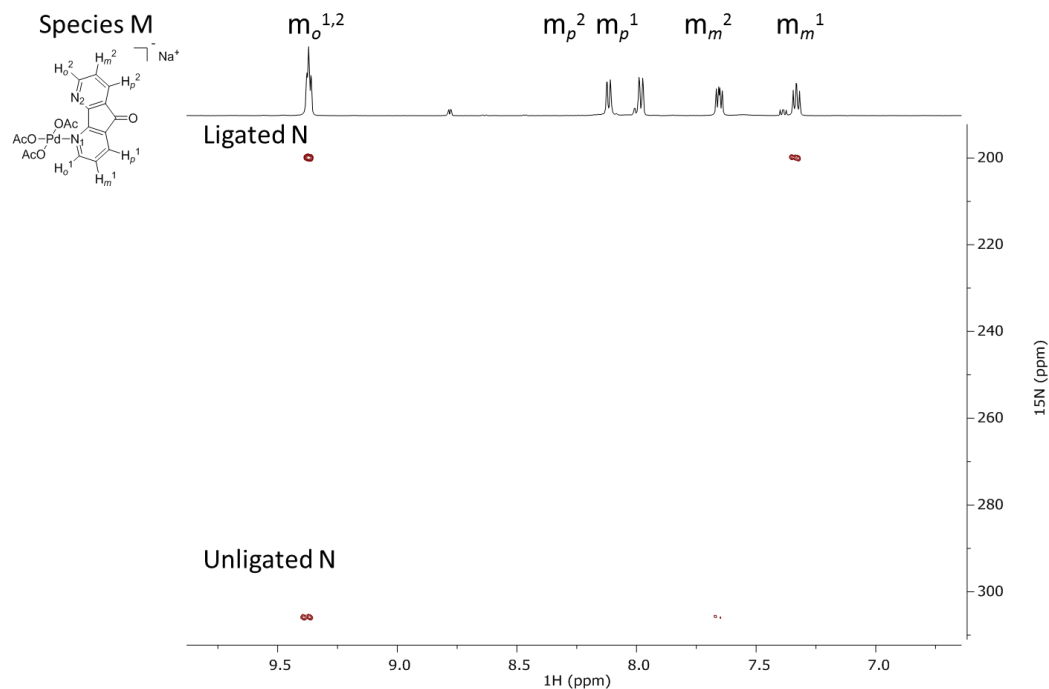
Figure D 3: ^{1}H-^{15}N HMBC spectrum of κ^1-Species observed in 54 mM NaOAc, 13.5 mM DAF/Pd(OAc)$_2$ in 3:1 Dioxane/AcOH. Spectra recorded at 5 °C. NS = 32, ni = 325, d1 =4s, sw(f1) = 200 ppm, o1p = 250 ppm, $^1J_{NH}$ = 100 Hz, $^nJ_{NH}$ = 8 Hz.
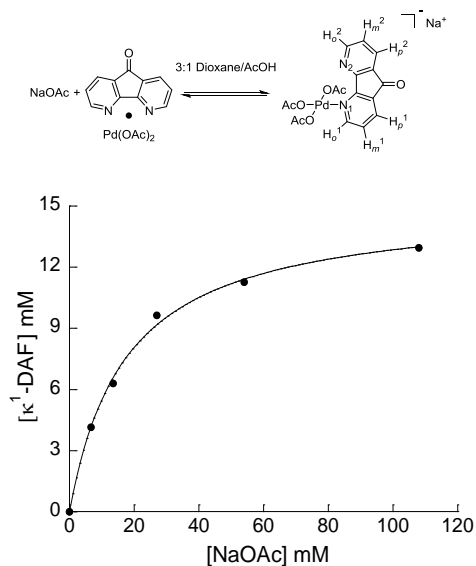
Figure D 4: NaOAc titration curve over 0, 6.7, 13.5, 27, 54, 108 mM of NaOAc with 13.5 mM DAF/Pd(OAc)$_2$ in 3:1 Dioxane-h$_8$/AcOD-d$_4$. Solvent suppression at 4.98 ppm
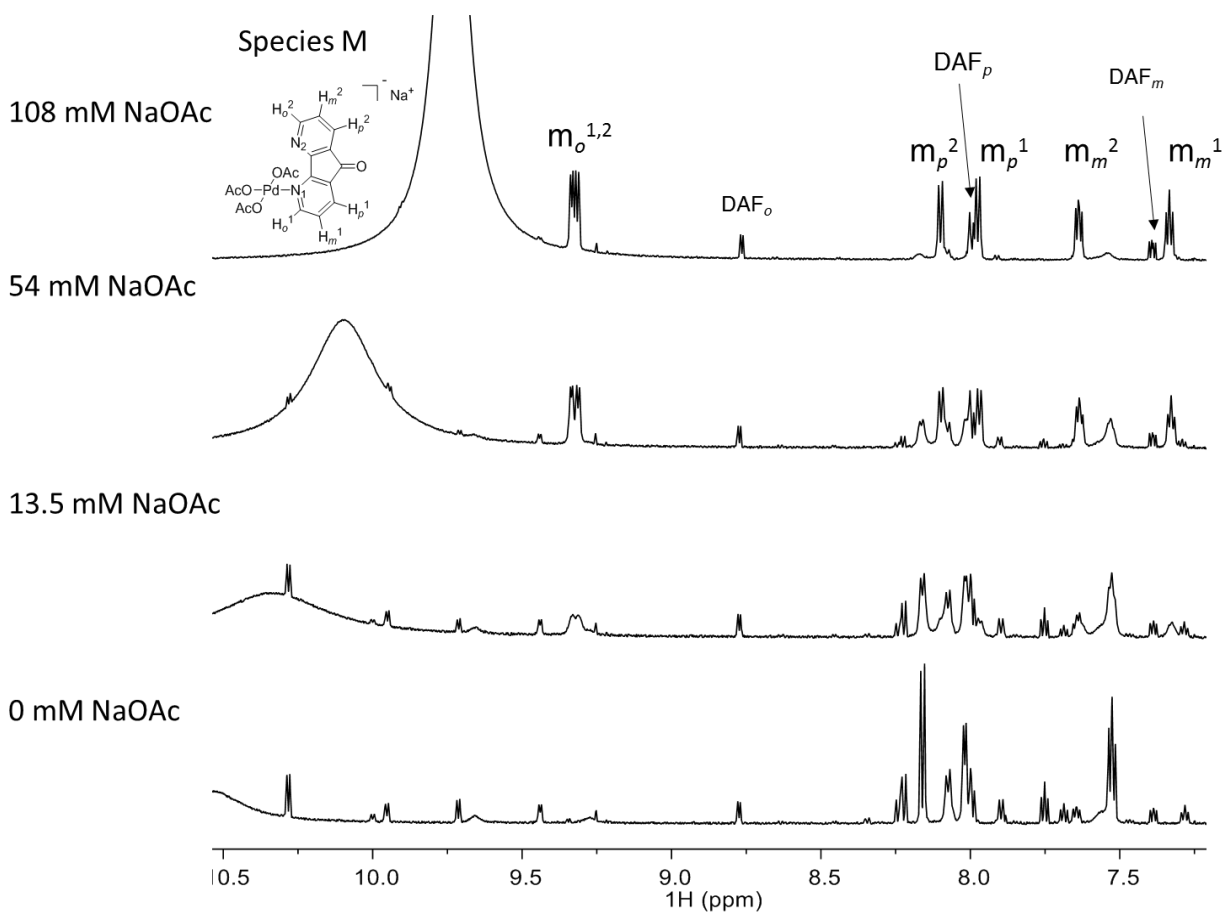
Figure D 5: ^{1}H 1D Stacked NMR Spectra of 13.5 mM DAF/Pd(OAc)$_2$ mixtures with different amounts of NaOAc in 3:1 Dioxane-h$_8$/AcOD-d$_4$. Spectra recorded at 24 °C. DS = 2, NS = 16, d1 = 30s.

D3. NMR Titration of DAF with [Pd^{II}(cinnamyl)(OAc)]$_2$
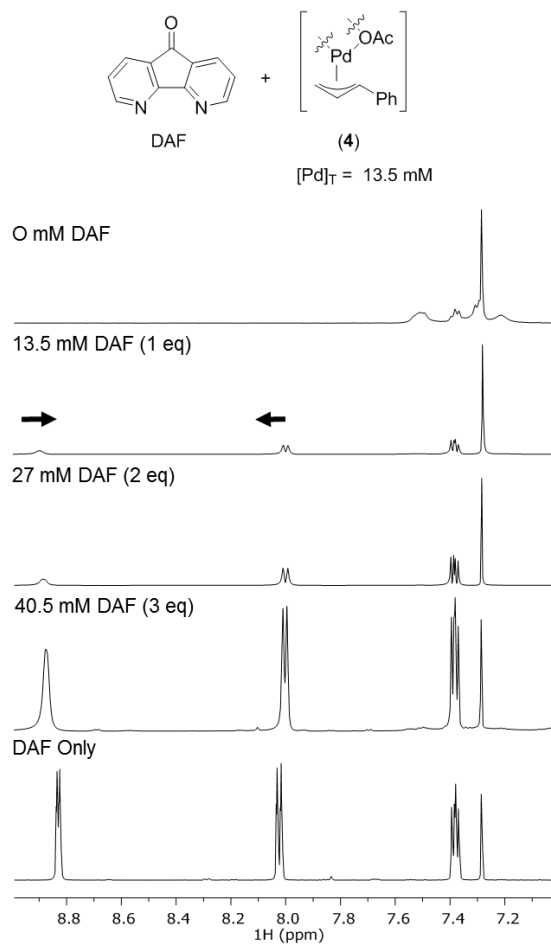
Figure D 6: NMR Titration of DAF with [Pd^{II}(cinnamyl)(OAc)]$_2$ in CDCl$_3$. [Pd]$_T$ = 13.5 mM, [DAF] = 13.5 – 40.5 mM, 24 °C. ns = 16, ds = 2, d1 = 25 s.

D4. Kinetic Isotope Experimental Details

   Kinetic isotope experiments were performed in a 48-well orbital mixer with an attached manifold that delivers an ambient atmosphere of O_2. The reactions performed at 80 °C with 1 atm of pure O_2 and initiated by injection of a 200 μL starting material stock solution. Trimethoxybenzene was utilized as an internal standard. 100-50 μL aliquot were pulled with syringe, quenched with a stock solution of 0.2 M pyridine in EtOAc and flushed through a silica plug to remove residual Pd.[1] The solvent was then evaporated in a centrifugal evaporator at room temperature and the pellet was dissolved in $CDCl_3$ and analyzed by ^{1}H NMR.

Synthesis of KIE Probes:
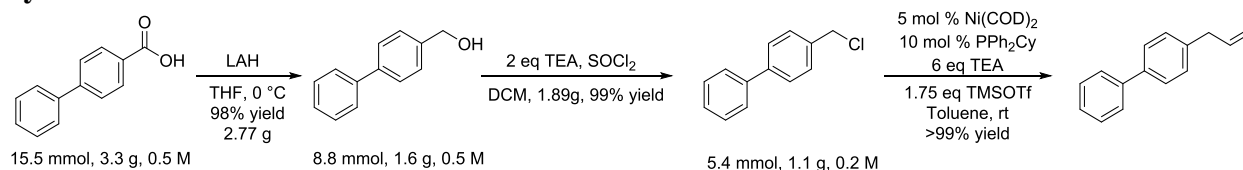
Synthesis of 4-Phenylbenzyl Alcohol: In a flame dried 250 mL round bottom, 30 mL of dry THF was added under nitrogen. 500 mg of grey LAH pellets were added and the reaction was cooled to 0 °C. The heterogeneous mixture was stirred vigorously to break up any solid LAH pellets and when the pellets were completely powdered in solution, 3.3g of solid ester was added slowly batch wise to minimize bubbling. The reaction was then left to warm over night to room temperature. Disappearance of starting material was monitored (SM RF 0.2 in 10/90 EtOAc/Hexanes). The reaction was worked up by quenching slowly with water at 0 °C. The aqueous layer was then extracted with ethyl acetate, dried with magnesium sulfate and solvent removed with rotary evaporation. Product was purified further with column chromatography using 1-5% MeOH in DCM. 2.77 g (98% yield) of product was obtained of a white solid.

4-Phenylbenzyl Alcohol
^{1}H NMR (400 MHz, $CDCl_3$) δ 7.59 (m, 4H), 7.44 (m, 4H), 7.35 (m, 1H), 4.74 (br s, 2H), 1.71 (br s, OH, 1H). ^{13}C NMR (101 MHz, $CDCl_3$) δ 140.83, 140.67, 139.88, 128.80, 127.48, 127.35, 127.11, 65.15. HRMS (ASAP-MS) calculated m/z for $C_{13}H_{12}O$: 184.0888, observed [M-H]$^+$ 183.0805, [M-H$_2$O+H]$^+$ 167.0856.

Synthesis of 4-Phenylbenzyl Chloride: Synthesis of In a flame dried round bottom flask, 25 mL of DCM was added under nitrogen. Anhydrous trimethylamine (1.78g, 2.5 mL, 17.6 mmol) was added via syringe injection followed by addition of solid alcohol (1.6 g, 8.8 mmol) under nitrogen. Fresh $SOCl_2$ (2.1 g, 1.2 mL, 17.6 mmol) was then added dropwise to the reaction mixture with a needle vent to allow fumes to escape into the hood. This was stirred until all starting material disappeared by TLC. The reaction was quenched with water, 0.1 M citric acid, dried with $MgSO_4$, concentrated under rotary evaporation and purified with a silica plug. It is important to remove all contaminating sulfur and the product is powdery white or the next step will fail.

4-Phenylbenzyl Chloride:
^{1}H NMR (500 MHz, $CDCl_3$) d 7.59 (m, 4H), 7.45 (m, 4H), 7.36 (m, 1H), 4.94 (s, 2H). ^{13}C NMR (126 MHz, $CDCl_3$) 141.40, 140.49, 136.43, 129.05, 128.82, 127.53. 127.49, 127.12, 46.06. HRMS (ASAP-MS) calculated m/z for $C_{13}H_{11}Cl$: 202.0549, observed [M]$^+$ 202.0547

Synthesis of h_2-4-Allylbiphenyl: Prep was used from Matsubara, R.; Gutierrez, A. C.; Jamison, T. F. *J. Am. Chem. Soc.* **2011**, *133*, 19020-19023 and product was obtained in quantitative yield. Rotatory evaporation at 50 °C was necessary to remove all of the cyclooctadiene.

h_2-4-Allylbiphenyl:
^{1}H NMR (500 MHz, CDCl$_3$) δ 7.58 (d, J = 7.8 2H), 7.53 (d, J = 7.8 Hz, 2H), 7.42 (m, 2H), 7.32 (m, 1H), 7.26 (m, J = 7.8 Hz, 2H), 6.01 (comp m, 1H), 5.20 – 5.02 (comp m, 2H), 3.43 (d, J = 6.7 Hz, 2H). ^{13}C NMR (126 MHz, CDCl$_3$) δ 141.03, 139.14, 137.29, 129.17, 128.69, 127.15, 127.03, 127.00, 115.92, 39.85. HRMS (ASAP-MS) calculated m/z for C$_{15}$H$_{14}$: 194.1096, observed [M+H]$^+$ 195.1169.

Synthesis of d_2-4-Allylbiphenyl:
Synthesis of the intermolecular deuterated probe for the KIE experiment, d_2-4-allylbiphenyl, was synthesized in the same way as above but using lithium aluminium deuteride.

d_2-4-Phenylbenzyl Alcohol: ^{1}H NMR (400 MHz, CDCl$_3$) δ 7.6 (m, 4H), 7.45 (m, 4H), 7.35 (m, 1H), 1.65 (br s, OH, 1H). ^{13}C NMR (126 MHz, CDCl$_3$) δ 140.81, 140.68, 139.74, 128.78, 127.51, 127.34, 127.32, 127.09, 64.46 (p, $^1J_{CD}$ = 21.7 Hz) HRMS (ASAP-MS) calculated m/z for C$_{13}$H$_{10}$D$_2$O: 186.1014, observed [M-D]+ 184.0807, [M-H$_2$O+H]$^+$ 169.0981.

d_2-4-Phenylbenzyl Chloride: ^{1}H NMR (500 MHz, CDCl$_3$) δ 7.59 (m, 4H), 7.45 (m, 4H), 7.36 (m, 1H), 6.00 (app dd, J = 16.0, 10 Hz, 1H), 6.11 (comp m, 2H). ^{13}C NMR (126 MHz, CDCl$_3$) δ 141.41, 140.49, 136.31, 129.05, 128.84, 127.53, 127.50, 127.15, 45.52 (p, $^1J_{CD}$ = 22.8 Hz) HRMS (ASAP-MS) calculated m/z for C$_{13}$H$_9$D$_2$Cl: 204.0675, observed [M+H]$^+$ 205.0748, [M-Cl]$^+$ 169.0981.

d_2-4-Allylbiphenyl: ^{1}H NMR (500 MHz, CDCl$_3$) δ 7.58 (app d, $^3J_{HH}$ = 7.5 Hz, 2H), 7.53 (app t, $^3J_{HH}$ = 8.1 Hz, 2H), 7.43 (app t, $^3J_{HH}$ = 7.5 Hz, 2H), 7.33 (app t, $^3J_{HH}$ = 7.5 Hz, 1H), 7.27 (app d, $^3J_{HH}$ = 8.1 Hz, 2H). ^{13}C NMR (126 MHz, CDCl$_3$) δ 141.05, 139.10, 139.07, 137.25, 128.96, 128.70, 128.49, 127.17, 127.05, 127.01, 115.96, 39.18 (p, $^1J_{CD}$ = 19.4 Hz), HRMS (ASAP-MS) calculated m/z for C$_{15}$H$_{12}$D$_2$: 196.1221, observed [M+H]$^+$ 197.1294.

Synthesis d_1h_1-4-Allylbiphenyl:
The intramolecular probe was synthesized using 4-phenylbenzaldehyde (2.23 g, 12.3 mmol) and lithium aluminium deuteride (215 mg) and the corresponding aldehyde.

d_1h_1-4-Phenylbenzyl Alcohol: ^{1}H NMR (500 MHz, CDCl$_3$ δ 7.59 (m, 4H), 7.44 (m, 4H), 7.35 (m, 1H), 4.72 (br s, 1H), 1.66 (br s, OH, 1H) ^{13}C NMR (126 MHz, CDCl$_3$) δ 140.81, 140.67, 139.80, 128.78, 127.48, 127.34, 127.32, 127.09, 64.80 (1:1:1 t, $^1J_{CD}$ = 21.8 Hz). HRMS (ASAP-MS) calculated m/z for C$_{13}$H$_{11}$DO: 185.0951, observed [M-H$_2$O+H]$^+$ 168.0919

d_1h_1-4-Phenylbenzyl Chloride: ^{1}H NMR (500 MHz, CDCl$_3$) δ 7.44 (m, 4H), 7.30 (m, 4H), 7.22 (m, 1H), (app t, $^2J_{HD}$ = 1.5 Hz, 1H). ^{13}C NMR (126 MHz, CDCl$_3$) δ 140.24, 139.35, 135.28, 127.97, 127.74, 126.45, 126.36, 126.01, 44.69 (1:1:1 t, $^1J_{CD}$ = 23.0 Hz).
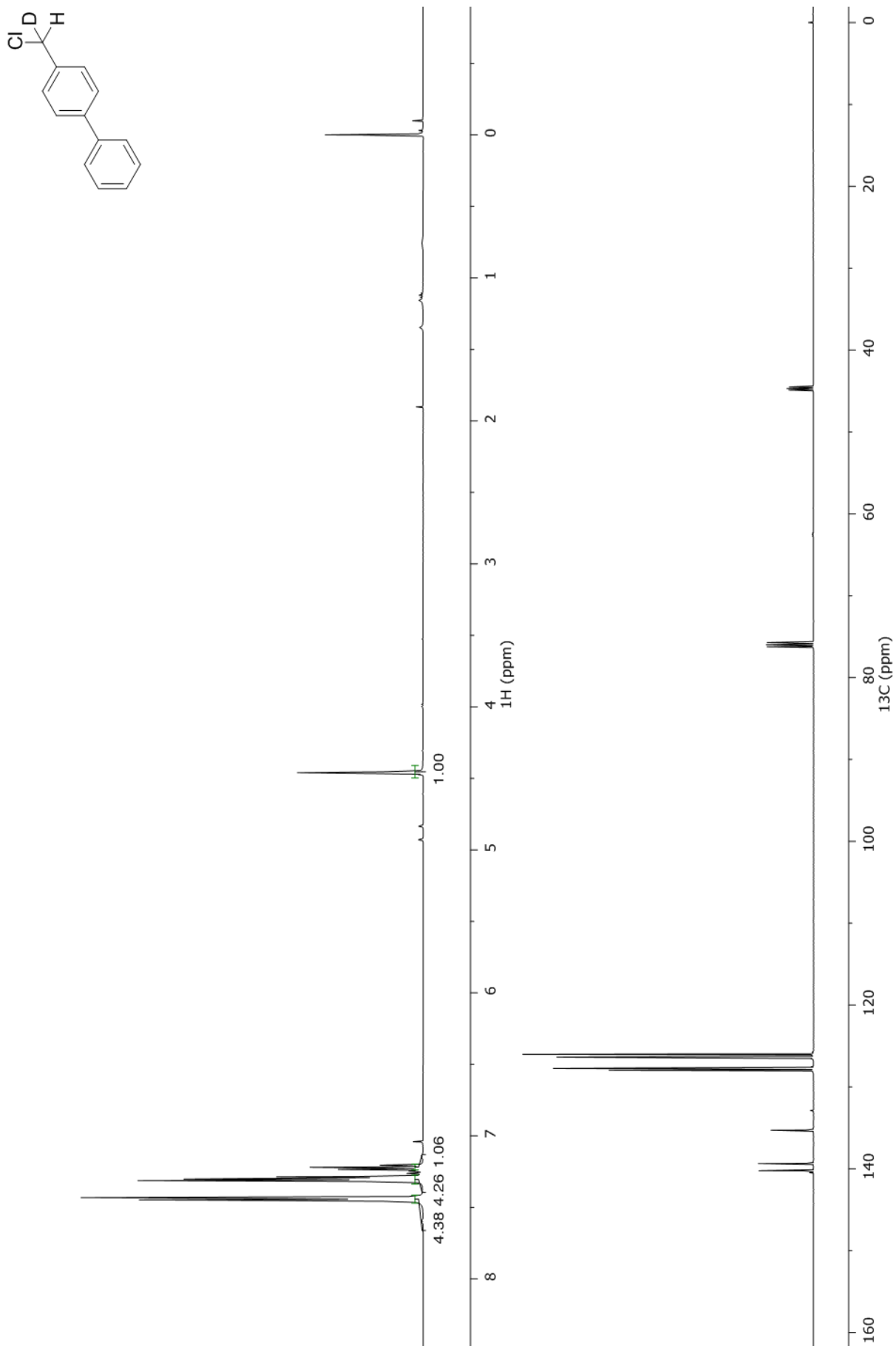
d_1h_1-4-Allylbiphenyl: ^{1}H NMR (500 MHz, CDCl$_3$) 7.58 (app d, $^3J_{HH}$ = 7.5 Hz, 2H), 7.53 (app d, $^3J_{HH}$ = 8.1 Hz, m), 7.43 (app t, $^3J_{HH}$ = 7.5 Hz, 2H), 7.33 (app t, $^3J_{HH}$ = 7.5 Hz, m), 7.27 (app d, $^3J_{HH}$ = 8.1 Hz, 2H, m), 6.10, (app ddd, 1H), 5.15 – 5.08 (comp m, 2H), 3.42 (br s, 1H) ^{13}C NMR (126 MHz, CDCl$_3$) δ 141.04, 139.13, 139.06, 137.28, 128.97, 128.70, 127.17, 127.05, 127.01, 115.95, 39.52 (1:1:1 t, $^1J_{CD}$ = 19.4 Hz).
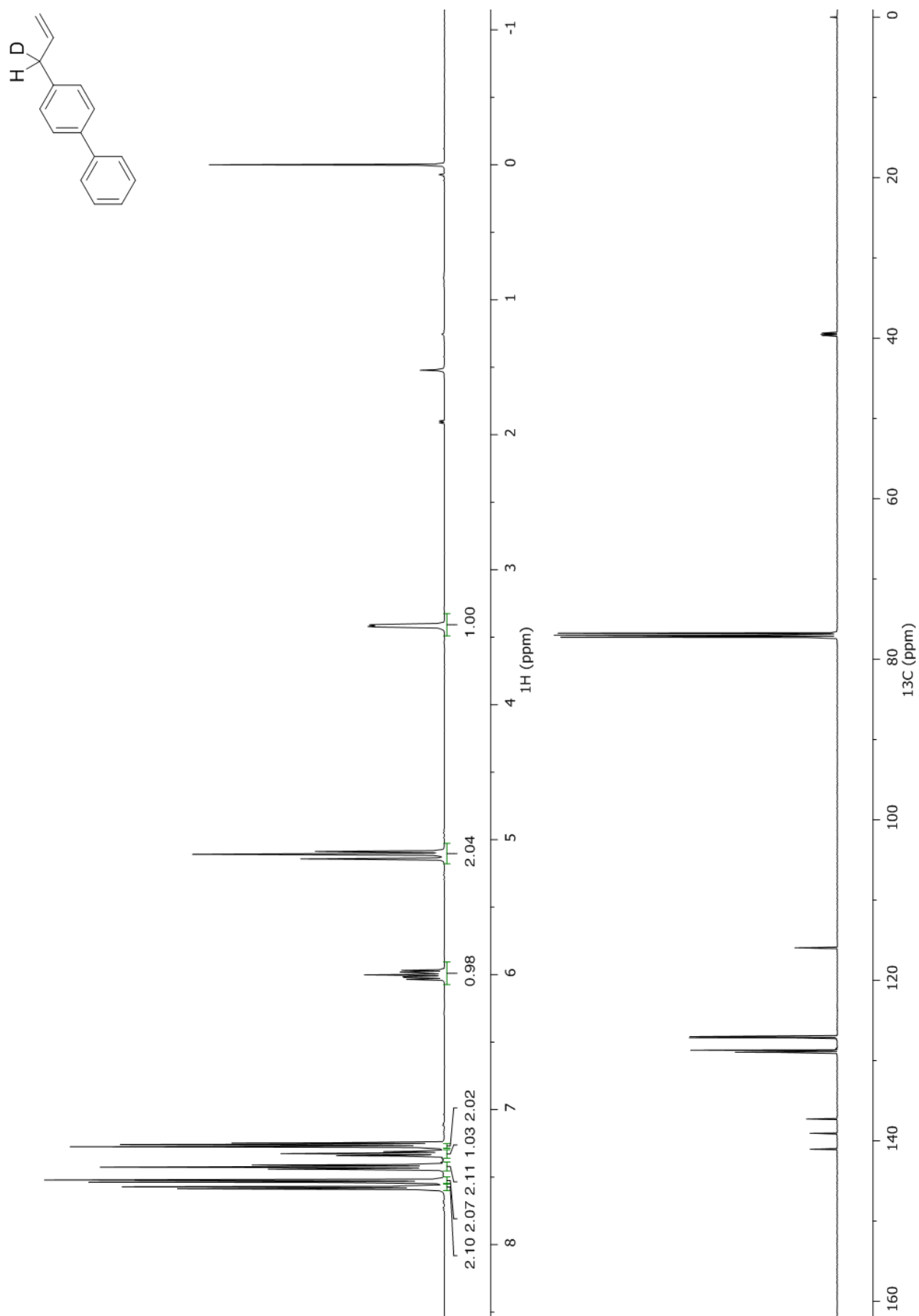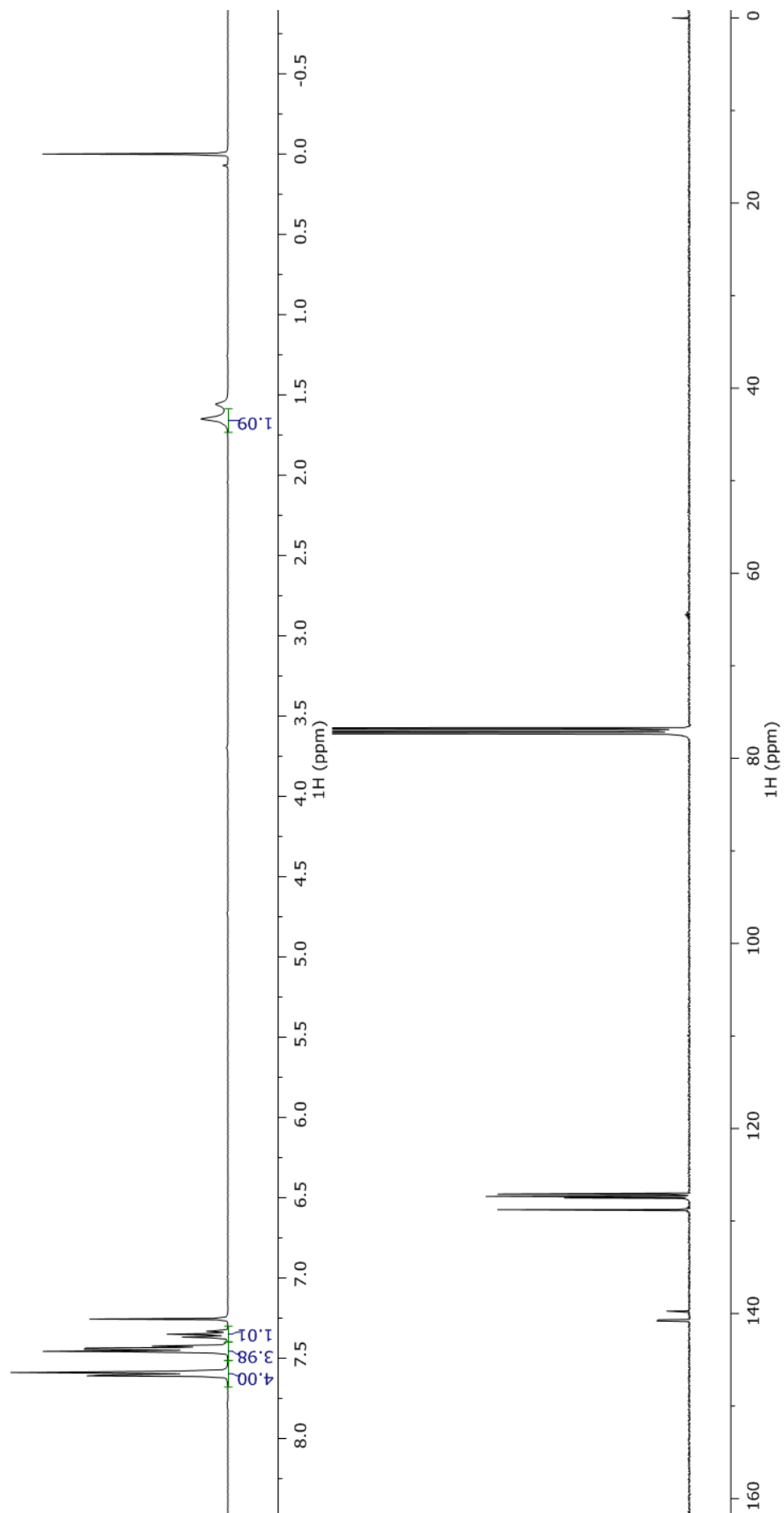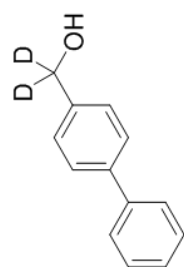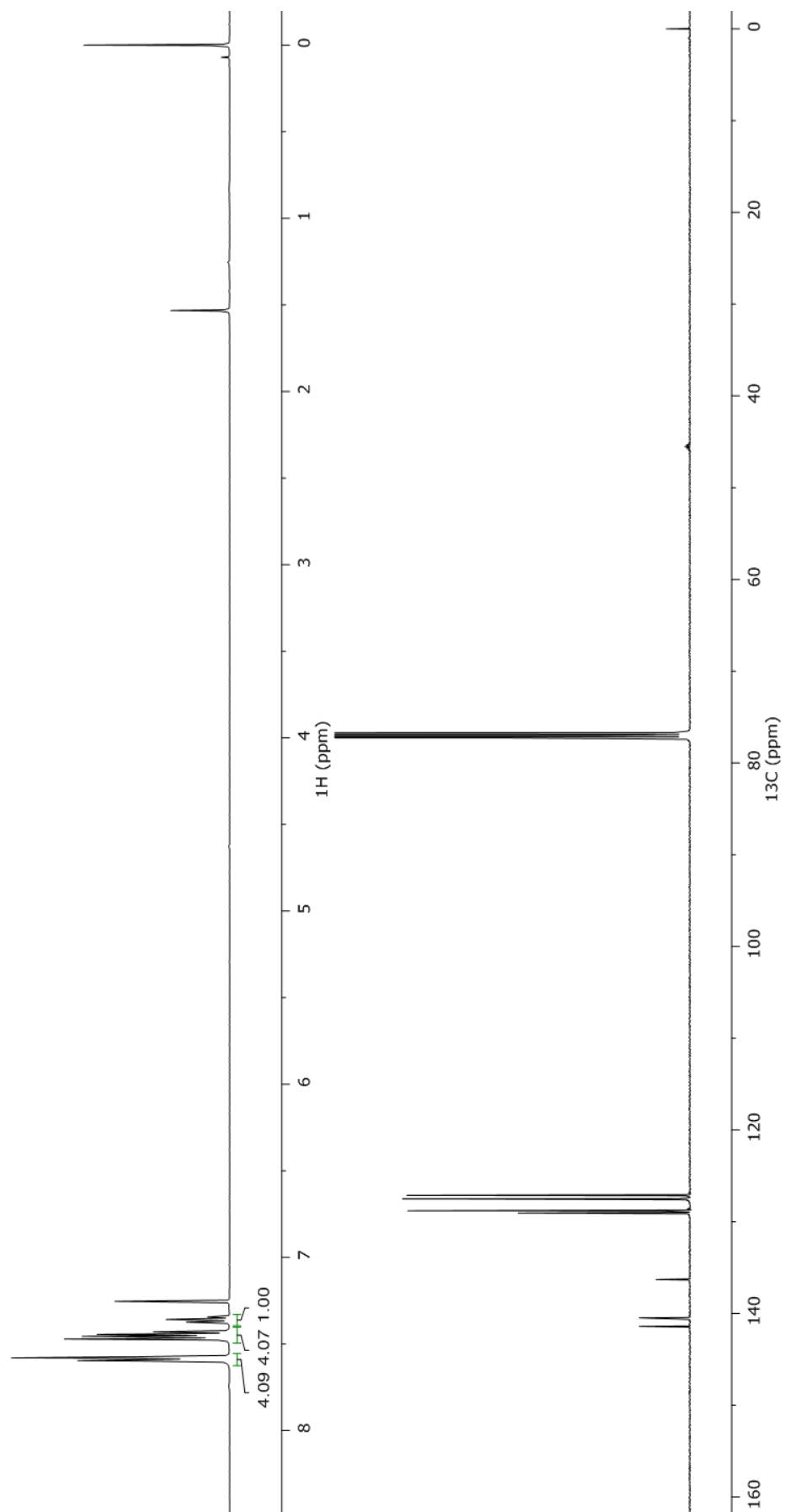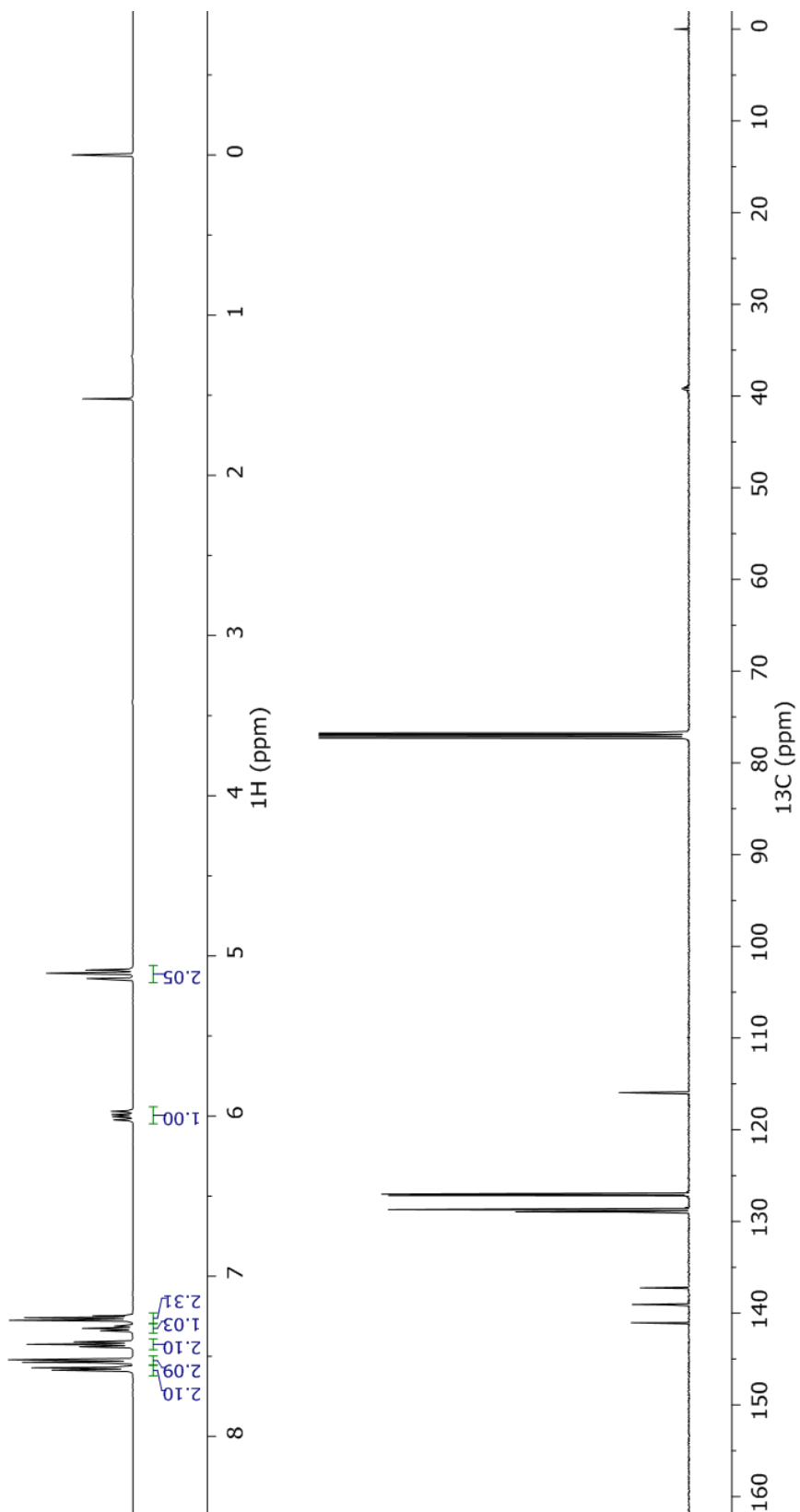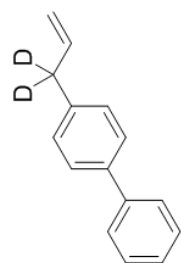
1H (ppm)

13C (ppm)
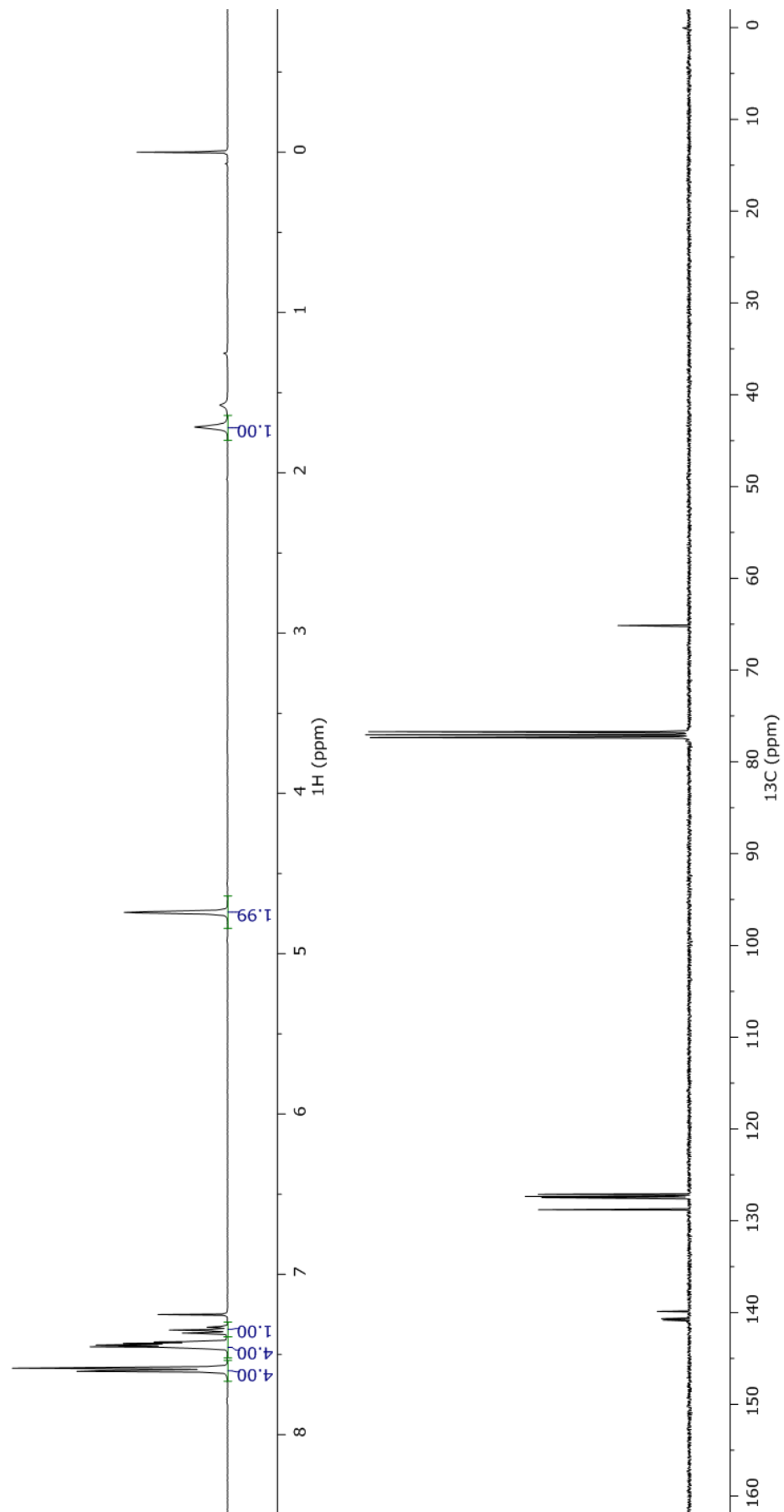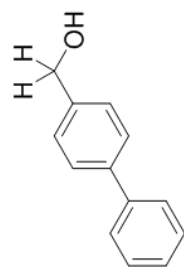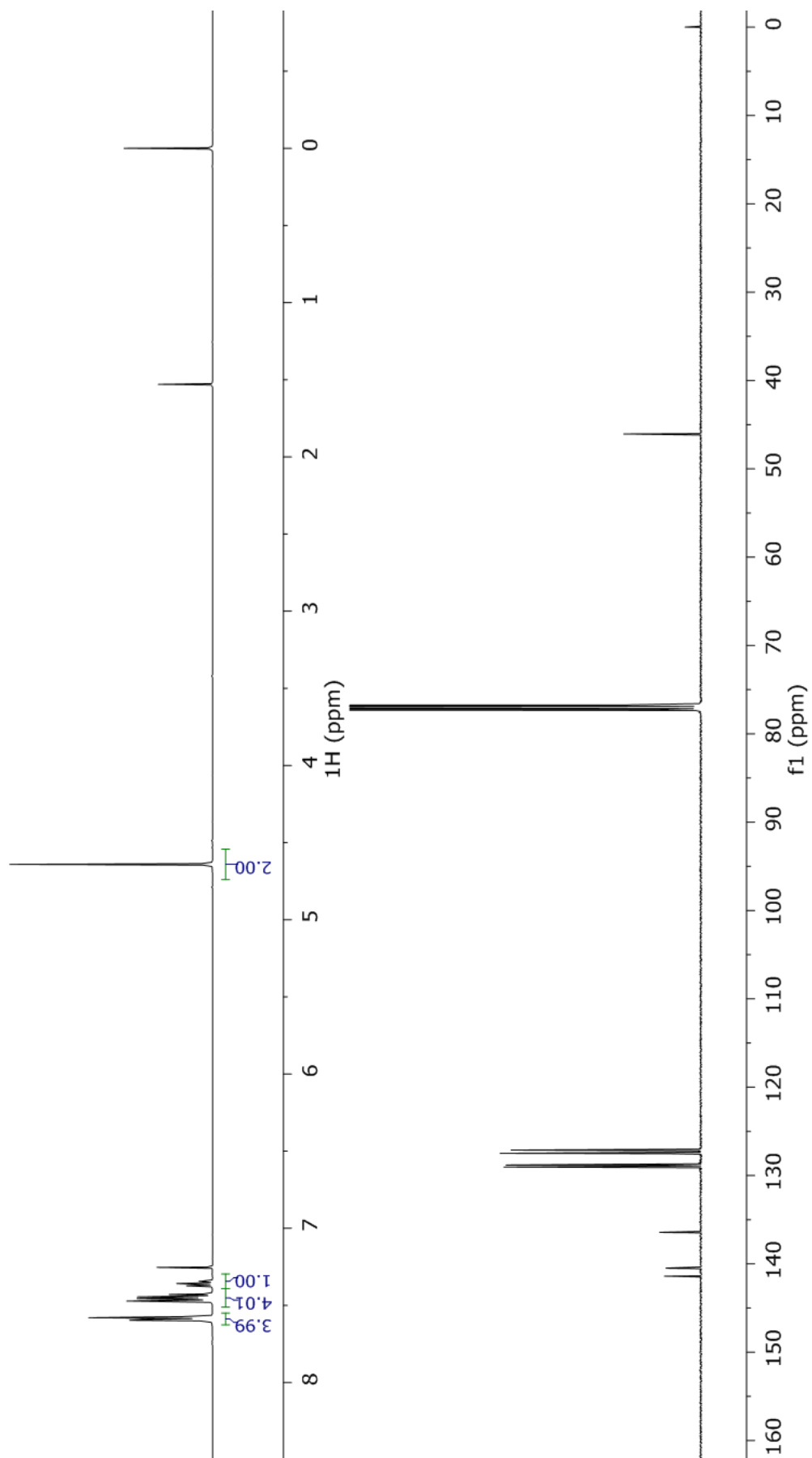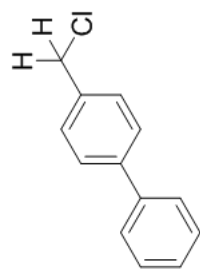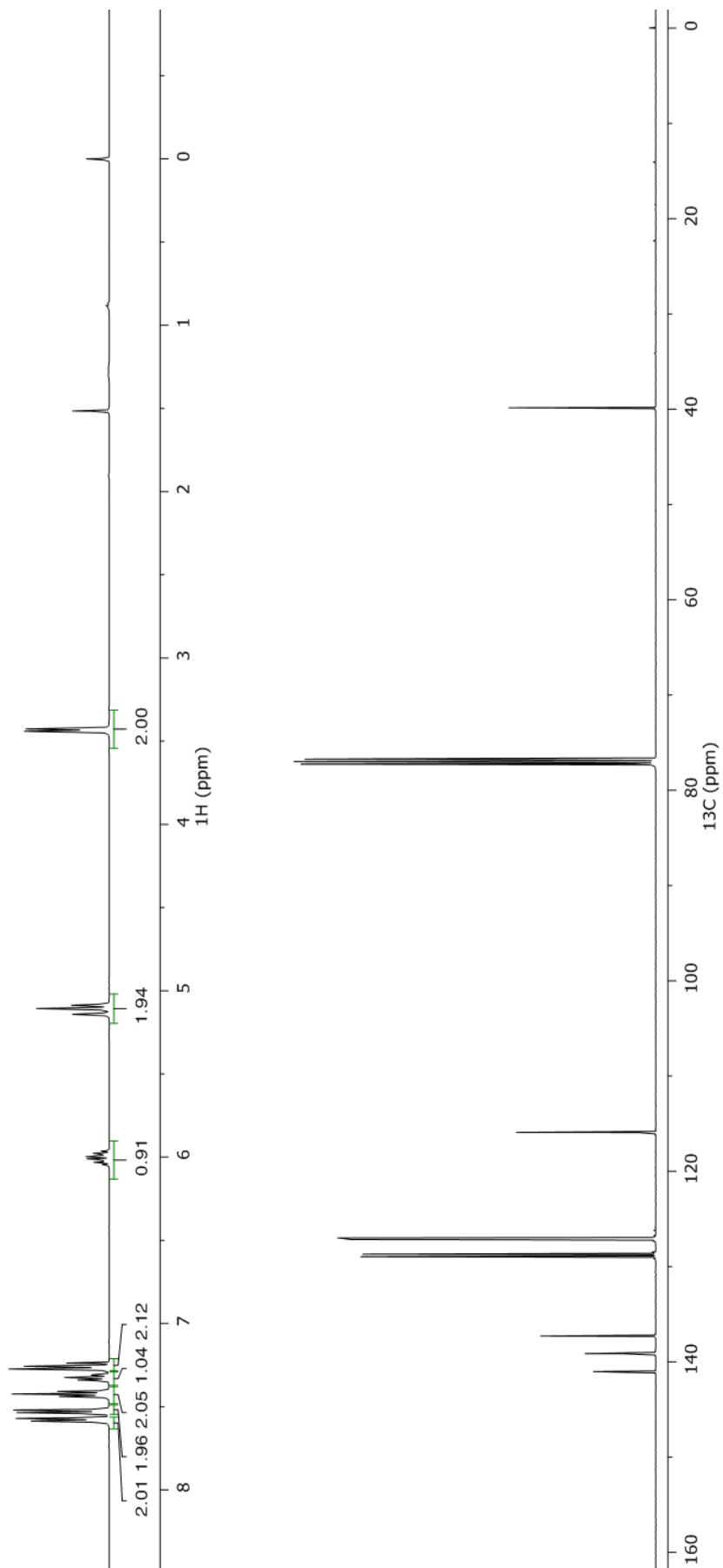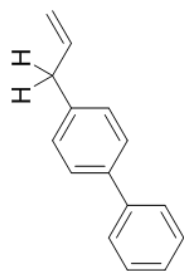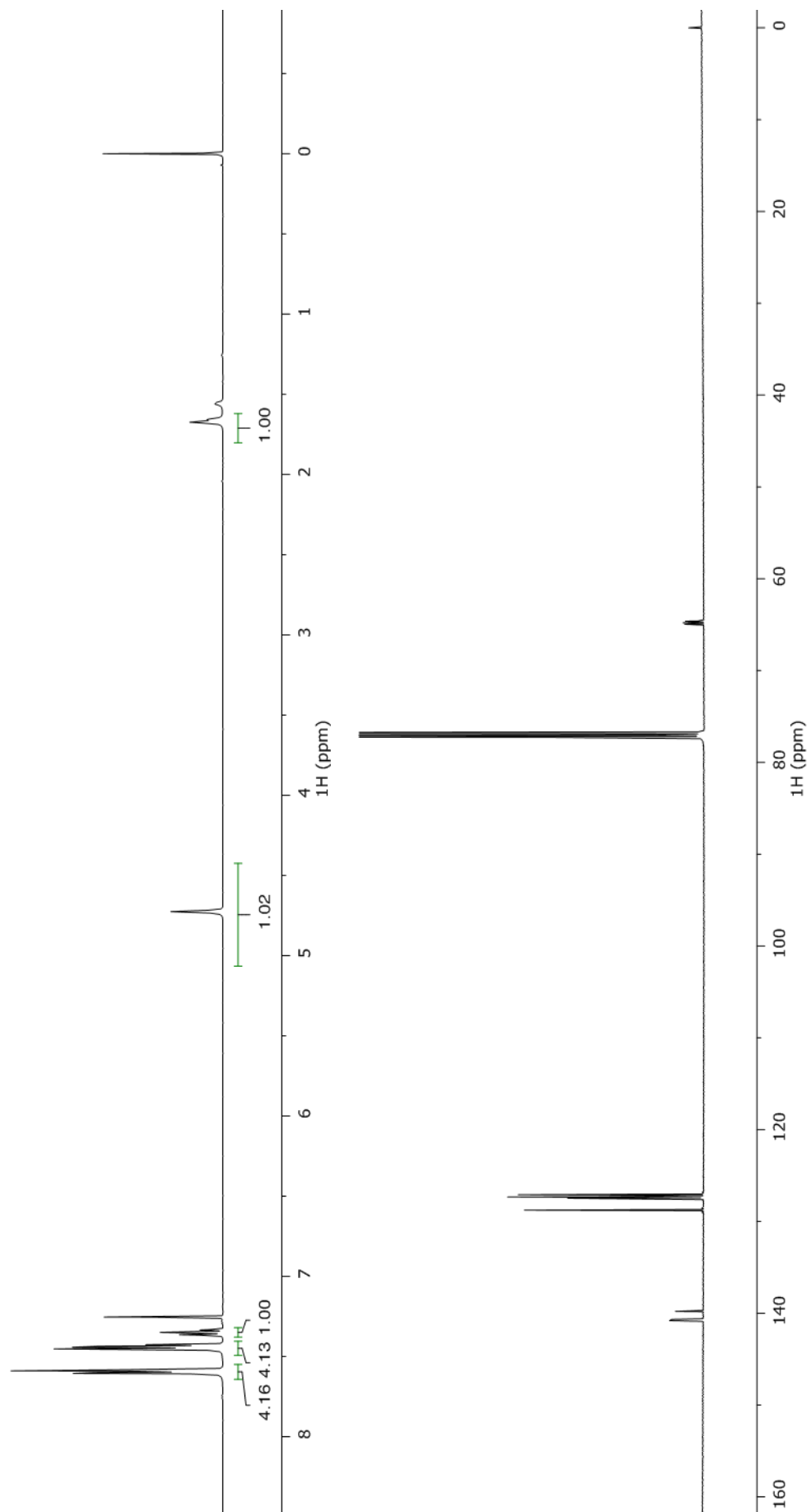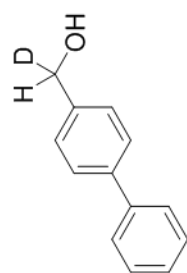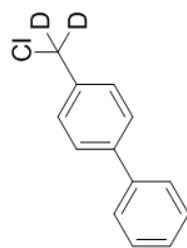
D5. Stoichiometric Experiments

Stoichiometric reductive elimination reactions were assembled in the glovebox. 200 μL stock solution of 10 mM [Pd(η^3-cinnamyl)(OAc)]$_2$ in toluene-d_8 was added to an NMR tube. An additional 200 μL of a stock solution of 20 mM DAF in toluene-d_8 was then layered on top. The NMR was then capped and removed from the glovebox. 5 μL of AcOH (88 μmol, 0.22 M) and/or 22 μL of allylbenzene (166 μmol, 0.42 M) was then added to the NMR directly but no special precautions were taken to exclude O$_2$ or moisture after assembly in the glove box.
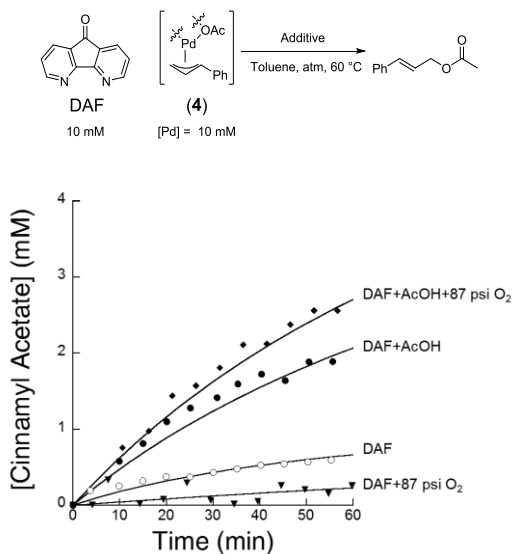
Stoichiometric reductive elimination reactions with O$_2$ were performed using a reaction apparatus from Wilmad-LabGlass. The NMR tube used was a 5 mm heavy wall precission pressure/vacuum NMR tube with a 1.4 mm I.D. fitted with a glass connector and PTFE valve (522-PV). A stainless steel manifold was constructed using Swagelok components to interface the NMR tube with a high pressure O$_2$ regulator. The pressure of the atmosphere was determined by a digital pressure transducer from Omega (500 psi, USB, part # PX409-500AUSBH) using Omega's USB output pressure transducer data logging and chart recording software v. 1.0.13.1030 on a Windows XP desktop computer.
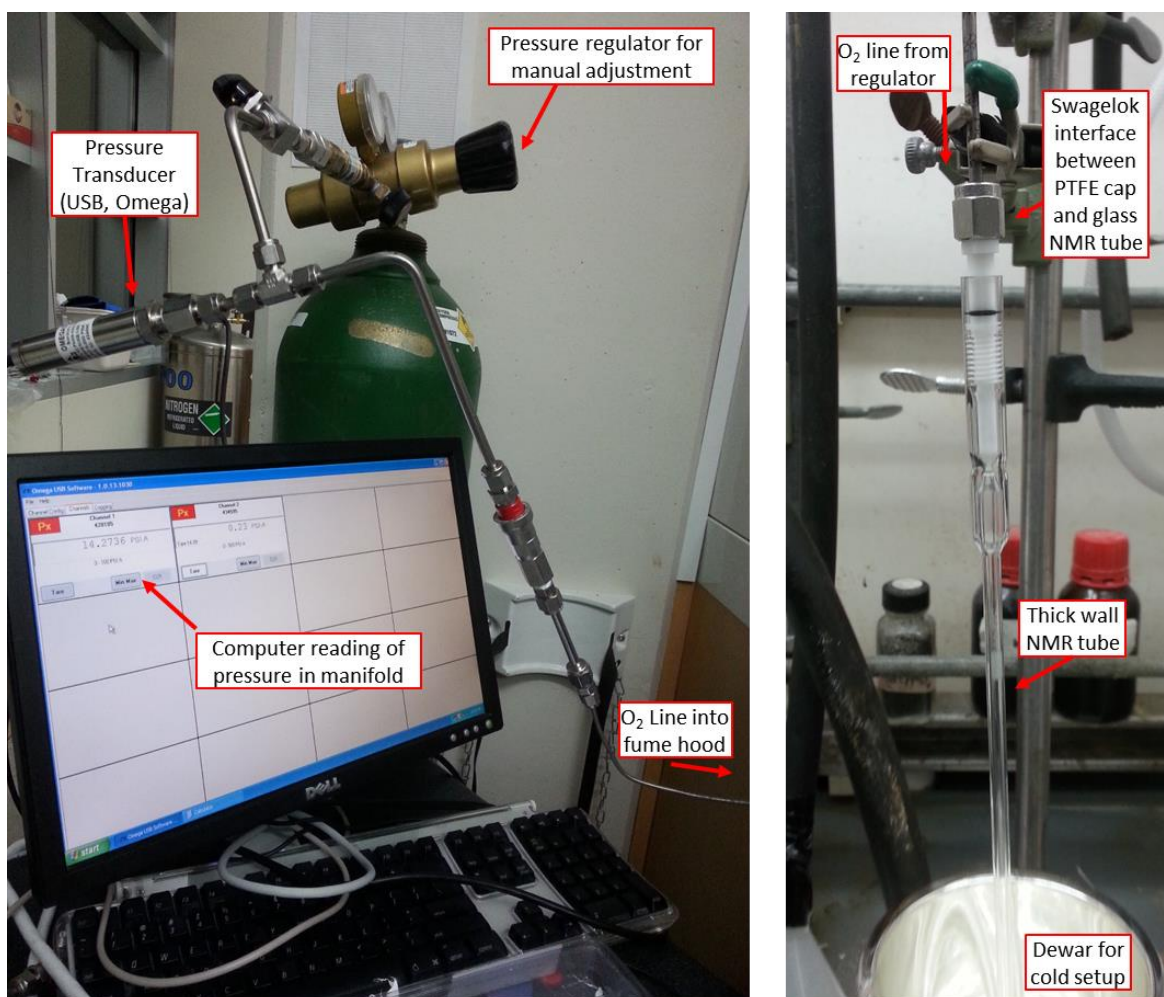
Figure D 7: NMR Tube Pressurization Manifold
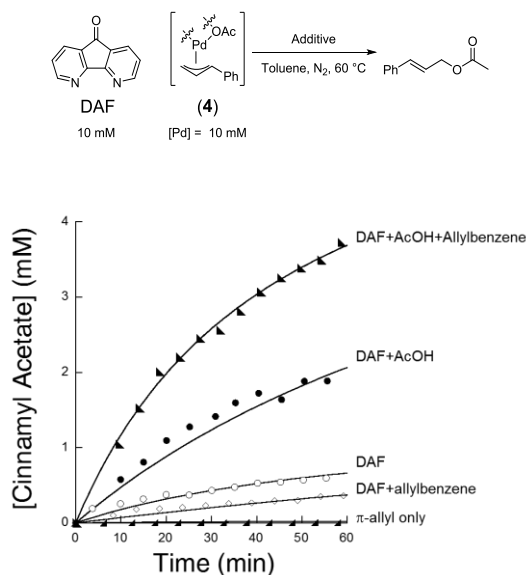
Figure D 8: Stoichiometric Reductive Elimination Experiments with DAF and [Pd(cinnamyl)(OAc)]₂ (**4**).Time course analysis of the addition of DAF, allylbenzene and AcOH Conditions: [Pd(cinnamyl)(OAc)]₂ = 5 mM, [DAF] = 10 mM, [Allylbenzene] = 0.42 M, [AcOH] = 0.22 M, 60 °C, Toluene, N₂.


Figure D 9: Stoichiometric Reductive Elimination Experiments under O₂ with DAF and [Pd(cinnamyl)(OAc)]₂ (**4**) under aerobic conditions. A. Time course analysis of the addition of DAF, allylbenzene and AcOH Conditions: [Pd(cinnamyl)(OAc)]₂ = 5 mM, [DAF] = 10 mM, [AcOH] = 0.22 M, 60 °C, Toluene.

D6. X-Ray Absorption Spectroscopy Experimental Details

D6.1 Determination of E° and Fitting of XANES

Data was acquired on the 10-ID line at the Advanced Photon Source of Argonne National Laboratories. This beamline is a high photon flux beamline and allows for real-time acquisition of dilute of metals solutions. K-edge and EXAFS data was measured for all samples over the edge region of 24.10 keV to 25.1 keV. Raw data was analyzed using Athena (Ifeffit 1.2.11d), a program from the Demeter XAS analysis suite vers. 0.9.24 by Ravel and Newell.[2] K-edge and EXAFS data was measured for all samples over the edge region of 24.10 keV to 25.1 keV. All samples were referenced to Pd-foil at 24.3500 keV by calibrating one reference foil and then aligning all other references and adjusting the spectra correspondingly the shift in the reference shift in Athena. Using data with excessive points or too few in the extended region could greatly impact normalization and subsequently fits so so data, including references during spectral alignment, were truncated where appropriate to provide consistent referencing. It is important to check the height of the edge as well as alignment of the 1st derivative.

Spectra were then normalized and exported to Igor Pro (vers. 6.3.7.2) where the edge was then smoothed with a binomial smoothing algorithm 6 times. The first derivative was obtained via a central difference algorithm and an E° value was determined by fitting two Gaussian curves and determining the maximum of the first Gaussian.[3] The edge energy, E°, was reported as the maximum of the first Guassian (first inflection point of the edge) and E^1 was reported as the maximum of the second Gaussian (second inflection point of the edge).
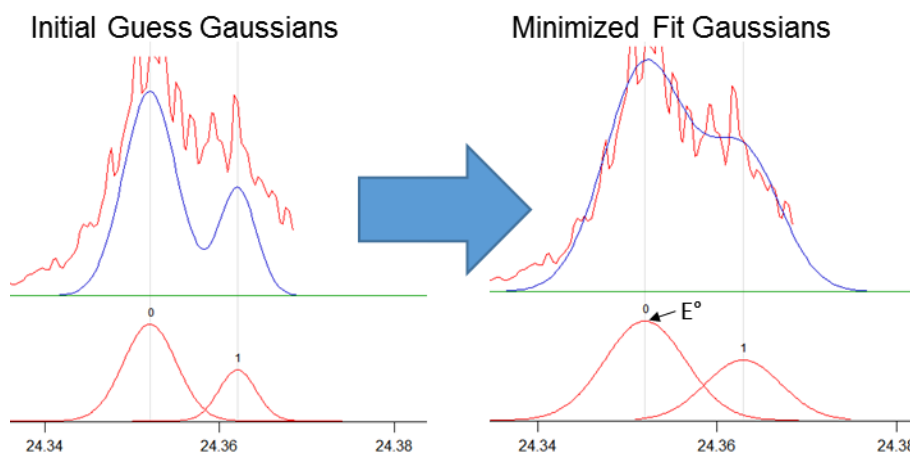
Figure D 10: Representation Example of Gaussians Fit to Smoothed 1st Derivative. E° and E^1 were assigned by determining the maximum of the two Gaussians.

Linear combination of references for the XANES edge was performed using the fitting package included in Athena.

Fitting output is as follows:

LCF fit of merge ss as flattened mu(E) from 24336.718 to 24386.718

Fit included 127 data points and 1 variables, and approximately 6.454 measurements

Weights sum to 1: yes

Weights forced between 0 and 1: yes
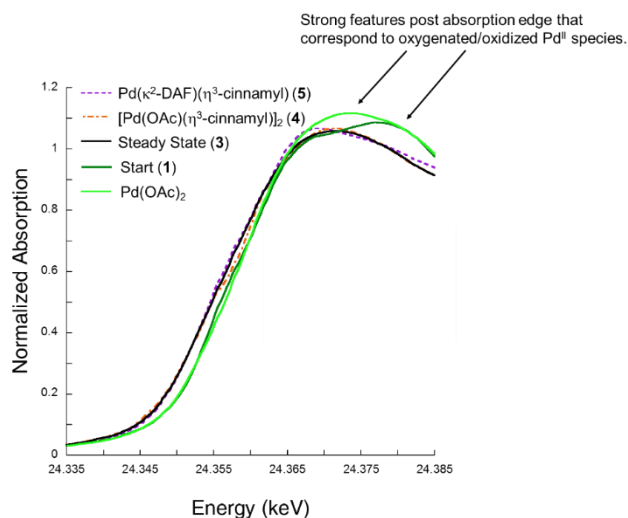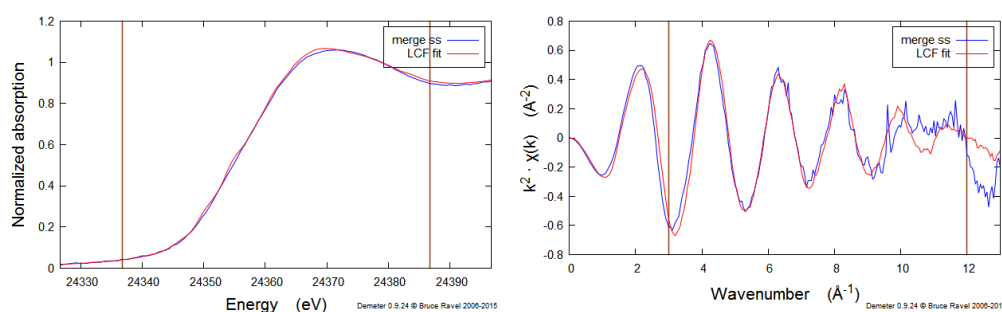
Overall e0 shift used: no

Noise added to data: 0

R-factor = 0.0006406

Chi-square = 0.01231

Reduced chi-square = 0.0000962

. standard	weight	e0 adjustment
. Pd_UWis_Pd_DAF_CinnamylAllyl_BF4_AirRT_Compound-4.001	0.584 (0.041)	0.000 (0.000)
. Jon-Pd_allyl_acetate_Pd_001.dat	0.416 (0.104)	0.000 (0.000)
	Sum 1.000	



Figure D 11: Overlaid XANES region of steady state, π-allyl references (4) and (5), DAF/Pd(OAc)$_2$ starting reaction mixture (1) and solid Pd(OAc)$_2$. A strong feature was observed in the region immediately following the absorption edge which is consistent with the highly oxidized nature of the (1) and Pd(OAc)$_2$ references.
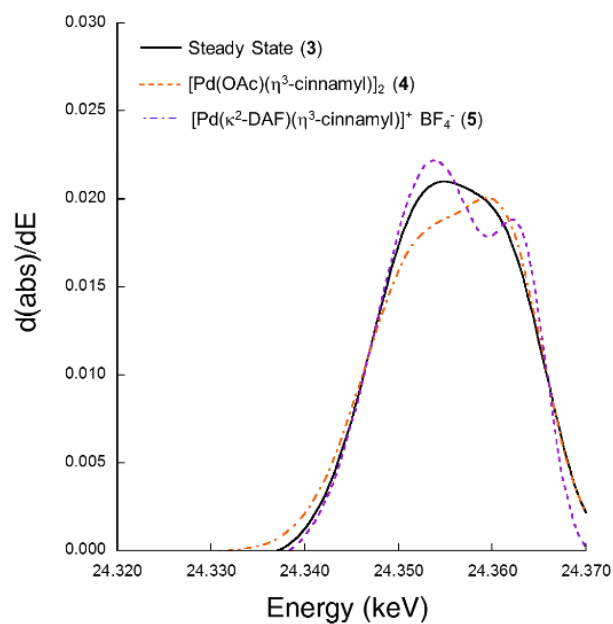
Figure D 12: Overlay of the fit gaussians of the two Pd π-allyl references (**4**) and (**5**) with the steady state (3).

D6.2 Illustrative EXAFS for 9 minutes and Steady State

A.   B.
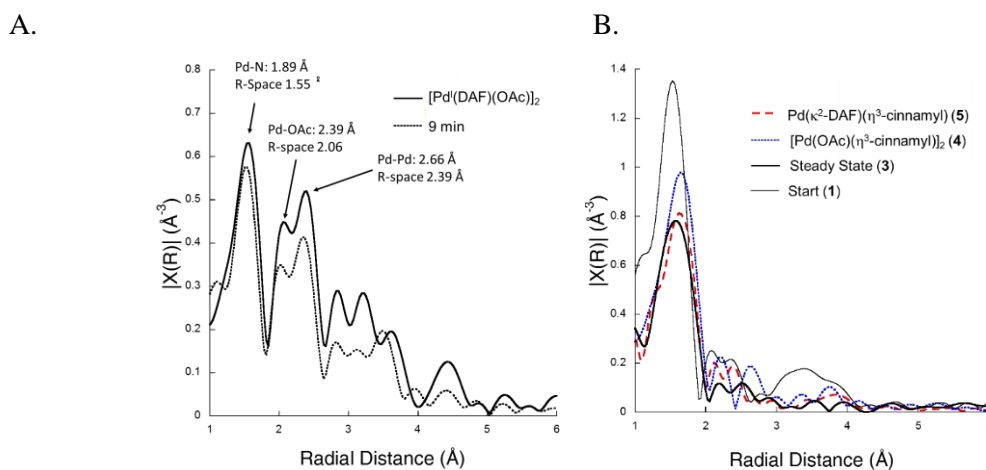
Figure D 13: EXAFS of the reaction at the starting 9 minutes and steady state. A. Starting 9 minutes compared to the $[Pd^I(DAF)(OAc)]_2$ (**2**) reference B. Comparison of π-allyl references (**4**) and (**5**), starting reaction mixture (**1**) without allylbenzene and steady state (**3**).

D6.3 Reactor Design and Reaction Experimental

A reactor was designed using PEEK as it tolerates high temperatures, a variety of solvents (such as ethereal and acidic solvents), and does not readily absorb x-ray photons. Additionally a simple heating block was crafted to interface with the reaction vessel and allow for the passage of heating fluid. Reactor designed with consultation with Steve Myers at the UW Madison Chemistry machine shop with assistance from Dr. Nick Beach. Reactor manifold was constructed by the machine shop while the PEEK cell and heating block were constructed by Jonathan Jaworski with assistance from Dr. Nick Beach and Kendall Schneider.

The reaction was performed by using an O_2 balloon with a needle through a pierced septum. A UV-Vis dip probe from (StellarNet Inc., DP400-VISNR) utilized with Blue-Wave spectrometer to collect UV-Vis data. The probe was pierced through a septum (**Figure D 14**) and real time absorbance data was collected. It was determined that a dilute solution of >5 mM Pd minimum provided adequate signal to noise at the 10-ID line and the reactor apparatus. The reaction was performed at a higher temperature of 80 °C but otherwise identical to the reaction conditions reported in the initial communication with a concentration of 13.5 mM $Pd(OAc)_2$ in a 3:1 Dioxane/AcOH solvent mixture.[4] A reaction volume of 3 mL was used. A stir rate of 700 rpm was utilized as higher stir rates resulted in strong vortexing where the solution was leaving the acquisition window (**Figure D 15**). The StellarNet Inc. dip probe is not recommended for this application and severely compromised after several uses. We have since switched to the Ocean Optics TL-300 with DH-2000 light source in combination with the StellarNet Inc. Blue-Spectrometer.
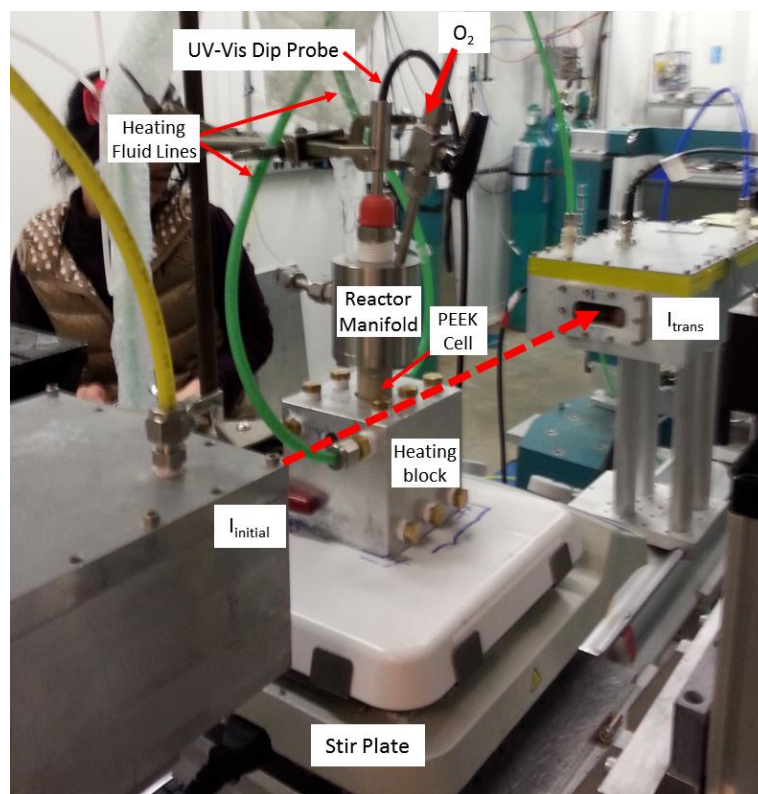
Figure D 14: Assembled reaction set up on the 10-ID line at Argonne
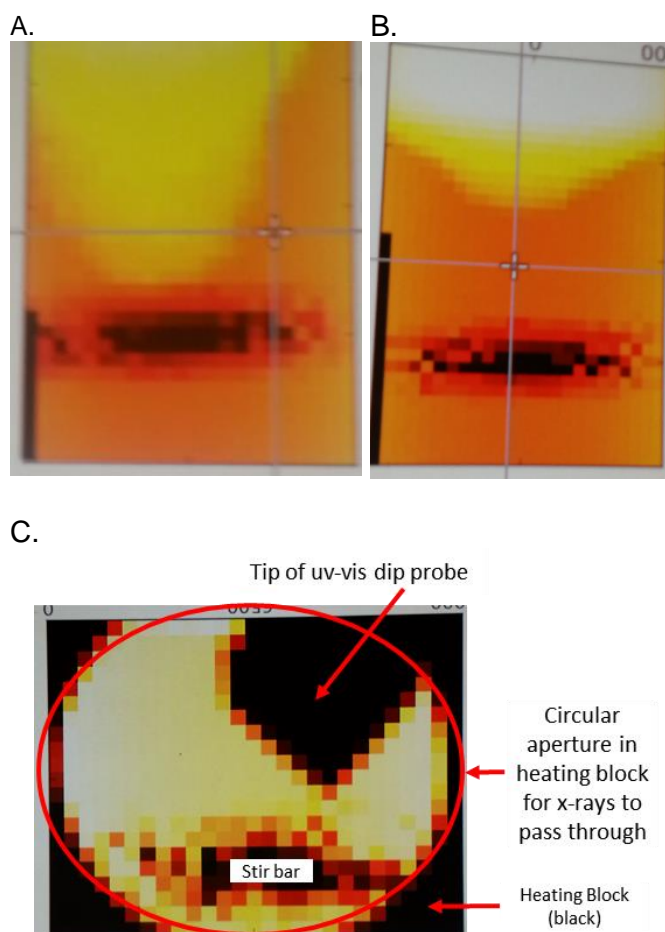
Figure D 15: Heat map for the reactor with 13.5 mM Pd(OAc)$_2$ in 3:1 Dioxane/AcOH. Orange color corresponds to absorbance and white corresponds to complete transmission. Dark bar at the bottom of the heat map is the stir bar. Figure D6A and D6B correspond to the PEEK cell alone with at 13.5 mM Pd(OAc)$_2$ solution. A. Extreme vortexing at 1600 rpm B. Moderate vortexing at 700 rpm C. Reaction apparatus completely assembled at temperature and dip probe immersed and stirring at 700 rpm.

Y

X

Gview:TOP   WCS:TOP   Cplane:TOP

1.0000
Inch
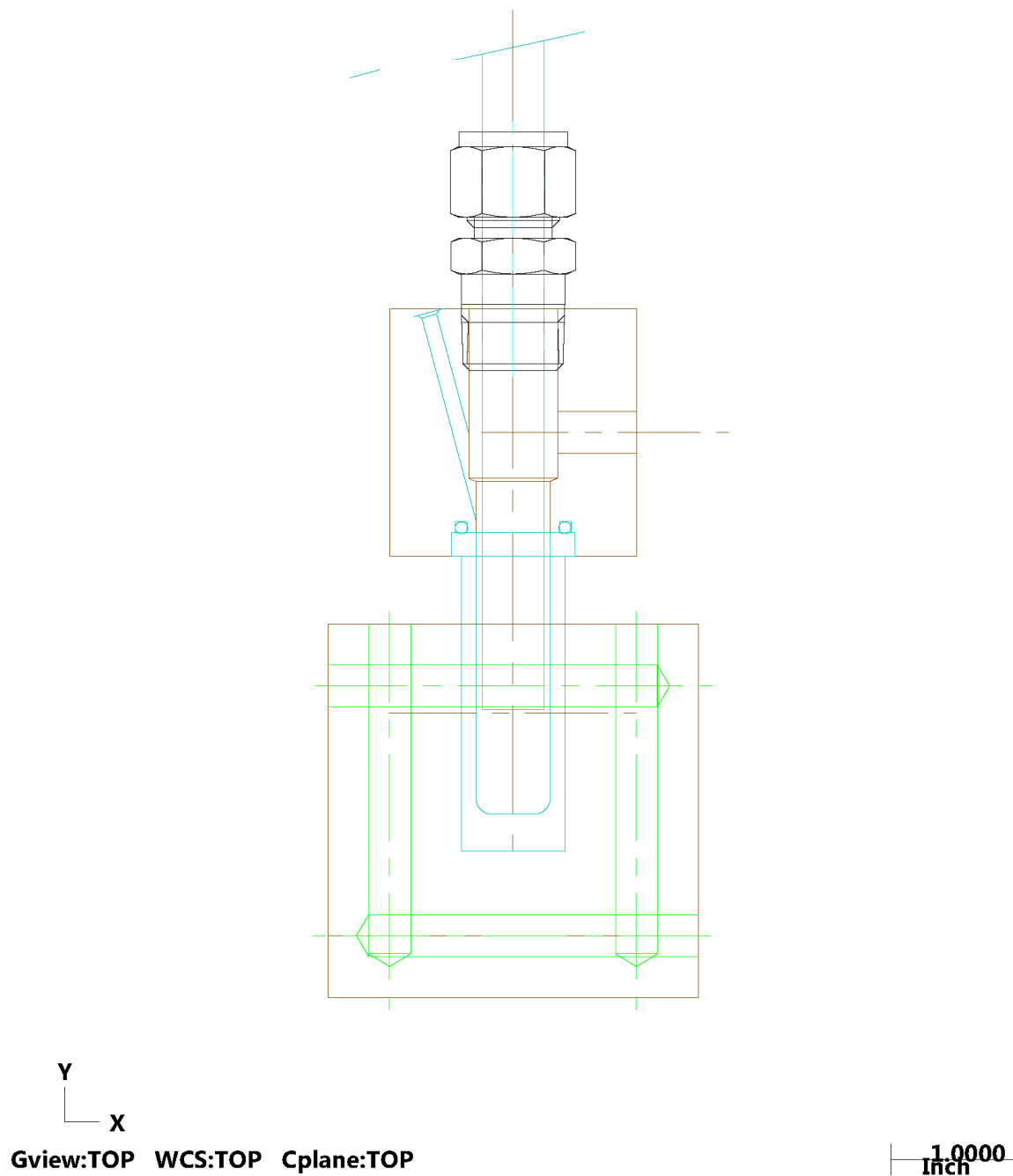
Figure D 16: Assembled Reaction Apparatus Schematic
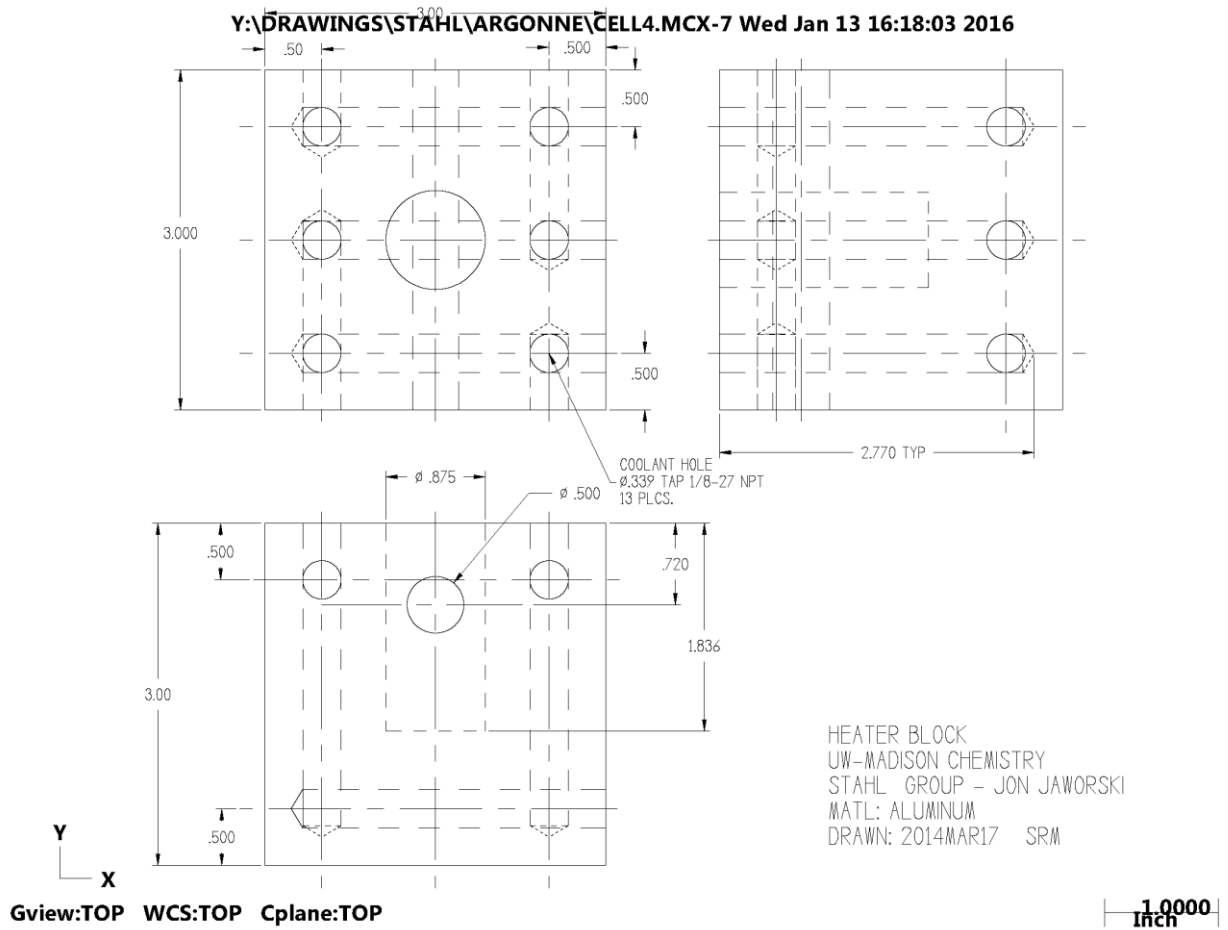
Figure D 17: Heating Block Schematic

Gview:TOP   WCS:TOP   Cplane:TOP
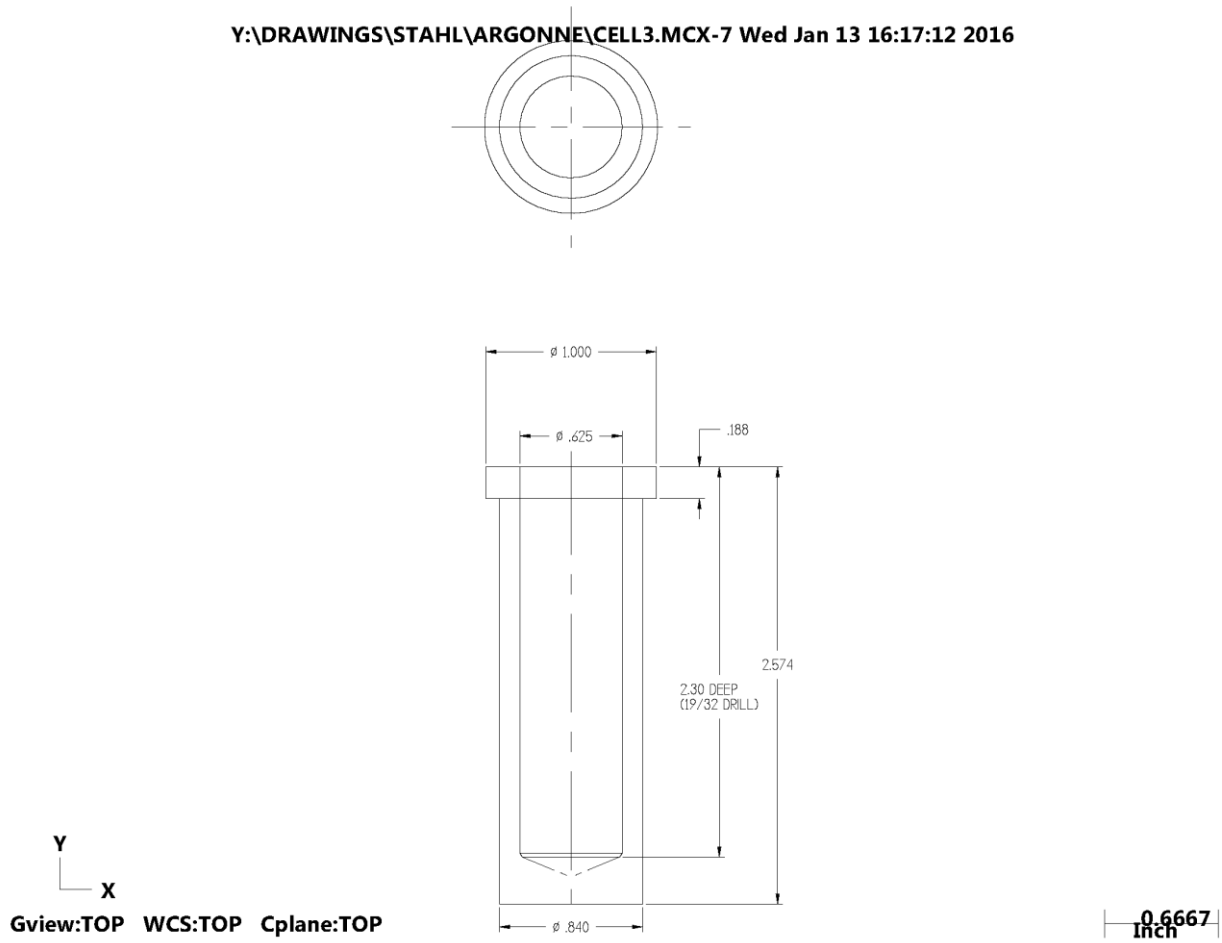
Figure D 18: PEEK Cell Schematic

Figure D 19: Reactor Manifold Schematic

D7. Characterization of π-allyls

D7.1 Synthesis of [Pd(η³-cinnamyl)(μ-OAc)]₂

Synthesis of [Pd(cinnamyl)(OAc)]₂ (**4**) was performed using [Pd(η³-cinnamyl)Cl]₂ with 2 equiv of AgOAc in DCM analogously to White co-workers to provide near quantitative crude yield.[5] The reaction was carried out in the glovebox and the reaction vessel was wrapped in aluminum foil to block light. Th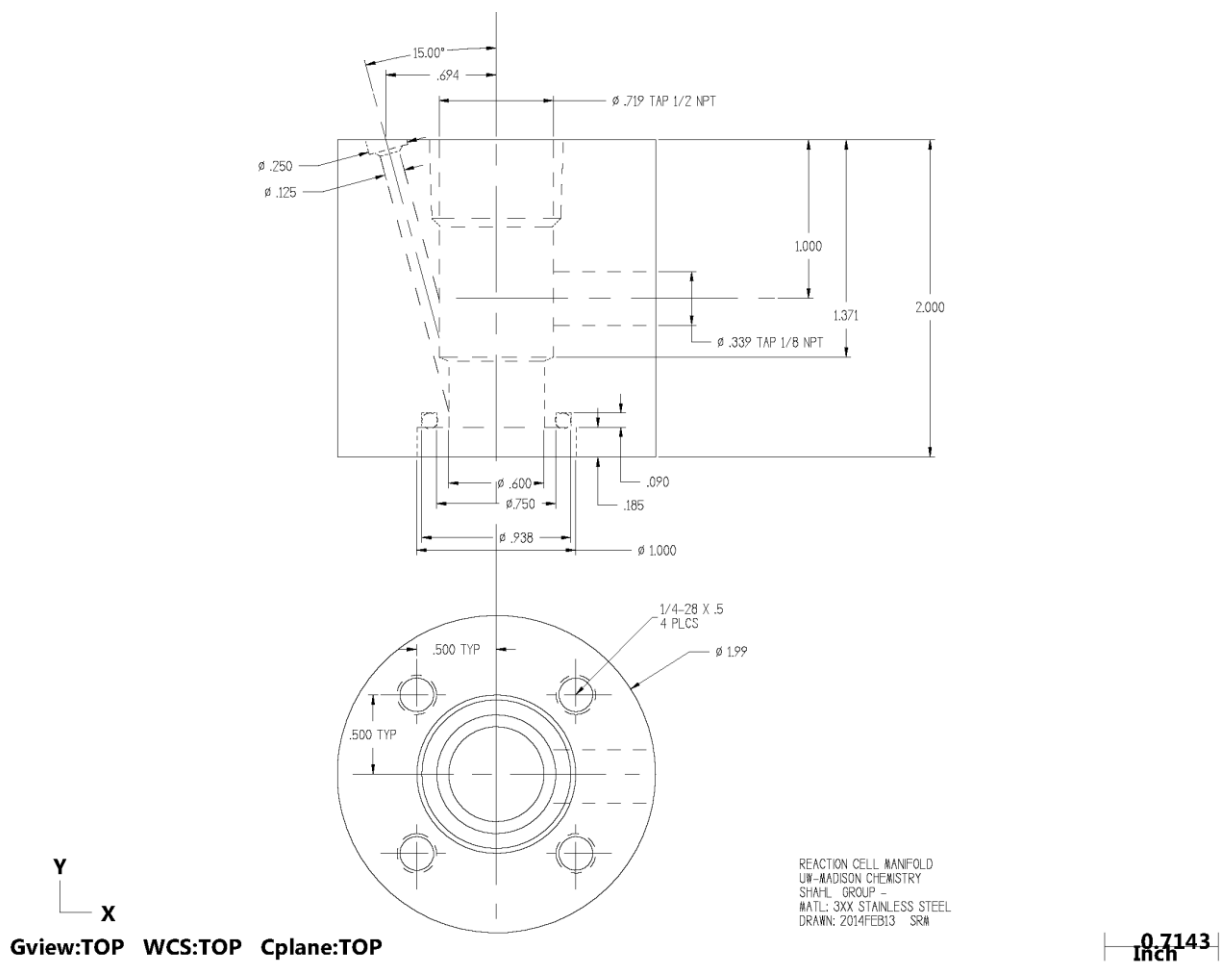e reaction mixture was filtered through a 0.45 μm PTFE syringe filter after an hour and concentrated *in vacuo*. Purification was necessary to remove small impurities. Crystallization from DCM/pentanes at -20 °C to give a bright yellow solid allowed for a 70% recovery.
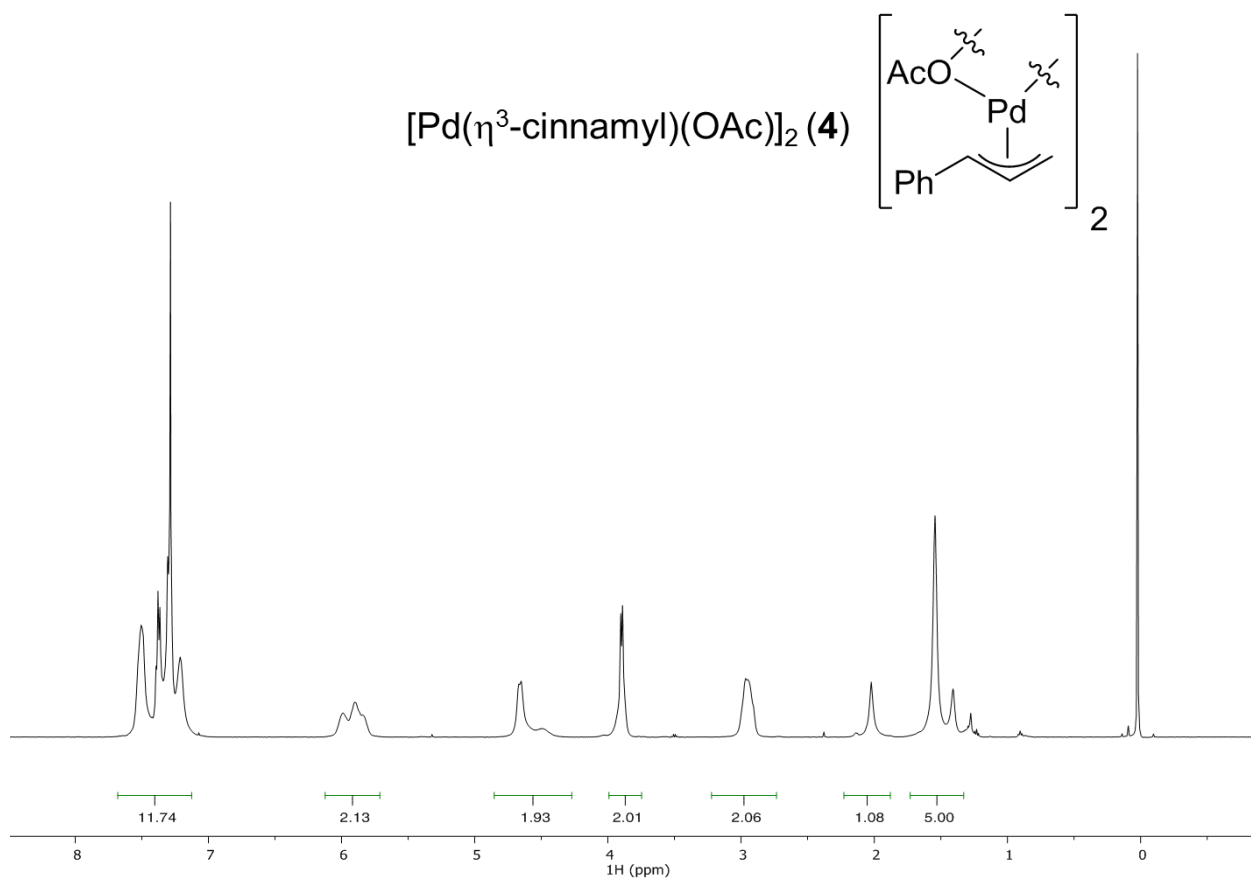
Figure D 20: ¹H NMR Spectrum of [Pd(η³-cinnamyl)(μ-OAc)]₂ (**4**) in CDCl₃ at 24 °C

D7.2 X-ray Structure of [Pd(η^3-cinnamyl)(μ-OAc)]$_2$

Data Collection

A yellow crystal with approximate dimensions $0.131 \times 0.089 \times 0.07$ mm^3 was selected under oil under ambient conditions and attached to the tip of a MiTeGen MicroMount©. The crystal was mounted in a stream of cold nitrogen at 100(1) K and centered in the X-ray beam by using a video camera.

The crystal evaluation and data collection were performed on a Bruker Quazar SMART APEXII diffractometer with Mo K$_\alpha$ ($\lambda = 0.71073$ Å) radiation and the diffractometer to crystal distance of 4.96 cm.[6]

The initial cell constants were obtained from three series of ω scans at different starting angles. Each series consisted of 12 frames collected at intervals of 0.5° in a 6° range about ω with the exposure time of 10 seconds per frame. The reflections were successfully indexed by an automated indexing routine built in the APEXII program suite. The final cell constants were calculated from a set of 9731 strong reflections from the actual data collection.

The data were collected by using the full sphere data collection routine to survey the reciprocal space to the extent of a full sphere to a resolution of 0.70 Å. A total of 56285 data were harvested by collecting 6 sets of frames with 0.5° scans in ω and φ with exposure times of 20 sec per frame. These highly redundant datasets were corrected for Lorentz and polarization effects. The absorption correction was based on fitting a function to the empirical transmission surface as sampled by multiple equivalent measurements.[7]

Structure Solution and Refinement

The systematic absences in the diffraction data were uniquely consistent for the space group $P2_12_12_1$ that yielded chemically reasonable and computationally stable results of refinement.[8]

A successful solution by the direct methods provided most non-hydrogen atoms from the E-map. The remaining non-hydrogen atoms were located in an alternating series of least-squares cycles and difference Fourier maps. All non-hydrogen atoms were refined with anisotropic displacement coefficients unless specified otherwise. All hydrogen atoms were included in the structure factor calculation at idealized positions and were allowed to ride on the neighboring atoms with relative isotropic displacement coefficients.

There is positional disorder present at the sites of both allyl ligands. The disorder manifested itself by the presence of small peaks of electron density in the difference Fourier map around the allyl groups, but not in the vicinity of the phenyl rings. Thus, for each ligand, the disorder was modelled at the positions of two C atoms of the allyl groups only. The existing Ph rings were refined at 100% site occupancy. Atoms C2 and C3 are disordered over two positions with the major component present 79.8(12)% of the time. Atoms C15 and C16 are disordered over two positions with the major component present 86.4(12)% of the time. The C atoms of the minor disorder components were refined isotropically. Distance restraints were applied to the disordered components.

The crystal is an inversion twin. The minor component is present 41(4)% of the time.

The final least-squares refinement of 276 parameters against 6420 data resulted in residuals R (based on F^2 for $I \geq 2\sigma$) and wR (based on F^2 for all data) of 0.0270 and 0.0646, respectively.

Summary Crystal Data for $C_{22}H_{24}O_4Pd_2$ ($M = 565.21$ g/mol): orthorhombic, space group $P2_12_12_1$(no. 19), $a = 9.804(3)$ Å, $b = 13.105(3)$ Å, $c = 16.366(5)$Å, $V = 2102.5(11)$Å^3, $Z = 4$, $T = 100.0$K, μ(MoKα)= 1.735 mm^{-1}, $Dcalc = 1.786$ g/cm^3, 56285 reflections measured ($3.982° \leq 2\Theta \leq 61.14°$), 6420 unique ($R_{int} = 0.0354$, $R_{sigma} = 0.0229$) which were used in all calculations. The final R_1 was 0.0270 ($I > 2\sigma(I)$) and wR_2 was 0.0646 (all data).
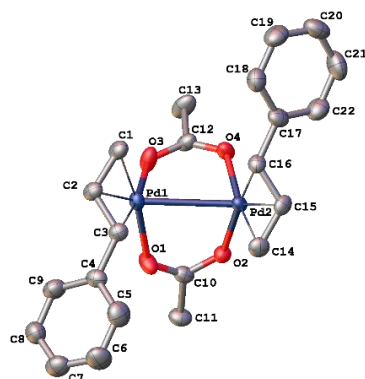
Figure D 21: A molecular drawing of [Pd(η^3-cinnamyl)(μ-OAc)]$_2$ shown with 50% probability ellipsoids. All H atoms and minor disorder components are omitted.
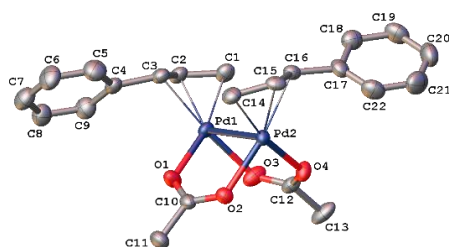
Figure D 22: A molecular drawing of [Pd(η^3-cinnamyl)(μ-OAc)]$_2$ shown with 50% probability ellipsoids. All H atoms and minor disorder components are omitted.
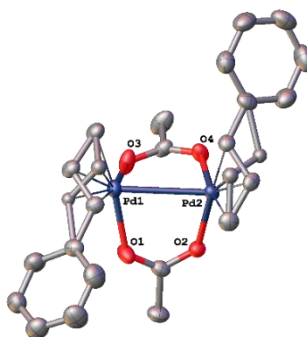

Figure D 23: A molecular drawing of [Pd(η^3-cinnamyl)(μ-OAc)]$_2$ shown with 50% probability ellipsoids. All H atoms are omitted but both disorder components are shown.

Table D 1: Crystal data and structure refinement for [Pd(η^3-cinnamyl)(μ-OAc)]$_2$.

Identification code	stahl222
Empirical formula	$C_{22}H_{24}O_4Pd_2$
Formula weight	565.21
Temperature/K	100.0
Crystal system	orthorhombic
Space group	$P2_12_12_1$
a/Å	9.804(3)
b/Å	13.105(3)
c/Å	16.366(5)
α/°	90
β/°	90
γ/°	90
Volume/Å^3	2102.5(11)
Z	4
ρ_{calc}g/cm^3	1.786
μ/mm^{-1}	1.735
F(000)	1120.0
Crystal size/mm^3	$0.131 \times 0.089 \times 0.07$
Radiation	MoKα (λ = 0.71073)
2Θ range for data collection/°	3.982 to 61.14
Index ranges	$-14 \le h \le 14$, $-18 \le k \le 18$, $-23 \le l \le 23$
Reflections collected	56285
Independent reflections	6420 [R_{int} = 0.0354, R_{sigma} = 0.0229]
Data/restraints/parameters	6420/8/276
Goodness-of-fit on F^2	1.036
Final R indexes [I>=2σ (I)]	R_1 = 0.0270, wR_2 = 0.0636
Final R indexes [all data]	R_1 = 0.0307, wR_2 = 0.0646
Largest diff. peak/hole / e Å^{-3}	1.73/-0.75
Flack parameter	0.42(4)

D7.3 Synthesis of [Pd(κ^2-DAF)(η^3-cinnamyl)]BF$_4$

Synthesis of [Pd(κ^2-DAF)(η^3-cinnamyl)]BF$_4$ was performed using [Pd(η^3-cinnamyl)Cl]$_2$ (106 mg, 0.21 mmol) with 2 equiv of AgBF$_4$ (79 mg, 0.41 mmol) and 1 eq DAF (75 mg, 0.41 mmol) in DCM.[4] The reaction was carried out in the glovebox and the reaction vessel was wrapped in aluminum foil to block light. The reaction mixture was filtered through a 0.45 µm PTFE syringe filter after an hour and concentrated *in vacuo*. The crude was then crystallized by liquid diffusion using pentanes in DCM. 65 mg was obtained for a 44% yield. The complex appeared pale yellow. The complex has very low solubility in CDCl$_3$ and marginally more in DCM. The BARF salt was more soluble however appeared to be less stable in solution.
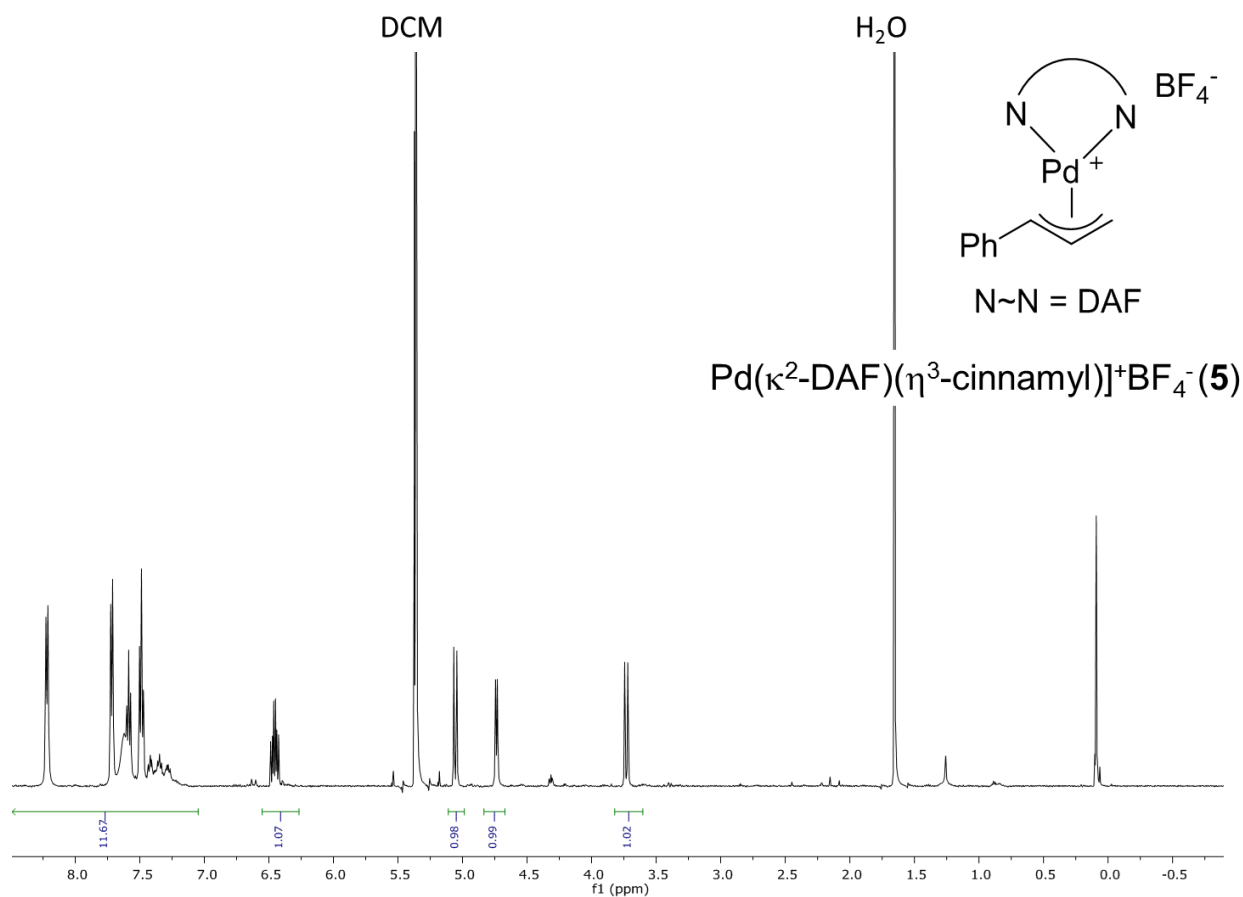
Figure D 24: ^{1}H NMR Spectrum of Pd(κ^2-DAF)(η^3-cinnamyl)]BF$_4$ (**5**) in CD$_2$Cl$_2$ at -20 °C

D7.4 X-ray Structure of [Pd(κ^2-DAF)(η^3-cinnamyl)]BF$_4$

Data Collection

A pale yellow crystal with approximate dimensions 0.08 x 0.2 x 0.3 mm^3 was selected under oil under ambient conditions and attached to the tip of a MiTeGen MicroMount©. The crystal was mounted in a stream of cold nitrogen at 100(1) K and centered in the X-ray beam by using a video camera.

The crystal evaluation and data collection were performed on a Bruker Quazar SMART APEXII diffractometer with Mo K$_\alpha$ (λ = 0.71073 Å) radiation and the diffractometer to crystal distance of 4.96 cm.

The initial cell constants were obtained from three series of ω scans at different starting angles. Each series consisted of 12 frames collected at intervals of 0.5° in a 6° range about ω with the exposure time of 10 second per frame. The reflections were successfully indexed by an automated indexing routine built in the APEXII program suite. The final cell constants were calculated from a set of 9980 strong reflections from the actual data collection.

The data were collected by using the full sphere data collection routine to survey the reciprocal space to the extent of a full sphere to a resolution of 0.73 Å. A total of 31196 data were harvested by collecting 5 sets of frames with 0.5° scans in ω and φ with an exposure time 60 sec per frame. These highly redundant datasets were corrected for Lorentz and polarization effects. The absorption correction was based on fitting a function to the empirical transmission surface as sampled by multiple equivalent measurements.[9]

Structure Solution and Refinement

The systematic absences in the diffraction data were uniquely consistent for the space group $C2/c$ that yielded chemically reasonable and computationally stable results of refinement.[10]

A successful solution by the direct methods provided most non-hydrogen atoms from the E-map. The remaining non-hydrogen atoms were located in an alternating series of least-squares cycles and difference Fourier maps. All non-hydrogen atoms were refined with anisotropic displacement coefficients. All hydrogen atoms were included in the structure factor calculation at idealized positions and were allowed to ride on the neighboring atoms with relative isotropic displacement coefficients.

The Pd-π-allyl fragment was disordered over two positions with the major component contribution of 0.744(7). Bond distance restraints and thermal parameter constraints were applied to the disordered π-allyl molecule to ensure a chemically reasonable and computationally stable refinement.

The final least-squares refinement of 317 parameters against 4790 data resulted in residuals R (based on F^2 for $I \geq 2\sigma$) and wR (based on F^2 for all data) of 0.0442 and 0.1058, respectively. The final difference Fourier map had one noticeable peak (ca. 1.10 e/Å^3) in the vicinity of the palladium center and was considered to be noise.

Summary Crystal Data for $C_{20}H_{15}BF_4N_2OPd$ (M =492.55 g/mol): monoclinic, space group C2/c (no. 15), a = 18.3325(5) Å, b = 9.5102(3) Å, c = 20.9624(5) Å, β = 95.6799(14)°, V = 3636.76(17) Å^3, Z = 8, T = 99.92 K, μ(MoKα) = 1.074 mm^{-1}, $Dcalc$ = 1.799 g/cm^3, 30039 reflections measured (3.906° $\leq 2\Theta \leq$ 57.968°), 4790 unique (R_{int} = 0.0407, R$_{sigma}$ = 0.0306) which were used in all calculations. The final R_1 was 0.0442 (I > 2σ(I)) and wR_2 was 0.1058 (all data).
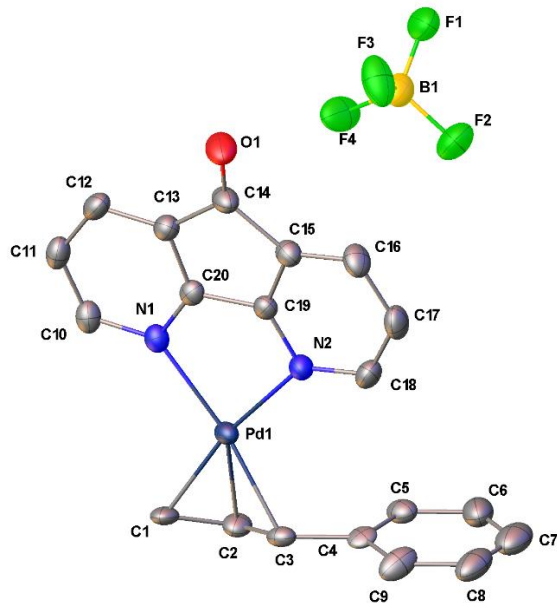
Figure D 25: A molecular drawing of the Palladium complex of [Pd(κ^2-DAF)(η^3-cinnamyl)]BF$_4$ shown with 50% probability ellipsoids. All H atoms and minor components of the disordered atoms are omitted.
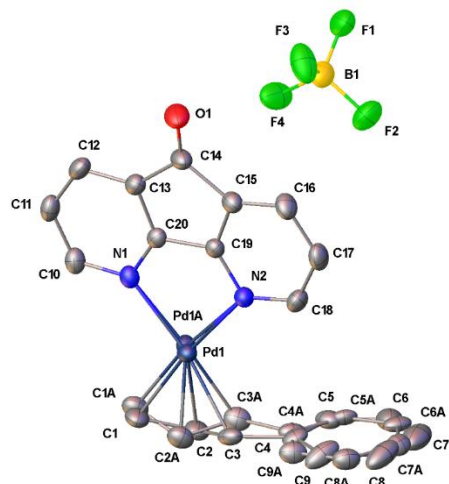
Figure D 26: A molecular drawing of the asymmetric unit of [Pd(κ^2-DAF)(η^3-cinnamyl)]BF$_4$ with all disordered parts shown with 50% probability ellipsoids. All H atoms are omitted.

Table D 2: Crystal data and structure refinement for [Pd(κ^2-DAF)(η^3-cinnamyl)]BF$_4$

Identification code	stahl208
Empirical formula	$C_{20}H_{15}BF_4N_2OPd$
Formula weight	492.55
Temperature/K	99.92
Crystal system	monoclinic
Space group	C2/c
a/Å	18.3325(5)
b/Å	9.5102(3)
c/Å	20.9624(5)
α/°	90
β/°	95.6799(14)
γ/°	90
Volume/Å^3	3636.76(17)
Z	8
ρ_{calc}g/cm^3	1.799
μ/mm^{-1}	1.074
F(000)	1952.0
Crystal size/mm^3	$0.3 \times 0.2 \times 0.08$
Radiation	MoKα ($\lambda = 0.71073$)
2Θ range for data collection	3.906 to 57.968
Index ranges	$-24 \leq h \leq 24, -12 \leq k \leq 12, -28 \leq l \leq 28$
Reflections collected	30139
Independent reflections	4805 [$R_{int} = 0.0407$, $R_{sigma} = 0.0307$]
Data/restraints/parameters	4805/154/329
Goodness-of-fit on F^2	1.189
Final R indexes [I>=2σ (I)]	$R_1 = 0.0475$, $wR_2 = 0.1109$
Final R indexes [all data]	$R_1 = 0.0535$, $wR_2 = 0.1139$
Largest diff. peak/hole / e Å^{-3}	1.21/-1.67

1. Same prep was used for monitoring the amidation reaction, see White, P. B.; Jaworski, J. N.; Geyunjian, H. Z.; Stahl, S. S., *ACS Catal.* **2016**, *6*, 3340-3348.
2. B. Ravel and M. Newville, ATHENA, ARTEMIS, HEPHAESTUS: data analysis for X-ray absorption spectroscopy using IFEFFIT, Journal of Synchrotron Radiation 12, 537–541 (2005) doi:10.1107/S0909049505012719
3. (a) Bearden, J. A.; Burr, A.F., *Rev.Mod.Phys.* **1967**, *39*, 125-142 (b) *Reference X-Ray Spectra of Metal Foils*, Exafs Materials, Danville, CA.
4. Campbell, A. N.; White, P. B.; Guzei, I. A.; Stahl S. S. *J. Am. Chem. Soc.* **2010**, *132*, 15116–15119.
5. Chen, M. S.; Prabagaran, N.; Labenz, N. A.; White, M. C., *J. Am. Chem. Soc.* **2005,** *127*, 6970-6971
6. Bruker-AXS (2015). APEX3. Version 2015.9-0. Madison, Wisconsin, USA.
7. Krause, L., Herbst-Irmer, R., Sheldrick, G. M. & Stalke, D. *J. Appl. Cryst.* **2015**, *48*. 3-10.
8. (a) Sheldrick, G. M. (2013b). XPREP. Version 2013/1. Georg-August-Universität Göttingen, Göttingen, Germany. (b) Sheldrick, G. M. (2013a). The SHELX homepage, http://shelx.uni-ac.gwdg.de/SHELX. (c) Sheldrick, G. M. *Acta Cryst. A*, **2015a**, *71*, 3-8. (d) Sheldrick, G. M. *Acta*

Cryst. C, **2015b**, *71*, 3-8. (e) Dolomanov, O. V., Bourhis, L. J., Gildea, R. J., Howard, J. A. K. & Puschmann, H. *J. Appl. Crystallogr.*, **2009**, *42*, 339-341. (f) Guzei, I. A. (2007-2013). Programs Gn. University of Wisconsin-Madison, Madison, Wisconsin, USA.

9. Bruker-AXS. (2007-2013) APEX2 (Ver. 2013.2-0), SADABS (2012-1), and SAINT+ (Ver. 8.30C) Software Reference Manuals. Bruker-AXS, Madison, Wisconsin, USA.

10. (a) Sheldrick, G. M. *Acta Cryst*. **2008**, *A64*, 112-122. (b) Sheldrick, G.M., *Acta Cryst.* **2015**, *C71*, 3-8. (c) Dolomanov, O.V.; Bourhis, L.J.; Gildea, R.J.; Howard, J.A.K.; Puschmann, H. "OLEX2: A complete structure solution, refinement and analysis program". *J. Appl. Cryst.* **2009**, *42*, 339-341.